UNIVERSIDADE FEDERAL DE SÃO CARLOS

CENTRO DE CIÊNCIAS EXATAS E TECNOLOGIA

PROGRAMA DE PÓS-GRADUAÇÃO EM ENGENHARIA QUÍMICA

ESTUDO SOBRE O DESEMPENHO DE VÁLVULAS NÃO-MECÂNICAS COMO ALIMENTADORES DE BIOMASSA RESIDUAL DE BORRA DE CAFÉ EM REATORES DE LEITO PNEUMÁTICO CIRCULANTE: EXPERIMENTAÇÃO E MODELAGEM VIA CFD-TFM

LUCAS MASSARO SOUSA

SÃO CARLOS – SP

2020

UNIVERSIDADE FEDERAL DE SÃO CARLOS

CENTRO DE CIÊNCIAS EXATAS E TECNOLOGIA

PROGRAMA DE PÓS-GRADUAÇÃO EM ENGENHARIA QUÍMICA

Lucas Massaro Sousa

Estudo Sobre o Desempenho de Válvulas Não-Mecânicas como Alimentadores de Biomassa Residual de Borra de Café em Reatores de Leito Pneumático Circulante: Experimentação e Modelagem via CFD-TFM

Tese de doutorado apresentada ao Programa de Pós-Graduação em Engenharia Química da Universidade Federal de São Carlos como parte dos requisitos necessários para a obtenção do título de Doutor em Engenharia Química.

Orientadora: Dra. Maria do Carmo Ferreira

SÃO CARLOS – SP

2020

UNIVERSIDADE FEDERAL DE SÃO CARLOS

Centro de Ciências Exatas e de Tecnologia
Programa de Pós-Graduação em Engenharia Química

Folha de Aprovação

Defesa de Tese de Doutorado do candidato Lucas Massaro Sousa, realizada em 24/08/2020.

Comissão Julgadora:

Profa. Dra. Maria do Carmo Ferreira (UFSCar)

Prof. Dr. Jose Teixeira Freire (UFSCar)

Prof. Dr. Rodrigo Béttega (UFSCar)

Prof. Dr. Marcos Antônio de Souza Barrozo (UFU)

Prof. Dr. Rodrigo Condotta (FEI)

O presente trabalho foi realizado com apoio da Coordenação de Aperfeiçoamento de Pessoal de Nível Superior - Brasil (CAPES) - Código de Financiamento 001.
O Relatório de Defesa assinado pelos membros da Comissão Julgadora encontra-se arquivado junto ao Programa de Pós-Graduação em Engenharia Química.

Dedico este trabalho aos meus pais, André e Elaine, com muito amor.

“O espírito sem limites é o maior tesouro do homem”. *(J. K. Rowling)*

AGRADECIMENTOS

A elaboração desta tese contou com o suporte intelectual e emocional de diversas pessoas e agradecer nominalmente a todos é uma tarefa árdua pela qual peço perdão antecipado no caso de eventuais lapsos de memória. Em especial, gostaria de agradecer:

Aos meus pais por todo o apoio, orientação e amor.

À Profª Maria do Carmo pela cuidadosa orientação desta tese, pelos ensinamentos e pelas conversas que colaboraram imensamente em minha formação pessoal e profissional.

Aos Profs. Aibing Yu e Qinfu Hou pelos ensinamentos e supervisão da etapa de simulação numérica em CFD deste trabalho no SIMPAS da *Monash University*.

Aos Profs. José Teixeira Freire, Fábio Freire, Thiago Faggion, Rodrigo Béttega e Gustavo Maia e aos técnicos Edilson Milaré, Oscar e Samuel pelos incentivos e colaboração no trabalho durante minha passagem pelo Centro de Secagem do DEQ/UFSCar.

Aos Profs. Ruiping Zou, Shibo Kuang, Jieqing Gan e Md Khan pelas discussões acadêmicas e acolhimento durante minha passagem pelo SIMPAS da *Monash University*.

Ao Prof. Rodrigo Condotta do Centro Universitário FEI pelas discussões e colaboração na determinação dos parâmetros de fluxo das borras de café com o reômetro.

Aos amigos do Centro de Secagem, do DEQ e do SIMPAS pelas conversas acadêmicas, companhia diária e bons momentos que nunca serão esquecidos.

Aos meus amigos de Itatiba, de São Carlos, da Graduação e da Austrália pelos momentos de alegria e descontração.

Por fim, agradeço à FAPESP (Processos 2016/25946-2 e 2018/11031-8) pelo suporte financeiro e confiança no trabalho.

SUMÁRIO

LISTA DE FIGURAS

Capítulo 7

LISTA DE TABELAS

Capítulo 6

Capítulo 7

RESUMO

A alimentação contínua e estável de materiais particulados sólidos a reatores é imprescindível para a cogeração de energia em processos industriais, por exemplo, utilizando resíduos de biomassa. Apesar disso, instabilidades na vazão de sólidos e bloqueio das partes móveis de alimentadores mecânicos são comumente reportados com esses materiais, impactando no desempenho, automação e segurança do processo. Desta forma, este trabalho teve como objetivo avaliar o desempenho de dispositivos não-mecânicos tipo válvula-L e tipo leito de jorro para promover a alimentação de borras de café a reatores tipo leito pneumático circulante (LPC). Inicialmente, foi realizada a caracterização física e de escoabilidade de borras de café secas com tamanhos médios entre 225 e 550 μm, bem como de amostras com umidades de até 60%. Algumas das propriedades determinadas foram: massa específica real e aparente, densidade *bulk*, velocidade de mínima fluidização, índice de Hausner, ângulo de repouso estático e dinâmico e ângulo de atrito interno efetivo. Em seguida, foram realizados experimentos de alimentação dos pós a reatores LPC em escala piloto (diâmetro e altura do *riser* de 21 mm e 2 m), disponíveis no Centro de Secagem/UFSCar, utilizando ambos os alimentadores. A fluidodinâmica dos sistemas operando com borras de café foi caracterizada por meio de medidas de pressão e vazão de sólidos (W_S) em diversas condições de operação, isto é, diferentes vazões de ar no *riser* e no alimentador, bem como com diferentes alturas entre o *riser* e a entrada de ar com o leito de jorro. Verificou-se, experimentalmente, W_S entre 0,6 e 10,0 g/s com a válvula-L e entre 1,2 e 11,0 g/s com o leito de jorro, assim como boa correlação entre W_S e a pressão medida nos alimentadores. O desempenho dos alimentadores foi relacionado com as propriedades das amostras, observando-se instabilidades no transporte e menores valores de W_S com as amostras de pior escoabilidade. Finalmente, concluiu-se que o leito de jorro foi mais

versátil que a válvula-L para a dosagem de borras de café secas e úmidas ao LPC utilizado. Os resultados experimentais foram utilizados para validar simulações baseadas na fluidodinâmica computacional, utilizando modelos do tipo duplo-fluido (*Two-Fluid Model*, TFM). A diferença entre a vazão de sólidos experimental e a simulada foi inferior a 20% para diversas condições de operação com os alimentadores. Com as simulações TFM validadas, verificou-se detalhes sobre a dinâmica de escoamento gás-sólido nas diversas regiões dos alimentadores e do *riser*, em termos de contornos de fração volumétrica e vetores de velocidade do ar e sólido, o que são informações de difícil obtenção experimentalmente. Por fim, novas condições de operação e diferentes geometrias de alimentador e *riser* foram investigadas numericamente para o alimentador leito de jorro e a vazão de sólidos máxima pôde ser aumentada de 11 para 30 g/s. As simulações se mostraram ferramentas eficazes e com vantajoso custo-benefício para otimizar a alimentação de borras de café ou implementar os alimentadores em aplicações comerciais de maior escala.

ABSTRACT

The continuous and stable feeding of particulate solids to reactors is essential for energy cogeneration in industrial processes, for example, by using biomass residues. Nevertheless, flow instabilities and blockage of mechanical feeder's moving parts are commonly reported with these materials, which jeopardizes the process' performance, automation, and safety. This study is aimed at evaluating the performance of non-mechanical devices (an L-valve and a spouted bed) to promote the feeding of spent coffee grounds to circulating fluidized bed (CFB) units. The physical and flow properties were determined for dry spent coffee grounds with mean sizes between 225 and 550 μm, as well as for samples with moisture content up to 60%. Some of the properties determined were the true, apparent, and bulk densities, minimum fluidization velocity, Hausner ratio, static and dynamic repose angle, and effective internal friction angle. Then, feeding experiments using both feeders were carried out at pilot-scale CFB reactors (riser diameter and height of 21 mm and 2 m), available at the Drying Center/UFSCar. The fluid dynamics of the systems with spent coffee grounds was assessed by pressure and solids flowrate (W_S) measurements under different operating conditions, such as different air flowrates in the riser and feeder, as well as with different distances between the riser and air inlets with the spouted bed. The solids flowrate with the L-valve lies between 0.6 and 10.0 g/s, while it ranges from 1.2 to 11.0 g/s with the spouted bed feeder. The pressure measured at the feeders and W_S were accurately related by linear equations. The feeders' performance was related to the samples' properties, then flow instabilities and lower values of W_S were observed for samples with poorer flowability. Overall, the spouted bed exhibited improved performance and flexibility than the L-valve in handling dry and wet spent coffee grounds to the CFB unit. The experimental data was used to validate simulations based on computational fluid dynamics with the Two-Fluid model (TFM)

approach. The difference between experimental and simulated solids flowrate was less than 20% for different operating conditions with the feeders. From the validated TFM simulations, details on the gas-solid flow dynamics in the feeders and riser were verified by means of volume fraction contours, and velocity vectors for gas and solid phases. Finally, new operating conditions and different feeder and riser geometries were numerically investigated for the spouted bed feeder, and the maximum solid flowrate could be increased from 11 to 30 g/s. The simulations proved to be reliable and cost-effective tools to optimize spent coffee grounds handling or to implement the feeders in larger-scale commercial applications.

CAPÍTULO 1 - INTRODUÇÃO

O desempenho de válvulas de alimentação e sistemas de transporte pneumático vêm sendo estudado no Centro de Secagem do DEQ/UFSCar, desde a década de 90, a partir da proposta de utilização de um leito de jorro como válvula não-mecânica para a alimentação de sólidos em um leito pneumático (FERREIRA; FREIRE, 1992). O escopo destas pesquisas foi ampliado com a avaliação de outros tipos de alimentadores, como o parafuso helicoidal, alimentador tipo Venturi e válvulas-L (COSTA; FERREIRA; FREIRE, 2004; LOPES et al., 2011a). Nestes trabalhos, o foco foi a avaliação do desempenho dos alimentadores com partículas de formato regular, como esferas de vidro e *pellets* de polietileno de tamanhos grandes (*coarse*), uma vez que o objetivo principal era a caracterização fluidodinâmica do sistema de transporte de sólidos. A operação dos alimentadores com partículas não-convencionais, contudo, é uma aplicação potencial, dado o grande número de operações unitárias que utilizam este tipo de material, para a geração de energia, fabricação de compósitos poliméricos, entre outros. Assim, a continuidade desta linha de trabalho prevê a aplicação das válvulas na alimentação de partículas com razões de aspecto baixas e/ou materiais coesivos.

Os resíduos de biomassa são uma das fontes de geração de energia com maior potencial de crescimento nos próximos anos, sendo considerados excelentes alternativas para a diversificação da matriz energética e redução da dependência dos combustíveis fósseis. Biomassa é o termo dado a todo material orgânico proveniente de árvores, plantas, algas e culturas agrícolas, em que a energia solar está armazenada na forma de ligações químicas (MCKENDRY, 2002). A quantidade de biomassa existente na terra é da ordem de dois trilhões de toneladas, o que, em termos energéticos, corresponde a mais ou menos oito vezes o consumo mundial de energia primária (RAMAGE; SCURLOCK, 1996).

Dentre os resíduos de biomassa, a borra de café merece destaque no âmbito nacional tendo em vista que o Brasil é o principal produtor de café do mundo e que o consumo deste produto tem sido crescente na última década, com aumento em média de 2,1% ao ano e atingindo quase 10 milhões de toneladas em 2019 (INTERNATIONAL COFFEE ORGANIZATION, 2019). Como consequência do alto consumo, a geração de borras de café tem aumentado drasticamente e o seu descarte sem tratamento em aterros sanitários pode gerar sérios problemas ambientais devido a sua alta carga orgânica e acidez (MUSSATTO et al., 2011). Embora a geração e o descarte de borras de café sejam descentralizados no caso de residências e pequenos comércios, quase 50% da produção mundial de café é destinada à produção de café solúvel, o que representa cerca de 2,5 milhões de toneladas de borras de café gerados anualmente e disponíveis para o processamento nessa indústria.

Nos últimos anos, foram reportadas diversas aplicações objetivando a valorização desse resíduo, por exemplo, na preparação de filmes para embalagem de alimentos e flores (THIAGAMANI et al., 2017); na adubação de agriculturas orgânicas (SANTOS et al., 2017); na produção de biocombustíveis e biogás (AL-HAMAMRE et al., 2012; ATABANI et al., 2019; KONDAMUDI; MOHAPATRA; MISRA, 2008), como substrato em fermentações em estado sólido (MURTHY; NAIDU, 2012), entre outros. Essas aplicações parecem ser promissoras para o gerenciamento de borras de café coletadas em comunidades descentralizadas e/ou empresas de pequena a média escala.

No entanto, para processos em larga escala, a utilização das borras de café deve estar alinhada às necessidades da empresa para facilitar a implementação de soluções. Mais especificamente, no caso da produção de café solúvel há uma grande demanda por vapor e ar quente nas etapas de extração e secagem (SILVA et al., 1998). Dessa forma, a borra de café pode ser usada para cogeração de energia renovável na própria indústria,

tendo em vista o seu alto poder calorífico, o qual é de aproximadamente 25 kJ/kg e semelhante ao do carvão (SILVA et al., 1998), seu baixo teor de cinzas (MUSSATTO et al., 2011) e sua alta disponibilidade neste setor.

Com este intuito, as borras de café devem ser alimentadas a reatores de queima continuamente e de maneira estável com alimentadores apropriados. Apesar disso, a alimentação de pós de biomassa é considerada a operação mais problemática de todo o sistema do reator (DAI; CUI; GRACE, 2012; RAMÍREZ-GÓMEZ, 2016), em decorrência da alta variabilidade das propriedades desses resíduos em termos de tamanho de partícula, umidade e formato. Na prática, dispositivos de alimentação ineficientes ou mal projetados fornecem fluxo de sólidos instáveis ou inexistentes para o reator, comprometendo a estabilidade, automação, segurança e desempenho do processo.

Em vista das características diferenciadas das biomassas, uma análise do desempenho de alimentadores não-mecânicos para o manuseio destes pós parece ser promissora, visto que estes alimentadores não possuem partes móveis para o controle da vazão de sólidos, são menos expostos ao desgaste e mais baratos em comparação com alimentadores mecânicos. Dentre os alimentadores não-mecânicos, a válvula-L e o alimentador tipo leito de jorro se destacam. O primeiro caracteriza-se como o alimentador não-mecânico mais comumente acoplado a linhas de transporte pneumático e a reatores tipo Leito Pneumático Circulante (LPC) industrialmente (SWART; BOATENG, 2012; TONG et al., 2003), enquanto o segundo representa uma aplicação potencial, tendo em vista os bons resultados na alimentação de materiais convencionais (FERREIRA; FREIRE, 1992; LOPES et al., 2011a; SOUSA et al., 2010). O avanço do estado da arte para esses alimentadores consiste em testar sua operabilidade para materiais com características de escoamento dificultado, com baixas razões de aspecto e potencialmente coesivos, como é o caso da borra de café.

1.1. Objetivos

Desta forma, esta tese teve como objetivo avaliar o desempenho de válvulas de alimentação não-mecânicas, a válvula tipo L e o leito de jorro, como alimentadores de pós de biomassa (borras de café com diferentes propriedades) em reatores tipo LPC.

Para atender o objetivo geral, fez-se necessário o cumprimento das seguintes etapas:

1) Avaliar as propriedades físicas e de escoabilidade de borras de café com diferentes distribuições granulométricas e umidades;
2) Avaliar experimentalmente a alimentação de borras de café a um LPC em escala piloto com a válvula-L por meio de medidas de vazão de sólidos e pressão estática;
3) Avaliar experimentalmente a alimentação de borras de café a um LPC em escala piloto com o leito de jorro por meio de medidas de vazão de sólidos e pressão estática;
4) Relacionar as características físicas e de escoabilidade das borras de café com o desempenho dos alimentadores;
5) Efetuar simulações em CFD para a alimentação de borras de café com válvula-L, visando obter detalhes fluidodinâmicos no alimentador e reator;
6) Efetuar simulações em CFD para a alimentação de borras de café com leito de jorro, visando obter detalhes sobre a fluidodinâmica no alimentador e reator;
7) Realizar simulações em CFD com novas geometrias e condições de operação para o leito de jorro com foco na implementação do alimentador em reatores de maior escala.

Em virtude dos vários tópicos analisados, optou-se por estruturar esta tese em 8 capítulos, divididos em 1-Introdução, 2-Revisão Bibliográfica, 8-Considerações Finais e mais 5 capítulos visando o cumprimento dos objetivos propostos, sendo: 3-Caracterização

Física e de Escoabilidade de Borras de Café; 4-Alimentação de Borras de Café ao LPC com Válvula-L: Análise Experimental; 5- Alimentação de Borras de Café ao LPC com Válvula-L: Análise via CFD; 6- Alimentação de Borras de Café ao LPC com Leito de Jorro: Análise Experimental; 7- Alimentação de Borras de Café ao LPC com Leito de Jorro: Análise via CFD.

Nos capítulos 3 a 6 serão reproduzidos, na íntegra, os textos de publicações em congressos internacionais e periódicos nos quais são apresentados os procedimentos experimentais e resultados que suportam as conclusões desta tese. Os desenvolvimentos experimentais do trabalho foram realizados no período de Março/2016 a Dezembro/2018 no Centro de Secagem de Pastas, Suspensões e Sementes do DEQ/UFSCar, enquanto as simulações em CFD foram desenvolvidas em 2019 no *Laboratory for Simulation and Modelling of Particulate Systems* da *Monash University*.

CAPÍTULO 2 - REVISÃO BIBLIOGRÁFICA

Neste capítulo, será apresentada uma revisão bibliográfica sobre o transporte de pós, evidenciando os principais índices de escoabilidade e as propriedades físicas dos pós que impactam no seu escoamento. Na sequência, será apresentada uma revisão sobre os alimentadores que são normalmente utilizados para controlar a dosagem de pós a reatores, com destaque para o funcionamento e o estado da arte dos alimentadores não-mecânicos tipo válvula-L e tipo leito de jorro, os quais são o foco desta tese.

2.1. Escoamento de pós

Os sólidos particulados são encontrados na natureza, entre outras formas, como grãos, sementes, folhas e pós e ocupam a segunda posição entre os materiais mais manuseados pelos seres humanos, logo atrás da água (ZHAO, 2018). Em termos de aplicabilidade industrial, os pós merecem destaque como produtos em indústrias químicas, farmacêuticas e alimentícias, ou como matérias-primas de diversos outros processos produtivos. Em torno de 75% dos processos químicos utilizam sólidos na forma de partículas finas em algum de seus estágios de processamento (NELSON, 1999).

Apesar da larga aplicabilidade, prever o escoamento de pós é uma tarefa complexa e, quando comparado ao escoamento de gases e líquidos, esse é um tópico relativamente pouco estudado. Em geral, o escoamento de um fluido pode ser descrito a partir de equações de conservação de massa e momento, contudo, no caso dos sólidos particulados, as características do escoamento dependem fortemente das propriedades do material particulado, das interações com a parede dos equipamentos, da forma como o material é empacotado e das condições ambientes, entre outros.

Esse cenário tem contribuído para que operações unitárias de alto custo energético, como a secagem e o transporte de materiais particulados, sejam operados em escalas

industriais como processos tipo “caixa-preta” e, consequentemente com baixa eficiência, distanciando a operação da planta industrial de sua capacidade de projeto. Além disso, dificuldades adicionais no transporte e manuseio de pós geralmente são observadas na presença de finos (tamanho inferior a 100 μm) ou de umidade na amostra, em decorrência da significância de forças coesivas, do atrito interparticular e da formação de pontes líquidas (ALTHAUS; WINDHAB, 2012; CASTELLANOS, 2005).

Na próxima seção serão apresentadas algumas considerações sobre a escoabilidade de sólidos particulados e os principais índices utilizados para sua quantificação.

2.2. Considerações sobre a escoabilidade

A escoabilidade de um material particulado sólido, apesar de não ter uma definição precisa na literatura, pode ser entendida como a facilidade ou dificuldade de um conjunto de partículas rearranjarem a sua estrutura organizacional em relação às vizinhanças quando são submetidas à ação de uma força. A consequência desse rearranjo pode ser visualizada macroscopicamente pela diminuição do volume ocupado pelo material particulado em um reservatório (compactação) ou até mesmo pelo deslocamento do material entre as diversas operações unitárias.

Apesar das vizinhanças e das forças envolvidas variarem conforme a aplicação específica a que o material particulado é submetido, geralmente as vizinhanças são constituídas: i) pelo próprio material particulado; ii) pelas paredes de um equipamento ou iii) por um fluido que envolve a superfície das partículas. Enquanto as forças que geralmente atuam são: i) o peso das partículas; ii) forças de compressão e cisalhantes; iii) força centrífuga, em equipamentos rotativos; ou iv) o momento fornecido por uma corrente de fluido em escoamento que permeia ou transporta o material particulado.

Na Fig. 2.1. são mostrados exemplos de vizinhanças das partículas em um leito de alumina em pó. A partícula P1 possui majoritariamente outras partículas de alumina como vizinhança, enquanto P2 possui somente as paredes do equipamento restringindo o seu rearranjo e P3 possui ambas as interações do tipo partícula-partícula e partícula-parede. Caso uma força externa fosse aplicada ao conjunto de partículas mostrado na micrografia é evidente que a escoabilidade das partículas P1, P2 e P3 seriam diferentes entre si e, mais ainda, a escoabilidade do sólido *bulk* seria dada por uma média da capacidade de rearranjo de todas as partículas presentes no conjunto analisado.

Note que, se o estado inicial apresentado na Fig. 2.1. fosse diferente, por exemplo, devido à presença de umidade na superfície das partículas, partículas com diferentes tamanhos ou composições químicas, diferentes estados de compactação ou até mesmo se a força aplicada fosse de natureza e intensidade diferente, seria esperado que a escoabilidade do material particulado também se alterasse.

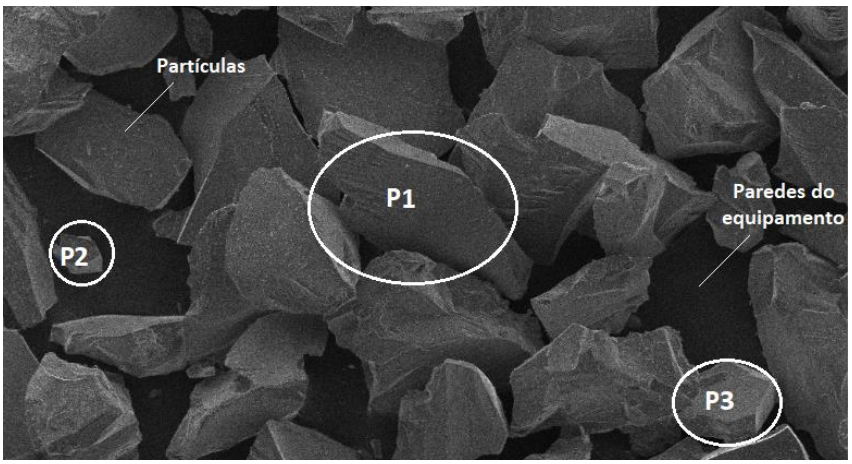

Fig. 2.1. Exemplo de vizinhanças de partículas em um leito de pós de alumina.

Em suma, a escoabilidade não somente é dependente das propriedades das partículas (rugosidade superficial, composição química, formato, distribuição granulométrica e massa específica) e das propriedades *bulk* (densidade *bulk*, arranjo das partículas, etc.), mas também é afetada pelas características do equipamento (geometria, dimensões, material da parede, etc.), pelo tempo de armazenamento, pelo estado de

compactação do material e pelas características do fluido que envolve as partículas (viscosidade, densidade, composição, entre outros).

Na literatura foram propostos diferentes índices para quantificar a escoabilidade de sólidos particulados baseados nas operações unitárias e condições de processamento a que esses materiais geralmente são submetidos. Os índices mais utilizados são os ângulos de repouso estático (AoR^e) e dinâmico (AoR^d), o índice de Hausner (*IH*), o índice de Carr (IC) e a função de fluxo (*ff*) obtida em ensaios de cisalhamento em células de Jenike, de Schulze ou reômetro de pós.

Na Tab. 2.1. são mostradas as classificações de escoabilidade para os diferentes índices. Detalhes adicionais sobre as metodologias de medição podem ser consultados em outros trabalhos da literatura (BODHMAGE, 2006; CAMPOS; FERREIRA, 2013; LUMAY et al., 2012; SANTOS; CONDOTTA; FERREIRA, 2017; TAN; MORTON; LARSON, 2015).

Apesar da complexidade inerente em se quantificar a escoabilidade, cabe destacar aqui que os índices apresentados na Tab. 2.1. têm se mostrado suficientemente sensíveis para classificar materiais com escoabilidades diferentes, bem como podem ser comparados entre si, como é o caso das relações exponenciais existentes entre o ângulo de repouso estático e o índice de Hausner (GELDART et al., 2006; MASSARO SOUSA; FERREIRA, 2019a; WOUTERS; GELDART, 1996). Esse fato tem contribuído para que operações unitárias tradicionalmente operadas como processos “caixa-preta” na indústria transitem para processos “caixa-cinza”, relacionando a operação com as propriedades dos materiais particulados. Um dos exemplos mais importantes são as operações de alimentação e dosagem de sólidos particulados, as quais são cruciais para a estabilidade e rendimento de plantas industriais, já que constituem as entradas e saídas de cada operação unitária.

Tab. 2.1. Critérios de classificação da escoabilidade

***IH* (-)**	***IC* (-)**	***AoR*^{e} (º)**	***AoR*^{d} (º)**	***ff* (-)**	**Escoabilidade**
1,00 - 1,11	< 0,10	25 – 30	-	-	Excelente
1,12 - 1,18	0,11 – 0,15	31 – 35	-	> 10	Muito boa
1,19 - 1,25	0,16 – 0,20	36 – 40	30 – 45	4 - 10	Boa
1,26 - 1,34	0,21 – 0,25	41 – 45	45 – 55	2 - 4	Razoável
1,35 - 1,45	0,26 – 0,31	46 – 55	55 – 65	1 - 2	Ruim
1,46 - 1,59	0,32 – 0,37	56 – 65	≥ 66	< 1	Muito ruim
≥ 1,60	> 0,38	≥ 66	-	-	Péssima

Fonte: Adaptado de (LUMAY et al., 2012; TAN; MORTON; LARSON, 2015).

Na próxima seção serão apresentadas algumas considerações sobre a alimentação de sólidos e os principais tipos de alimentadores encontrados na literatura, bem como os seus princípios de funcionamento.

2.3. Considerações sobre a alimentação de pós

A alimentação de sólidos particulados, embora seja primordial para a estabilidade, automatização, segurança e rendimento de uma planta industrial, ainda é uma operação reconhecida por ser um dos principais gargalos nos processos produtivos. Na prática, a probabilidade de ocorrência de problemas de operação em alimentadores é da ordem de 80% quando se opera com materiais de escoabilidade difícil como biomassas em pó (DAI; CUI; GRACE, 2012; ILIC et al., 2018; MARINELLI; CARSON, 1992). Essa alta probabilidade está relacionada a diversos fatores, dentre eles:

i) Raramente as metodologias utilizadas para o projeto de alimentadores estão dissociadas de empirismos, os quais não são suficientemente abrangentes para garantir que não haja problemas de alimentação durante o processamento;
ii) Como os sólidos particulados são muito diferentes entre si e as propriedades que interferem na sua escoabilidade são diversas, o desenvolvimento de alimentadores eficientes geralmente é realizado para cada processo ou operação

específica, resultando em uma dinâmica de desenvolvimento tecnológico lenta no que diz respeito à resolução do problema global de alimentação de sólidos;

iii) Geralmente não há consenso sobre qual alimentador é melhor para se trabalhar com determinado sólido particulado ou para alimentar uma determinada operação unitária;

iv) Os cursos de Engenharia Química e de Processos abordam majoritariamente em suas grades curriculares o estudo de operações unitárias relacionadas ao escoamento de gases e líquidos, como a destilação, a absorção, o bombeamento, entre outros, o que compromete a tomada de decisão dos futuros engenheiros com agilidade e efetividade na resolução de problemas relacionados a sistemas particulados.

Um sistema de alimentação ideal deve fornecer alimentação estável e contínua do material particulado, com controle preciso da taxa de alimentação e com baixas oscilações de vazão mássica. Além disso, o sistema deve apresentar baixa sensibilidade às variações de tamanho, forma e umidade da amostra, bem como deve manter uma selagem suficiente para evitar o refluxo de gás da operação unitária seguinte, caso esteja pressurizada.

Existem diversos tipos de alimentadores de sólidos que são utilizados industrialmente, os quais podem ser classificados em duas categorias: alimentadores mecânicos e não-mecânicos. Os alimentadores não-mecânicos são aqueles que não possuem partes móveis no interior do dispositivo, sendo totalmente dependentes da gravidade ou da vazão de gás para o controle da vazão de sólidos alimentada. Por não possuírem partes móveis, os alimentadores não-mecânicos são menos expostos ao desgaste e mais baratos quando comparado aos mecânicos e, geralmente, são indicados para alimentar operações unitárias que trabalham em altas pressões e temperaturas. Na Fig. 2.2. são mostrados esquemas de alguns dos principais alimentadores do tipo

mecânico (parafuso helicoidal e válvula rotativa) e não-mecânico (silo, válvulas pneumáticas e leito de jorro).

A vazão de sólidos alimentada por parafusos helicoidais e válvulas rotativas, além de ser dependente da geometria dos alimentadores e das propriedades dos materiais, é ajustada por meio da rotação de suas partes móveis. No caso do parafuso helicoidal operando com pós de escoabilidade classificada como ruim, a formação de incrustações e de bloqueios nas partes móveis são comuns, sendo recomendada a utilização de dois parafusos entrelaçados girando em direções opostas para promover a autolimpeza do alimentador. Contudo, isso torna o custo do dispositivo elevado, assim como as diretrizes de seu projeto em função das características dos materiais não serem bem definidas (DAI; CUI; GRACE, 2012). Além disso, a utilização do parafuso helicoidal é dificultada em aplicações sob alta temperatura, já que é necessário acoplar um sistema de resfriamento ao alimentador. Por exemplo, reatores de gasificação e combustão de biomassa geralmente são operados próximos a 1000°C, mas a temperatura do parafuso helicoidal não pode ultrapassar 550°C. Finalmente, as válvulas rotativas são menos eficazes que os parafusos helicoidais para operar com materiais coesivos ou úmidos, devido aos problemas de aderência dos particulados nos compartimentos da válvula, à falha no preenchimento dos compartimentos por obstrução e entupimento das entradas e saídas do equipamento, além de problemas de vedação ao alimentar operações unitárias pressurizadas.

Os silos são equipamentos muito utilizados para armazenar e alimentar simultaneamente, por descarga gravitacional, a maioria dos materiais particulados, promovendo selagem adequada entre as operações unitárias. Apesar disso, a operação com pós com escoabilidade dificultada pode comprometer a capacidade do equipamento em fornecer vazões de sólidos estáveis, pela alternância entre escoamentos afunilados e

mássicos no interior do silo, bem como pela interrupção da vazão de sólidos devido à formação de arcos coesivos e mecânicos próximos ao bocal de saída. Em geral, a utilização de aeração e vibração no silo não é suficiente para eliminar esses problemas e o dimensionamento de silos com maiores inclinações e orifícios de saída pode não ser economicamente atrativo para a indústria.

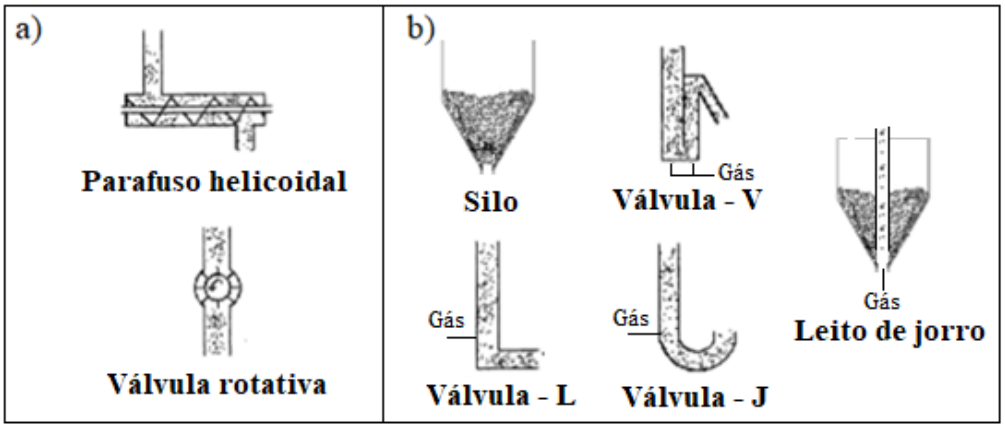

Fig. 2.2. Alguns alimentadores de sólidos a) mecânicos e b) não-mecânicos.
Fonte: Adaptado de (LOPES, 2011).

As válvulas pneumáticas L, J e V e o alimentador tipo leito de jorro são equipamentos com geometrias simples e de baixo custo fixo que utilizam a injeção de uma vazão de gás para ajustar a vazão de alimentação de sólidos para as operações unitárias, consequentemente apresentando maiores gastos energéticos durante a operação quando comparados aos alimentadores mecânicos. Esses equipamentos em geral apresentam alta perda de carga e podem sofrer problemas de segregação de partículas em decorrência da sua geometria e do escoamento multifásico, contudo a sua ampla faixa de operação e o princípio de funcionamento simples são características atrativas para a sua utilização com pós de difícil escoabilidade. Entre os dispositivos apresentados, a válvula-L é o alimentador mais utilizado industrialmente para operações com escoamento em fase densa e diluída (WANG; FAN, 2015) e o leito de jorro é um dispositivo com potencial de aplicação, portanto eles serão abordados em detalhes nas próximas seções.

2.4. Alimentador tipo válvula-L

A válvula-L é um alimentador do tipo não-mecânico que utiliza o acionamento pneumático para transportar e dosar os materiais particulados para as operações unitárias. Na Fig. 2.3. é mostrado um esquema de uma válvula-L que possui duas secções: vertical e horizontal. Os materiais particulados entram no alimentador pela secção vertical, normalmente por ação exclusiva da força gravitacional, e são direcionados para a secção horizontal da válvula por meio do ganho de momento fornecido pela vazão de gás injetada na parede do tubo vertical, normalmente ar comprimido. Ao final da seção horizontal da válvula-L são acoplados os equipamentos utilizados nas operações unitárias subsequentes do processo produtivo, sendo essas, usualmente: peneiras de separação, silos pulmões e de armazenamento, secadores e reatores pneumáticos.

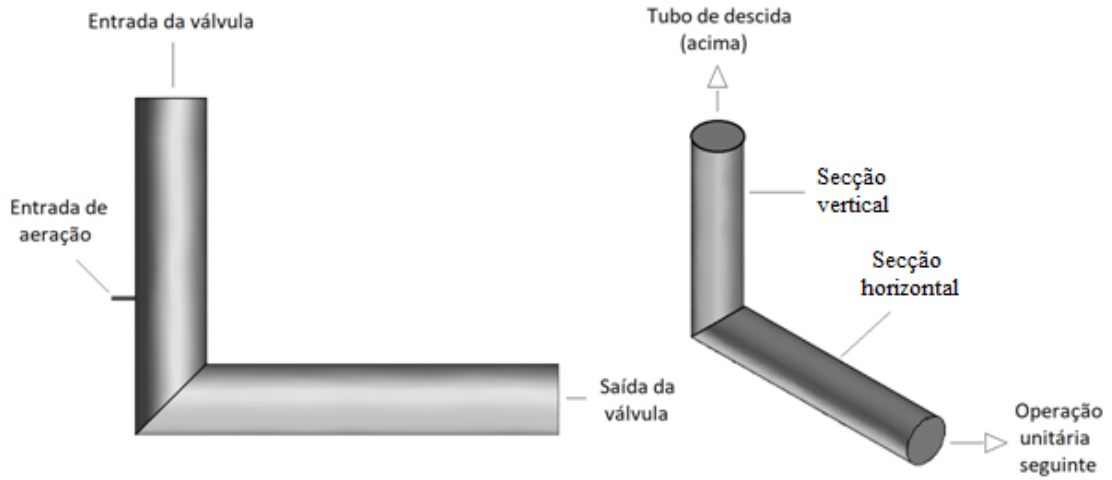

Fig. 2.3. Alimentador tipo válvula-L e suas secções.

No próximo tópico será mostrado que a válvula-L pode apresentar diferentes regimes de escoamento dependendo da vazão de aeração inserida na região vertical, o que impacta diretamente na vazão de sólidos transportados e na estabilidade da alimentação. Além disso, será destacada a importância de se manter uma boa selagem na entrada de sólidos da válvula-L, chamado de *standpipe* ou tubo de descida, a fim de evitar problemas de operação do alimentador.

2.4.1. Funcionamento

A Fig. 2.4. mostra os diferentes regimes de escoamento possíveis na válvula-L em função da vazão de aeração inserida no alimentador. Imaginando um tubo de descida com altura infinita acoplado a uma válvula-L, ambos preenchidos com sólidos particulados, tem-se que é necessária a inserção de uma aeração mínima (Q_{min}) no alimentador, dependente das propriedades do material e da configuração da válvula-L, para o rompimento do leito fixo nas secções vertical e horizontal e consequentemente escoamento do material. Portanto, se $Q<Q_{min}$ a vazão de sólidos transportada pela válvula-L (W_S) será igual a zero.

Aumentando-se a vazão de aeração até a vazão de mínima fluidização do material ($Q_{min}<Q<Q_{mf}$), nota-se o início do escoamento na válvula-L com a maior parte do material particulado estagnado na parte horizontal inferior, com propriedades similares às de um leito fixo, e a formação de um pequeno canal de escoamento no topo da parte horizontal em que as partículas se movem rapidamente (Fig. 2.4a). Para vazões de aeração médias, mas inferiores à vazão mínima de *slugging* ($Q_{min}<Q<Q_{ms}$) há a contínua formação de dunas e ondulações periódicas no topo da parte horizontal, com flutuações tanto nas medidas de pressão como em W_S (Fig. 2.4b).

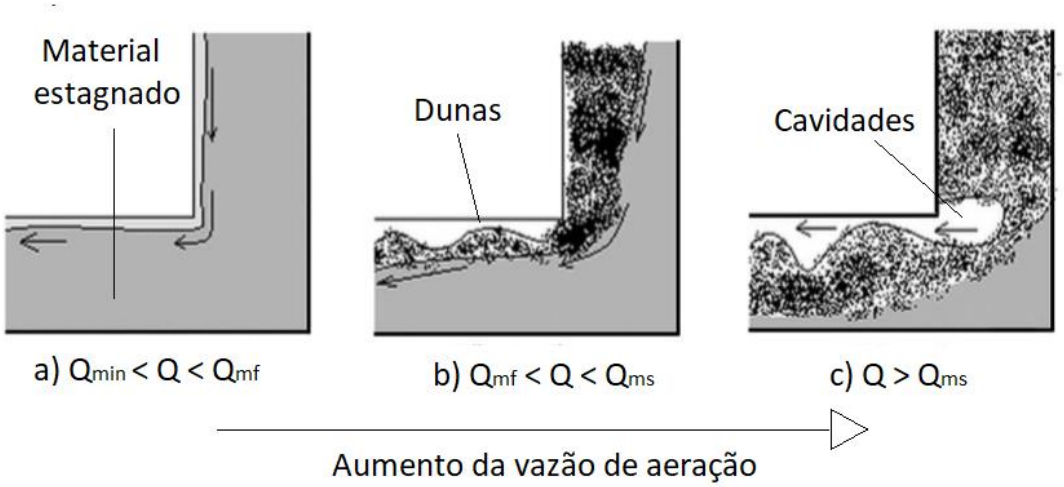

Fig. 2.4. Diferentes regimes de escoamento na válvula-L para diferentes aerações. Fonte: adaptado de (CHAN et al., 2009).

Para vazões de aeração altas ($Q>Q_{ms}$), tanto a pressão quanto a vazão de sólidos se tornam instáveis em decorrência da formação de grandes bolhas de ar ou cavidades no tubo de descida que, quando superadas pelo peso do leito de partículas, são direcionadas para a parte horizontal da válvula-L, dando origem a grandes dunas e vórtices (Fig. 2.4c). Por fim, para aerações altíssimas ($Q>>Q_{ms}$), o momento fornecido pela vazão de aeração começa a equilibrar o peso do leito de partículas no tubo de descida e sustentá-lo; vórtices são formados nas proximidades da região de entrada de aeração e uma pequena quantidade de sólidos é direcionada para a região horizontal da válvula, onde as partículas são submetidas a um transporte pneumático diluído, com poucas flutuações de pressão e W_S estável. Nesse regime não há mais mudança de W_S com a aeração, chegando-se ao limite de operação do alimentador.

Em geral, se a válvula-L for operada com Q entre Q_{min} e Q_{ms}, quanto maior a vazão de aeração inserida na válvula-L maior será a vazão de sólidos na saída do alimentador. Note que esse comportamento não é muito diferente de uma válvula mecânica, por exemplo, uma válvula rotativa, no sentido de que a abertura da válvula rotativa é controlada por meios mecânicos e na válvula-L é acionada pneumaticamente, com Q_{min} representando a válvula totalmente fechada e Q_{ms} quase que totalmente aberta (YANG; KNOWLTON, 1993).

Em situações de partida de operação ou de alteração da vazão de aeração fornecida ao alimentador, é esperado que ocorram instabilidades na vazão de sólidos e na pressão acima da aeração da válvula-L, devido ao rompimento do leito fixo ou à transição de regimes de escoamento nas secções vertical e horizontal. Entretanto, o alimentador tende a se estabilizar rapidamente em alguns minutos, o que é plenamente aceitável em operações contínuas. Além disso, para que a operação do alimentador seja adequada, é importante que sempre haja um leito de sólidos no tubo de descida até uma altura

localizada acima do ponto de aeração, para proporcionar perda de carga ou resistência suficiente de modo a direcionar o escoamento do ar majoritariamente para a secção horizontal da válvula-L, atuando como um selo. Caso isso não ocorra, a vazão de sólidos transportada pelo alimentador decairá a zero e será necessário interromper a aeração na válvula-L para restabelecer o leito de sólidos antes de retornar à operação normal.

Por fim, cabe ressaltar que a transição entre os comportamentos qualitativos de escoamento mostrados na Fig. 2.4, bem como os valores de Q_{min}, Q_{mf} e Q_{ms}, dependem tanto das propriedades dos materiais transportados como das configurações geométricas da válvula-L. Nas próximas seções será mostrado como algumas variáveis importantes influenciam na operação da válvula-L, bem como quais os principais trabalhos na literatura e suas conclusões sobre o alimentador.

2.4.2. Principais variáveis de projeto e de operação

Na seção anterior foi detalhada a importância da vazão de aeração no controle da vazão de sólidos descarregada pela válvula-L, contudo outras variáveis de operação e de projeto também influenciam no funcionamento do alimentador. Em termos de operação, as principais variáveis são o diâmetro, a distribuição granulométrica e a densidade das partículas, enquanto as principais variáveis de projeto são o diâmetro da válvula-L, a quantidade de bocais de entrada de aeração e a sua posição.

Em geral, a vazão de sólidos em uma válvula-L é menos suscetível à flutuações quando são utilizadas partículas Geldart B com maior diâmetro médio e maior densidade (ARENA; LANGELI; CAMMAROTA, 1998), contudo a vazão de aeração requerida para o início da operação do alimentador (Q_{min}) será maior (ARENA; LANGELI; CAMMAROTA, 1998; GELDART; JONES, 1991; KNOWLTON; HIRSAN, 1978). Além disso, para uma mesma velocidade de aeração no interior da válvula, tem-se que

Ws é maior quando é utilizado um ponto de aeração ao invés de múltiplos bocais (GELDART; JONES, 1991); quando a entrada de aeração está posicionada acima, mas o mais próximo possível, da curva da válvula-L (KNOWLTON; HIRSAN, 1978); bem como quando são utilizadas válvulas-L com maior diâmetro (GELDART; JONES, 1991). Por fim, existe uma relação diretamente proporcional entre *Ws* e a pressão no ponto de aeração da válvula-L quando o material é descarregado para operações unitárias que trabalhem à pressão atmosférica ou para um leito pneumático circulante (ARENA; LANGELI; CAMMAROTA, 1998; GELDART; JONES, 1991; SMOLDERS; BAEYENS, 1995).

Pelo exposto anteriormente, infere-se que uma das condições de operação mais desfavoráveis para o alimentador tipo válvula-L seria utilizando tubulações com pequenos diâmetros e operando com materiais de baixa densidade e com distribuição granulométrica contendo partículas finas, o que são características típicas de resíduos de biomassa. Portanto, é necessário avaliar o desempenho do alimentador nessas condições de operação extrema.

2.4.3. Modelagem matemática e equações empíricas

O escoamento de materiais particulados em válvulas-L foi tratado até o momento de forma qualitativa, mostrando o funcionamento do alimentador e como as principais variáveis de projeto e de processo afetam a sua operação. Nesta seção uma abordagem quantitativa será adotada, apresentando os principais avanços em termos de modelagem matemática, de equações empíricas e de fluidodinâmica computacional que descrevem o escoamento gás-sólido no alimentador.

O modelo hidrodinâmico para escoamento de materiais particulados em válvulas-L se baseia nas teorias de escoamento multifásico e mecânica de sólidos particulados

(TONG et al., 2003). O modelo pode ser utilizado para prever a vazão de sólidos descarregada pelo alimentador, bem como a perda de carga e as vazões de ar que são direcionadas para as diversas regiões da válvula-L por meio do fornecimento das propriedades do gás (densidade e viscosidade) e dos sólidos (diâmetro médio, esfericidade, massa especifica, coeficiente de atrito com a parede, porosidade compactada e de mínima fluidização), das propriedades geométricas da válvula-L (comprimento das regiões horizontal e vertical, altura da entrada de aeração e diâmetro do tubo) e das condições de operação (pressão na entrada e saída do alimentador). O sistema de equações que deve ser resolvido é apresentado abaixo:

$$Q_v = \frac{\pi D_{VL}^2 \varepsilon_v u_{fy}}{4} = \frac{(p^* - p_2)\varepsilon_v \pi D_{VL}^2}{4(L_v - L_e)k_v} - \frac{G_s \varepsilon_v}{\rho_p(1-\epsilon_v)} \tag{2.1}$$

$$k_v = \left(\frac{1-\varepsilon_v}{\varepsilon_v}\right)^2 \frac{\mu_f}{(\emptyset_s d_s)^2} \tag{2.2}$$

$$\Delta P_h = p^* - p_1 = 4{,}266\left(\frac{d_s}{D_h}\right)^{0{,}25} u_{sx}^{0{,}45}\rho_p(1-\varepsilon_h)gL_h - \sigma_{x0} \tag{2.3}$$

$$G_s = \frac{\rho_p U_{sx}\pi D_h^2}{4} = \frac{\rho_p(1-\varepsilon_h)u_{sx}\pi D_h^2}{4} \tag{2.4}$$

$$Q_h = \frac{\pi D_h^2 \epsilon_h u_{fx}}{4} = \frac{(p^* - p_1)\varepsilon_h \pi D_h^2}{4L_h k_h} + \frac{G_s \varepsilon_h}{\rho_p(1-\varepsilon_h)} \tag{2.5}$$

$$k_h = 154\left(\frac{1-\varepsilon_h}{\varepsilon_h}\right)^2 \frac{\mu_f}{(\emptyset_s d_s)^2} \tag{2.6}$$

$$Q = \frac{(p^* - p_1)\varepsilon_h \pi D_h^2}{4L_h k_h} + \frac{(p^* - p_2)\varepsilon_v \pi D_{VL}^2}{4(L_v - L_e)k_v} + \frac{G_s}{\rho_p}\left(\frac{\varepsilon_h}{1-\varepsilon_h} - \frac{\varepsilon_v}{1-\varepsilon_v}\right) \tag{2.7}$$

Os autores do modelo relatam que as previsões com dados experimentais da literatura foram satisfatórias, contudo cabe levantar aqui três pontos que dificultam a utilização desse modelo com praticidade e segurança: i) trata-se de um sistema de equações não-lineares com vários parâmetros e variáveis, o que pode ocasionar em problemas de convergência na solução; ii) o modelo envolve vários parâmetros nem

sempre conhecidos ou de determinação simples, como é o caso da tensão σ_{x0} ou as porosidades dos leitos nas diferentes secções da válvula e iii) durante o desenvolvimento do modelo foram utilizadas expressões empíricas para o cálculo do termo referente à perda de carga na tubulação devido ao escoamento dos sólidos, o que pode comprometer a validade do modelo para situações diferentes daquelas nas quais a correlação foi estabelecida.

Em termos práticos, uma alternativa à utilização do modelo hidrodinâmico seria a utilização de correlações empíricas propostas na literatura, as quais foram ajustadas a partir de dados experimentais do transporte de materiais com diferentes propriedades e em diferentes alimentadores. Essas correlações relacionam a perda de carga (ΔP_{VL}) com o fluxo de sólidos (*Gs*) na válvula-L em função de características do material, como o diâmetro médio (d_S) e a densidade *bulk* aerada (ρ_{ba}), e de características geométricas do alimentador, como o diâmetro interno da válvula-L (D_{VL}) e o comprimento da parte horizontal (L_h). Algumas das principais correlações podem ser visualizadas na Tab. 2.2.

Tab. 2.2. Correlações utilizadas para prever a vazão de sólidos na válvula-L.

Equação	Correlação	Validade	Ref.
(2.8)*	$\frac{\Delta P_{VL}}{L_h} = 216\ {G_s}^{0,17} D_{VL}^{-0,63} d_s^{-0,15}$	280<d_S<790µm 1527<ρ_b<1562 kg/m³ 40<D_{VL}<100 mm	(GELDART; JONES, 1991)
(2.9)*	$\frac{\Delta P_{VL}}{L_h} = 3500\ {G_s}^{0,3} \frac{{d_s}^{0,10}}{L_h^{0,70}}$	137<d_S<2000µm 1246<ρ_b<1685 kg/m³ 20< D_{VL}<40 mm	(SMOLDERS; BAEYENS, 1995)
(2.10)**	$\frac{\Delta P_{VL}}{L_h} = 0{,}0649\ (G_s)^{0,178} {\rho_{ba}}^{0,996} D_{VL}^{-0,574} d_S^{-0,237}$	45<d_S<630 µm 960<ρ_b<2710 kg/m³ D_{VL}=27 mm	(ARENA; LANGELI; CAMMAROTA, 1998)

* Descarga para a atmosfera; ** Descarga para um leito pneumático circulante.

Note que a aplicabilidade das correlações para outras válvulas-L está condicionada tanto à faixa de validade de cada uma das variáveis mostradas na Tab. 2.2., bem como à características específicas dos materiais particulados transportados pela válvula-L que eventualmente tenham sido desconsiderados nas correlações, por exemplo: umidade,

escoabilidade facilitada ou dificultada, porosidade do escoamento e do leito estático, material da válvula, etc.

Por fim, a utilização de técnicas de fluidodinâmica computacional (CFD) para descrever escoamentos multifásicos tem se destacado nos últimos anos em resposta ao rápido desenvolvimento tecnológico computacional. Em geral, simular o escoamento de sólidos em válvulas-L é complexo devido à variação de porosidade e regimes de escoamento que os materiais particulados sofrem dentro do alimentador (GHADIRIAN; ARASTOOPOUR, 2017), portanto o estágio atual das pesquisas encontra-se em comparar e validar os resultados das simulações em CFD com resultados experimentais de queda de pressão, vazão de sólidos e perfil qualitativo de escoamento. Nesse contexto, as duas principais abordagens utilizadas para a simulação de escoamentos multifásicos gás-sólido são a Euler-Euler e a Euler-Lagrange, nas quais se destacam, respectivamente, o modelo duplo-fluido (*Two-Fluid Model*, TFM) e o acoplamento entre a CFD e o Método do Elemento Discreto (*Discrete Element Method*, DEM).

No modelo duplo-fluido, a fase sólida e a fase gás são tratadas como contínuas e interpenetrantes, sendo descritas por meio do conceito de fração volumétrica de fase. As equações de conservação de quantidade de movimento são aplicadas individualmente para cada fase e a Teoria Cinética do Escoamento Granular (LUN et al., 1984) é usualmente empregada para descrever a continuidade da fase sólida, introduzindo os conceitos de temperatura granular, bem como viscosidade e pressão dos sólidos. Em geral, resultados satisfatórios e com custos computacionais reduzidos são obtidos com o TFM desde que seja realizada uma etapa de calibração dos parâmetros do modelo relativos à interação gás-sólido, colisão sólido-sólido e sólido-equipamento (ARASTOOPOUR, 2013; ARASTOOPOUR; GIDASPOW; ABBASI, 2017; GIDASPOW, 1994; GIDASPOW; JIRADILOK, 2009).

Por outro lado, no acoplamento CFD-DEM, a fase gás é tratada como contínua e descrita por meio das equações de Navier-Stokes, enquanto a fase sólida é discreta e o movimento de cada partícula no domínio computacional segue a segunda lei de Newton. Em geral, com esta formulação é possível estudar a transferência de quantidade de movimento com detalhes na escala de partículas e as principais limitações desta abordagem estão relacionadas ao tamanho do problema, ao número de partículas envolvidas e à determinação dos parâmetros de interação partícula-partícula e partícula-equipamento (CHU et al., 2018; HOU et al., 2019; WAHYUDI; CHU; YU, 2016; ZHAO, 2018; ZHONG et al., 2016a, 2016b; ZHU et al., 2011).

Nos próximos anos, espera-se que o papel da fluidodinâmica computacional seja cada vez mais relevante, auxiliando na compreensão dos fenômenos envolvidos na alimentação sem a necessidade de medidas experimentais intrusivas e, até mesmo, contribuindo para a redução do número de experimentos em unidades experimentais.

2.4.4. Considerações sobre o estado da arte

Na Tab. 2.3. são apresentados os principais trabalhos da literatura que investigaram a utilização de uma válvula-L para alimentação de materiais particulados descarregando para a atmosfera ou na entrada de reatores pneumáticos. Os trabalhos foram organizados cronologicamente, destacando-se os materiais particulados utilizados com as suas principais propriedades, as dimensões da válvula-L, informações sobre o ambiente para o qual a válvula-L realizava a alimentação, bem como outras observações adicionais relevantes.

Em geral, é possível concluir que o comportamento fluidodinâmico do alimentador se encontra bem caracterizado para materiais convencionais, isto é, sólidos particulados com elevada massa específica, formato regular e distribuição granulométrica em uma

faixa de tamanho estreita, como esferas de vidro e areias. Para esses materiais, a influência das principais variáveis de operação e de projeto já foi analisada, utilizando alimentadores de escala de bancada à industrial e, algumas vezes, utilizando técnicas refinadas de medição, como o tratamento de sinais provenientes de ondas, análises com traçadores radioativos, entre outras, além de abordagens inovadoras, como a teoria do caos. Destacam-se, também, os esforços em desenvolver modelos matemáticos que representem o escoamento no alimentador, seja por meio do modelo hidrodinâmico, de equações empíricas ou, mais recentemente, pela utilização da fluidodinâmica computacional com abordagens Euler-Euler e Euler-Lagrange.

Por fim, identifica-se que um dos possíveis avanços do estado da arte para esse tipo de alimentador consiste em realizar análises experimentais e via fluidodinâmica computacional abordando a alimentação de materiais particulados de difícil escoabilidade, com partículas de baixa densidade *bulk*, formato irregular e distribuição granulométrica heterogênea.

Tab. 2.3. Principais trabalhos de alimentação de sólidos utilizando válvulas-L.

Ano	Referência	Materiais (d_p - ρ_b)	Válvula-L	Alimentação	Observações Adicionais
1978	Knowlton e Hirsan	Areia (175, 260 e 510 μm – 2600 kg/m³) Siderita (190 μm – 4150 kg/m³) Carvão (200 μm – 1230 kg/m³)	D=38, 51, 76 e 152 mm	Atmosfera	Estudo sobre posição de entrada de aeração.
1991	Geldart e Jones	Areia (280 500 e 790 μm – 2600 kg/m³)	D=40, 70 e 100 mm	Atmosfera	Estudo sobre inclinação da válvula-L e pontos de aeração.
1993	Yang e Knowlton	-	-	Atmosfera	Propõe correlações para válvulas-L por analogia com equações de válvulas mecânicas.
1995	Smolders e Baeyens	Areia (137, 190, 260, 406, 607, 755, 850, 950 e 1490 μm – 2600 kg/m³) Esfera de vidro (450 μm – 2600 kg/m³) Cascalho (2000 μm – 2600 kg/m³)	D=20, 25, 30 e 40 mm L=200, 300 e 400 mm	Atmosfera	Comportamento de válvulas-L com D<20 mm difere do observado em válvulas de diâmetros grandes.
1998	Arena, Langeli e Cammarota	Areia (73, 156 e 341 μm – 2550 kg/m³) Magnetita (170 μm – 4460 kg/m³) FCC (68 μm – 1770 kg/m³)	D=27 mm	Leito Pneumático Circulante (LPC)	Primeiro estudo de válvula-L alimentando um equipamento com contrapressão.
1998	Daous e Al-Zahrani	Areia (470 μm – 2680 kg/m³) Cascalho (3000μm – 2680 kg/m³)	D=25, 36 e 50 mm L=170 e 290 mm	Atmosfera	Propõe um modelo simplificado supondo $\varepsilon_v=\varepsilon_h$.
2003	Tong et al.	-	-	Atmosfera	Propõe o modelo hidrodinâmico para sólidos em válvula-L.
2008	Kim, Tachino e Tsutsumi	FCC (70 μm – 1740 kg/m³)	D=50 mm	LPC	Análise espectral de Fourier (Teoria do caos).
2008	Yang e Leu	Areia (194 e 937 μm – 2635 kg/m³)	D= 80 mm	LPC	Utilização da técnica *multi-resolution analysis (MRA) of wavelet transform*
2009	Chan et al.	Areia (95 μm – 2260 kg/m³)	D=45 mm	Atmosfera e LPC	Utilização de traçador radioativo e determinação de perfil de velocidade em 3D na válvula-L
2010	Karmakar e Datta	Areia (147, 211, 334 e 416 mm – 2650 kg/m³)	D= 50 mm	Duplo Leito Fluidizado	-

Ano	Referência	Materiais (d_p - ρ_b)	Válvula-L	Alimentação	Observações Adicionais
2012	Yazdanpanah et al.	Ilmenita (128 μm – 4750 kg/m³) Areia (368 μm – 2650 kg/m³)	D= 17 mm	Leito Fluidizado Borbulhante	Utilização de hélio como traçador; comportamento dinâmico da válvula.
2013	Lim et al.	KR40 (70 μm – 1730 kg/m³), FCC (85 μm, 1880 kg/m³), Esfera de vidro (65 e 160 μm – 2500 kg/m³), Alumina (80 μm - 3700 kg/m³) e PVC (148 μm - 1350 kg/m³)	D= 16 mm	LPC	Alguns materiais particulados do tipo Geldart A podem ser alimentados usando válvula-L.
2013	Chovichien, Pipatmanomai e Chingpai-Bulpatana	Areia (474 μm – 2675 kg/m³)	D=100 mm	LPC	Transporte na válvula relacionado com comportamento no *riser.*
2013	Xueyao et al.	Areia (191 μm – 2630 kg/m³)	D=150 mm	LPC	Simulação em CFD-2D com abordagem Euler-Euler.
2018	Xu, Musser e Li	Polietileno (871 μm – 863 kg/m³)	D=25 mm	LPC	Análise experimental e via simulação CFD-DEM.
2018	Monazam et al	Esferas de vidro (180 μm – 2500 kg/m³)	D=230 mm	LPC	Alimentador em escala industrial e perfil de porosidade no LPC.

2.5. Alimentador tipo leito de jorro

Assim como a válvula-L, o alimentador tipo leito de jorro é não-mecânico e utiliza o acionamento pneumático para transportar e dosar os materiais particulados para reatores e linhas de transporte pneumático. Na Fig. 2.5. é mostrado um esquema de um alimentador tipo leito de jorro cônico-cilíndrico, o qual possui duas principais regiões: ânulo e canal de transporte. Os materiais particulados entram no alimentador pelo topo da seção cilíndrica e são direcionados para a seção cônica principalmente pelo efeito da força gravitacional. A partir da seção cônica, os sólidos são direcionados ao tubo central por meio do ganho de momento fornecido pela vazão de gás injetada na base do alimentador.

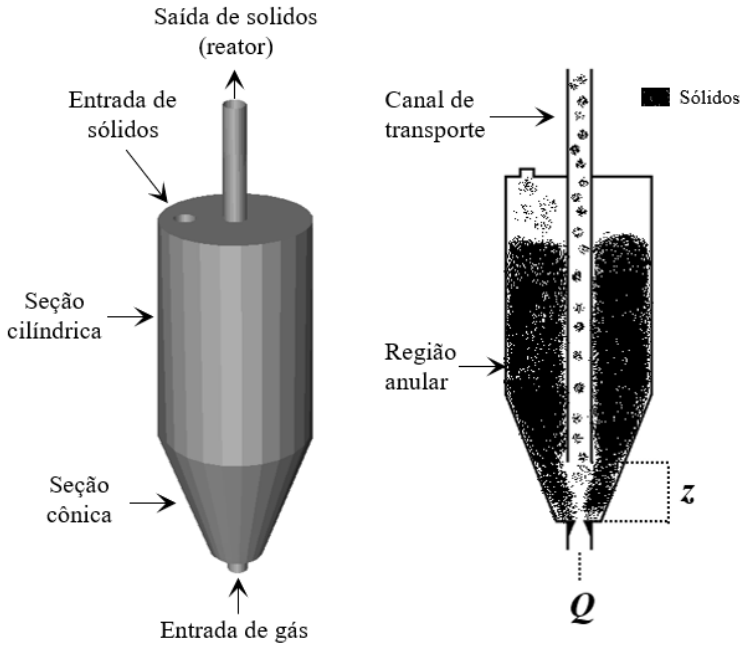

Fig. 2.5. Alimentador tipo leito de jorro e suas principais regiões.

Em operações estáveis, a maioria dos sólidos fica armazenada na região cônica-cilíndrica, a qual atua como uma resistência à passagem do ar (selagem), consequentemente a maior parte do ar injetado é direcionado ao tubo central. Dessa forma, no canal de transporte a fração volumétrica de sólidos é baixa, geralmente menor que 10%, enquanto na região anular essa fração se aproxima do empacotamento de um

leito descendente de sólidos. Em decorrência da interação gás-sólido, podem surgir zonas mortas ou zonas de recirculação de gás na região anular dependendo das condições operacionais.

Cabe salientar aqui que, quando acoplado a reatores tipo leito pneumático circulante, a recirculação de sólidos tipicamente observada em um leito de jorro com tubo *draft* ocorre no sistema como um todo, com formação da fonte de sólidos no topo do tubo central e retorno de sólidos ao alimentador por um tubo de descida.

2.5.1. Principais variáveis de projeto e de operação

Além da vazão de gás, existem diversas variáveis de operação e de projeto relacionados ao alimentador tipo leito de jorro que impactam na alimentação de sólidos ao canal de transporte. Em termos de operação, até o momento foram avaliados o diâmetro médio do sólido particulado, distância *z* (Fig. 2.5), vazão de gás e enchimento do alimentador. Enquanto, em termos de projeto, foram analisados o diâmetro e comprimento do tubo central (*riser*) e a inserção de bocais na entrada de ar.

Em geral, a vazão de sólidos (W_S) aumenta com a adição de maiores vazões de ar (Q) ao sistema até que a condição de transporte pneumático diluído seja atingida no *riser* ou tubo central. A partir desta condição, W_S se mantém praticamente constante com aumentos em Q (COSTA; FERREIRA; FREIRE, 2004; FERREIRA; FREIRE, 1992). A vazão de sólidos cresce com o aumento de *z* até o limite em que o transporte de sólidos se torna instável, possivelmente, pela maior quantidade de gás desviada para a região anular (FERREIRA; FREIRE, 1992; SOUSA et al., 2010). Além disso, para uma mesma condição de aeração, a vazão de sólidos é menor ao se transportar sólidos com menores diâmetros médios ou ao se diminuir a razão entre o diâmetro do *riser* e o da seção cilíndrica do leito de jorro (COSTA; FERREIRA; FREIRE, 2004).

A introdução de um bocal tipo Venturi na entrada de ar melhora a estabilidade de alimentação, tendo em vista que maior quantidade de gás é direcionado ao tubo central (SILVA; FERREIRA; FREIRE, 1996; SOUSA et al., 2010). Por fim, a vazão de ar necessária para se atingir o transporte pneumático estável aumenta com o comprimento do *riser* e não foram verificadas influências do enchimento do alimentador e *z* na queda de pressão do sistema (FERREIRA; FREIRE, 1992). Na próxima seção são destacados os principais trabalhos e os possíveis avanços do estado da arte para o alimentador tipo leito de jorro.

2.5.2. Considerações sobre o estado da arte

Na Tab. 2.4. são apresentados os principais trabalhos da literatura que investigaram a utilização de um leito de jorro como alimentador de sólidos a leitos pneumáticos circulantes. Os trabalhos foram organizados cronologicamente, destacando-se os materiais particulados utilizados com as suas principais propriedades, as dimensões do leito de jorro e *riser*, bem como observações adicionais relevantes. Note que existem menos trabalhos publicados para esse dispositivo comparativamente à válvula-L, tendo em vista que o alimentador tipo leito de jorro ainda é uma aplicação potencial para a indústria.

Em geral, é possível concluir que o comportamento fluidodinâmico do alimentador se encontra bem caracterizado para esferas de vidro que é um material *coarse*, com formato regular e alta massa específica (*Geldart D*). Com este material, foram investigadas as influências das principais variáveis de operação (*Q*, *z* e enchimento do leito de jorro) e de algumas variáveis de projeto (bocal de entrada de ar, diâmetro e comprimento do *riser*) sobre a vazão de sólidos, pressão e porosidade no *riser*.

Alguns dos possíveis avanços do estado da arte para este alimentador consistem em avaliar o seu desempenho com materiais particulados com diferentes propriedades, como: diferentes formatos, distribuições granulométricas e umidades, bem como avaliar a alimentação de pós classificados como *Geldart A* e *Geldart B*. Além disso, outras variáveis de projeto devem ser investigadas visando aplicações em maior escala, como: ângulo do cone e material da parede do leito de jorro, comprimento e diâmetro do *riser*, influência de diferentes bocais de entrada de ar, entre outros.

Por fim, apesar de terem sido reportados esforços em prever o escoamento no *riser* via modelos unidimensionais, não foram encontrados trabalhos que descrevessem numericamente o escoamento no alimentador, bem como com o alimentador conectado à linha de transporte pneumático. A utilização da fluidodinâmica computacional (CFD) com abordagens Euler-Euler e Euler-Lagrange parecem ser promissoras nesta questão, permitindo obter informações detalhadas sobre o escoamento no *riser* e alimentador, bem como permitindo analisar o efeito de variáveis de operação e de projeto sem a construção de novas unidades experimentais.

Tab. 2.4. Principais trabalhos de alimentação de sólidos utilizando leito de jorro.

Ano	Referência	Materiais (d_p - ρ_b)	Leito de jorro	Riser	Observações Adicionais
1992	Ferreira e Freire	Esfera de vidro (2,8 mm – 2500 kg/m³) Esferas de polipropileno (3,7 mm – 890 kg/m³)	*z*=27 a 60 mm	*D*=55 mm *L*=2,8 m	Influência de *z*, *Q* e enchimento do leito de jorro na vazão de sólidos e pressão no sistema. O transporte de sólidos diluído no *riser* foi atingido com o alimentador tipo leito de jorro. Foram observados efeitos eletrostáticos no escoamento das esferas de polipropileno.
1993	Littman et al.	Esfera de vidro (1 mm – 2500 kg/m³)	-	*D*=28,5 mm *L*=5,5 m	Determinação do coeficiente de arraste efetivo para o transporte pneumático diluído de sólidos no *riser*.
1996	Silva, Ferreira e Freire	Esfera de vidro (1,0 e 2,05 mm – 2500 kg/m³)	*z*=60 mm	*D*=53.4 mm *L*=3,0 m	Adição de um bocal de entrada melhorou a estabilidade da alimentação de sólidos com o leito de jorro. Estimativa de coeficiente de arraste efetivo.
1998	Ferreira, Silva e Freire	Esfera de vidro (1,0, 1,7, 2,0, 2,4, 2,8 mm – 2500 kg/m³)	*z*=20 a 70 mm	*D*=53,4, 81,4, 104,8, 148 mm *L*=4,2 m	Análise de um modelo unidimensional para prever o transporte pneumático no *riser*. Verificou-se boa previsão dos gradientes de pressão, contudo com parâmetros de interações gás-sólido e velocidades de deslizamento fisicamente inconsistentes.
2004	Costa, Ferreira e Freire	Esfera de vidro (1, 1,7 e 2,8 mm – 2500 kg/m³)	*z*=50 mm	*D*=81,4, 104,8, 148 mm *L*=3,4 m	Influência do diâmetro do riser no transporte com leito de jorro. Análise comparativa do desempenho de alimentador tipo jorro, gravitacional e parafuso helicoidal.
2010	Sousa et al.	Esfera de vidro (2,7 mm – 2500 kg/m³)	*z*=50 a 70 mm	*D*=53,4 mm *L*=4 m	Caracterização fluidodinâmica do sistema e utilização do mesmo para a secagem de esferas de vidro úmidas (secagem de pastas).
2015	Littman e Paccione	Esfera de vidro (1 mm – 2500 kg/m³)	-	*D*=28,5 mm *L*=5,5 m	Discussão sobre problemas tipicamente encontrados na modelagem do escoamento de sólidos na zona de aceleração do *riser* em transporte pneumático diluído.

CAPÍTULO 3 – CARACTERIZAÇÃO FÍSICA E DE ESCOABILIDADE DE BORRAS DE CAFÉ

Neste capítulo são apresentados os resultados e discussões referentes à caracterização física e de escoabilidade das amostras de borras de café, o que está relacionado ao objetivo específico número (1) desta tese. Abaixo são descritas a lógica de preparação e seleção das amostras e, na sequência, as principais conclusões sobre a caracterização das borras de café. Na Seção 3.1 constam os detalhes sobre as metodologias empregadas, bem como sobre as análises realizadas.

A amostra original de borra de café foi obtida por meio da filtração de café em pó comercial (Três Corações, Brasil) com água em ebulição e posterior secagem em estufa a 105°C por 24h. A distribuição granulométrica do pó seco foi determinada por peneiramento e os tamanhos médios variaram entre 100 e 2400 μm, com cerca de 80% da fração de sólidos limitada entre os tamanhos médios de 150 e 600 μm.

Experimentalmente foi possível perceber que as frações de maiores tamanhos (superiores a 600 μm) eram constituídas por agregados de partículas muito heterogêneos, os quais tinham seu tamanho reduzido facilmente com a aplicação de forças mecânicas. Assim, preparou-se por peneiramento três amostras denominadas "base" com distribuições granulométricas mais homogêneas e representativas da amostra de borra de café original: borra de café A (sólidos retidos entre as peneiras de 600 e 500 μm), B (sólidos retidos entre as peneiras de 500 e 300 μm) e C (entre as peneiras de 300 e 150 μm), as quais estão mostradas na Fig. 3.1.

Fig. 3.1. Amostras base de borras de café a) A_{100}, b) B_{100} e c) C_{100}.

Por se tratar de um resíduo industrial, borras de café geralmente apresentam uma grande variabilidade na distribuição granulométrica e umidade, as quais podem influenciar na eficiência de seu processamento/transporte. Dessa forma, foram preparadas misturas dos pós base com frações mássicas de 20, 40, 60 e 80%, resultando em 12 amostras binárias (AB, AC e BC) e 6 amostras ternárias (ABC) de borra de café. Além disso, as amostras base foram reumidificadas até umidades de 60%, resultando em 12 amostras úmidas. No total, 33 amostras de borra de café com diferentes distribuições granulométricas e umidades foram preparadas para as análises, o que engloba as principais variações dessas propriedades observadas na indústria de café solúvel (SILVA et al., 1998). A nomenclatura das amostras é apresentada como $A_xB_xC_x^y$, em que *x* corresponde à fração mássica de cada amostra base na mistura e *y* corresponde à umidade aproximada do pó em base úmida.

Na Seção 3.1 foi analisada a influência da distribuição granulométrica e umidade na escoabilidade das borras de café, utilizando como indicativos o ângulo de repouso estático e o índice de Hausner. Em linhas gerais, verificou-se que a escoabilidade de borras de café é sensível à alteração dessas propriedades, sendo classificada de *boa* a *muito ruim* à medida que há o aumento da umidade ou a presença de maior quantidade de partículas finas (C) na amostra. Por exemplo, verificou-se escoabilidade *ruim* para borras de café secas com tamanho médio de 350 μm ou com 40% de partículas finas na

mistura. Ademais, a escoabilidade das borras piorou com umidades superiores a 50%. Essa piora da escoabilidade está relacionada à intensificação de forças coesivas por pontes líquidas e por interações de van der Waals (ALTHAUS; WINDHAB, 2012; CASTELLANOS, 2005). A partir dos dados, foram propostas relações empíricas entre o ângulo de repouso e o índice de Hausner, bem como um diagrama ternário para identificar o índice de Hausner para misturas de borras de café com diferentes composições granulométricas, visando facilitar o monitoramento da escoabilidade de borras de café em processos industriais.

Além disso, outras propriedades foram determinadas, como a densidade *bulk* aerada e compactada, massa específica aparente e real, as quais serão úteis nos próximos capítulos. Por fim, por meio de microscopias eletrônicas de varredura, verificou-se que as partículas de borra de café possuem formato irregular e superfícies rugosas, o que é coerente por se tratar de um resíduo de biomassa.

Nos próximos capítulos serão descritos os ensaios experimentais no LPC utilizando os alimentadores tipo válvula-L e tipo leito de jorro. Esses ensaios foram realizados com as amostras B_{100}, $B_{90}C_{10}$ e $B_{100}^{30\%}$ de forma a avaliar o desempenho dos alimentadores operando com borras de café de diferentes distribuições granulométricas e umidades. As principais propriedades físicas dessas amostras estão resumidas na Tab. 3.1., sendo o diâmetro médio entre duas peneiras (d_{50}), umidade em base úmida, velocidade de mínima fluidização (U_{mf}), densidade *bulk* aerada (ρ_{ba}), índice de Hausner (*IH*), ângulos de repouso estático (AoR^e) e dinâmico (AoR^d).

Note que essas amostras foram selecionadas tendo em vista que: 1) a escoabilidade das borras de café é majoritariamente influenciada pela fração de C na mistura e as amostras base A_{100} e B_{100} apresentam índices de escoabilidade similares; 2) ensaios preliminares no descarregamento de pós a partir do silo do LPC enquanto desacoplado

do sistema mostraram que não ocorria descarga gravitacional de borras de café com frações de finos iguais ou superiores a 20%, possivelmente pela formação de arcos coesivos/mecânicos no orifício de saída; 3) umidades próximas a 30% são recomendadas para a queima de borras de café nas fornalhas de cogeração de energia das indústrias de café solúvel (SILVA et al., 1998).

Tab. 3.1. Propriedades físicas e de escoabilidade para amostras selecionadas.

Amostras	d_{50} **(µm)**	**Umidade (%)**	U_{mf} **(m/s)**	ρ_{ba} **(kg/m³)**	***IH*** **(-)**	AoR^e **(°)**	AoR^d **(°)**
$B_{100}{}^{30\%}$	400	30,0 ± 0,3[a]	0,20 ± 0,01[a]	342 ± 3[a]	1,21 ± 0,01[a] Boa	45,0 ± 1,0[a] Razoável	42 ± 2[a] Boa
B_{100}	400	2,8 ± 0,1[b]	0,14 ± 0,01[b]	380 ± 20[a]	1,21 ± 0,05[a] Boa	42,3 ± 0,8[b] Razoável	62 ± 3[b] Ruim
$B_{90}C_{10}$	370	3,2 ± 0,1[b]	0,15 ± 0,01[b]	335 ± 5[a]	1,26 ± 0,03[a] Razoável	42,5 ± 0,6[b] Razoável	70 ± 3[c] Muito ruim

Valores com letras diferentes na mesma coluna são estatisticamente diferentes com significância de 0,05.

Os procedimentos experimentais para a caracterização física e de escoabilidade dos pós, bem como os resultados obtidos foram publicados no artigo "*Spent Coffee Grounds as a Renewable Source of Energy: Analysis of Bulk Powder Flowability*", que será apresentado a seguir.

Em especial, a velocidade mínima de fluidização (U_{mf}) foi determinada por meio do método clássico de cruzamento entre as curvas características de leito fixo e leito fluidizado. Os ensaios foram realizados em um leito vertical de acrílico com diâmetro de 0,114 m, altura de pós de 9 cm e com injeção de ar uniforme pela base. Por outro lado, o ângulo de repouso dinâmico dos pós foi medido em um tambor rotativo de 10 cm de diâmetro e 4 cm de largura, preenchido 50% por borras de café, operando sob o regime de rolamento (SANTOS; CONDOTTA; FERREIRA, 2017).

3.1. "Spent Coffee Grounds as a Renewable Source of Energy: Analysis of Bulk Powder Flowability"

L. MASSARO SOUSA, M. C. FERREIRA

Artigo publicado na revista Particuology, volume 43, páginas 92-100, 2019.

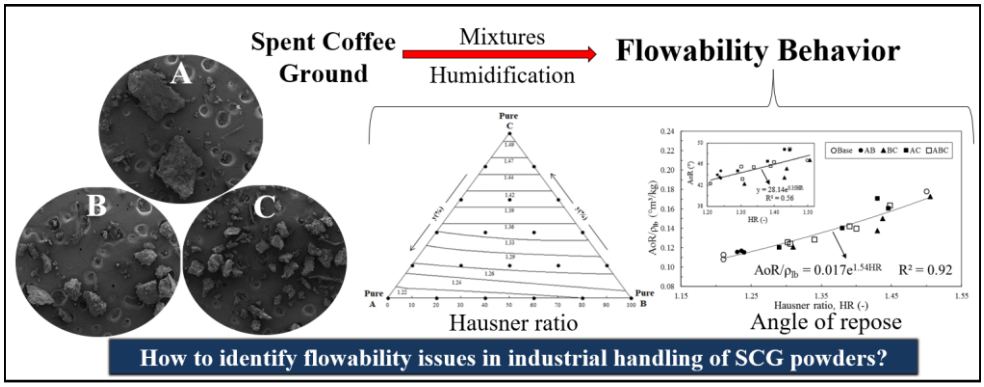

Fig. 3.2. Graphical abstract.

3.1.1. Abstract

The main use for Spent Coffee Ground (SCG) produced in the soluble coffee industry is the thermal energy generation in the industry itself. Throughout processing, SCG is submitted to unit operations strongly dependent on the powder flow behavior. In this study, we evaluated two classical flowability indexes of non-consolidated SCG powder: the angle of repose (*AoR*) and the Hausner ratio (*HR*). The influence of the mean diameter, particle size distribution and moisture content on *AoR* and *HR* of SCG was analyzed for powders with particle mean sizes from 225 to 550 μm. Values of *HR*>1.35 and *AoR*>45^{o}, which characterize a poor flowability, were observed for powders of mean particle size close to 350 μm and for mixtures with more than 40% of fine particles in their composition. The *AoR* was sensitive to powder size distribution, and powders with similar mean sizes presented higher values of *AoR* when the mixture size span was larger. For powders with moisture content up to 50%, the flowability indexes were not significantly affected by the moisture content. The Linear Mixture-Packing Model was used to predict the packed-bed void fraction for binary and ternary mixtures made up

from the combination of three base powders of different sizes. The model was used to build up a ternary diagram that can estimate *HR* of the powder mixtures. Additionally, an equation was fitted to correlate *HR* and *AoR*. The proposed diagram and the fitted equation may provide insight into the flow behavior and help process design of industrial plants that handle SCG.

3.1.2. Introduction

In 2016, more than 9 million tons of coffee beans were produced worldwide (INTERNATIONAL COFFEE ORGANIZATION, 2017), generating a revenue around US$ 25 billion (BRAZILIAN COFFEE EXPORTERS COUNCIL, 2017). In emerging countries well-known as traditional coffee producers, such as Brazil, Colombia and Vietnam, coffee is a commodity that plays a major contribution in the trade market. Fruit and beans are processed to produce the coffee powder, which is further sent to the Soluble Coffee Industry (SCI) or directly for domestic brewing. These processes generate a huge amount of solid residue, the Spent Coffee Ground (SCG). Around 2.5 million tons of SCG were produced in 2016, which was readily available for industrial processing (INSTANT COFFEE MARKET, 2018; MUSSATTO et al., 2011). If disposed of in landfills without a previous treatment, this residue might cause serious environmental issues due to its high organic load and acidity (MUSSATTO et al., 2011). The high calorific power of SCG (close to 25 kJ/kg, which is similar to that of the coal) (SILVA et al., 1998), makes it an attractive biomass for thermal energy generation in SCI facilities. Applications involving the production of biodiesel (AL-HAMAMRE et al., 2012; KONDAMUDI; MOHAPATRA; MISRA, 2008; LIU et al., 2017), fuel pellets (KONDAMUDI; MOHAPATRA; MISRA, 2008; LI; KANDA; MAKINO, 2014), hydrogen and ethanol (MUSSATTO et al., 2011) have been reported for this solid waste but most of it is burned

in SCI furnaces for steam production. Almost the total energy required in SCI is supplied by SCG (SILVA et al., 1998), thus significantly reducing the soluble coffee cost production. An effective handling of biomass powders through the related unit operations is of key importance to the success of those thermochemical processes.

In spite of the attractive energy balance, some critical issues can arise in handling biomass powders, such as the blockage of pipes, feeding devices or silos outlets (DAI; CUI; GRACE, 2012). Such occurrences may prevent a continuous and uniform flow to furnaces, reactors and so on, thus disrupting operations and reducing the overall efficiency and productivity. The effectiveness of feeding, storage, compaction and transport operations is strongly dependent on the powder flow behavior. The ability of a powder to flow is ruled by complex interactions between attractive and external field forces. If the weight of the particles is much larger than the attractive interparticle forces they will flow well, otherwise, a cohesive behavior is expected. Interparticle adhesion is originated by intermolecular forces including van der Waals forces, local chemical bonds, electrostatic charges, and bridging forces originated by liquid surface tension (LI et al., 2004). Van der Waals forces of molecular origin are dominant in fine dry powders and the bridging forces become significant as the water saturation in moist bulk powders increases (ALTHAUS; WINDHAB, 2012; CASTELLANOS, 2005). The numerous mechanisms that play a role in powder flowability have not been fully understood yet and quantifying flowability is quite a challenging task. However, it is known to depend on a number of factors including the particle size, size distribution, shape, surface texture, surface energy, chemical composition, moisture content, vessel geometry, packing history, among others (LI et al., 2004).

The Hausner ratio (*HR*) and the Angle of Repose (*AoR*) are indexes based on easily measurable properties that serve as useful flowability indicators for bulk powders in

industrial and practical applications. The first one is based on the ratio of tapped to loose bulk density and is considered a measure of powder cohesion, while the latter is obtained from powder flow under gravitational discharge (ABDULLAH; GELDART, 1999). As particle size distribution and moisture content of SCG produced in SCIs can vary in a wide range (SILVA et al., 1998), assessing how SCG flowability is affected by these variables is useful for monitoring process operations and quality features. Although the composition and energetic characteristics of SCG have been widely investigated in the literature (BALLESTEROS; TEIXEIRA; MUSSATTO, 2014; CAMPOS-VEGA et al., 2015; MUSSATTO et al., 2011; SILVA et al., 1998), to the best of authors' knowledge, no study was focused on assessing their basic flowability characteristics.

This study is aimed at evaluating flow indexes of non-consolidated SCG powders. The *AoR* and *HR* were determined for dry and moist powders in a size range from 225 to 550 μm and the influence of mean size and moisture content on the flowability indexes was evaluated. To be able to cover a wide range of particle's size and particle size distribution, three SCG powder samples made of fine, intermediary and coarse size particles were used to produce binary and ternary mixtures. A ternary diagram was built up to predict *HR* of SCG powder mixtures based on the Modified-Linear Mixture Packing model and an equation correlating *HR* and *AoR* was fitted based on the experimental data.

3.1.3. Material and Methods

The procedures used for sample preparation, particle and bulk powder characterization and measurement of flow indexes will be presented in this section.

3.1.3.1. Sample preparation

The SCG was obtained after brewing an ordinary Brazilian ground coffee made up from a blend of Arabica and Robusta grains (brand Três Corações), acquired in São Carlos-SP, Brazil. To reduce the powder's moisture content, 5 mm thick layer samples were oven-dried at 105±2ºC for 24h and stored under ambient temperature until further use.

The particle size analysis of the original dried sample was performed by sieving it according to the ASTM standards (ASTM INTERNATIONAL, 2010), in triplicate assays. SCGs samples of 100 g were poured into a set of stainless-steel sieves, with size apertures decreasing from 2360 to 63 μm. The set of sieves was coupled to a shaker (RETSCH AS200) and vibrated during 30 min at an amplitude of 1.5 mm. The powder mass fraction retained in the sieves of size aperture above 600 μm, which was only 20% of the total, was discarded and the remaining portion was sieved again from 600 to 150 μm. This portion was separated into three fractions denominated as the base samples, A, B and C. Sample A is made up of particles with sizes between 600 and 500 μm (d_{svA}=550 μm), sample B contains the particles retained between 500 and 300 μm (d_{svB}=400 μm), and sample C those retained between 300 and 150 μm (d_{svC}=225 μm). Additional mixtures were produced by combining mass fractions (y) of 20, 40, 60 and 80% of the base samples, resulting in 12 binary and 6 ternary mixtures. The mixtures were homogenized prior to the assays. Tests were carried out in triplicate for the base powders, binary and ternary mixtures, therefore 63 dry samples were prepared and analyzed.

3.1.3.2. Powder characterization

The samples were characterized according to the methods described in the following sections.

- *Mean diameter*

The mean diameter of the base samples, binary and ternary mixtures were calculated from Eq. (3.1), in which y_i is the mass fraction of the base sample (A, B or C) in the mixture and d_{svi} is the sieve mean diameter of the base sample.

$$d_S = 1/\sum(y_i/d_{svi}) \quad (3.1)$$

- *Initial moisture content*

The initial moisture content was determined by the gravimetric method, in triplicate. Powder samples of 3 g were kept in an oven (FANEM, model 315SE) at 105 ºC for 24 h.

- *Solid and particle densities*

The solid density (ρ_s) was determined for the SCG original dry sample using a helium gas pycnometer (Ultrapycnometer 1000, Quantachrome Instruments), in triplicate. The particle density (ρ_p) was determined for the dry base powders A, B and C using a liquid pycnometer, with a replicate. The pycnometer has a volume of 25 cm^3 and the liquid used was methanol.

- *Particle morphology*

Particles shape and surface texture were evaluated through a scanning electron microscope (SEM). The SCG base samples were glued over a carbon tape and coated with gold. The analysis was performed using a microscope (FEI Inspect S50) under a high vacuum atmosphere.

- Loose and tapped bulk densities

The loose and tapped bulk densities were obtained according to the procedure described elsewhere (WORLD HEALTH ORGANIZATION, 2012), in triplicate. Powder samples (50-70g) were poured through a funnel into a 250 cm^3 and 2.2 cm diameter graduated glass cylinder. In all the assays, the powder filled more than 60% of the cylinder volume. The vessel was placed into a proper tapping device that allowed the vessel to be successively lifted at a height of 3 cm and released (CAMPOS; FERREIRA, 2013). The powder volume was periodically recorded from N=0 up to N=1250 taps, when no more variation in the powder volume was observed. The assays were performed at ambient temperature and relative humidity between 45 and 70%, which is sufficient to eliminate static charges. Both the loose (initial) and tapped (final) bulk densities were obtained by dividing the powder mass in the cylinder by its respective volume. The loose or tapped void fractions were determined according to:

$$\varepsilon = 1 - \left(\rho_b^* / \rho_p\right) \tag{3.2}$$

where ρ_b^* is the loose (ρ_{lb}) or tapped (ρ_{tb}) bulk densities and ρ_p is the particle density. It is worth noting that Eq. (3.2) applies to estimate the void fractions of dry samples.

- Powder humidification

To vary the powder moisture content, a humidification procedure was performed. A powder sample of 50 g was mixed with water in glass flasks, which were sealed and stored at 4°C for 60 h. After every 24 h, the flasks were opened, and the powders were homogenized to ensure uniform moisture distribution.

The water amount added to the flasks were determined based on the established moisture content for a sample and covered a range of moisture content up to 50% (wet basis). For each base sample, four different moisture contents were analyzed in triplicate,

therefore a set of 36 moist samples was prepared. The moisture content in wet basis and the water saturation stage (*S*) in the bulk powders were calculated by:

$$MC = m_w/(m_w + m_s) \quad (3.3)$$

$$S\ (\%) = V_w/(V_t - V_s) \quad (3.4)$$

where m_w is the mass of liquid water in the packed-bed, m_s is the mass of solids, V_w is the total volume of liquid water in the packed-bed; V_t is the total volume of the compacted dry bed, and V_s is the volume occupied by the solids (based on ρ_s).

3.1.3.3. Flowability indicators

The powder flowability was assessed through measurements of *AoR* and *HR*, as described in the following sections. The criteria for flowability classification based on these indexes are described in details elsewhere (TAN; MORTON; LARSON, 2015). According to these criteria, the transition from a *passable* to a *poor* flowability, which defines the likely limit to flow issues occurs for *AoR* and *HR* higher than 45º and 1.35, respectively.

- Hausner ratio (HR)

The *HR* was calculated from the ratio of the tapped to the loose bulk density, according to:

$$HR = \rho_{tb}/\rho_{lb} \quad (3.5)$$

- Angle of Repose (AoR)

The angle of repose was determined by the funnel method, according to (ASTM INTERNATIONAL, 2000). The powders were poured into the funnel and discharged by gravity over a white paper surface, forming a conical heap of height *H*. The conical bed

circumference was drawn with a pen and its diameter (*D*) was taken as the average of four records. The experiments were performed in triplicate and *AoR* was calculated by:

$$AoR = \tan^{-1}(2H/(D-d)) \quad (3.6)$$

3.1.3.4. Statistical analysis

The one-way analysis of variance (ANOVA) based on the Tukey test was used to verify whether there was any statistically significant difference (p<0.05) between the means of the different groups of bulk densities and flow properties. The data are reported as mean values and their standard deviations.

The empirical equations fitted to the experimental data using the Excel software (Microsoft) and the determination coefficients for the equations (R^2) are reported.

3.1.4. Results and Discussion

The results for powder characterization and measurement of flowability indexes are presented in the following sections.

3.1.4.1. Characterization of SCG base dry samples

The main physical properties of the base samples are summarized in Tab. 3.2. The particle densities (ρ_p) of the base samples are similar to the value reported by Silva et al. (1998) for SCGs (1200 kg/m³) (SILVA et al., 1998). The solid density is equal to 1315±3 kg/m³, which is similar to values reported for fresh coffee powders from Colombia and Mexico (respectively 1361 and 1355 kg/m³) (SINGH et al., 1997). Based on their mean size and particle density, the base powders A and B are classified as *Geldart B* and powder C is classified as *Geldart A* (GELDART, 1973). According to this classification, samples

A and B are coarse powders and sample C is categorized as a fine powder, but not a cohesive type.

Tab. 3.2. Sieve mean diameter, moisture content, particle density, loose and tapped bulk densities and porosities for the base powders.

SCG Powder	d_{sv} (μm)	Moisture content (% w.b.)	ρ_p (kg/m³)	ρ_{lb} (kg/m³)	ρ_{tb} (kg/m³)	ε_{lb} (-)	ε_{tb} (-)
A	550	5.4 ± 0.1[a]	1130 ± 10[a]	390 ± 20[a]	471 ± 7[a]	0.655 ± 0.010[a]	0.583 ± 0.009[a]
B	400	2.8 ± 0.1[b]	1120 ± 20[a]	380 ± 20[a]	460 ± 10[a]	0.660 ± 0.010[a]	0.590 ± 0.010[a]
C	225	3.2 ± 0.1[c]	1120 ± 10[a]	262 ± 2[b]	393 ± 7[b]	0.766 ± 0.001[b]	0.649 ± 0.006[b]

Values with different letters in the same column are significantly different at a 0.05 significance level.

The loose bulk densities of powders A and B are higher than those of sawdust, rice straw (GUO et al., 2015), sugarcane bagasse and corn stover (DHIMAN et al., 2016). Due to the high combustion heat value of SCG powders, this is an appealing result concerning economic feasibility of using SCG as a fuel feedstock, as the costs for storage and transport would be lower and its energy density (in MJ/m³) higher in comparison to those biomasses. After drying, the maximum moisture content of the base samples is equal to 5.4% (w.b.), and the saturation level (*S*) is less than 4%, characteristic of a pendular state in which discrete liquid bridges bind the particles together (ALTHAUS; WINDHAB, 2012). Therefore, the contribution of the capillary forces is negligible to powder cohesion in the conditions tested.

The particle morphology and surface of powders A, B and C can be observed in Fig. 3.3. In all samples one can notice particles with quite irregular shapes and rough surfaces, with asperities on them, characteristics which are similar to those reported in the literature for SCG powders (BALLESTEROS; TEIXEIRA; MUSSATTO, 2014; ZARRINBAKHSH et al., 2016).

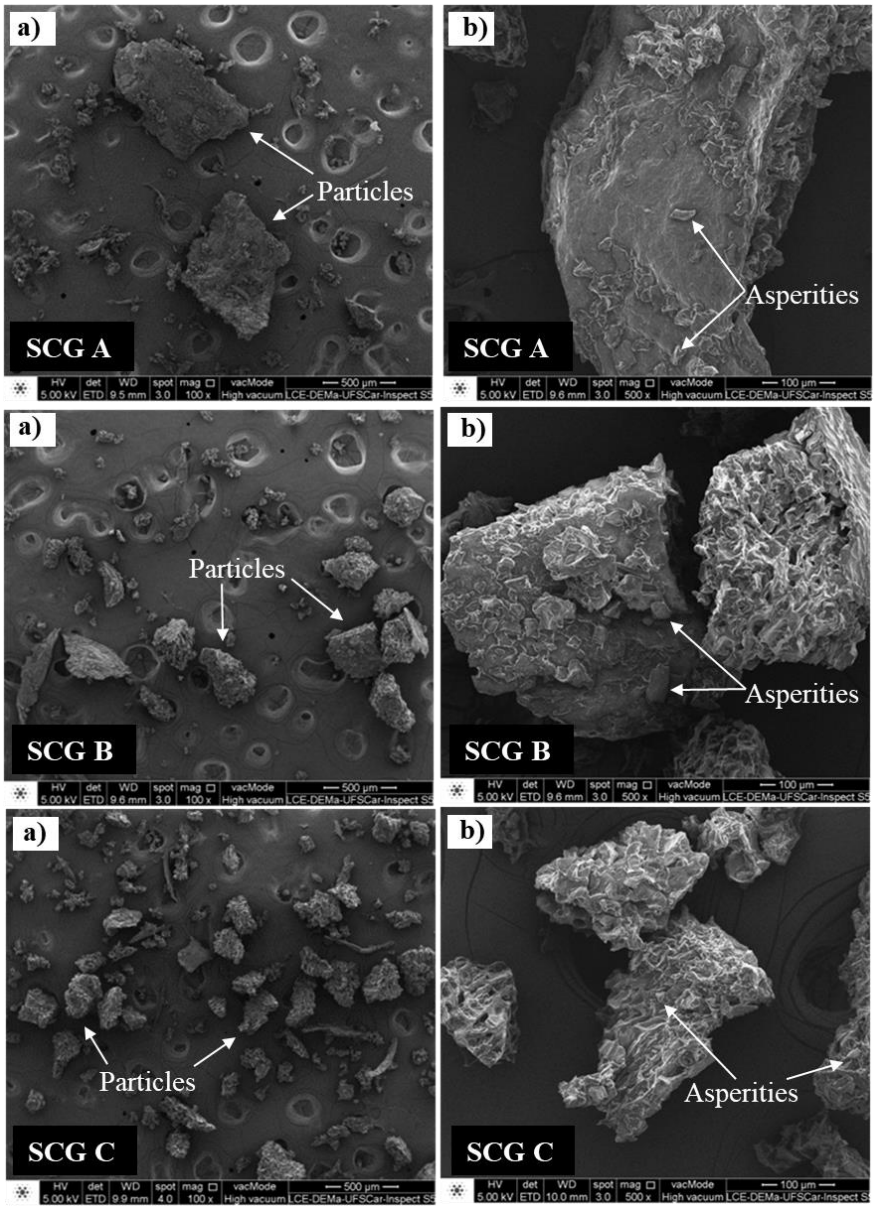

Fig. 3.3. Micrographs of A, B and C samples. (a) 100x and (b) 500x magnification.

3.1.4.2. Effect of d_S and particle size distribution on the flowability indexes

The measured values of *HR* are presented in Fig. 3.4. as a function of the mean diameter. The literature reports that flow indexes may be poorly reproducible because it is difficult to eliminate the past history of powders and to reproduce a macroscopically equivalent initial state in all the experiments (CASTELLANOS, 2005). In the present study, the standard deviations of *HR* (triplicate measurements) were in general lower than 5%, corroborating that the experimental procedures were effective to reduce variability.

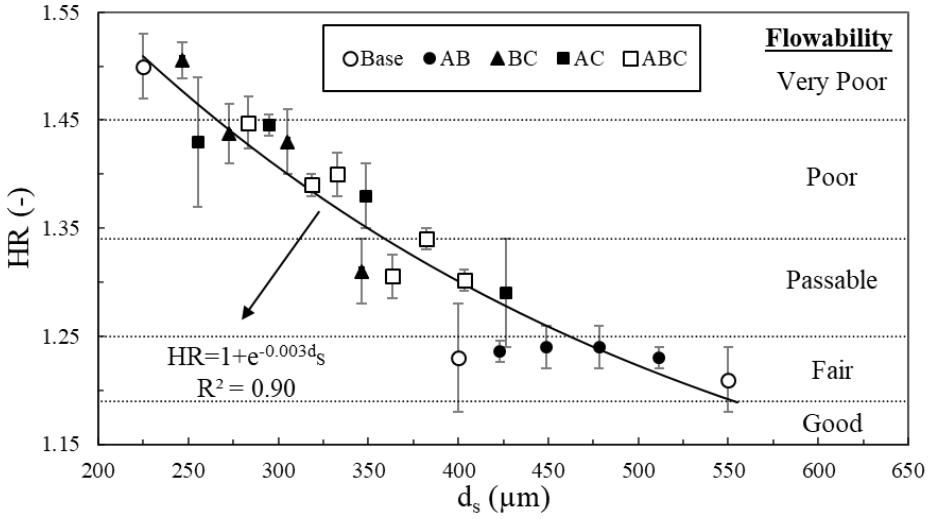

Fig. 3.4. Hausner ratio as a function of mean diameter for the base samples, binary (AB, AC, and BC) and ternary mixtures (ABC) of SCG powders.

In Fig. 3.4., the results for the base powders A, B and C are indicated by hollow circles, while the binary (AB, BC, and AC) and ternary mixtures (ABC) are indicated by solid symbols and hollow squares, respectively. The mixtures were obtained by combining the base powders, as described in Section 3.1.3.1, therefore some powders have similar mean sizes but different particle size distribution (PSD).

According to Fig. 3.4., the coarse powders A and B have similar *HR* (1.21±0.03 and 1.21±0.05, respectively) and both are categorized as *free-flowing* materials. As for sample C, which is the fine powder, *HR* increases to 1.50±0.03, which characterizes a *very poor* flowability. The transition from a *passable* to a *poor* flowability (*HR*>1.35) is observed at a particle size of 350 μm. Some authors (LI et al., 2004) observed that *HR* can be a misleading flowability indicator for particles having high adhesiveness, or a very broad size distribution and irregular shapes and in tests with pharmaceutical powders they found discrepancies between the *HR* results in comparison to real flow situations. However, the cohesive behavior of powder C was clearly noticeable during the experiments and is corroborated by the *AoR* results, as will be discussed ahead.

The boundary size for a transition between cohesive and non-cohesive powders is not precisely defined in the literature, but it is agreed that the intensity of van der Waals

forces is enhanced by the presence of particles of sizes less than 100 µm, owing to the increase in the specific superficial area and in the number of contacts between particles per unit of volume (CASTELLANOS, 2005). To investigate the possible reasons for the poor flowability of powder C, its particle size distribution was measured using a laser diffraction technique, in Malvern Mastersizer (MAF5001). Triplicate measurements were performed, and the data revealed that 14% of the volume fraction in this sample was composed of particles with sizes less than 100 µm. In spite of the small volume fraction, these fines correspond to about 93% of the specific superficial area in this sample. Therefore, the tendency towards a cohesive behavior of sample C is justified by the presence of these fine particles which were not detected in the sieving analysis, possibly because they agglomerate and are retained in the sieve with an aperture of 150 µm. Although the presence of fines is noticed in all the samples in the micrographs from Fig. 3.3., the amount is greater in sample C and the impact of fines on powder cohesiveness is more significant in this sample owing to the substantial increase in the specific superficial area. The presence of agglomerates in sample C is corroborated by its high void fraction, as seen in Tab. 3.2.

The data in Fig. 3.4. shows that *HR* of the mixtures initially decreases steeply at a practically linear rate in the range of d_s from 225 to 550 µm and tend to a constant value close to 1.25 for particle sizes over 400 µm. An exponential equation, represented by the solid line in Fig. 3.4., was fitted to the experimental data, with a correlation coefficient R^2=0.90. The equation is given by:

$$HR = 1 + e^{-0.003 d_S} \tag{3.7}$$

The uniform distribution of the data around the fitting line in Fig. 3.4. suggests no evidence of an influence of the particle size distribution in *HR*.

The results for *AoR* are shown in Fig. 3.5. The wider dispersion in *AoR* measurements in comparison to *HR* can be attributed to the uncertainties that arise from the loose consolidation state of the conical heap formed in the *AoR* measurements, as the random arrangement of particles is hardly reproducible in different assays in spite of the attempts to standardize the experimental procedures. This problem is minimized in the *HR* measurements, as the initially loose-packed bed goes towards a quasi-consolidated state throughout tapping.

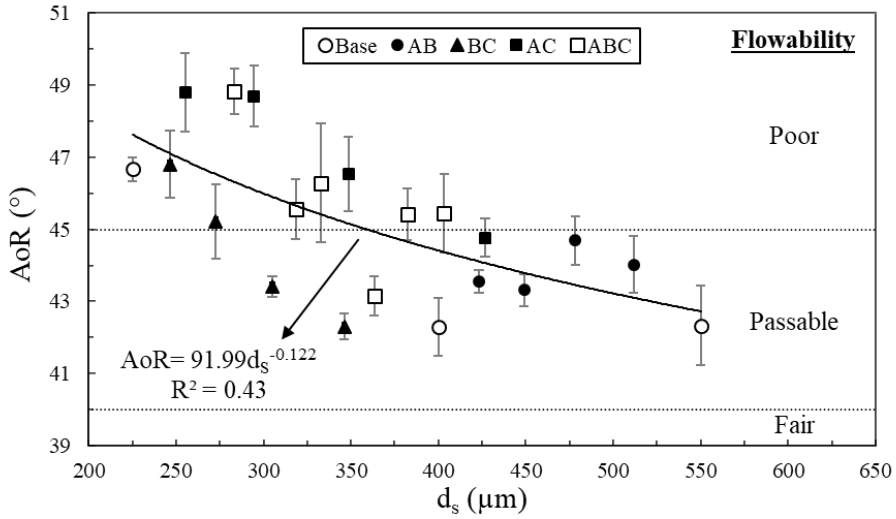

Fig. 3.5. Repose angle as a function of mean diameter for the base samples, binary (AB, AC, and BC) and ternary mixtures (ABC) of SCG.

Despite the wide dispersion, the data show a consistent decrease in *AoR* as the particle size increases. Like the results for *HR*, the values of *AoR* for powders A and B are quite similar (respectively 42±1^{o} and 42.3±0.8^{o}) and indicative of a *passable* flowability. The *AoR* increased up to 46.7±0.3^{o} for powder C, which was characteristic of *poor* flowability. The results for the powder mixtures are intermediate between powders A (the coarsest sample) and C (the finest sample). A polynomial equation was fitted to experimental data (represented by the solid line in Fig. 3.5.), however, in view of the wide dispersion of data, the correlation coefficient was too low (R^2=0.43). The equation is given by:

$$AoR = 91.99 d_S^{-0.122} \quad (3.8)$$

As suggested by some authors (GELDART et al., 2006; WOUTERS; GELDART, 1996), the correlation could be improved by using the weighted *AoR* (defined as the ratio of *AoR* to the loose bulk density) to replace *AoR*.

It is worth noting in Fig. 3.5. that, even at similar mean particle sizes, the *AoR* of the binary mixtures made of A and C powders are always significantly higher than the ones measured for the mixtures of B and C, suggesting that the angle is sensitive to the relative size of powders in the mixture and also to particle size distribution.

The transition from a *passable* to a *poor* flowability (*AoR*>45º) is observed for a particle size close to 350 μm, which agrees with the results observed for *HR*. This result confirms that both indexes are good indicators of powder flowability and yields to consistent predictions, despite the mean size obtained from sieving is not representative of powders' PSD.

A comparison of *HR* and *AoR* of powders A and B to those of other biomasses with similar mean sizes (LAM; SOKHANSANJ, 2014) shows that SCG flowability indexes obtained in the present study are close to those reported for switchgrass, which is an ease flow biomass. It is worth noting that the flowability indexes of SCG were more sensitive to the variation of particle mean size than other regular biomasses. A decrease in d_s from 550 to 225 μm increased *HR* and *AoR* indexes of SCG by approximately 19.3 and 13.7%, respectively, while a similar variation increased *HR* and *AoR* of switchgrass, corn stover and wheat straw in only 5%.

The correlation between the weighted *AoR* and *HR* can be observed in Fig. 3.6. The experimental data fitted an exponential equation with R^2=0.92. The equation is given by:

$$AoR/\rho_{lb} = 0.017e^{1.54HR} \quad (3.9)$$

The detail in Fig. 3.6. shows the data of the pure *AoR* as a function of *HR*, which clearly yields a significantly poorer fitting.

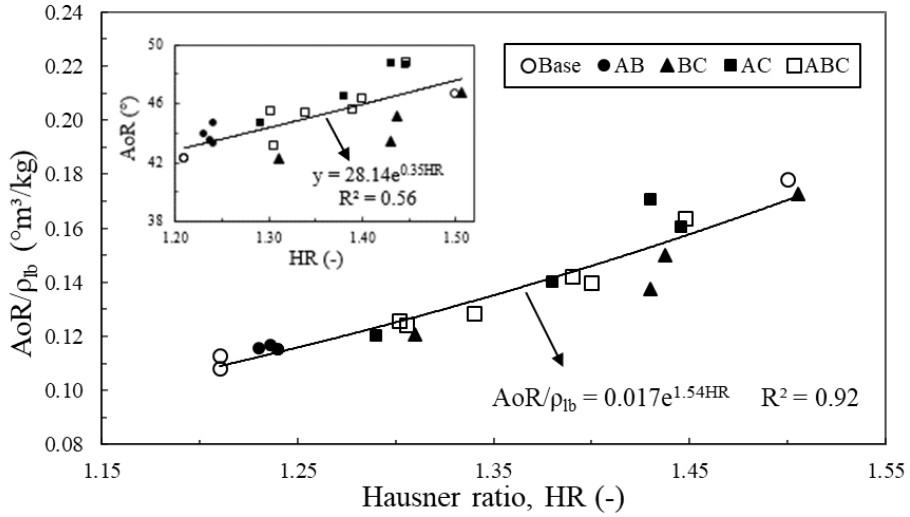

Fig. 3.6. Weighted *AoR* versus *HR* for SCG powders.

As aforementioned, the AC binary mixtures (with coarser particles and wider size span), always presented worse flowability in comparison to the BC mixtures, which is evidence of the influence of the particle size distribution (PSD) on *AoR*. We observed that the loose bulk densities of AC mixtures were on average 5% higher than those of BC mixtures, which contributes to form taller heaps with higher *AoR* in AC mixtures.

Presenting the flowability of powders as a function of the mean diameter is a useful and common practice. However, this approach may lead to misleading conclusions as powders with different PSD and similar mean diameter can present distinct flow behavior. This is the case, for example, of the base powder B (d_S=400 μm, *AoR*=42.3° and *HR*=1.21) and the ternary mixture $A_{60\%}B_{20\%}C_{20\%}$ (d_S=403 μm, *AoR*=45.4° and *HR*=1.30). Based on these values, the flowability of the first powder is classified as *passable* and the second's as *poor*.

In the next section, the validity of the Modified Linear-Packing model (YU; STANDISH, 1991) to predict the loose and tapped packed-bed void fractions for the powder mixtures is evaluated.

3.1.4.3. Modified Linear-Packing model to predict ε_b of the SCGs mixtures

According to Fig. 3.4 and Fig. 3.5, the flowability indexes of the binary and ternary mixtures are in between the values obtained for the largest (A) to the finest (C) powders. Therefore, the Modified Linear-Packing model (YU; BRIDGWATER; BURBIDGE, 1997) was applied to predict the void fraction of packed-beds of variable composition. The small-to-large ratios of the mixtures (R_{ij}) were calculated from the mean sizes of A, B and C ($d_{SA}>d_{SB}>d_{SC}$), and yielded the values R_{BA}=0.73, R_{CB}=0.56, and R_{CA}=0.41. The interaction functions $f(R_{ij})$ and $g(R_{ij})$, that depend only on R_{ij}, were determined by Eqs. (3.10) and (3.11), recommended for spherical and non-spherical particles (YU; ZOU; STANDISH, 1996).

$$f(R_{ij}) = (1 - R_{ij})^{3.33} + 2.81.R_{ij}.(1 - R_{ij})^{2.77} \quad (3.10)$$

$$g(R_{ij}) = (1 - R_{ij})^{1.97} + 0.36.R_{ij}.(1 - R_{ij})^{3.67} \quad (3.11)$$

The bed void fraction (ε) was then calculated by Eq. (3.12), in which V is the specific volume of the powder mixture. In this study, the mixtures were produced by combining the three base powders, therefore variable V was obtained from Eqs. (3.13) to (16). The values of V_A, V_B, and V_C were calculated from Eq. (3.12) using the experimental values of loose or tapped void fractions (Tab. 3.2.), according to the packing state to be determined.

$$\varepsilon = (V - 1)/V \quad (3.12)$$

$$V = \max\{V_A^T, V_B^T, V_C^T\} \quad (3.13)$$

$$V_A^T = V_A.y_A + V_B.\big(1 - f(R_{BA})\big).y_B + V_C.[1 - f(R_{CA})].y_c \quad (3.14)$$

$$V_B^T = [V_A - (V_A - 1).g(R_{BA})].y_A + V_B.y_B + V_C.[1 - f(R_{CB})].y_C \quad (3.15)$$

$$V_C^T = [V_A - (V_A - 1).g(R_{CA})].y_A + [V_B - (V_B - 1).g(R_{CB})].y_B + V_C.y_C \quad (3.16)$$

As shown in Fig. 3.7., the experimental void fractions are quite well predicted by the model, for both loose and tapped conditions, with mean deviations less than 2%. The

experimental values of void fractions were estimated by Eq. (3.2) as the base samples present low moisture content, as shown in Tab. 3.2.

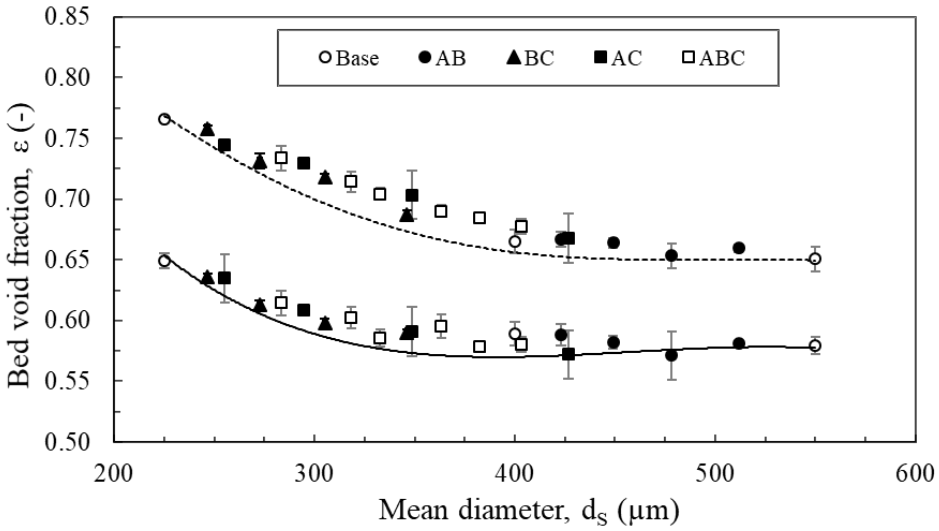

Fig. 3.7. Porosities as a function of mean diameter for the SCG base samples, binary and ternary mixtures: —, tapped and ---, loose porosities predicted by the Modified Linear-Packing model.

The loose and tapped predicted void fractions were used in Eq. (3.2) to calculate the bulk densities of powders and *HR* was obtained for the binary and ternary mixtures. The predicted (solid lines) and measured (symbols) values of *HR* are presented in Fig. 3.8. as a ternary diagram, where each vertex corresponds to a pure base sample (A, B or C), the edges correspond to the binary mixtures (AB, AC, and BC) with a variable mass fraction from 0 to 100%, and the interior corresponds to the ternary mixtures (ABC). For example, the point marked with the star symbol on sideline A-C of Fig. 3.8. shows that *HR* of a binary mixture composed of 60% of A and 40% of C is equal to 1.33. For a ternary mixture with 60% of A, 20% of B and 20% of C (the star symbol inside the triangle), the value of *HR* is 1.26. According to (YU; STANDISH, 1991), when the ratio between particle sizes is higher than 0.154, as is the case of our mixtures, powder compaction occurs mainly by the occupation mechanism, in which the voids are filled in throughout packing as the smaller particles occupy the spaces opened by particle rearrangement. In a packing ruled by such a mechanism, all the components in the mixture

contribute to the compaction kinetic. In spite of that, *HR* of the SCG mixtures was affected mostly by the mass fraction of the finer particles (powder C), as the smaller and more cohesive particles limit the packed-bed structure rearrangement in order to achieve a closer packing (LAM; SOKHANSANJ, 2014).

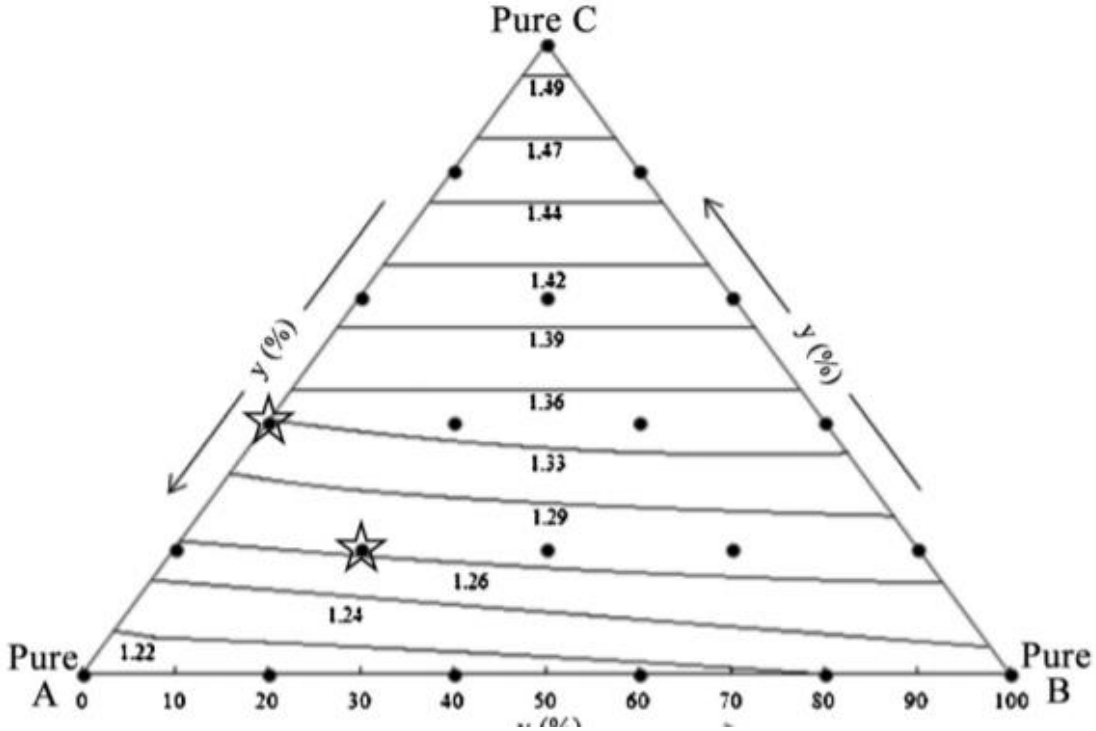

Fig. 3.8. *HR* values for SCG powders as a function of base samples composition (*y*): ●, *HR* measured points; —, predicted by the Modified Linear-Packing model.

Based on *HR* results shown in Fig. 3.8., it can be seen that powder flowability worsen as the mass fraction of powder C is raised. Therefore, powders with y_c=0 have flowability categorized as *fair*; with y_c=0.2 the flowability is *passable*; in the interval 0.4≤ y_c≤ 0.6 it is *poor* and with y_c≥0.8 it is *very poor*. For y_c>0.5 the *HR* increases linearly with the increase in y_c, indicating that powder flowability is governed by the finest particles and the presence of coarse particles did not alter the flowability. As *AoR* is directly correlated to *HR*, as shown in Fig. 3.6. (or Eq. 3.9), the increase in the amount of powder C in a mixture also increases *AoR*.

It is worth noting that the ternary diagram proposed in Fig. 3.8. can be used to predict the *HR* for a sample sieved and cut into three fractions with mean sizes similar to

the base samples A, B and C. New diagrams would need to be made for fractions with different sizes. Nevertheless, using a ternary diagram as a graphical representation of changes in *HR* could be a useful tool for a rapid and reliable estimation of *HR* and the method can be extended for other powders.

In the next section, the flowability indexes of SCG will be evaluated for moistures up to approximately 50% w.b., which cover the usual processing range (SILVA et al., 1998).

3.1.4.4. Effect of moisture content on the flowability indexes

The values of *HR* and *AoR* data for powders under different moisture contents are presented in Tab. 3.3.

As the moisture content of the base samples was raised up to 50% w.b., *HR* stays practically constant and *AoR* shows a discrete increase, although in most conditions the difference is within the range of experimental uncertainty. It is known from the literature that increasing moisture content is likely to affect the powder flow behavior and mechanical strength as the packing reaches the funicular state, at saturation levels between 25% and 50%, when saturated clusters and liquid bridges coexist (ALTHAUS; WINDHAB, 2012). In the range of conditions tested, a slight deterioration in flowability was observed for powder C only at a saturation level close to 42%, corresponding to a moisture content of 59.2%. This indicates that the bridging forces were strong enough to significantly affect the flowability index in this condition. Therefore, for S<42% the samples may be in the pendular state, in which liquid bridges exist but do not play a significant role on the flow behavior. It is worth noting that the value of S=42% found in this study is between 25% and 50%, which is reported as a transition range from the pendular to the funicular states for real systems (ALTHAUS; WINDHAB, 2012).

Tab. 3.3. Flowability of base samples under different moisture content and water saturation level.

SCG Sample	*MC* (% w.b.)	*S* (%)	*HR* (-)	*AoR* (º)
A	5.4 ± 0.1	3.8 ± 0.1	1.21 ± 0.03^{ab}	42.0 ± 1.0^{ab}
	21.1 ± 0.5	13.3 ± 0.3	1.19 ± 0.01^{ab}	43.0 ± 1.0^{ab}
	30.4 ± 0.2	17.3 ± 0.1	1.17 ± 0.01^{ab}	43.2 ± 0.7^{ab}
	37.9 ± 0.1	20.8 ± 0.1	1.17 ± 0.01^{a}	43.2 ± 0.6^{ab}
	47.0 ± 1.0	27.3 ± 1.0	1.21 ± 0.02^{b}	44.1 ± 0.4^{b}
B	2.8 ± 0.1	2.1 ± 0.1	1.21 ± 0.05^{a}	42.3 ± 0.8^{a}
	19.4 ± 0.9	12.5 ± 0.3	1.23 ± 0.02^{a}	45.8 ± 0.2^{b}
	28.6 ± 0.7	16.1 ± 0.5	1.21 ± 0.01^{a}	45.0 ± 1.0^{b}
	36.8 ± 0.9	20.0 ± 0.8	1.25 ± 0.02^{a}	44.8 ± 0.8^{b}
	44.5 ± 0.5	26.3 ± 0.3	1.30 ± 0.07^{a}	46.1 ± 0.5^{b}
C	3.2 ± 0.1	1.8 ± 0.1	1.50 ± 0.03^{ab}	46.7 ± 0.3^{a}
	29.6 ± 0.3	14.5 ± 0.4	1.45 ± 0.04^{ab}	48.7 ± 0.9^{b}
	42.0 ± 0.1	21.6 ± 0.2	1.44 ± 0.02^{a}	50.9 ± 0.2^{c}
	52.4 ± 0.4	31.1 ± 0.6	1.53 ± 0.02^{b}	52.0 ± 0.5^{c}
	59.2 ± 0.1	42.0 ± 0.2	1.62 ± 0.05^{c}	54.9 ± 0.3^{d}

Values with different letters in the same column are significantly different at a 0.05 significance level.

Since the dried and moist base samples presented similar *HR* up to 50% w.b., the diagram presented in Fig. 3.8. can be used for moist powders up to this range. Based on the analysis of the previous sections, some alternatives to estimate *HR* and *AoR* of non-consolidated SCG powders are suggested:

- The Eq. (3.7), valid in the range 225<*ds*<550 μm can be used to estimate *HR* if the powder mean diameter is known. In addition, by measuring powder loose bulk density, Eq. (3.9) can provide estimates for *AoR*.
- If the powder size can be expressed as a composite of three mass fractions of different sizes, the ternary diagram presented in Fig. 3.8. can be used to estimate *HR* and *AoR* can be estimated from Eq. (3.9).
- Inversely, Eq. (3.9) can be used to obtain *HR* if powder *AoR* and loose bulk density are measured. Based on the measured values of *HR*, the ternary diagram

can be used as a tool to evaluate the mass fraction of each base sample in the binary or ternary mixtures.

These procedures are based on quick and easy measurements and may be useful to help in process design and monitoring unit operations involved in renewable energy generation in soluble coffee facilities.

3.1.5. Conclusions

This study presented experimental data of *HR* and *AoR* of non-consolidated SCG powder mixtures prepared from combinations of three base samples and with mean sizes from 225 to 550 μm. The measured indexes showed that a *poor* flowability is observed for SCG powders with d_S<350 μm or for mixtures with a fraction greater than 40% in mass of fines. The *AoR* of SCG mixtures was influenced by the PSD, as samples with wider size span presented higher *AoR*. The *HR* of the mixtures increased significantly as the amount of the finest and more cohesive sample rose. The flowability behavior of moist SCGs was similar to that of dried powders for moisture contents up to 50% (w.b.). It was verified that SCGs present a higher energy density and worse flowability indexes when compared to other ordinary biomasses. Finally, some procedures to identify flowability indexes based on fitted correlations and on the Linear Mixture-Packing Model were proposed. These procedures may be useful to improve handling and monitoring operations in plants that use SCGs for thermochemical applications.

3.1.6. Acknowledgements

The authors would like to thank the São Paulo Research Foundation (FAPESP), grant 2016/25946-2, for the financial support.

3.1.7. Nomenclature

AoR	Angle of repose, defined by Eq. (3.6) (°)
D	Mean diameter of the circumference of the conical powder bed (cm)
d	Diameter of the funnel discharge orifice (cm)
d_s	Mean diameter, defined by Eq. 1 (µm)
d_{svi}	Mean sieve diameter of a base sample, i = A, B or C (µm)
$f(R_{ij})$	Interaction function defined by Eq. (3.10) (-)
$g(R_{ij})$	Interaction function defined by Eq. (3.11) (-)
H	Height of the conical bed (cm)
HR	Hausner ratio, defined by Eq. (3.5) (-)
MC	Moisture content (%)
N	Number of taps (-)
p	Significance level (-)
R_{ij}	Ratio of small (i) to large (j) mean diameter (-)
S	Water saturation level, defined by Eq. (3.4) (-)
y_i	Mass fraction of a base sample in the mixture, i = A, B or C (-)
V	Specific volume, defined by Eq. (3.13) (-)
V_i	Specific volume of a base sample, i = A, B or C, determined by Eq. (3.12) (-)
V_i^T	Specific volume for i = A, B or C, defined by Eqs. (3.14) to (3.16)
V_s	Volume occupied by solids in the packed bed (m^3)
V_t	Total volume of the dry tapped packed bed (m^3)
V_w	Total volume of liquid water in the packed bed (m^3)
Greek letters	
ε	Void fraction, defined by Eq. (3.2) (-)
ε_{lb}	Void fraction for loose bulk condition (-)
ε_{tb}	Void fraction for tapped bulk condition (-)
ρ_{lb}	Loose bulk density for N=0 ($kg \cdot m^{-3}$)
ρ_p	Particle density ($kg \cdot m^{-3}$)
ρ_s	Solid density ($kg \cdot m^{-3}$)
ρ_{tb}	Tapped bulk density for N=1250 ($kg \cdot m^{-3}$)

CAPÍTULO 4 – ALIMENTAÇÃO DE BORRAS DE CAFÉ AO LPC COM VÁLVULA-L: ANÁLISE EXPERIMENTAL

Neste capítulo, são apresentados os resultados experimentais da alimentação de borras de café ao LPC utilizando o alimentador tipo válvula-L, o que está relacionado aos objetivos específicos (2) e (4) desta tese. Conforme mencionado anteriormente, os ensaios foram realizados com as amostras B_{100}, $B_{90}C_{10}$ e $B_{100}^{30\%}$ de forma a avaliar o desempenho do alimentador operando com borras de café de diferentes distribuições granulométricas e umidades.

Na seção 4.1 é mostrado o funcionamento da válvula-L alimentando as borras de café ao LPC, operando sob diversas vazões de ar no alimentador (*U*) e no *riser* (*Q*). Essas variáveis de operação estão ilustradas na Figura 4.1. Em geral, os resultados foram promissores para a alimentação da amostra úmida ($B_{100}^{30\%}$), tendo em vista que a recirculação de sólidos foi estável e pôde ser ajustada e controlada entre 1,2 e 10 g/s com a simples mudança da vazão de ar na válvula-L. O alimentador foi robusto já que alterações da ordem de ±15% na vazão de ar no *riser* não afetaram a vazão de sólidos. Os níveis das variáveis *U* e *Q* foram selecionados com base nos limites de operação estável com o alimentador na unidade experimental utilizada.

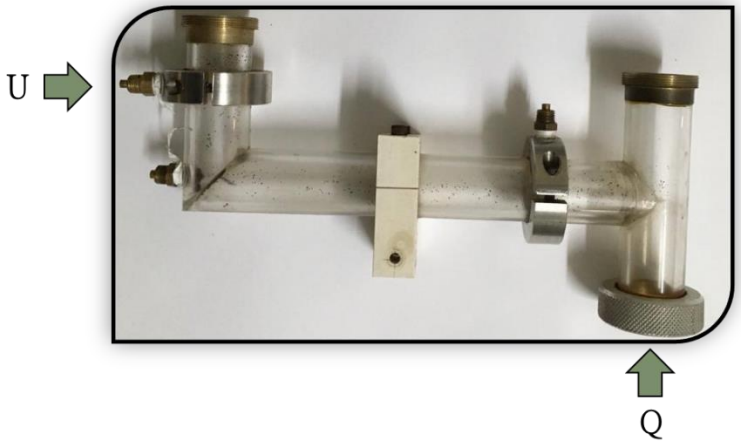

Fig. 4.1. Válvula-L em acrílico e principais variáveis de operação do alimentador para dosagem de pós a reatores LPC.

Além disso, foram observadas duas regiões distintas de operação da válvula-L com esta amostra. Para vazões de aeração baixas e médias (*U* inferiores a 14 L/min), observou-se que a vazão de sólidos aumentou com o aumento da vazão de aeração, comportamento similar ao reportado na literatura para a alimentação de partículas Geldart B. Contudo, sob altas aerações foi verificado transporte diluído de sólidos na região horizontal do alimentador, com a formação de vórtices e baixa vazão de sólidos, o que não havia sido verificado previamente.

As propriedades das borras de café afetaram a operação da válvula-L, observando-se instabilidades na alimentação e menores vazões de sólidos para as amostras com piores escoabilidades (B_{100} e $B_{90}C_{10}$). Com essas amostras, a vazão de sólidos se manteve aproximadamente constante ao se aumentar a vazão de aeração, sendo de 2,6 g/s para B_{100} e 0,7 g/s para $B_{90}C_{10}$. Pelo exposto anteriormente, nota-se que o funcionamento da válvula-L com biomassas em pó difere do comportamento tipicamente reportado na literatura, sendo verificados diferentes regimes de escoamento em decorrência das distintas propriedades físicas deste material (baixa massa específica, formato irregular e diferentes distribuições granulométricas e umidades), as quais refletem em sua escoabilidade.

Note que relacionar índices de escoabilidade com o escoamento de pós é em geral uma tarefa complexa, visto que os índices são medidos em condições controladas que são dificilmente reproduzidas em sistemas de transporte. Nesse sentido, dentre os índices de escoabilidade apresentados no Capítulo 3, o ângulo de repouso dinâmico foi considerado o mais apropriado para inferir sobre o transporte de sólidos na válvula-L, já que foi medido sob condição de escoamento de pós e sem a aplicação de forças externas de consolidação ou cisalhantes.

Por fim, os perfis de pressão no LPC foram estudados e a perda de carga na válvula-L foi correlacionada com a vazão de sólidos, o que permite inferir a taxa de recirculação no LPC baseado em simples medidas de pressão. Além disso, verificou-se que a pressão no *riser* aumenta quando são adicionadas maiores vazões de ar ao sistema, bem como quando há maior recirculação de sólidos.

Detalhes dos procedimentos experimentais e os resultados referentes à análise do desempenho da válvula-L foram relatados no artigo "*Analysis of the Performance of an L-Valve Feeding Spent Coffee Ground Powders into a Circulating Fluidized Bed*", que será apresentado a seguir.

4.1. "Analysis of the Performance of an L-Valve Feeding Spent Coffee Ground Powders into a Circulating Fluidized Bed"

L. MASSARO SOUSA, M. C. FERREIRA

Artigo publicado na revista Powder Technology, volume 362, páginas 759-769, 2020.

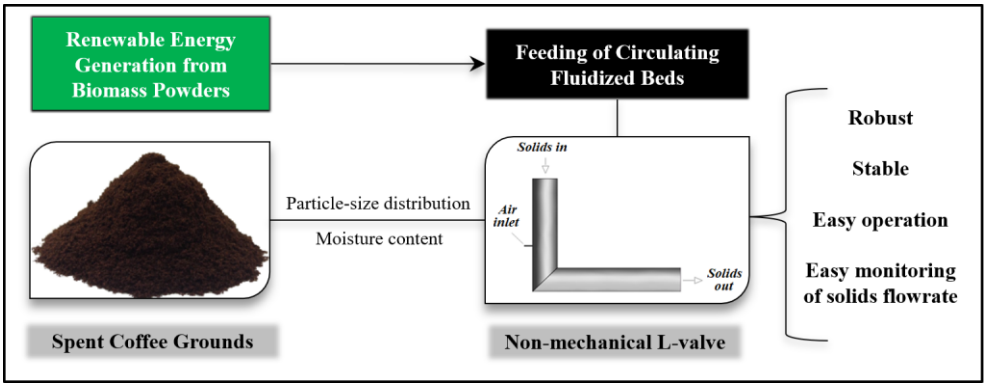

Fig. 4.2. Graphical abstract

4.1.1. Abstract

Using waste biomass powders is appealing to generate renewable energy and to reduce the dependence on fossil fuels, however, feeding reactors is still a challenge in processing. This paper examines the performance of a non-mechanical L-valve in feeding dry and moist Spent Coffee Ground (SCG) powders to a circulating fluidized bed under

a broad range of conveying and aeration flowrates. The L-valve performed as a robust feeder, providing stable solids circulation rate (W_S) for most of the conditions tested, and with W_S unaffected by fluctuations up to ±15% in the riser air flowrate. We verified that the L-valve performance is limited by the deterioration of powders' flowability, with lower W_S and narrower operation range in feeding dry SCGs and samples with the presence of fine particles. Nevertheless, the feeder can be considered a good option in handling SCGs with moisture content close to 30% w.b. and mean particle size of 400 μm, showing stable solids feeding in a range of $1.2<W_S<10.0$ g/s and easy operation. This is an appealing result since the moisture content of SCGs burned in the soluble coffee industry range within 25 and 50%. Finally, a correlation to predict *Ws* from the pressure drop in the L-valve is proposed, which fitted our data better than other equations available in the literature.

4.1.2. Introduction

Circulating Fluidized Beds (CFBs) are widely used in industrial processes for combustion and gasification due to the high solids throughputs, temperature uniformity, effective gas-solid contact, and continuous operation (GRACE; AVIDAN; KNOWLTON, 1997). A gas-solid CFB is usually composed by a riser, where the solids react and simultaneously are transported upwards by a fast gas flow; a separator placed at the top of the riser to collect and return the solids to the bottom; and a feeder to continuously reintroduce the particles into the riser, thus completing the circulation loop.

An effective feeding of particulate materials into CFB reactors is still a challenge. The feeding device and its operating conditions have a major impact on the riser's entrance length, solids distribution and hold-up (COSTA; FERREIRA; FREIRE, 2004; KIM; TACHINO; TSUTSUMI, 2008; LOPES et al., 2011b; PÁDUA; BÉTTEGA;

FREIRE, 2015; WANG et al., 2019). Inefficient or poorly designed feeders may provide an unstable or no solids flow to the reactor, yielding to deficient gas-solid contact in the riser and compromising process stability, automation, safety, and performance.

A wide variety of biomass powders with attractive higher heating values are used as a renewable source in energy generation, which is a quite convenient usage for many by-products produced in industrial processes. The Spent Coffee Ground (SCG) is a residue from the soluble coffee industry produced at rates of approximately 2.5 million tons per year. Generally, SCG powders are composed of a significant fraction of fine particles (<100 μm), with a wide size span and variable moisture content. Depending on powders' particle-size distribution (PSD) and moisture level, their flowability under non-consolidated conditions can vary from *good* to *very poor* (MASSARO SOUSA; FERREIRA, 2019a), hence these powders might clog feeding devices and hopper discharge orifices. Ideal feeding devices to handle such residues should be able to provide stable solids mass flowrate regardless of the particle sizes or moisture content.

Non-mechanical L-valves have been widely used to control the solids circulation rate in CFBs and have already proven to be suitable for processing conventional particles, such as sand and glass beads (ARENA; LANGELI; CAMMAROTA, 1998; LIM et al., 2013). These devices might also be attractive to handle biomass particles, as they have no moving parts to control the solids flow. Besides, these feeders are usually less expensive and easier to maintain and can be used at conditions of high pressure and temperature with a reduced risk of wear and seizure.

To the best of the authors' knowledge, a limited number of studies have been published on the analysis of flow behavior and performance of L-valves feeding particles categorized as Geldart B with density under 2,000 kg/m^3 and none of these studies deals with residue-based powders. An in-depth assessment of non-mechanical valves'

performance in feeding residue-based powders is crucial for their successful application in CFB reactors for renewable energy generation. This paper is aimed at evaluating the performance of an L-valve feeding dry and moist SCG powders to a CFB under a broad range of conveying and aeration velocities.

4.1.3. Theoretical background

The L-valve is a non-mechanical feeder that uses pneumatic actuation to transport and control the solids flowrate. It consists of a vertical standpipe and a horizontal pipe, with an aeration injection located next to the standpipe bottom. The powder is introduced into the feeder through the vertical section, usually by the sole action of the gravitational force, and then it is directed towards the valve's horizontal section by a compressed airflow. The L-valve horizontal section is connected to the unit to be charged with solids, which may be a silo, a storage vessel, a dryer or a reactor.

The powders already tested in L-valves feeding CFBs are indicated in the Geldart's diagram shown in Fig. 4.3. (ARENA; LANGELI; CAMMAROTA, 1998; CHAN et al., 2009; CHOVICHIEN; PIPATMANOMAI; CHUNGPAIBULPATANA, 2013; KARMAKAR; DATTA, 2010; KIM; TACHINO; TSUTSUMI, 2008; LIM et al., 2013; MONAZAM et al., 2018; XU et al., 2018; XUEYAO et al., 2013; YANG; LEU, 2008). It can be noticed that most studies focused on Geldart B particles of particle densities close to 2,500 kg/m^3, including glass spheres, sand, magnetite, and alumina. Most of the tested powders are composed of particles with uniform or well-defined shapes and with narrow PSDs. Some authors who evaluated the performance of L-valves with Geldart A particles reported on different gas-solid flow dynamic behavior and feeder workability from those observed for conventional Geldart B powders (LIM et al., 2013).

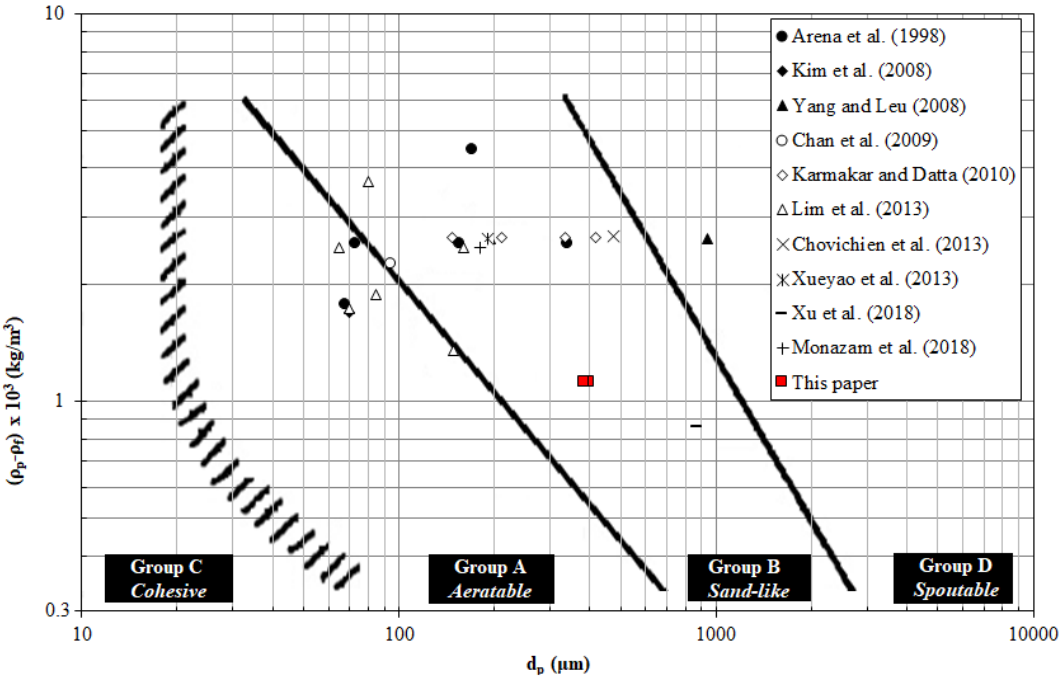

Fig. 4.3. Geldart's classification of powders already tested in L-valves feeding particulate materials to CFBs, and dry powders evaluated in this paper.

The powder investigated in this paper, with particle density under 2,000 kg/m^3, is indicated by the square symbol in Fig. 4.3. It is categorized as a Geldart B powder, but it is in a region of Geldart's diagram that has not been investigated so far. Samples of dry and moist powders are evaluated, as well as a mixture of coarse and fine powders. Below some results from the literature are reviewed as the tested powders show properties close to those of SCGs (ARENA; LANGELI; CAMMAROTA, 1998; LIM et al., 2013; XU et al., 2018).

Some authors compared the performance of an L-valve feeding Geldart A and Geldart B powders into a pilot-scale CFB (ARENA; LANGELI; CAMMAROTA, 1998). Their results showed that small variations in the aeration flowrate produced a sharp increase in the solids circulation rate (*Ws*) for Geldart A particles and that an unstable flow pattern arises under higher aeration velocities, possibly due to the formation of air bubbles in the standpipe that restricts the stable flow of solids downwards. On the other hand, *Ws* could be well controlled for Geldart B powders, with a linear increase in *Ws* as *U* rises. Finally, the authors added a bulk density term to a previous equation from the

literature (GELDART; JONES, 1991) to correlate the pressure drop in the valve (ΔP_{LV}) to the solids mass flux (G_s), and fitted new exponents for a broad variety of powders with different sizes and densities, resulting in the equation:

$$\Delta P_{LV}/L = 0.0649 G_S^{0.178} \rho_{lb}^{0.996} D_{LV}^{-0.574} d_S^{-0.237} \quad (4.1)$$

The prediction of the solids flux for the FCC powders using Eq. (4.1) overestimated G_S by factors of up to 20%.

An in-depth assessment of the L-valve operation with Geldart A powders with particle density under 2,000 kg/m^3 was performed by some authors (LIM et al., 2013). They tested a catalyst powder named KR40 (d_S=70 μm, and ρ_p=1730 kg/m^3), an FCC powder (d_S=85 μm, and ρ_p=1880 kg/m^3), and a PVC sample (d_S=148 μm, and ρ_p=1350 kg/m^3). In the Geldart diagram, these powders are located from the medium region of aeratable powders (Group A) to the transition-boundary of Group B powders. The authors reported that solids mass flux of PVC and FCC powders could be well controlled, with maximum values of *Gs* observed at 3.5 U_{mf}, where gas slugs were likely to be formed. After this peak, the solids mass flux of PVC showed a decreasing pattern as *U* rises, while G_S remained constant for the FCC sample. Moreover, the pressure drop in the L-valve was accurately predicted by Eq. (4.1), but the solids flux did not agree with the values estimated from the equations of the literature (SMOLDERS; BAEYENS, 1995). Based on this, the authors proposed a new correlation for powders in the size ranges of $70<d_S<148$ μm and $1350<\rho_p<1880$:

$$G_S/D_{LV} = 2.48x10^{-8}\left(U/U_{mf}\right)^{1.75} d_S^{-2.62} \quad (4.2)$$

The solids circulation rates for their samples were accurately predicted using Eq. (4.2) up to the peak point of *Gs*. After, *Gs* was gradually overestimated by the correlation as *U* increased.

Recently, the experimental behavior of a CFB unit operating with polyethylene beads (d_S=871 μm, and ρ_p=863 kg/m^3, Geldart B) has been compared to numerical simulations using the CFD-DEM method (XU et al., 2018). It was shown that some key variables in the CFB loop could be reasonably predicted by the simulations, such as the pressure drop in the riser, cyclone, and standpipe sections, as well as the inventory of solids in the standpipe. However, the predictions of ΔP and G_S at the L-valve section still deviated from the experimental values. Generally, the predicted G_S varied from 0.3 to 2.5 times of the experimental values, while ΔP_{LV} was overpredicted by 2 times. This highlights that more research is needed to quantitatively describe the feeding of powders to CFBs by L-valves.

4.1.4. Materials and Methods

4.1.4.1. Materials

The SCG samples were obtained after brewing an ordinary Brazilian coffee powder (Três Corações, Minas Gerais, Brazil) with boiling water. The samples' moisture content was reduced by keeping them in an oven for 24h at 105±2ºC. The original SCG sample was sieved to produce two base samples: sample B, composed of particles with sizes from 300 to 500 μm (dsv=400 μm), and sample C, composed of particles with sizes from 150 to 300 μm (dsv=225 μm).

The cold-flow experiments in the CFB unit were performed using three different SCG samples. Sample B_{100} was composed of 1.5 kg of the base sample B. Sample $B_{90}C_{10}$ was prepared by mixing 1.35 kg of the base sample B with 0.15 kg of the base sample C. Finally, an additional sample with moisture content equal to 30%, denominated as sample B_{100wet}, was prepared by mixing sample B_{100} with water in glass flasks, which were sealed and stored at 4°C for 60 h. The sizes and moisture content of the samples were chosen to

match the properties of SCG powders usually burned in the soluble coffee industry (SILVA et al., 1998).

The nomenclature adopted for the SCG mixtures is the same used in previous papers that focused on the characterization of physical and flow properties of SCG powders, hence details on the SCG properties and on the characterization methods can be verified in a straightforward way (MASSARO SOUSA; FERREIRA, 2019a, 2019b). The dynamic angle of repose (AoR^d) of the samples were measured using a 10 cm diameter and 4 cm width rotating drum under the rolling flow regime. The experimental procedure is described elsewhere (SANTOS; CONDOTTA; FERREIRA, 2017). Some key physical properties and the dynamic angles of repose for the tested powders are shown in Tab. 4.1.

Tab. 4.1. Sieve mean diameter, moisture content, minimum fluidization velocity, particle density, loose bulk density and dynamic angle of repose of tested powders.

SCG sample	d_{SV} (μm)	MC (% w.b.)	U_{mf} (m/s)	ρ_p (kg/m³)	ρ_{lb} (kg/m³)	AoR^d (°)	Flowability classification
B_{100wet}	400	30.0 ± 0.3^a	0.20 ± 0.01^a	-	342 ± 3^a	42 ± 2^a	Passable
B_{100}	400	2.8 ± 0.1^b	0.14 ± 0.01^b	1120 ± 20^a	380 ± 20^b	62 ± 3^b	Very Poor
$B_{90}C_{10}$	370	3.2 ± 0.1^b	0.15 ± 0.01^b	1120 ± 10^a	350 ± 5^c	70 ± 3^c	Very Very Poor

Values with different letters in the same column are significantly different at a 0.05 significance level.

4.1.4.2. CFB unit with L-valve feeder

The experiments were carried out using the experimental unit shown schematically in Fig. 4.4a. The CFB unit was built of stainless steel, except for the gray filled parts that were made of acrylic to verify the flow patterns. It consists basically of a conical reservoir and a standpipe connected to a riser by a non-mechanical L-valve. At the top, the riser is connected to an inclined separator and to a Lapple cyclone (internal diameter of 8 cm). The solids collected at the cyclone underflow are returned to the reservoir.

Two air flowrates were introduced in the system, one at the aeration point and another at the riser inlet. The air to the riser was supplied by a 7.5 HP blower and its

flowrate (Q) was measured by a previously calibrated orifice-plate. The aeration was supplied by a compressor and its flowrate (U) was measured by a gas rotameter model 51101 (Gilmont Instruments Incorporated, Illinois, USA). The cross-sectional areas of the aeration and riser inlets are 0.36 and 3.46 cm^2, respectively. The assays were performed under ambient conditions (air temperature from 20-35˚C and relative humidity from 50-80%).

The dimensions of the CFB unit are shown in Fig. 4.4b, the riser is 2 m high and has an internal diameter of 0.021 m; the reservoir volume is 0.0125 m^3. Fig. 4.4c shows the L-valve dimensions (internal diameter of 0.021 m, and length of 0.22 m). The aeration point is located at a distance of 0.051 m from the bottom of the valve.

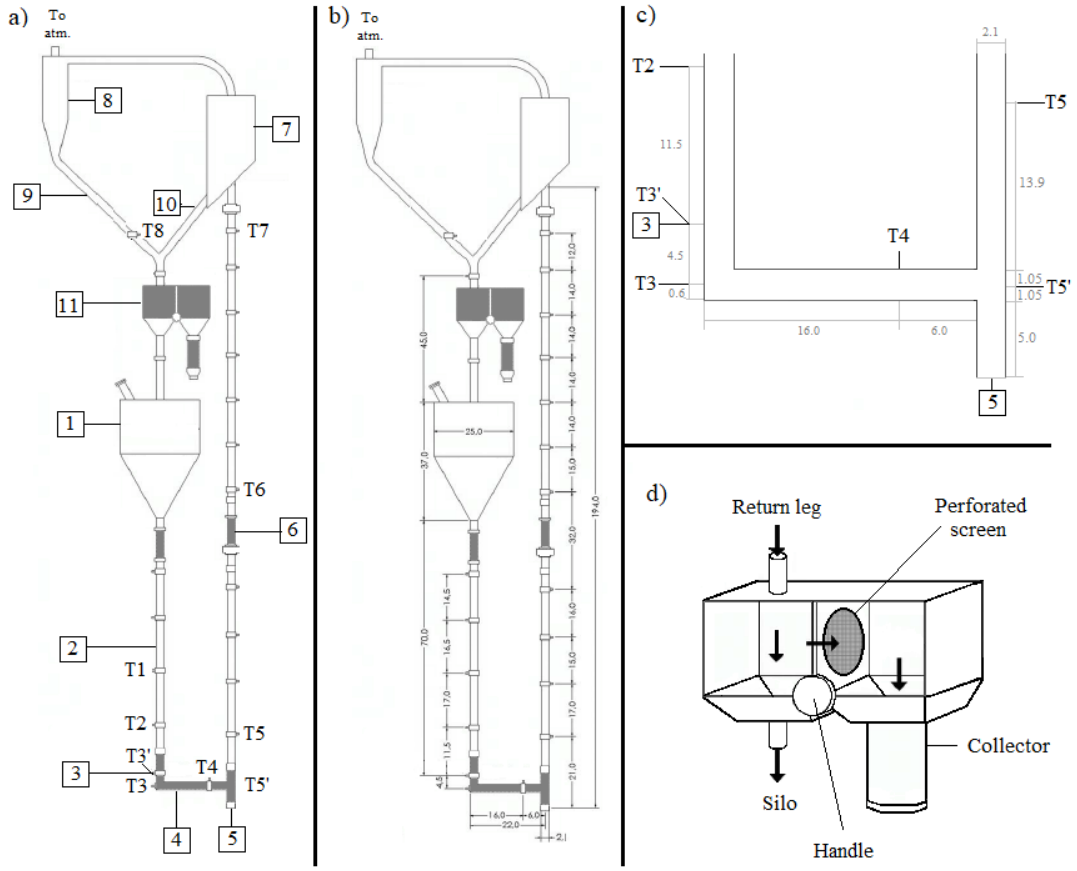

Fig. 4.4. Experimental setup. a) T1 to T8 are the pressure taps, while the components are (1) silo, (2) standpipe, (3) aeration inlet, (4) L-valve feeder, (5) riser air inlet, (6) riser, (7) inclined separator, (8) cyclone, (9) cyclone return leg, (10) inclined separator return leg, and (11) solids' flowrate measurement system. b) CFB unit. c) L-valve feeder. d) Solids' flowrate measurement system. All dimensions are in cm.

The solids circulation rate (W_S) in the CFB unit was measured using the system shown in Fig. 4.4d. It consists of a reservoir divided by a perforated screen plate that can be moved to deviate the solids flow for sampling during 10 s with minimum flow disturbance (COSTA; FERREIRA; FREIRE, 2004). The mass was weighted in a digital balance model BG-4000 (Gehaka, São Paulo, Brazil) with an accuracy of 0.01 g. Measurements of *Ws* were performed with three repetitions for each flow condition.

The manometric pressures were measured by pressure transducers model 860 (AutoTran Incorporated, Wisconsin, USA) connected to 8 taps distributed around the CFB loop at the positions shown in Fig. 4.4. The specifications of the pressure transducers and their tap positions are given in Tab. 4.2.

Tab. 4.2. Specification of the pressure transducers and taps positions in the CFB unit.

Pressure tap	Height (m)*	Region	Range (Pa)
T1	0.336	Standpipe	0-1250
T2	0.166	Standpipe	0-1250
T3’	0.051	Standpipe	Calculated
T3	0.006	L-valve	0-1250
T4	0.021	L-valve	0-2500
T5'	0.011	Riser	Calculated
T5	0.160	Riser	0-2500
T6	0.960	Riser	0-2500
T7	1.790	Riser	0-1250
T8	1.690	Cyclone return leg	0-1250

*The height reference (h=0 m) was located at the bottom of the L-valve.

The data acquisition was managed by a software based on LabView 7.1 Express (National Instruments, Texas, USA), using a cDAQ-9172 chassis (National Instruments, Texas, USA) with the NI 9205 module (32-channel, +/−10 V, 250 kS/s, 16-bit analog input). The pressures were measured at a sampling rate of 2500 samples/s and the mean pressure value for each transducer was recorded at every 5s.

In particular, T3’ and T5’ were obtained by linear regression of the experimental values measured at T3 and T5, respectively, so that the pressure drops in the L-valve

(ΔP_{LV}=T3'-T5') could be calculated based on the same procedures adopted in the literature.

4.1.4.3. Experimental conditions

The experiments were designed to evaluate the influence of the aeration flowrate (*U*), riser air flowrate (*Q*) and SCG properties on the performance of the L-valve. To cover a wide range of operating conditions with samples B_{100}, $B_{90}C_{10}$, and B_{100wet}, four aeration velocities (*U*=7.0, 14.0, 21.0, and 28.0 L/min) and three air velocities in the riser (*Q*=220, 250, and 280 L/min) were tested, as summarized in Tab. 4.3.

The ranges of *Q* and *U* were set based on preliminary experiments in the CFB unit. The lower limit of *Q* corresponds to the minimum air velocity that provided a stable flowrate in the riser, while the upper one was chosen to prevent a significant loss of powders in the cyclone overflow. Similarly, the upper value of *U* was set by the compressor capacity, while the lower one was set as 1.5 the minimum air flowrate required to move the solids through the valve when discharging the powders to the atmosphere (without backpressure at the outlet).

L-valve performance was tested with sample B_{100} under all combinations of *U* and *Q* (assays No. 1 to 12). Additional experiments were performed under some specific conditions of *U* and *Q* to evaluate the performance with samples containing a fraction of fine particles (assays No. 13 to 17) and with samples with a higher moisture level (assays No. 18 to 22). Three repetitions of each assay were carried out. The mean values and standard deviations of the pressures measured throughout the loop and of *Ws* are reported.

Tab. 4.3. Summary of the **e**xperimental conditions.

Experimental condition	**SCG sample**	***U* (L/min)**	***Q* (L/min)**
Number 1	B_{100}	7.0	220
No. 2	B_{100}	7.0	250
No. 3	B_{100}	7.0	280
No. 4	B_{100}	14.0	220
No. 5	B_{100}	14.0	250
No. 6	B_{100}	14.0	280
No. 7	B_{100}	21.0	220
No. 8	B_{100}	21.0	250
No. 9	B_{100}	21.0	280
No. 10	B_{100}	28.0	220
No. 11	B_{100}	28.0	250
No. 12	B_{100}	28.0	280
No. 13	B_{100wet}	7.0	220
No. 14	B_{100wet}	7.0	280
No. 15	B_{100wet}	14.0	220
No. 16	B_{100wet}	21.0	220
No. 17	B_{100wet}	28.0	220
No. 18	$B_{90}C_{10}$	7.0	220
No. 19	$B_{90}C_{10}$	14.0	220
No. 20	$B_{90}C_{10}$	14.0	250
No. 21	$B_{90}C_{10}$	21.0	250
No. 22	$B_{90}C_{10}$	28.0	220

4.1.4.4 Experimental procedure

Each experiment was initiated by loading 1.5 kg of an SCG sample (B_{100}, $B_{90}C_{10}$ or B_{100wet}) into the silo (Fig. 4.4a), filling in the standpipe (2) and around 30% of the reservoir volume (1). The gas was inserted in the riser (6) at a fixed flowrate. The pressures over the CFB loop (taps T1 to T8) were recorded at every 5 s by the acquisition system. The aeration flowrate was inserted in the L-valve (4) and, as soon as a stable solids flow was observed, the solids circulation rate (W_S) was measured. For this, solids were collected in the sampler (11) for 10 s and the mass was determined. The flow was disturbed by solids sampling, but as the collection time was very short, stable flow conditions were fast recovered. Three measurements of the solid's flowrate were carried

out at each condition. Mean values and standard deviations of pressures and *Ws* are reported.

The experiments were filmed with a digital camera model PowerShot SX170IS (Canon, Tokyo, Japan) to access the qualitative flow patterns in the L-valve.

At the end of each assay, the powder accumulated in the CFB unit was collected and weighted. The loss of powder in the cyclone overflow was estimated by a mass balance. The production of fine particles by attrition was determined by sifting the collected powder. The change in the powder's moisture content was also estimated by comparing the water content in the samples before and after the assays. It was found that the loss of powder at the cyclone overflow was less than 1% of the loaded mass. Particle-particle and particle-wall attrition were not relevant in the conditions tested, as the production of particles with sizes under 300 μm was less than 0.5%. The changes in the moisture content of sample B_{100wet} after the experiments were less than 2% for all conditions tested.

4.1.5. Results and Discussion

4.1.5.1. CFB transient flow behavior

To assess the dynamic flow behavior during a run, the dynamic variation of the pressures in the CFB loop for a typical experiment is discussed in this section. Fig. 4.5. shows that different dynamic patterns can be distinguished. The initial period corresponds to the solids loading (a), in (b) the pressures are shifted up as the air is inserted in the riser. A peak (b') is observed as the solids transport begins as soon as the aeration flowrate is injected in the L-valve. The subsequent regions (c, d, and e) of constant pressures are observed under solids stable flow. The peaks (c', d' and e') coincide with solids sampling

for *Ws* measurement. Finally, the aeration to the valve is turned off (f) and so is the air to the riser (g), thus the solids flow ceases.

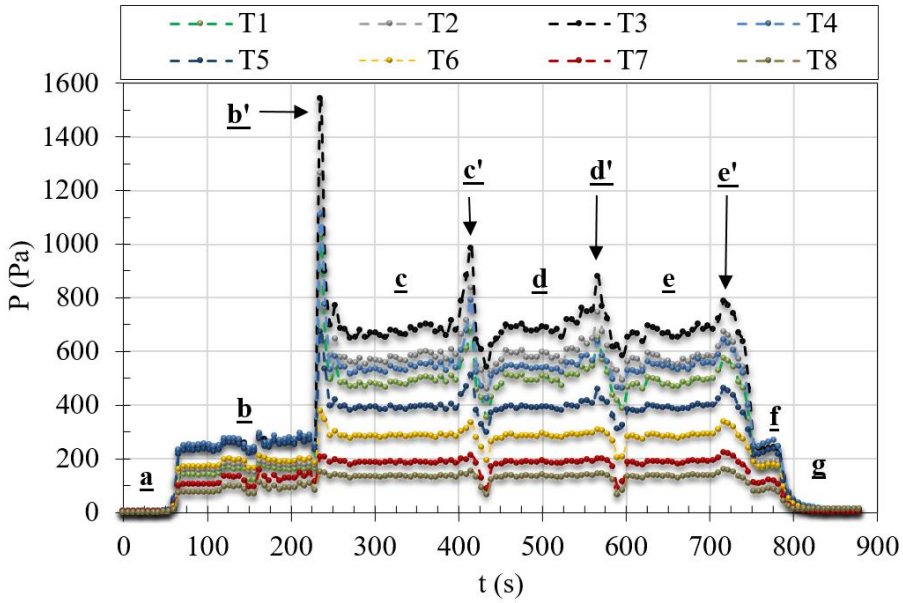

Fig. 4.5. Manometric pressures at taps T1 to T8 as a function of time (exp. No. 7).

Tab. 4.4. Pressure and solids circulation rate for all experimental conditions.

Experimental condition	T1 (Pa)	T2 (Pa)	T3' (Pa)	T3 (Pa)	T4 (Pa)	T5' (Pa)	T5 (Pa)	T6 (Pa)	T7 (Pa)	T8 (Pa)	*Ws* (g/s)
No. 1	531	615	816	734	442	336	321	238	145	97	2.0±2.0
No. 2	541	606	783	734	562	464	446	353	231	166	2.0±3.0
No. 3	754	853	1102	1032	783	633	608	472	312	231	2.0±1.0
No. 4	472	517	731	662	416	318	301	209	122	82	3.0±1.0
No. 5	590	623	860	792	551	465	445	335	203	146	2.7±0.3
No. 6	643	661	917	853	626	556	532	406	255	189	2.3±0.5
No. 7	488	576	715	676	540	411	391	284	187	125	3.4±0.2
No. 8	491	501	702	667	544	475	455	345	212	152	2.0±0.3
No. 9	662	736	906	882	798	634	610	483	326	241	1.7±0.2
No. 10	502	585	718	690	591	444	423	311	204	137	2.9±0.3
No. 11	694	709	953	900	713	588	560	415	250	180	3.8±0.1
No. 12	759	855	1050	1020	915	707	679	527	356	264	3.0±1.0
No. 13	967	1107	1419	1296	856	602	570	394	244	163	8.0±0.7
No. 14	1329	1460	1845	1717	1262	886	846	629	415	307	7.7±0.8
No. 15	1100	1269	1592	1477	1068	760	711	450	273	183	10.0±1.0
No. 16	435	500	638	609	504	402	384	286	188	126	1.4±0.1
No. 17	421	481	612	592	518	398	382	296	196	131	1.2±0.1
No. 18	-	-	-	-	-	-	-	-	-	-	-
No. 19	298.8	335	400	383	325	287	273	201	131	88	0.7±0.2
No. 20	395.9	431	528	513	463	417	399	301	199	143	0.7±0.2
No. 21	403.4	435	533	519	470	405	387	291	197	142	0.6±0.2
No. 22	-	-	-	-	-	-	-	-	-	-	-

Similar dynamic behaviors were observed in all the assays. The average values of pressures and *Ws* are shown in Tab. 4.4. The standard deviations of pressures were omitted for the sake of concision, but they were always less than 10% of the mean values. Based on data shown in Tab. 4.4, the influence of the SCG properties, *Q* and *U* on the pressures and *Ws* will be discussed in the following sections.

4.1.5.2. Influence of riser (*Q*) and air (*U*) flowrates on the solids rate (*Ws*)

The variation of *Ws* as a function of *Q* is shown in Fig. 4.6.

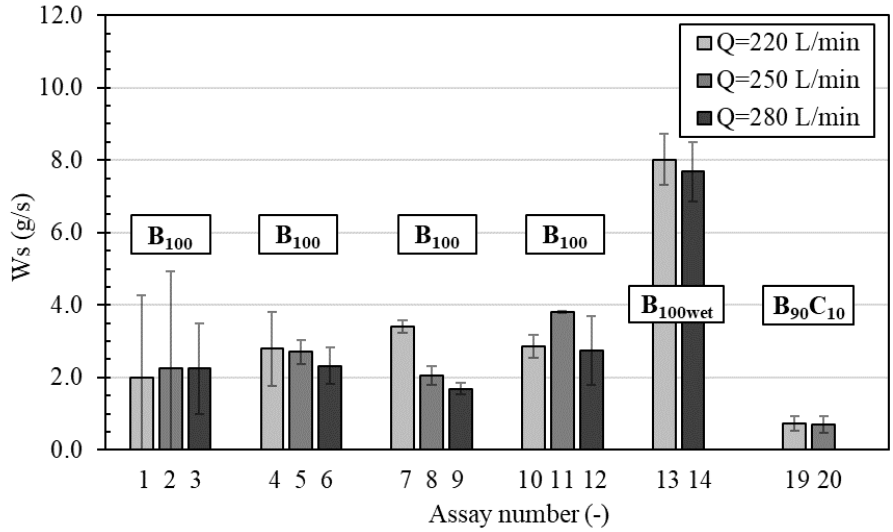

Fig. 4.6. Values of *Ws* for dry and wet SCG samples: B_{100} (assays 1 to 12), B_{100wet} (assays 13-14), and $B_{90}C_{10}$ (assays 19-20) under different values of *Q*.

The influence of *Q* on *Ws* for the dry sample B_{100} can be analyzed from the results of assays No. 1 to 12. The mean values of *Ws* were similar for the experiments performed under the same value of *U* (set of experiments 1 to 3, 4-6, 7-9, and 10-12). A two-way analysis of variance based on Tukey's test was performed ($p<0.05$) and *Ws* was not significantly affected by *Q* in the range investigated. Also, increasing *Q* did not affect *Ws* for either the sample with fines (assays No. 19 and 20) or the wet sample (assays No. 13 and 14). The data show evidence that the L-valve is able to maintain stable solids

circulation rates regardless of small variations in *Q*, which is an appealing feature in the operation of industrial reactors.

Once *Ws* was not affected by *Q*, the average values of *Ws* obtained under equal values of *U* were calculated to evaluate the influence of *U* on *Ws*. The results for *Ws* as a function of *U* are shown in Fig. 4.7. for all SCG samples.

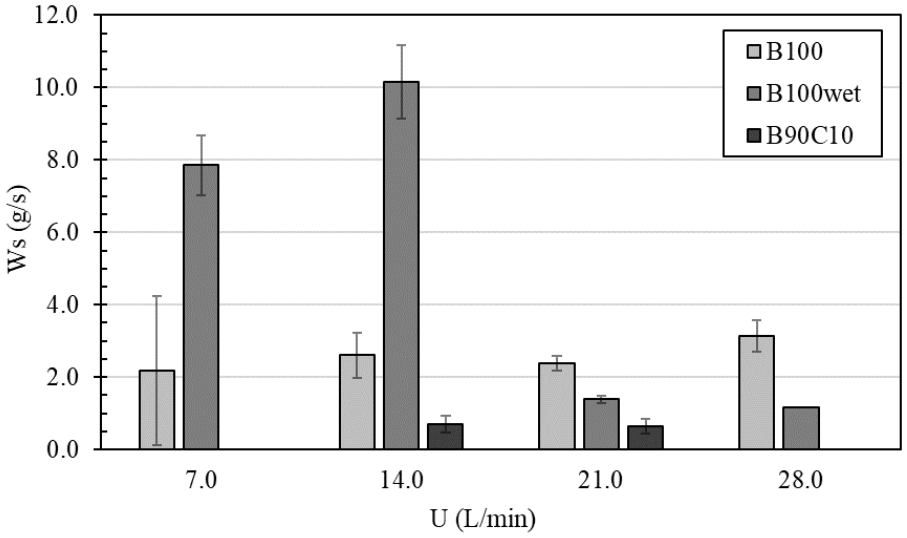

Fig. 4.7. Values of W_s as a function of U for dry and moist SCG samples.

For sample B_{100}, *Ws* remained constant at a value of approximately 2.6 g/s in the range of *U* investigated. The addition of fine particles to sample B_{100} not only reduced Ws to 0.7 g/s but also affected the workability of the L-valve, as stable operations were only observed in a narrow range of aeration velocities. The presence of fine particles in the sample contributes to increasing the specific surface area and the contact among particles (CASTELLANOS, 2005). Both the inter-particle attractive forces and mechanical interlocking are increased, which limits the valve operating range. A comparison among the powders' flowability can be performed based on their dynamic angles of repose (AoR^d), which can be considered a good index to characterize the powders' flowability under the free-flowing regime observed in the horizontal section of the L-valve. The higher repose angle of sample $B_{90}C_{10}$ compared to that of sample B_{100} corroborates the poorer flowability of sample $B_{90}C_{10}$ (see Tab. 4.1).

The results show that *Ws* depend on the mean particle size and on the powder size distribution and that *Ws* of dry SCG samples could not be effectively controlled by adjusting *U* in the L-valve. This result contradicts earlier studies of L-valves operating with Geldart B particles, which reported a linear increase in *Ws* as *U* rises (ARENA; LANGELI; CAMMAROTA, 1998). In the conditions evaluated, the combination of a low particle density powder and a small diameter L-valve seems to restrict the valve performance. Both factors, the low powder bulk density, and the strong powder-wall interaction limit powder availability at the base of the standpipe, leading to similar solid throughput regardless of the aeration in the valve. Possibly, the L-valve workability operating with dry SCG powders could be enhanced by increasing the standpipe and L-valve internal diameters, however further research is required to confirm this hypothesis.

It must be noted that there is a minimum aeration flowrate to initiate the solids transport through the L-valve. When operating close to this minimum value, such as in the assays No. 1-3 (*U*=7.0 L/min), an unstable solids flow is observed, with fluctuations in the solids circulation rates throughout time. This unstable flow pattern explains the high standard deviation in the values of *Ws* measured in the mentioned assays (see Tab. 4.4). These instabilities were not observed under other conditions.

Operating with moist samples, on the other hand, had a positive effect on *Ws*, which ranged from 1.2 to 10.0 g/s. The solids circulation rates could be easily varied by adjusting the aeration flowrate in the L-valve, the flow was stable in the whole aeration range, and *Ws* presented low standard deviations, as can be observed in Tab. 4.4. This is an appealing result for feeding SCG powders in combustion reactors, as the moisture content of SCG samples should vary from 25 and 50% to be burned in the soluble coffee industry furnaces. The lower limit is set to avoid spontaneous combustion and the upper one to preserve the burning efficiency (SILVA et al., 1998).

From Fig. 4.7., it seems that a critical air flowrate is achieved between U=14 and 21 L/min, which delimits two different regions of operation for the L-valve with sample B_{100wet}. Under high aerations, the solids flowrate is predominantly controlled by the gas phase and the solids are conveyed in a dilute regime to the riser with low values of W_S. For aerations up to U=14 L/min, the interaction of both gas and solid phases at the entrainment zone is important for W_S.

Two features may contribute to the decrease of W_S under high aeration flowrates: 1) more air is deviated to the standpipe as U increases (MASSARO SOUSA et al., 2020), hence decreasing the flow of solids downwards and 2) the formation of gas vortices at the base of the standpipe, which limits the transport of solids to the horizontal section of the valve, and consequently to the riser. Turbulent vortices were observed at the base of the standpipe for the assays with U higher than 14 L/min. For the valve operating under lower aerations, it was verified on the shot videos a large amount of powder near to the aeration inlet. At U=14 L/min, the weight of the solids at the standpipe seemed to be in sync with the buoyancy force generated by the aeration flowrate, which led to the highest values of *Ws*. It is worth noting that the *Ws* trend for sample B_{100wet} is similar to that reported for powders located in the transition A-B boundary of Geldart's diagram (LIM et al., 2013), as described in Section 4.1.3.

The improvement of the valve's performance when using the wet powder in comparison to the dry powders is evident by noting the increase in *Ws* as well as the low standard deviations under U=7.0 L/min. This result is possibly justified by a lubricant effect produced by the water content under this saturation level, which contributes to enhancing powder flowability. The measured values of AoR^d of samples B_{100} and B_{100wet} were equal to 62±3˚ and 42±2˚ (Tab. 4.1) respectively, which categorize their flowability as *very poor* and *passable*, respectively (LUMAY et al., 2012).

4.1.5.3. The effect of *Q* and *U* on the CFB pressure loop

In this section, the pressures measured at the taps T1 to T8 are presented as a function of the height of the CFB unit to evaluate the influence of *Q* and *U* on the pressure profiles in feeding SCG powders. The results for sample B_{100} are presented in Fig. 4.8a and for samples $B_{90}C_{10}$ and B_{100wet} in Fig. 4.8b.

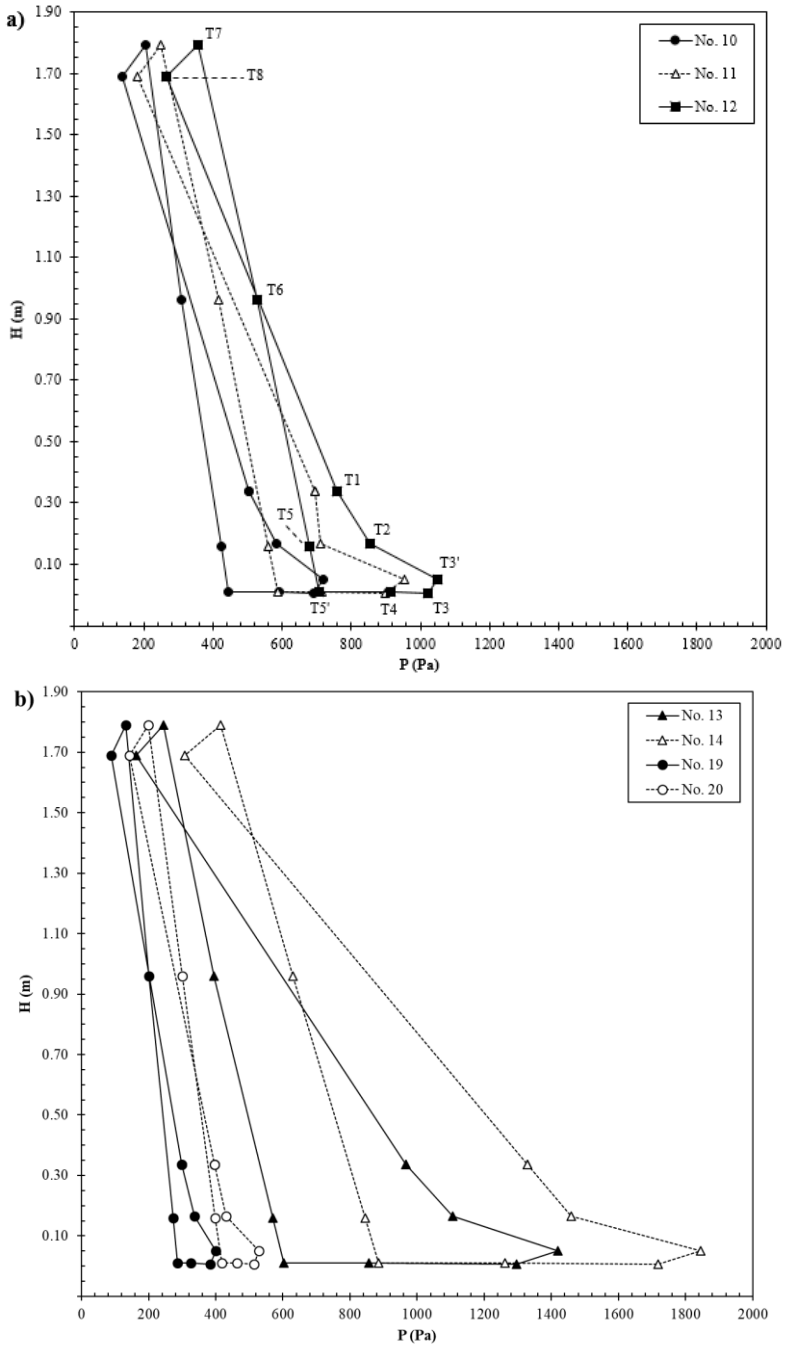

Fig. 4.8. Pressures around the CFB loop under different aeration flowrates for samples a) B_{100}, and b) $B_{90}C_{10}$ (assays No. 19-20) and B_{100wet} (assays No. 13-14).

The profiles are always similar and, despite the solids circulation rates were not affected by changes in *Q* (see Fig. 4.5.), data in Fig. 4.8. show that the pressures in the CFB loop increase as *Q* rises, as expected. It can be observed in Fig. 4.8a that the pressure profiles were shifted to the right at similar rates when *Q* rise from 220 to 280 L/min at step intervals of 30 L/min. The proportional increase in the pressure profiles was also observed for other aeration flowrates in the transport of sample B_{100} (assays No. 1 to 9). The pressure drop in the L-valve is higher in feeding sample B_{100wet} and is lower for samples B_{100} and $B_{90}C_{10}$, in this order, since $W_{SB100wet}>W_{SB100}>W_{SB90C10}$ under constant aeration flowrate.

The influence of *Ws* on the CFB pressure loop can be better observed in Fig. 4.9., in which the pressures for the transport of different SCG powders, under constant values of *U* and *Q*, can be compared.

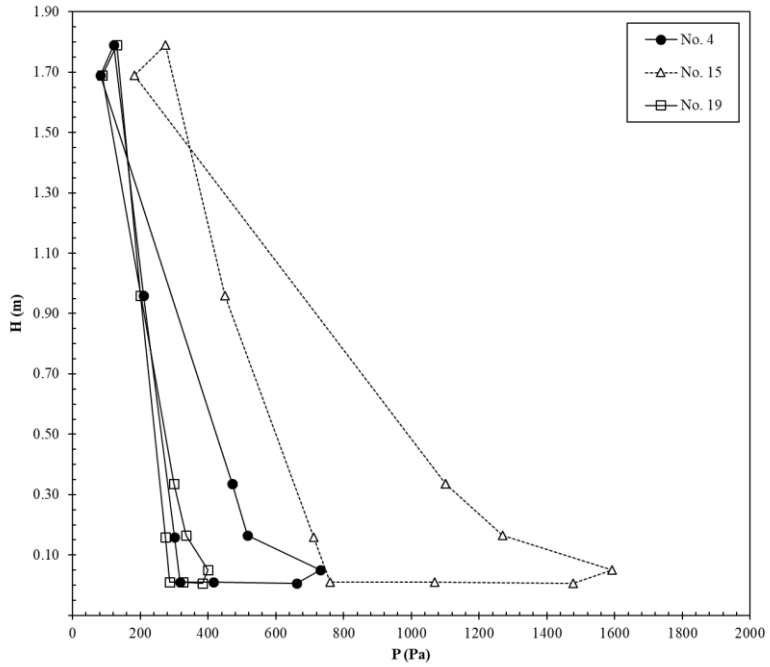

Fig. 4.9. CFB pressure for different SCGs, with *U*=14.0 L/min and *Q*=220 L/min.

For the conditions shown in Fig. 4.9., $W_{SB100wet}>W_{SB100}>W_{SB90C10}$, consequently the pressure profile of sample B_{100wet} (assay No. 15) is shifted to the right compared to the profiles of samples B_{100} (No. 4) and $B_{90}C_{10}$ (No. 19). Besides, the higher is *Ws*, the higher

is the pressure drop at the bottom of the curve, which corresponds to the L-valve section, T3' to T5'.

The effect of *U* on the pressure profiles is presented in Fig. 4.10a for sample B_{100}, and in Fig. 4.10b for sample B_{100wet}, under *Q*=220 L/min. It can be observed in Fig. 4.10a that the pressure profiles are nearly coincident regardless of *U*, especially when considering the measurement uncertainties. This behavior is consistent for two reasons: 1) the aeration flowrate is from 8 to 40 times lower than the riser air flowrate, hence variations in *U* are not significant to alter the line pressures and 2) as shown in Fig. 4.7., the solids flowrate of sample B_{100} is approximately constant at 2.6 g/s regardless of the aeration flowrate. The same patterns apply to the transport of sample $B_{90}C_{10}$, which were not shown in the graphs. In the case of sample B_{100wet}, the aeration flowrate affects *Ws*, which is higher under low aerations flowrates (*U*=14.0 and 7.0 L/min, respectively), and equal to 1.3 g/s for *U*=21.0 and 28.0 L/min (see Fig. 4.7.), consequently the pressures in the system change accordingly. The pressure profiles are shifted to the right under the highest values of *Ws* (assays 15 and 13) and are coincident in assays 16 and 17, in which *Ws* are similar.

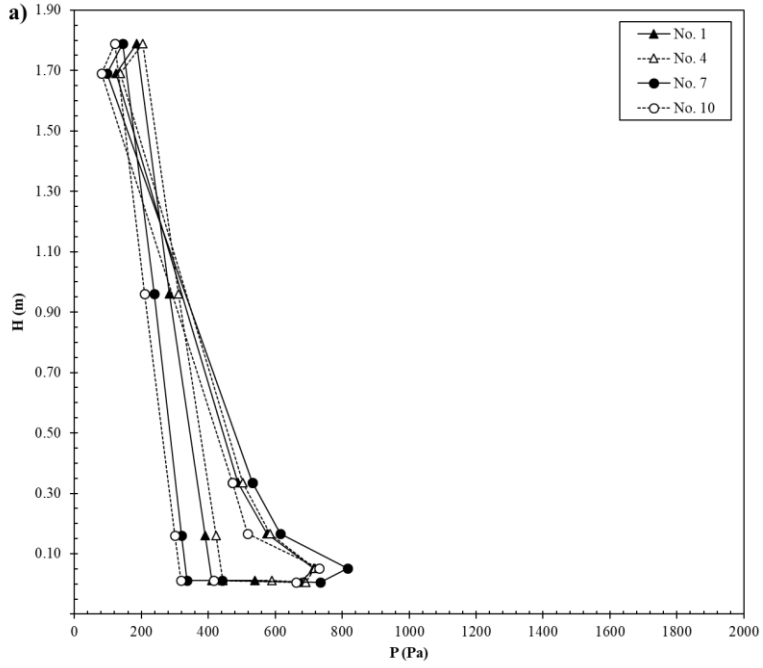

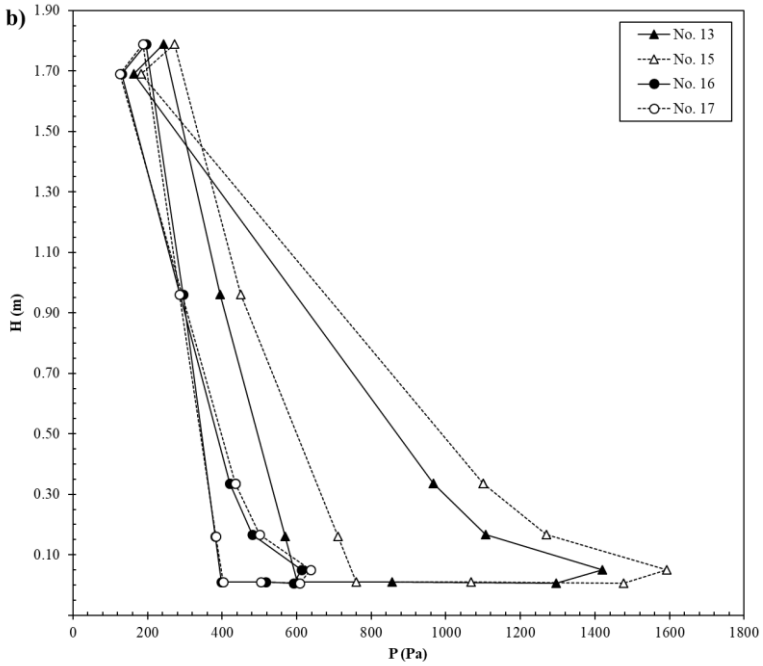

Fig. 4.10. Pressures at the CFB for different *U* with samples a) B_{100} and b) B_{100wet}.

4.1.5.4. Correlations for solids flux (*Gs*) and pressure drop in the L-valve (ΔP_{LV})

As discussed in Section 4.1.3, some correlations between the solids mass flux (*Gs*) and the pressure drop in the L-valve (ΔP_{LV}=*T3'-T5'*) have been proposed to predict the performance of L-valves feeding different types of powders to CFBs. Reliable correlations between *Gs* and ΔP_{LV} might be a valuable tool in industrial applications, as once *Gs* could be estimated instantly based on simple pressure measurements, it would be possible either setting *Gs* to the desired target or anticipating flow problems to improve the operation.

In Tab. 4.5, the experimental values of *Gs* are compared to those predicted by Eqs. (4.1) and (4.2). *E* (%) is the deviation between experimental and predicted values. The correlations were developed in terms of the solid mass fluxes (*Gs*) and of the aeration velocity inside the L-valve (*U'*), hence the aeration and solids circulation flowrates were divided by the cross-sectional area of the L-valve (0.000346 m^2).

As can be seen in Tab. 4.5, the tested correlations were not suitable to predict the flow of SCG powders in the L-valve. Overall, Eq. (4.2) overpredicted *Gs* by 2 to 20 times, and Eq. (4.1) underestimated and overestimated it by 2 to 45 times. The higher the aeration velocity is, the higher is the deviation, which is not surprising as the correlations fitted accurately the literature data only under low aeration, as mentioned in Section 4.1.3.

A modified correlation was fitted to estimate *Gs* from measurements of ΔP_{LV} for the SCG powders tested in this study, with moisture content up to 30% w.b. and percentage of fine particles up to 10%:

$$\Delta P_{LV}/L = 0.073 G_S^{0.778} \rho_{lb}^{1.434} D_{LV}^{0.0183} d_{sv}^{0.0014} \quad (4.3)$$

Tab. 4.5. Pressure and solids circulation rate for all experimental conditions.

Experimental conditions				**Eq. (4.1)**		**Eq. (4.2)**		**Eq. (4.3) This paper**	
No.	*U'* (m/s)	ΔP_{LV} (Pa)	*Gs* (kg/m²s)	*Gs* (kg/m²s)	*E* (%)	*Gs* (kg/m²s)	*E* (%)	*Gs* (kg/m²s)	*E* (%)
1	0.34	480	6.0 ± 6.0	11.18	94	11.5	99	10.9	90
2	0.34	319	7.0 ± 8.0	1.13	-83	11.5	76	6.5	0
3	0.34	469	6.0 ± 4.0	9.83	51	11.5	77	10.6	64
4	0.68	413	8.0 ± 3.0	4.82	-40	38.6	378	9.0	12
5	0.68	395	7.8 ± 0.9	3.73	-52	38.6	394	8.5	9
6	0.68	361	7.0 ± 2.0	2.26	-66	38.6	476	7.6	13
7	1.02	304	9.9 ± 0.5	0.85	-91	78.4	695	6.1	-38
8	1.02	226	5.9 ± 0.7	0.16	-97	78.4	1230	4.2	-29
9	1.02	272	4.9 ± 0.5	0.46	-90	78.4	1509	5.3	8
10	1.36	275	8.3 ± 0.9	0.49	-94	129.7	1470	5.3	-35
11	1.36	365	11.0±0.1	2.42	-78	129.7	1083	7.7	-30
12	1.36	343	8.0 ± 3.0	1.69	-79	129.7	1531	7.1	-11
13	0.34	817	23.0±2.0	401	1633	11.5	-51	26.4	14
14	0.34	959	22.0±2.0	988	4352	11.5	-48	32.4	46
15	0.68	832	29.0±3.0	443	1413	38.6	32	27.0	-8
16	1.02	236	4.0 ± 0.3	0.37	-91	78.4	1853	5.3	33
17	1.36	214	3.4 ± 0.1	0.22	-94	78.4	2239	4.7	41
19	0.68	113	2.1 ± 0.6	0.01	-99	44.1	2014	2.0	-4
20	0.68	110	2.0 ± 0.7	0.01	-99	44.1	2090	1.9	-4
21	1.02	128	1.9 ± 0.6	0.01	-99	89.7	4710	2.3	25

Eq. (4.3) was obtained from a regression analysis in which the exponents of the four parameters in Eq. (4.1) (G_S, D_v, d_S, and ρ_{lb}) were varied to minimize the differences between experimental and estimated values. A regression coefficient of 0.85 was obtained and the experimental values differ from the estimated ones by 25% on average, as shown in Tab. 4.5. Besides, the experimental data are randomly distributed around the fitting line for Eq. (4.3), indicating a non-biased fitting.

The experimental values of ΔP_{LV} as a function of G_S are plotted in Fig. 4.11. and compared to the fitted equations. It can be seen that the data is reasonably well predicted by Eq. (4.3). The results show that the higher is the solids flowrate, the higher is the pressure drop in the L-valve.

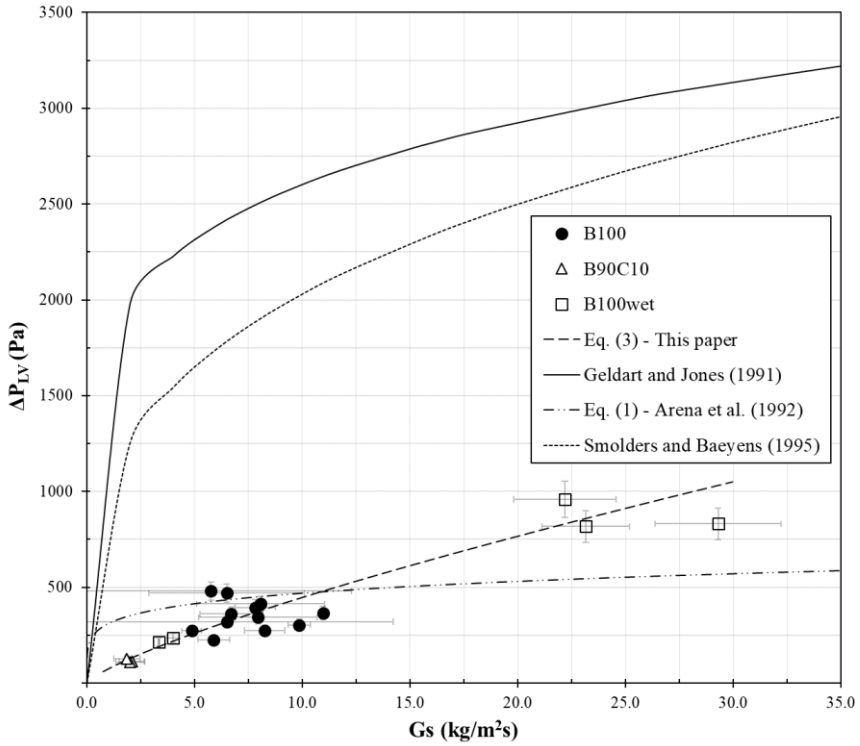

Fig. 4.11. Comparison between Eq. (4.3) and the pressure drop predicted by other correlations from the literature.

To the best of authors' knowledge, there is only one correlation in the literature correlating ΔP_{LV} to G_S for small-scale L-valves (diameter under 20 mm) (ARENA; LANGELI; CAMMAROTA, 1998). This equation did not predict accurately the data of

ΔP_{LV} and G_S, either qualitatively or quantitatively, as can be observed in Fig. 4.11. and in Tab. 4.5. The other correlations (GELDART; JONES, 1991; SMOLDERS; BAEYENS, 1995) were developed for L-valves feeding conventional Geldart B powders to the atmosphere, although these equations have been used sometimes to estimate *Gs* in CFB units operating with L-valve feeding devices (LIM et al., 2013). It can be observed in Fig. 4.11. that these equations did not predict well the L-valve performance feeding SCGs to a CFB.

The previous findings indicate that the performance of L-valves feeding residue-based powders with a low particle density might differ significantly from data reported in the literature for Geldart B powders.

4.1.5.5. Mean voidage in the riser (ε_r)

The mean voidage in the riser section (ε_r) were estimated by (ARENA; LANGELI; CAMMAROTA, 1998):

$$\Delta P_r = \rho_p(1-\varepsilon_r)g\Delta h_r \quad (4.4)$$

where ΔP_r is the pressure loss in the distance Δh_r measured between taps T5 and T7.

The estimated mean voidages in the riser are equal to 0.986±0.005 based on all the assays. Based on the air properties (ρ_{air}= 1.283 kg/m^{3,} μ_{air}=0.000018 Pa.s), particle density and on the values of *Q* and *Ws* it was verified that CFB was operated always under a dilute regime, according to Bi and Grace diagram (GRACE; AVIDAN; KNOWLTON, 1997), with porosity generally higher than 0.98.

4.1.6. Conclusions

The L-valve tested in the present study can be considered a reliable feeding device to control the solids circulation rate in a CFB when operating with SCG powders with

moisture content close to 30% w.b. and mean particle size of 400 μm. By varying the aeration flowrate, the valve provided stable solids feeding in a range of $1.2<Ws<10.0$ g/s. It was observed also that fluctuations up to ±15% in the riser air flowrate do not affect the L-valve operation.

Feeding dry SCG samples, however, was not so effective, as the valve operating range was narrowed, and the solids flowrate could not be effectively controlled by changing the aeration flowrate. This is attributed to the poorer powder flowability of the dry powders compared to the wet powder. Nevertheless, when solids transport could be achieved, the fluctuations in Ws were small and flow was stable, which is a positive aspect regarding the valve robustness.

As the moisture content of SCGs powders burned for energy generation might range from 25 and 50% w.b., using the L-valve as a feeding device can be recommended as an alternative in this case.

A correlation to predict *Ws* from the pressure drop in the L-valve was proposed which fitted our data better than other equations available in the literature. Finally, it was observed that the valve performance operating with the wet Geldart B SCG powders was similar to that reported in the literature for powders located in the boundary transition A-B of Geldart's classification.

4.1.7. Acknowledgements

The authors would like to thank the São Paulo Research Foundation (FAPESP), grants 2016/25946-2 and 2018/11031-8 and CAPES for financial support.

4.1.8. Nomenclature

AoR^d	Dynamic angle of repose (˚)
B_{100}	Dry powder sample (-)
$B_{90}C_{10}$	Powder sample with fine particles (-)
B_{100wet}	Moist powder sample (-)
D_{LV}	Internal diameter of the L-valve (m)
d_S	Sauter mean diameter (μm)
d_{SV}	Sieve mean sieve diameter (μm)
E	Deviation between experimental and predicted G_S values (%)
g	Gravity acceleration ($m^2 \cdot s^{-1}$)
G_S	Solids mass flux ($kg \cdot m^{-2} s^{-1}$)
h	Height reference of the system (m)
L	Horizontal length of the L-valve (m)
MC	Moisture content of the powder (% wet basis)
Q	Air flowrate in the riser inlet ($L \cdot min^{-1}$)
T	Pressure taps from T1 to T8 (-)
U	Air flowrate in the L-valve inlet ($L \cdot min^{-1}$)
U'	Air velocity inside the L-valve ($m \cdot s^{-1}$)
U_{mf}	Minimum fluidization velocity ($m \cdot s^{-1}$)
W_S	Solids circulation rate ($g \cdot s^{-1}$)
ΔP_{LV}	Pressure drop in the L-valve section, (=T3'-T5') (Pa)
ΔP_r	Pressure drop in the riser section, (=T5-T7) (Pa)
ε_{lb}	Void fraction for loose bulk condition (-)
ε_r	Mean voidage in the riser (-)
μ_{air}	Viscosity of the air (Pa·s)
ρ_{air}	Density of the air ($kg \cdot m^{-3}$)
ρ_{lb}	Loose bulk density ($kg \cdot m^{-3}$)
ρ_p	Particle density ($kg \cdot m^{-3}$)

CAPÍTULO 5 - ALIMENTAÇÃO DE BORRAS DE CAFÉ AO LPC COM VÁLVULA-L: ANÁLISE VIA CFD

Neste capítulo são apresentados os resultados e discussões referentes à simulação em CFD da alimentação de borra de café B_{100} ao LPC com o alimentador tipo válvula-L, o que está relacionado ao objetivo específico (5) desta tese.

O modelo TFM (*Two-Fluid Model*) foi primeiramente validado na Seção 5.1 para descrever a alimentação da amostra para a atmosfera, ou seja, com o alimentador desacoplado do *riser*. O perfil qualitativo para a pressão no sistema e a vazão de sólidos foram preditos com sucesso pelas simulações para uma ampla faixa de vazões de aeração na válvula-L. Nesta seção, constam ainda uma detalhada análise de sensibilidade dos parâmetros do modelo relacionados à fricção, colisão e arraste da borra B_{100} sobre as respostas, assim como resultados experimentais sobre o funcionamento da válvula-L com a biomassa em pó, os quais evidenciam padrões de escoamento adicionais aos previamente reportados na literatura com materiais convencionais. Note que as propriedades da borra de café consideradas no modelo numérico foram: diâmetro médio de 400 μm, massa específica aparente de 1120 kg/m³, porosidade do leito de 0,66 e ângulo efetivo de fricção interna de 38,5°. Essas propriedades foram determinadas como mostrado no Capítulo 3.

Na Seção 5.2 o modelo TFM previamente validado foi utilizado para prever a vazão de sólidos e fração volumétrica de borra de café no *riser*, obtendo-se desvios para os dados experimentais em média de 25 e 1%, respectivamente. Detalhes sobre a fluidodinâmica no tubo de descida, válvula-L e riser foram obtidos via CFD, os quais são difíceis de serem medidos experimentalmente. Além disso, a vazão de sólidos simulada, sob as mesmas condições de aeração na válvula-L (14 L/min), diminuiu em 75% quando alimentando pós ao *riser* (sistema com contrapressão) em comparação com

a alimentação de sólidos para a atmosfera (Seção 5.1), o que concorda com os resultados experimentais. Em suma, o modelo desenvolvido se mostrou robusto e efetivo para predizer as principais características fluidodinâmicas dos sistemas e pode ser utilizado para estudos adicionais relacionados à otimização da alimentação ou implementação de válvulas-L em reatores em maiores escalas.

As metodologias empregadas e a validação das simulações para o escoamento de borra de café na válvula-L foram relatadas no artigo "*Feeding Spent Coffee Ground Powders with a Non-Mechanical L-valve: Experimental Analysis and TFM Simulation*". Os resultados da utilização do modelo para a alimentação de borras de café ao reator LPC foi apresentado no 9° *Annual Chemical Engineering Postgraduate Association Conference*, *Monash University*, Austrália (Seção 5.2.).

5.1. "Feeding Spent Coffee Ground Powders with a Non-Mechanical L-valve: Experimental Analysis and TFM Simulation"

L. MASSARO SOUSA, M. C. FERREIRA, HOU, Q. F., YU, A. B.

Artigo publicado na revista Powder Technology, volume 360, páginas 1055-1066, 2020.

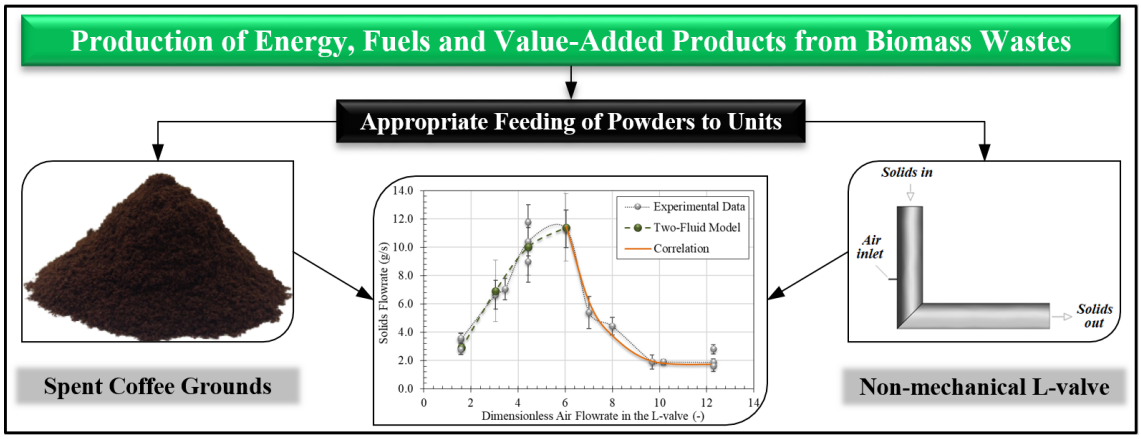

Fig. 5.1. Graphical abstract.

5.1.1. Abstract

A better understanding of feeding operations is pressing for value-added processing of waste biomass powders. This paper examines the feeding of Spent Coffee Grounds (SCGs) using a non-mechanical L-valve both experimentally and numerically. L-valve provides stable solids feeding, showing different flow regimes. Powders' height in the standpipe must be monitored to guarantee smooth operations with the valve, and the data for SCGs differ significantly from those reported for glass and sand powders. A new correlation to predict the solids flowrate from simple pressure measurements was proposed for valve operating under high air flowrates. For low to medium air flowrates, a two-fluid model (TFM) was proposed and validated. The SCGs' flowrate in the feeder was accurately predicted by the TFM and the correlation. Furthermore, key information for the design of L-valves was obtained from the TFM simulation. The findings are useful for producing renewable thermal energy and fuels with biomass SCGs.

5.1.2. Introduction

Soluble coffee and other food industries produce more than 2.5 million tons of Spent Coffee Grounds (SCGs) annually, which is a biomass residue generated from brewing coffee powders (INSTANT COFFEE MARKET, 2018; MUSSATTO et al., 2011). Although SCGs have been mainly disposed of in landfills, this practice is not considered a profitable or sustainable option from the resources management point of view (BRIDGWATER, 2003; CAMPOS-VEGA et al., 2015; MUSSATTO et al., 2011; OSMAN et al., 2019; XIONG et al., 2019). The main use of SCGs is as a renewable source to generate thermal energy in the industry itself (SILVA et al., 1998). Other reported uses include converting SCGs into bio-oil (KELKAR et al., 2015; YANG et al., 2018), hydrogen and ethanol (MUSSATTO et al., 2011), and other value-added products

(AL-HAMAMRE et al., 2012; ATABANI et al., 2019; KYZAS; LAZARIDIS; MITROPOULOS, 2012).

In processing SCG powders for renewable energy generation, gasification or pyrolysis, minimizing the probability of operational hazards in the reactor by maintaining stable powder flow throughout the units that come before and after the reactor is of paramount importance. Thus, SCG powders must be fed continuously under a stable mass flowrate to silos, storage vessels, dryers, and so on; consequently, using appropriate feeding devices is key for effective operations. The powders' particle size distribution, shape and moisture content are not uniform for biomass residues, and they are likely to clog moving parts of mechanical feeders and discharge hoppers' orifices. Therefore, using non-mechanical feeding devices might be appealing for operation with biomass residues as the feeders have simple geometry and no moving parts, hence they suffer less wear and are less expensive compared to mechanical feeders.

Tab. 5.1. L-valve operation as a function of the aeration flowrate (Q).

Aeration	Flow behavior
$Q<Q_{min}$	Solids are not transported by the L-valve; Packed bed in the standpipe.
$Q_{min}<Q<Q_{mf}$	A narrow channel of solids moving at the top of valves' horizontal section; Virtually no movement is detectable in the standpipe; Solids flowrate is usually low in this regime.
$Q_{mf}<Q<Q_{ms}$	Dunes and ripples flow at the top of the valves' horizontal section; Fluctuations in both solids discharge rate and pressure through the valve; Increasing U increases the solids flowrate; The maximum solids flowrate in the L-valve is achieved near $U_{ms.}$
$Q>Q_{ms}$	Flow is highly unstable with large bubbles in the standpipe; High-frequency dunes flow at the horizontal section of the valve; Increasing U causes a sharp reduction in the solid's flowrate; Pneumatic conveying of solids can occur at the horizontal section;

where Q_{min} is the threshold flowrate to initiate solids flow in the valve; Q_{mf} is the minimum fluidization flowrate; Q_{ms} is the minimum slug velocity.

L-valves are non-mechanical feeders that rely on hydrodynamic energy to control the solids flowrate. It consists of a vertical standpipe and a horizontal pipe, with an aeration injection located next to the standpipe bottom. The powder is introduced into the feeder through the vertical section, usually by the sole action of the gravitational force, and then it is directed towards the valve's horizontal section by an air flowrate (Q). As summarized in Tab. 5.1 different flow features are observed in the feeder depending on the magnitude of Q (CHAN et al., 2009; DAOUS; AL-ZAHRANI, 1998; GELDART; JONES, 1991; KNOWLTON; HIRSAN, 1978; SMOLDERS; BAEYENS, 1995; YANG; LEU, 2008). The unit to be charged with solids is connected at the end of the horizontal section.

Encouraging results and wide operation range have been reported for L-valves feeding conventional powders, such as siderite, gravel, glass, and sand to the atmosphere (CHAN et al., 2009; DAOUS; AL-ZAHRANI, 1998; GELDART; JONES, 1991; KNOWLTON; HIRSAN, 1978; SMOLDERS; BAEYENS, 1995). However, flow behavior can vary significantly with materials properties. Thus, evaluating the performance of L-valves in feeding residue-based biomass powders and classifying the flow regimes shown in Tab. 5.1 are very important.

The flow behavior of gas-solid systems can be described by the two-fluid model (TFM) (BENEDITO et al., 2018; HOU et al., 2019; MOLINER et al., 2019; SANTOS et al., 2013; WANG et al., 2016a; ZHU et al., 2011) with the conservation equations of continuity and momentum. These equations have to be solved simultaneously with turbulence models and with closure equations (drag forces, frictional stress models, among others) related to gas and solid properties, as well as to the operating conditions. The closure equations usually have a certain degree of empiricism and calibration of the parameters is necessary for predicting the gas-solid flow in the feeding device.

Some authors examined feeding sand, dolomite and polyethylene beads to circulating fluidized beds (discharged with back-pressure) by L-valves using both TFMs (GHADIRIAN; ABBASIAN; ARASTOOPOUR, 2019; XUEYAO et al., 2013) and CFD-DEM (XU et al., 2018) approaches. Generally, the solids flowrate in the valve by TFMs has not been compared to experimental data (GHADIRIAN; ABBASIAN; ARASTOOPOUR, 2019; XUEYAO et al., 2013), and when the predictions by CFD-DEM simulations are compared to experimental results large differences were observed, varying from 0.3 to 2.5 times of the experimental results (XU et al., 2018). Since neither the system presented in this paper (discharge to the atmosphere) nor the properties of the biomass SCGs powders are similar to those available in the literature, a TFM will also be developed and the effects of different model parameters are quantified, in addition to experimental measurements.

This paper is aimed at understanding the feeding of biomass SCG powders by L-valve. The behavior of the SCG powder is examined both experimentally and numerically. First, the transient and stable operations of the L-valve are assessed for a broad range of aeration flowrates. Then, a TFM with the properties of the solid phase described by the Kinetic Theory of Granular Flow (KTGF) is developed to describe the key flow features of the biomass powder in the feeder after the validation against the experimental data. Finally, the effects of different model parameters on the model prediction are quantified. The findings provide useful guidance for studying biomass materials with different materials properties and the operation of non-mechanical L-valve.

5.1.3. Material and Different Methods

5.1.3.1. Material

The main physical properties of the spent coffee grounds (SCGs) used in the feeding experiments are presented in Tab. 5.2. Sample B_{100} was mechanically sieved to achieve a narrow particle-size distribution for the assays, between 500 and 300 μm. The experimental procedure for sample characterization is described in detail elsewhere (MASSARO SOUSA; FERREIRA, 2019a, 2019b).

Tab. 5.2. Materials properties of the sieved powder sample B_{100}.

SCG Sample	d_s (μm)	*MC* (% w.b.)	U_{mf} (m/s)	ρ_p (kg/m³)	ρ_{lb} (kg/m³)	α_{slb} (-)	φ (°)
B_{100}	400	2.8 ± 0.1	0.14 ± 0.01	1,120 ± 20	380 ± 20	0.34 ± 0.01	38.5

The angle of internal friction (φ) was determined by performing shear tests under a normal consolidation of 3 kPa in a powder rheometer FT4 (Freeman Technology, Gloucestershire, UK). The yield locus for the biomass powder was linearized according to the Mohr-Coulomb equation. The minimum fluidization velocity (U_{mf}) was determined in a fluidized bed with a diameter of 0.114 m, a powder bed height of 9 cm, and with air injected uniformly at the bottom of the bed. The pressure drop through the bed was measured for a given gas flowrate, and U_{mf} was determined by the intersection of the fitting curves for the fluidized-bed and fixed-bed regions, in triplicate.

5.1.3.2. Experimental settings

The experiments were carried out using the unit shown in Fig. 5.2a. The unit was built of stainless steel, except for the gray filled parts that were made of acrylic to verify the occurrence of flow in the equipment. It consists basically of a non-mechanical L-valve that transports the solids from the standpipe and conical reservoir to the atmosphere by adding air at the aeration inlet. The aeration flowrate (Q) is supplied by a compressor and

measured by a gas rotameter model 51101 (Gilmont Instruments Incorporated, Illinois, USA), with values ranging from 4.6 to 35.7 L/min.

The dimensions of each section are shown in Fig. 5.2b, with a standpipe height of 0.753 m and a silo volume of 0.0125 m^3. The detail in Fig. 5.2b shows the dimensions of the L-valve, with an internal diameter of 0.021 m and a length of 0.22 m. The solids flowrate in this type of feeder is controlled by pneumatic actuation and the aeration inlet is situated at 0.051 m from the bottom of the valve. The cross-sectional areas of the aeration inlet and L-valve are equal to 0.04 and 3.46 cm^2, respectively.

The solids flowrate (W_S) in the L-valve was measured during the experiments with a digital balance model 9094 (Toledo, São Bernardo do Campo, Brazil) located below the exit of the L-valve. The change in powders' weight was recorded every 0.6 s by an acquisition routine coupled to a computer, and the instantaneous solids flowrate was determined.

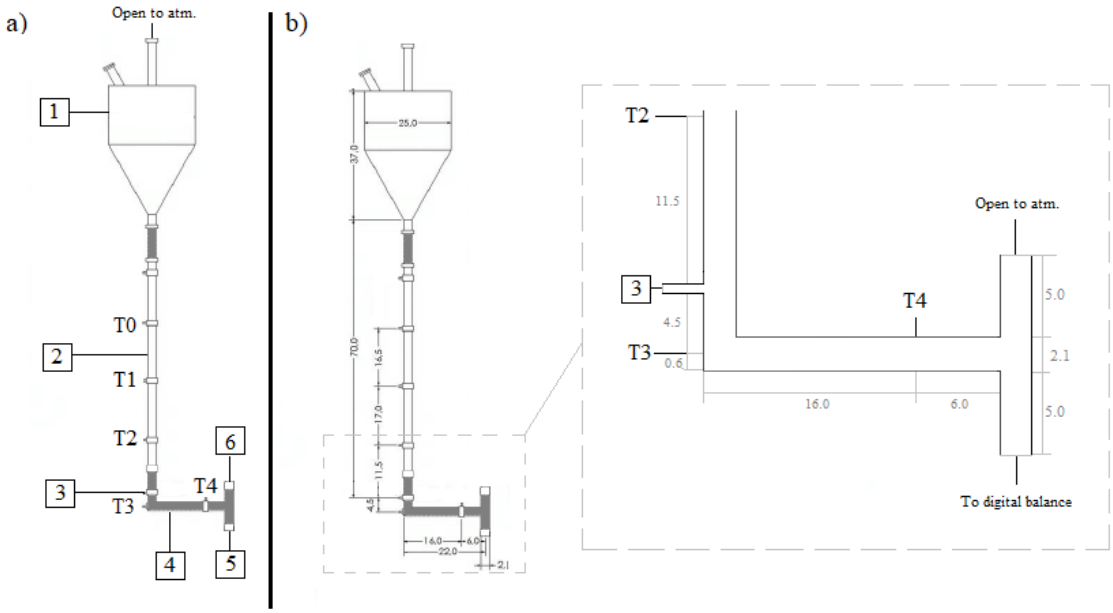

Fig. 5.2. Experimental setup for the feeding unit. a) The pressure taps are marked from T0 to T4, and the main components of the system are: (1) silo, (2) standpipe, (3) aeration inlet, (4) L-valve feeder, (5) solids' exit for instantaneous mass flowrate measurement, and (6) L-valve exit that can be coupled to other unit operations b) Dimensions in cm for the sections, and detail for the L-valve region.

The manometric pressures were measured by pressure transducers model 860 (AutoTran Incorporated, Wisconsin, USA) connected to 5 taps distributed along the standpipe and L-valve, as shown schematically in Fig. 5.2a. The specifications of each pressure transducer and the position of the pressure taps in the unit are shown in Tab. 5.3. The pressure data acquisition was managed by a software based on LabView 7.1 Express (National Instruments, Texas, USA), using a cDAQ-9172 chassis (National Instruments, Texas, USA) with the NI 9205 module (32-channel, +/−10 V, 250 kS/s, 16-bit analog input). The pressure time series data were collected at the same rate for each transducer signal, equal to 2,500 samples/s, and the mean pressure value for each transducer was recorded at every 0.6 s. The pressure drop in the standpipe (ΔP_{STD}) was measured between taps T2 and T0, while the L-valve pressure drop (ΔP_{LV}) was taken as the manometric pressure measured at T2, as the system is open to the atmosphere.

Tab. 5.3. Specifications of pressure transducers and tap positions in the unit.

Pressure tap	Height (m)*	Region	Range (Pa)
T0	0.501	Standpipe	0-1,250
T1	0.336	Standpipe	0-1,250
T2	0.166	Standpipe	0-1,250
T3	0.006	L-valve	0-1,250
T4	0.021	L-valve	0-1,250

*The height reference (h=0 m) was taken at the bottom of the L-valve.

The experimental procedure for the assays is outlined below. First, 0.8 kg of the sample B_{100} were inserted gravitationally into the system through the top of the silo, filling the standpipe and around 15% of the reservoir. The LabView acquisition routine was initiated, and the gas was inserted in the L-valve under a fixed value, between 4.6 and 35.7 L/min. The manometric pressure from taps T0 to T4 and the solids flowrate were recorded until the system is emptied. The assays were performed in triplicate for some selected flow conditions to verify the reproducibility of the results in the whole range of aeration rates. The experiments were filmed with a digital camera model PowerShot

SX170IS (Canon, Tokyo, Japan) so that the qualitative behavior of the flow in the L-valve feeder could be assessed for each flow condition.

Two correlations of the pressure drop in the valve (ΔP_{LV}) and the solids mas flux (G_S) were proposed by Geldart and Jones (GELDART; JONES, 1991) and by Smolders and Baeyens (SMOLDERS; BAEYENS, 1995), respectively:

$$\frac{\Delta P_{LV}}{L_h} = 216\ {G_s}^{0.17} D_{LV}^{-0.63} d_s^{-0.15} \tag{5.1}$$

$$\frac{\Delta P_{LV}}{L_h} = 3500\ {G_s}^{0.30} {d_s}^{0.10} {L_h}^{-0.70} \tag{5.2}$$

The validity of Eqs. (5.1) and (5.2) to predict the experimental data for L-valve feeding SCGs are evaluated.

5.1.3.3. Numerical model

The equations used for the multiphase model are detailed in Appendix A (Tab. A1), in which the gas and solid phases are treated as interpenetrating continua. The conservation equations for continuity and momentum for each phase are described by Eqs. (A1) to (A5). The granular temperature for the solid phase is introduced by the kinetic theory, and the transport equation takes the form of Eq. (A6). The solids pressure and viscosity are computed as a function of the granular temperature, as shown in Eqs. (A7) and (A8). The collisional, kinetic and frictional components of the solids shear viscosity are described by Eqs (A9) to (A11). The frictional part is added to the calculation only when the solids volume fraction exceeds the friction packing limit. The turbulence in the system was considered using the standard k-ε dispersed model with a standard treatment near the wall.

Drag, friction, and collision are the main forces involved in describing the gas-solid flow in L-valves. The frictional forces are included in the TFM approach by setting the

friction packing limit (FPL), and the effect of particle-particle and particle-wall collisions is accounted for, respectively, by the restitution (RC) and the specularity (SC) coefficients. Finally, some drag models suitable for gas-solid flows are revisited in Appendix A (Tab. A2) (DI FELICE, 1994; GIDASPOW; BEZBURUAH; DING, 1992; HUILIN; GIDASPOW, 2003; RONG; DONG; YU, 2013; SYAMLAL; O´BRIEN, 1989).

The Gidaspow (GD) and Huilin-Gidaspow (HG) drag models are a combination of the Wen and Yu model (Eq. A17), and the Ergun equation (Eq. A18), with the latter presenting a smooth switch at solid volume fraction equal to 0.2. The Syamlal-O'Brien model is based on the terminal velocities of particles in fluidized or settling beds. It uses the Dalla Vale's drag function (Eq. A24) and the solid terminal velocity as shown in Eq. (A25). The Di Felice (DF) drag model has the gas-solid exchange coefficient defined by Eq. (A29) with exponent given by Eq. (A30). Finally, the Rong drag model uses Eqs. (A28) and (A29) of Di Felice's model, but with exponent as presented in Eq. (A31), calibrated using Lattice-Boltzmann simulation of fluid flow through packed beds. Di Felice's and Rong's models were inserted into Fluent 17.1 code using user-defined functions.

In this paper, the effects of the drag models, FPL, RC, and SC on the solids flowrate and pressure profile in the L-valve system are evaluated. Tab. 5.4 lists the reference and tested options for all the studied parameters.

Tab. 5.4. Initial reference parameters and tested options for all the varied parameters.

Parameter	Reference	Tested options
Friction packing limit (FPL)	0.10	0.20, 0.25, 0.27, and 0.30
Drag model	Gidaspow (GD)	HG, SOB, DF, and RONG
Specularity coefficient (SC)	No-slip	0.10, 0.50, and 0.90
Restitution coefficient (RC)	0.99	0.90, 0.95, and 0.97

A wide range of values for FPL, SC, and RC coefficients were tested and their effect on the simulated results are analyzed. Note that FPL must be lower than the solids packing limit ($\alpha_{s,\,max}$=0.34) to account for frictional effects, while RC and SC range from 0 to 1, with typical values for RC higher than 0.90 (GHADIRIAN; ARASTOOPOUR, 2017; NIKOLOPOULOS et al., 2012; XUEYAO et al., 2013).

The model with the selected parameters is tested for different air flowrates in the valve, and the results are compared to the experimental data.

5.1.3.4. Simulation conditions

The simulations were performed using Fluent 17.1 (Ansys Inc., Pennsylvania, USA) in an i5-8600 CPU @ 3.10 GHz with six cores. The particle density, angle of internal friction, and mean diameter of the granular phase were set according to the SCG properties shown in Tab. 5.2. Initially, the granular phase was patched with α_{slb}=0.34 in the standpipe and silo up to a height of 0.910 m, matching the mass of solids used in the experiments (0.8 kg). The boundary conditions at the top of the silo, and at both L-valve exits were set as a gauge pressure outlet of 0 Pa since the discharge is to the atmosphere. At the aeration inlet, a fixed air velocity was used as a boundary condition. The simulations were performed until the system is completely discharged. The static pressure from taps T0 to T4 and the solids flowrate at the exit of the valve were evaluated under L-valve stable operation. The pressure and flowrate data were averaged for 10 s of simulation, and the mean values along with the standard deviation are reported for all conditions tested.

The pressure-velocity coupling was achieved using the SIMPLE algorithm. A first-order upwind scheme was used for discretization of the momentum, volume fraction and turbulence equations. The convergence criterion adopted for all the variables was 10^{-3}.

The system of equations was solved for the transient regime using integration steps of 10^{-3} s. The relaxation parameters for the momentum and volumetric fraction equations were kept at 0.4 and 0.5, respectively.

5.1.4. Results and Discussion

5.1.4.1. Experimental results for the L-valve feeding SCGs

- *Dynamic variation of solids flowrate and pressure*

To assess the dynamic flow behavior during a run, the dynamic variation of the pressures and solids flowrate (*Ws*) for a typical experiment is discussed below. The Fig. 5.3. shows that different dynamic patterns can be distinguished. At *t*=0s, as soon as the aeration is initiated, the pressures and *Ws* exhibit transient behavior, which is related to the collapse of the packed-bed in the standpipe and formation of a channel of flowing particles in the horizontal section of the valve. Between 50 and 225s, the L-valve operation is stable with fluctuations of pressures and *Ws* up to ±15%. Finally, from *t*=225s and onwards the pressures and *Ws* decrease sharply, which coincides with the decrease in the height of solids in the standpipe. When the height of solids is below pressure tap T1 (*h*=0.336 m, *t*=270 s), the decreasing trend of *Ws* shown in Fig. 5.3. corroborates the disruption of valves' operation. This might be due to the enhanced leakage of gas upwards as a consequence of the lower packed-bed resistance in the standpipe. The system is emptied after 320 s of operation.

Similar dynamic patterns were observed in all the experiments with *Q* ranging from 4.6 to 35.7 L/min. Therefore, SCGs flowrate can be well controlled using L-valves, with a wide region of stable operation, as long as the height in the standpipe is monitored during processing to prevent feeders' disruption. Note that this drawback can be overcome by properly designing silos and orifice discharges (providing solids

continuously to the standpipe), as well as by operating the system with the silo totally or partially filled with powders. In real applications, the solids level at the silo and at the standpipe can be monitored by simple pressure measurements, which can be used to trigger alarms, anticipating potential feeder's disruption.

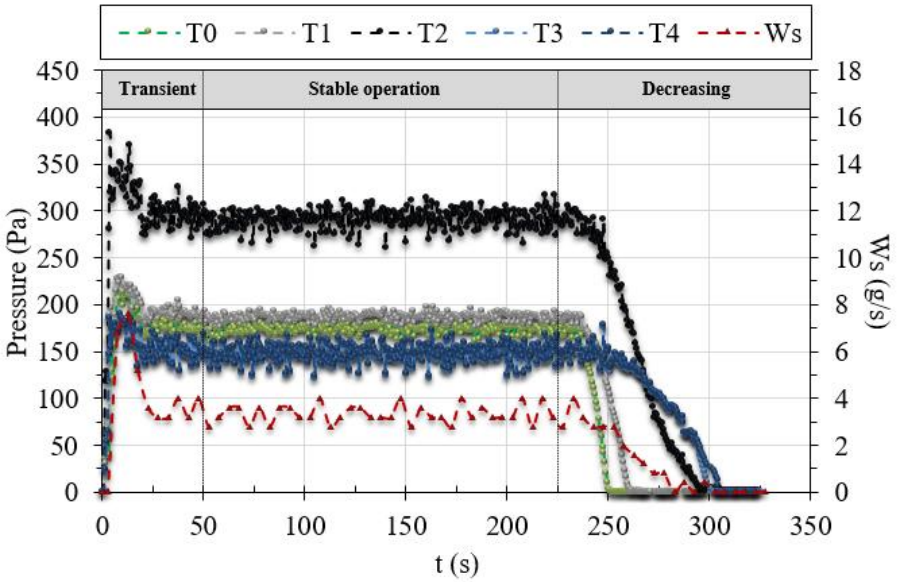

Fig. 5.3. Manometric pressures (T0 to T4) and solids flowrate (*Ws*) as a function of time for a typical run (Q/Q_{mf}=1.6).

- Different flow regimes

The average values of W_s in the stable operating region are shown in 5.4a as a function of the dimensionless aeration rate (Q/Q_{mf}). Note that Q_{mf} is equal to 2.9 L/min for the standpipe and L-valve cross-sections. Besides, the mean pressure drops in the L-valve and standpipe are shown in Fig. 5.4b and Fig. 5.4c, respectively. Based on the experimental data and on the observed flow behavior, three operating regions could be identified depending on the range of Q/Q_{mf}:

• For low aeration rates ($1.2<Q/Q_{mf}<4.0$): the packed-bed resistance near the aeration inlet controls the transport of solids in the valve, with a linear increase of *Ws*, $\Delta P_{LV,}$ and ΔP_{STD} as the aeration rate rises. There is only a narrow channel of solids moving

at the top of the horizontal part of the valve, while virtually no movement is detectable in the standpipe region.

• For medium aeration rates ($4.0<Q/Q_{mf}<6.4$): the packed-bed structure near the aeration inlet turns to a slugging flow with large bubbles moving downwards. At the horizontal part of the valve, continuous and periodical dunes and ripples are observed due to bubbles' flow. The lower values for ΔP_{LV} and ΔP_{STD} and the higher fluctuations in *Ws* are evidence of the mentioned behavior. At this condition, the maximum solids flowrate is reached in the valve, and ΔP_{LV} and ΔP_{STD} remain nearly constant as *Q* increases.

• For high aeration rates ($6.4<Q/Q_{mf}<12.8$): the downward flow of solids is hindered by turbulent vortices formed in the base of the standpipe, and the solids are conveyed in a dilute regime in the horizontal part of the valve. The decrease of ΔP_{STD}, $\Delta P_{LV,}$ and *Ws* as the aeration rises is evidence of the dilute conveying and corroborates that the transport is controlled by the gas phase in this condition.

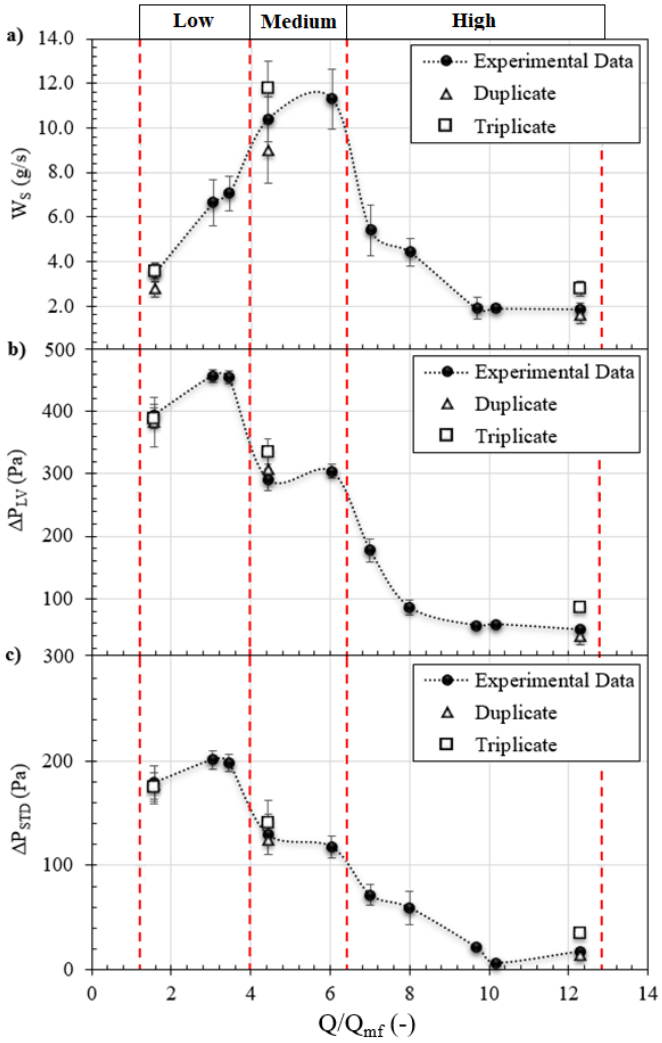

Fig. 5.4. Experimental data for the: solids flowrate (a), pressure drop in the L-valve (b), and pressure drop in the standpipe (c) as a function of the dimensionless aeration flowrate.

As shown in Fig. 5.4a, the solids flowrate could be easily varied from 1.6 to 11.8 g/s by adjusting the aeration flowrate in the L-valve. The flow was stable in the whole aeration range, and *Ws* presented standard deviations up to 15% of the mean value. A two-way analysis of variance based on Tukey's test was performed (p<0.05) for the experimental replicates and W_S were not statistically different among replicates for low, medium and high aeration flowrates. These are appealing results for feeding SCG powders with L-valves to silos, storage vessels, mechanical screens, dryers, and other units operated without back-pressure.

- Discussion of L-valve operation

Generally, it is recommended to operate L-valves below the slugging flowrate to ensure stable operation, and to guarantee that the valve works as a solid control device. However, the previous results show that the solids flowrate can be effectively controlled, from low to medium aeration rates, despite the presence of large bubbles. Furthermore, the results demonstrate that the solids flowrate can be controlled even at high aeration rates, under the presence of turbulent vortices. Using L-valves as a solid control device operated in the transition-region to dilute conveying (high aeration) has been neglected so far in the literature, however, this possibility of the valve is highlighted in Fig. 5.4a, in a range of $2.0<Ws<8.0$ g/s.

By visualizing L-valves as a pneumatically-actuated pseudo-mechanical valve, Yang and Knowlton (YANG; KNOWLTON, 1993) suggested that the operation of L-valves would be similar to that of slide valves. The opening area for solids flow is mechanically controlled in the slide valve, while it is controlled through aeration in the non-mechanical valve. Based on the previous discussion and Fig. 5.4., the operation of the SCG sample in the L-valve can be compared to that of butterfly valves. In the butterfly valve, rotating the disk up to 90˚ increases the opening area and *Ws* consequently. Additional rotation of the disk decreases *Ws* until no flow of solids is observed close to 180˚ of rotation. In the case of the L-valve, a maximum value for solids flowrate is observed at medium aerations. The opening area for solids flow is controlled by the packed-bed resistance under low aerations, and by the gas phase under high aerations. Besides, there is a threshold opening area to initiate the solids flow in both feeders. In the case of the L-valve, this value is equal to the minimum aeration rate that overcomes the packed-bed inertia, and was equal to 1.2 Q/Q_{mf}, as there is no flow of solids below this value.

- Correlations between the solids flowrate and the pressure drop

As discussed in Section 5.1.3.3, some correlations between the solids flowrate and the pressure drop in the L-valve have been proposed to predict the performance of L-valves feeding different materials. Reliable correlations between W_s and ΔP_{LV} might be a valuable tool in industrial applications, as they allow fast estimation of W_s from simple pressure measurements, hence it would be possible either setting W_s to the desired target or anticipating flow problems to improve operations.

The experimental values of ΔP_{LV} as a function of W_S are plotted and compared to the correlations of Geldart and Jones (Eq. 5.1) (GELDART; JONES, 1991) and Smolders and Baeyens (Eq. 5.2) (SMOLDERS; BAEYENS, 1995). Overall, the correlations underestimated *Ws* for a given pressure drop and were not suitable to predict the flow of SCG powders in the L-valve. This result indicates that the performance of L-valves feeding residue-based powders might differ significantly from data reported in the literature for materials such as sand and glass powders, which have a particle density of 2,500 kg/m^3. For the SCG sample, increasing the aeration rate causes a harsh transition of fluidization regimes compared to that observed for the other materials, because the particle density of the biomass sample is only 1,120 kg/m^3. Evidence of this behavior is shown in Fig. 5.5., where one can observe the region of increasing W_s with Q for the SCG sample (low to medium aeration) is much narrower than by Eqs. (5.1) and (5.2). This observation is related to the low bulk density of the biomass powder.

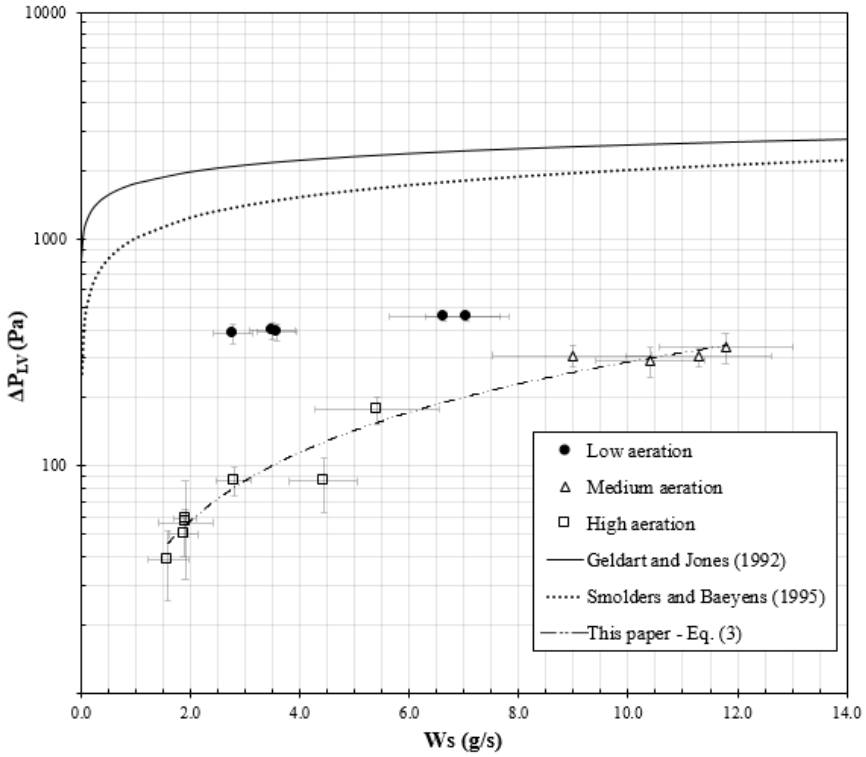

Fig. 5.5. Comparison between Eq. (5.3) and the pressure drop predicted by other correlations in the literature.

A linear relationship was fitted to estimate W_s from measurements of ΔP_{LV}, valid for the tested SCG sample from high to medium aeration rates in the valve ($6.0<Q/Q_{mf}<12.8$):

$$\Delta P_{LV} = 28.815\, W_S \tag{5.3}$$

A regression coefficient of 0.97 was obtained for Eq. (5.3), and the experimental values differ from the estimated ones by 10% on average, which is within the standard deviation of solids flowrate measurement. Besides, the experimental data are randomly distributed around the fitting line for Eq. (5.3), indicating a non-biased fitting. For low to medium aeration rates, fitting a correlation between ΔP_{LV} and W_s is not an effective approach, as small changes in the pressure drop (±100 Pa) generates significant changes in the solids flowrate ($1.6<W_s<11.8$ g/s). Hence, an additional effort was made to describe the solids flowrate in the valve, from the boundary-region of high to low aeration rates, using the TFM as discussed in the next section.

5.1.4.2. CFD simulations for the L-valve feeding SCGs

The effect of the drag models, friction packing limit (FPL), restitution coefficient (RC), and specularity coefficient (SC) on the solids flowrate and pressure profile in the L-valve system are evaluated below. These parameters are related to drag, friction and collision forces, which are the main forces involved for describing the gas-solid flow in L-valves. In the end, the TFM with the selected parameters is validated for other aeration flowrates, ranging from low to the boundary-region of high aeration rates.

- Mesh and grid independency study

The 3D computational meshes were mainly structured with hexahedral elements using Meshing (Ansys Inc., Pennsylvania, USA), and have the same dimensions of the experimental setup shown in Fig. 5.2. The guidelines for mesh generation consisted of refining the mesh in the cross-sectional area of the tube with 46 cells/cm^2, as shown in Fig. 5.6. Then, three grids with different refinement were built by changing the height of the computational cell (Ψ) from 0.010, 0.005 and 0.003 m. The referred Meshes I, II and III have 25,015, 47,626, and 78,058 cells, respectively.

The Grid Convergence Index (GCI) was used to check whether the solution for pressures throughout the equipment, solids fraction and solids flowrate under L-valve stable operation are within the asymptotic range of convergence for Meshes I, II, and III. The GCI calculation procedure is described elsewhere (ELSAYED; LACOR, 2011; ROACHE, 1994).

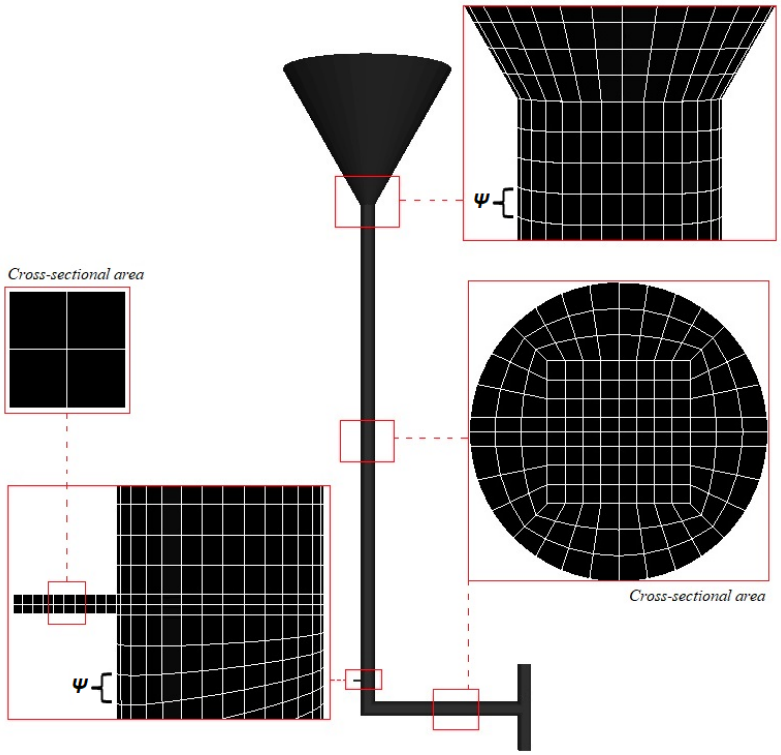

Fig. 5.6. Computational mesh for the L-valve system feeding powders to the atmosphere.

The results for the simulations using the reference parameters (Tab. 5.4) with Meshes I, II and III are shown in Fig. 5.7. Using Meshes II and III results in nearly identical results for the pressures, solids flowrate, and void fraction, while the coarse grid shows a discrepancy with the other grids. A two-way analysis of variance based on Tukey's test was performed (p<0.05) and the results for Meshes II and III are not statistically different.

Therefore, Mesh II was selected to achieve a compromise between accuracy and time of calculation. According to the GCI, the relative errors of Mesh II compared to the asymptotic solution (when the mesh spacing tends to zero) are less than 8% for pressure, flowrate, and void fraction responses.

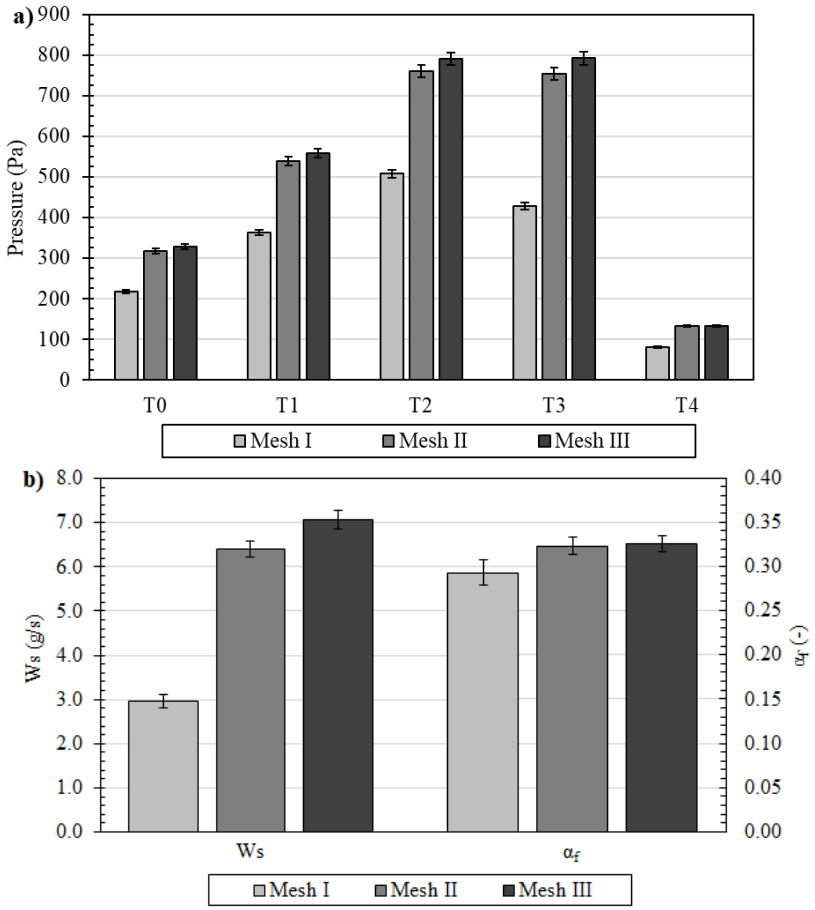

Fig. 5.7. Effect of grid sizes on the (a) static pressure from taps T0 to T4, and on the (b) solids flowrate (W_s) and void fraction (α_f) in the L-valve.

- F*riction packing limit (FPL)*

The results for solids flowrate using different FPL values are presented in Fig. 5.8. The dashed lines represent the experimental data for Q/Q_{mf}=4.4 (medium aeration), and the bars are the standard deviations for *Ws* under stable operation. It is shown that the simulated solids flowrate is under-predicted for FPL lower than 0.25 and that a sharp increase in *Ws* is observed above this value. Reducing FPL below the packing limit implies the inclusion of frictional stress for the solid phase at lower concentrations. The packing limit is equal to 0.34 for the SCG sample (Tab. 5.2), therefore the solids flowrate decreases as FPL decreases because the frictional contribution is added to the calculations.

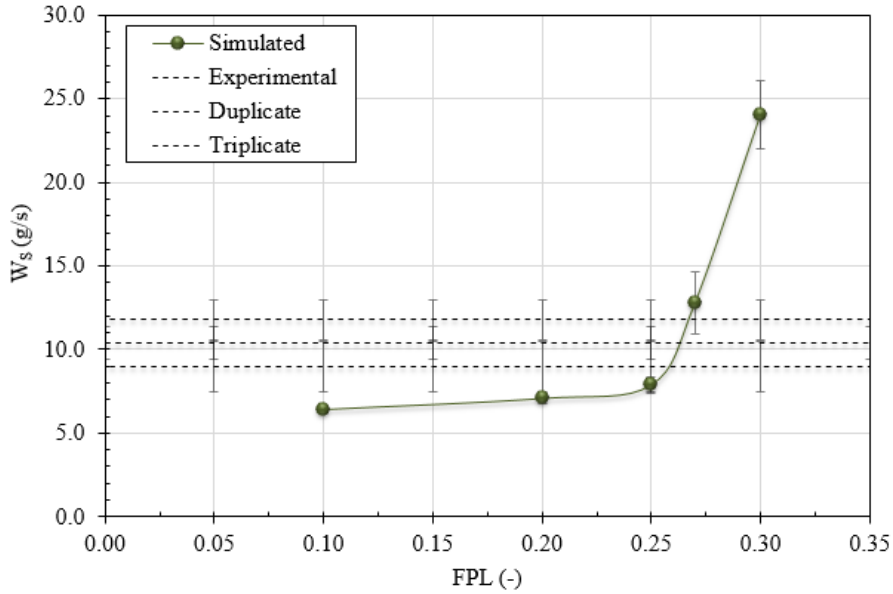

Fig. 5.8. Experimental and simulated results for the solids flowrate using different friction packing limit. The fixed parameters are: Gidaspow drag model, RC=0.99, no-slip condition at the wall, and Q/Q_{mf}=4.4.

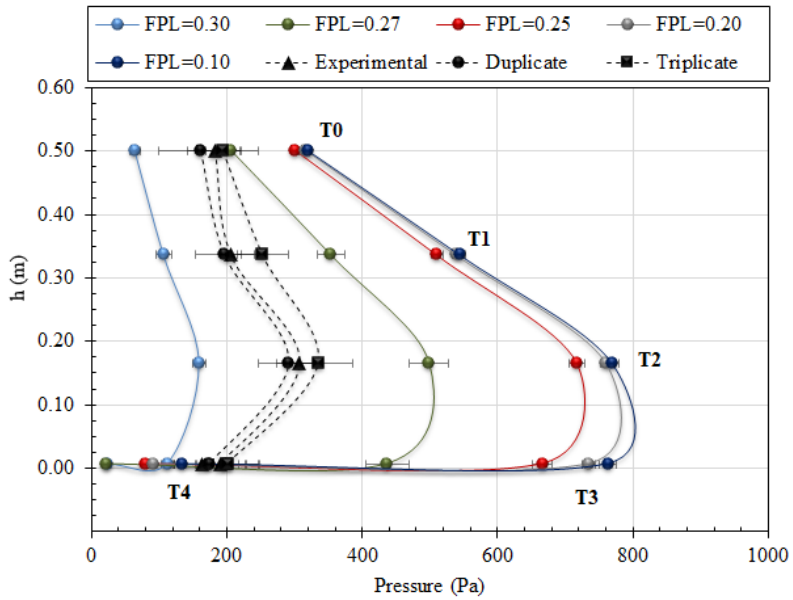

Fig. 5.9. Experimental and simulated results for the pressure in the system using different friction packing limit. The fixed parameters are: Gidaspow drag model, RC=0.99, no-slip condition at the wall, and Q/Q_{mf}=4.4.

The experimental pressures as a function of the system's height are shown in Fig. 5.9., as well as the simulated results using different FPL. All of the simulated profiles are qualitatively in agreement with the experimental behavior: the highest-pressure point is located near the aeration inlet (h=0.051 m), and the pressure drop variation is similar in the standpipe. Using FPL≤0.25 led to an over prediction of the pressure in the system,

while for FPL=0.30 the simulated pressures were lower than the experimental data. Based on a compromise between pressure and W_s, FPL=0.27 will be used for the simulations in the next sections.

- Drag models

The results for pressure and solids flowrate using different drag models are presented in Fig. 5.10.

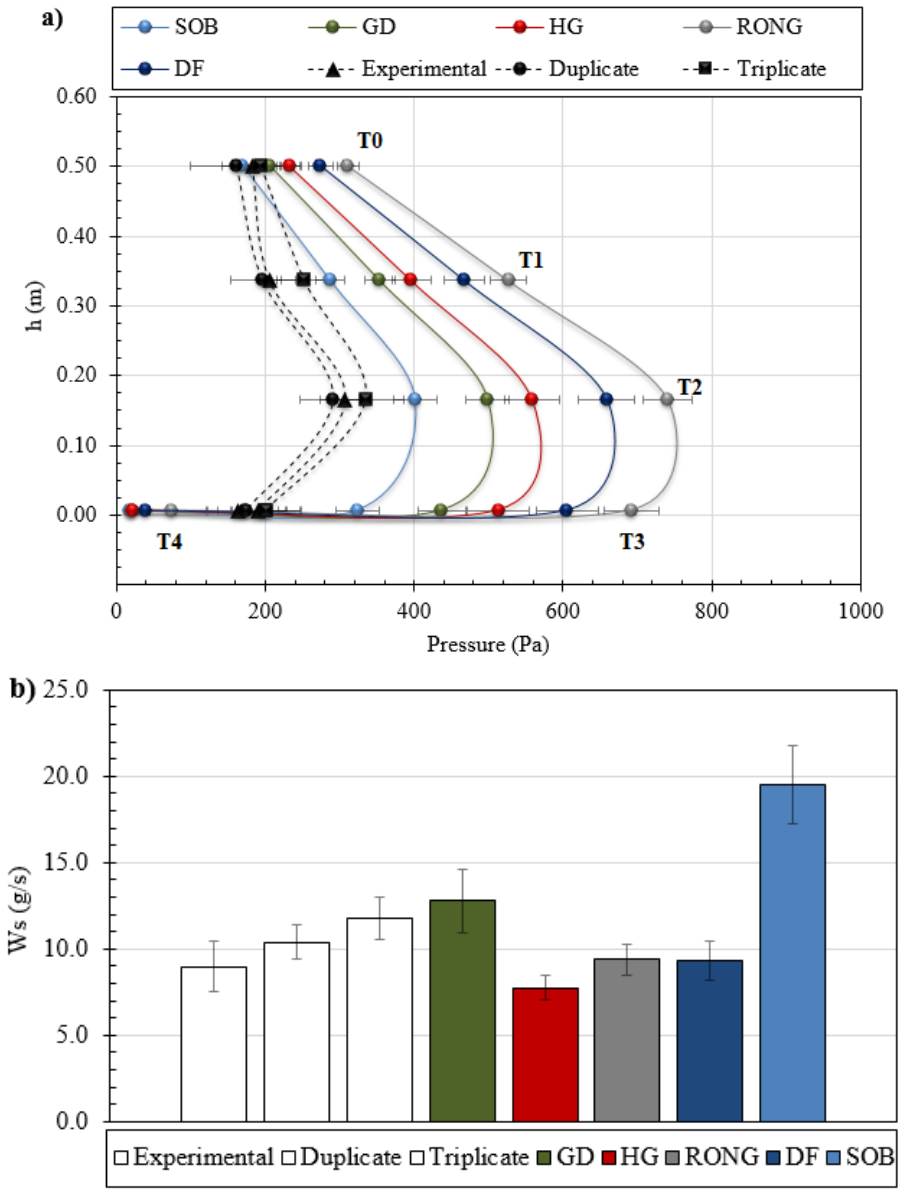

Fig. 5.10. Experimental and simulated results for the pressure in the system (a) and for the solids flowrate (b), using different drag models. The fixed parameters are: FPL=0.27, RC=0.99, no-slip condition at the wall, and Q/Q_{mf}=4.4.

Considering the mean deviations, the solids flowrate in the valve is accurately predicted by GD, DF and Rong models. The drag force generated by the Rong and DF models are similar for void fractions ranging from 0.66 to 0.75 (MARCHELLI et al., 2019), which encompass the void fraction observed in the L-valve simulations, hence similar values for W_s and pressures were calculated using these models. Although the pressure profile using the SOB model was closer to the experimental data, the solids flowrate was largely overpredicted by this model. Based on a compromise between W_s and pressure, the Gidaspow drag model was chosen to be used in the next sections.

- *Specularity coefficient (SC)*

The results for solids flowrate using different SC values are presented in Fig. 5.11. The specularity coefficient is an empirical parameter qualifying the nature of the particle-wall collision and depends on the roughness of the wall. A value of 0 is attributed to this parameter for perfect specular collisions, while SC=1 account for perfect diffuse collisions.

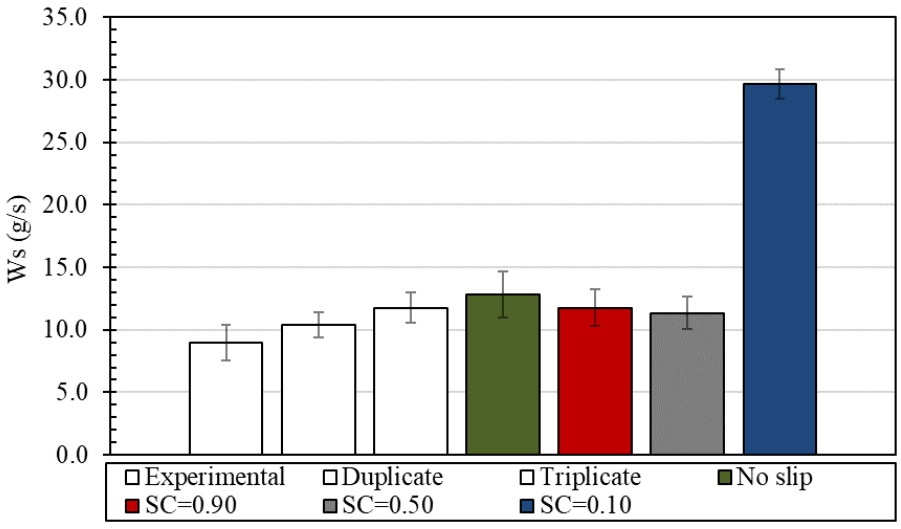

Fig. 5.11. Experimental and simulated results for the solids flowrate using different specularity coefficients. The fixed parameters are: FPL=0.27, Gidaspow drag model, RC=0.99, and Q/Q_{mf}=4.4.

Considering the mean deviations, the solids flowrate in the valve was similar using the no-slip condition at the wall, as well as SC higher than 0.50. Besides, decreasing SC to about 0.50 did not affect much the pressure in the system, which varied only ±50 Pa to the data (green line) shown in Fig. 5.10a. Using the no-slip condition means that the lateral momentum transfer at the wall is maximum, hence the solids velocity relative to the boundary is zero. At SC=0.1, the solids flowrate increases up to three times, because the system is closer to the condition of zero shear with the wall (SC=0). As both pressure and W_s were not sensitive for SC higher than 0.50, the no-slip wall condition was chosen to be used in the next sections for model simplicity.

- *Restitution coefficient (RC)*

The results for solids flowrate using different RC values are presented in Fig. 5.12. The restitution coefficient (RC) accounts for energy dissipation due to inelastic particle-particle collisions, and its value ranges from zero to unity, where RC=1 indicates that the momentum of solid particles before and after each collision is conserved. As shown in Fig. 5.12., RC is a critical parameter for simulating the gas-solid flow in L-valves. By decreasing RC from 0.99 to 0.90, W_s decreases from 13 to 0.6 g/s as the energy loss due to particles' collision is enhanced using RC=0.90. The pressures varied only ±50 Pa to the data (green line) shown in Fig. 5.10a in the interval $0.99 \leq RC \leq 0.90$, therefore the pressure profiles were not presented here. Using RC in the range of 0.97 to 0.99 gives a good match between simulated and experimental solids flowrate. Among the RC used, the best result was obtained with RC=0.97 and this value is used in the next sections. It must be noted that RC depends on particle's properties such as size, shape, roughness, among others, which makes this parameter difficult to be measured experimentally for residue-based powders.

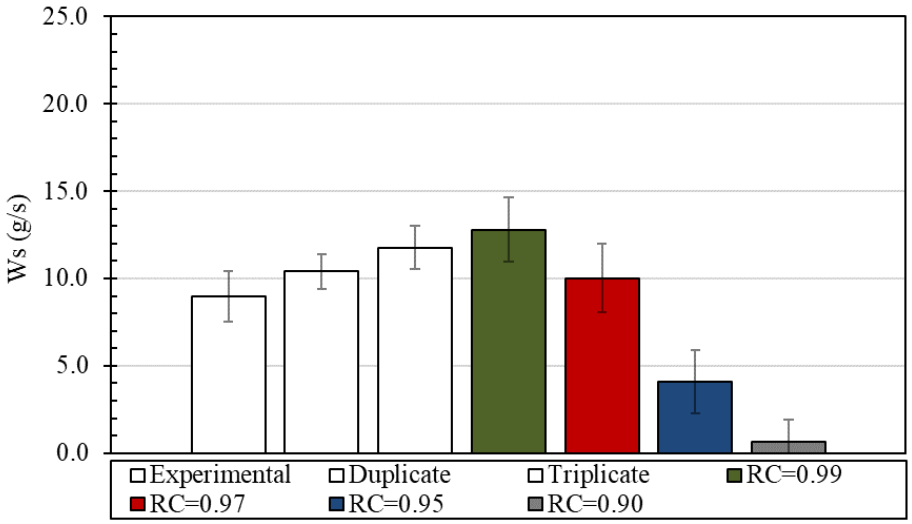

Fig. 5.12. Experimental and simulated results for the solids flowrate using different restitution coefficient. The fixed parameters are: FPL=0.27, Gidaspow drag model, no-slip condition at the wall, and Q/Q_{mf}=4.4.

- *Validation for other aeration flowrates (Q/Q_{mf})*

In the previous sections, the effects of drag models and model parameters on solids flowrate and on the pressure profile in the L-valve system were analyzed. Good predictions for *Ws* were obtained under Q/Q_{mf} =4.4 (medium aeration) using the Gidaspow drag model with FPL=0.27, RC=0.97, and no-slip condition at the wall. In this section, the proposed CFD model with the selected parameters is tested for Q/Q_{mf}=1.6, 3.0 and 6.0, which are within the low and medium aeration regions. The results for solids flowrate using different aeration flowrates are presented in Fig. 5.13.

As shown in Fig. 5.13., the mean solids flowrate in the L-valve is accurately predicted by the proposed TFM model, from low to medium aeration flowrates, with the relative difference between simulated and experimental values less than 20%. Note that this difference is almost within the experimental standard deviation for solids flowrate under stable operation (±15%, Sections 5.1.4.1.), which highlights the good quality of the numerical predictions. Unfortunately, the TFM could not be validated for high aeration rates because the system is emptied before a stable operation in the valve was achieved.

Nevertheless, using Eq. (5.3) was sufficient to predict accurately the data for high aerations, and the experimental values differ from the estimated ones by only 10% on average. Note that for predicting W_S with Eq. (5.3) it was only necessary to use the experimental data for the pressure drop in the L-valve, which are easily measured during processing.

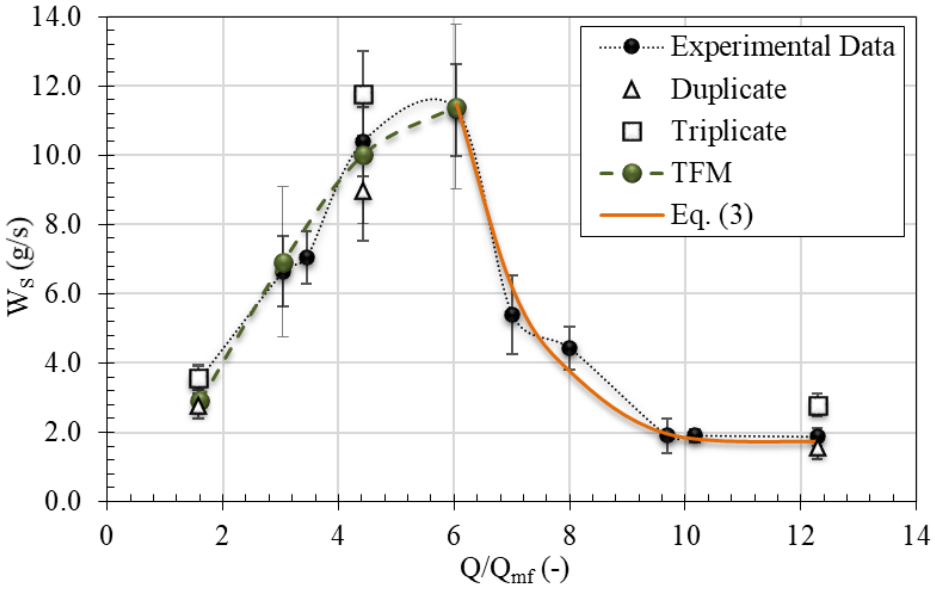

Fig. 5.13. Experimental data and predicted values for solids flowrate using Eq. (3) at high aerations, and TFM simulation from low to medium aerations. The optimized parameters for this case are: FPL=0.27, Gidaspow drag model, RC=0.97, and no-slip condition at the wall.

- *Flow dynamics*

Solids volume fraction, solids velocity profile and air flowrate in the standpipe are important information for the design and operation of L-valves. However, they are difficult to be obtained experimentally and data for biomass powders are still lacking in the literature. In our case, such information can be obtained from the validated TFM simulations for L-valve operated in the range of low to medium aeration flowrates.

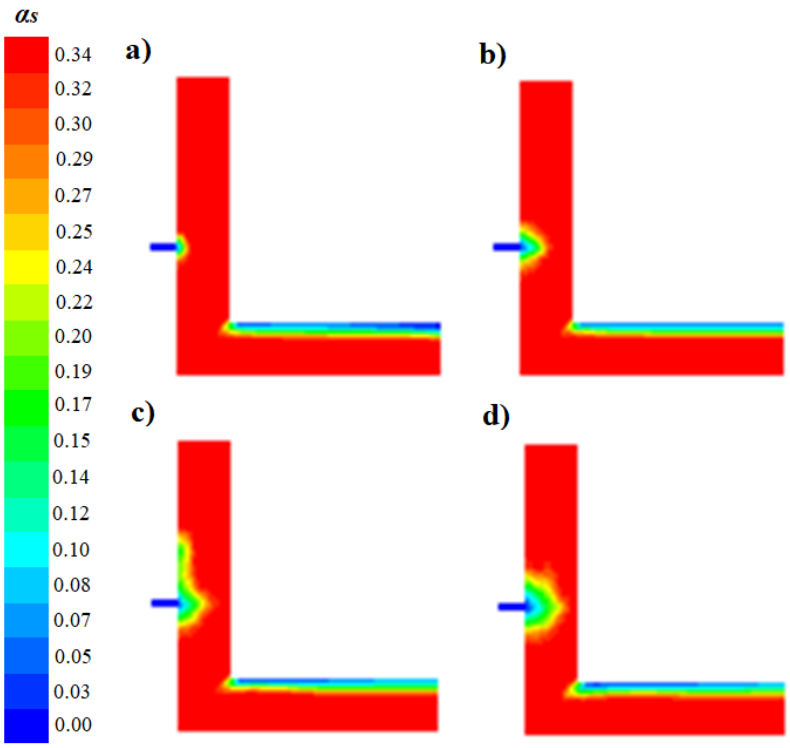

Fig. 5.14. Solids volume fraction in the standpipe and L-valve for different Q/Q_{mf} ratios: (a) 1.6, (b) 3.0, (c) 4.4, and (d) 6.0.

As shown in Fig. 5.14., the solids volume fraction is close to the packing limit (α_s=0.34) throughout the standpipe, except for the region near the aeration inlet where more voids are observed as the aeration rate rises. The solids flow in a channel at the top of the horizontal section of the valve, and the mean cross-sectional solids fraction is equal to 0.29±0.01 regardless of the aeration flowrate. Chan et al. (CHAN et al., 2009) also verified that the mean solids fraction in the valve is not affected by Q/Q_{mf}, and that α_S is equal to 0.50±0.10 for glass and sands (particle densities of 2,500 kg/m^3). The lower value of α_S for the biomass SCGs is consistent as this material has a lower bulk density than those of glass and sand powders (CHAN et al., 2009).

The cross-sectional contours of solids velocity at the horizontal section of the valve are shown in Fig. 5.15. The solids flow in a channel at the top of the valve, and the velocity is higher as the aeration rate increases. It means that the solids flowrate is higher at medium aerations than in low aerations, as shown in Fig. 5.13. Besides, the channel opening area increases as the aeration flowrate rises. Dunes and ripples were observed at

the flow channel under medium aerations, which agrees qualitatively to the experimental flow behavior.

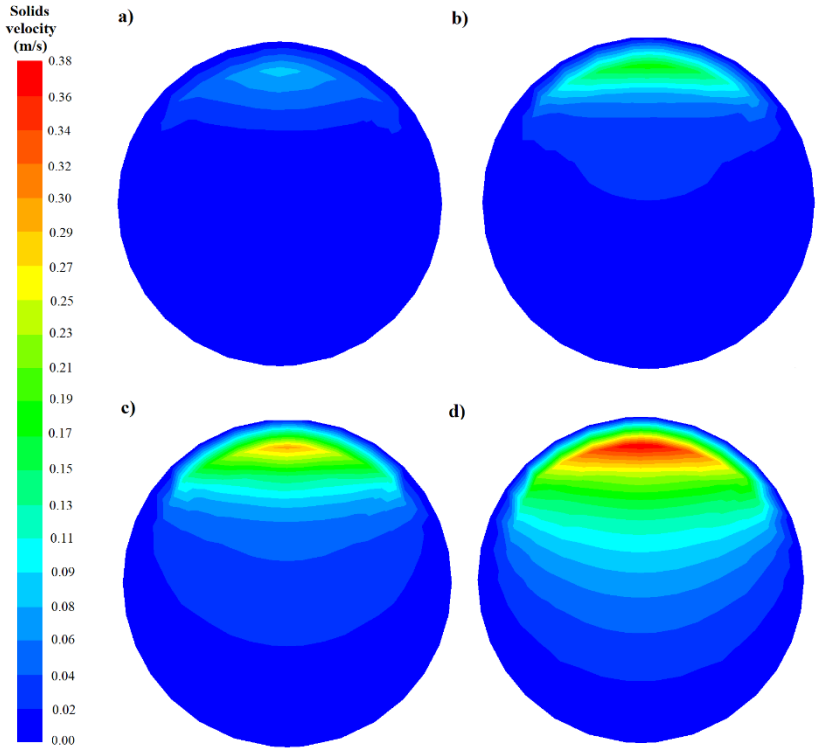

Fig. 5.15. Cross-sectional view of solids velocity contours at the L-valve horizontal length for different Q/Q_{mf} ratios: (a) 1.6, (b) 3.0, (c) 4.4, and (d) 6.0.

Finally, we verified that the ratio between the air diverted to the standpipe and the total air flowrate to the valve increases as Q/Q_{mf} rises. Increasing Q/Q_{mf} from 3.0 to 6.0 linearly increases the percentage of gas flowing upwards from 13 to 23%, which explains the nearly constant simulated solids flowrate at medium aerations (see Fig. 5.13.), since only gas flowing downwards contributes to the improvement of W_s. For Q/Q_{mf}=1.6, the amount of air diverted to the standpipe is negligible. These results agree qualitatively to the solids flow behavior proposed in Section 5.1.4.1. for L-valve operated under low and medium aerations.

5.1.5. Conclusions

A promising non-mechanical L-valve for feeding a biomass SCG powder is examined both experimentally and numerically. Key information for the operation and

design of non-mechanical L-valves with biomass SCG powder is described. The findings are useful for producing renewable thermal energy and fuels with SCGs and provide useful guidance for studying biomass materials with different materials properties, as summarized below.

L-valve's operation is rather stable with the SCG sample, with fluctuations of W_S less than 15%. The solids flowrate can be set to the desired target ($1.6<W_S<11.8$ g/s) by adjusting the aeration rate. The height of solids in the standpipe must be monitored to prevent the feeder's disruption.

The transition of fluidization regimes in L-valves is harsh with biomass powders, hence SCG's flowrate and pressure drop differ significantly from the data reported in the literature. Different flow regimes were identified in the L-valve, and the transition between them occurs as follows: low, $1.2<Q/Q_{mf}<4.0$; medium, $4.0<Q/Q_{mf}<6.4$; and high, $6.4<Q/Q_{mf}<12.8$. Using high aeration rates is presented as a new alternative to control solids flowrate with L-valves.

The flowrate can be predicted accurately by different approaches. From $1.2<Q/Q_{mf}<6.4$, SCGs' flowrate is accurately predicted by two-fluid model simulations. From $6.0<Q/Q_{mf}<12.8$, SCG's flowrate is accurately predicted by ΔP_{LV} measurements.

A comprehensive parametric study for the numerical model is conducted. The friction packing limit and restitution coefficient are critical parameters for describing the gas-solid flow in the L-valve.

The mean solid fraction in the horizontal section of the L-valve is equal to 0.29±0.01 for the SCG sample and this value is not affected by Q/Q_{mf} because of the air distribution into the standpipe. The percentage of air deviated to the standpipe is negligible for valve operated close to Q_{min}, and linearly increases from 13 to 23% as Q/Q_{mf} rises from 3.0 to 6.0.

5.1.6. Acknowledgements

The authors would like to thank the São Paulo Research Foundation (2016/25946-2 and 2018/11031-8), the Australian Research Council (IH140100035, DE180100266) and CAPES (Finance code 001) for financial support. We thank Dr. Rodrigo Condotta of the Faculty of Industrial Engineering/Brazil for measuring the angle of internal friction for the biomass sample.

5.1.7. Nomenclature

A	Coefficient defined in Eqs. (A26) and (A27)
B	Coefficient defined in Eqs. (A26) and (A27)
B_{100}	Spent coffee ground sample
C_D	Drag coefficient
D_{LV}	L-valve internal diameter (m)
d_s	Solid phase diameter (m)
FPL	Friction packing limit
g	Gravitational constant (ms^{-2})
G_s	Solids mass flux ($kg \cdot m^{-2} \cdot s^{-1}$)
$g_{0,ss}$	Radial distribution function
h	Height (m)
I_{2D}	Second invariant of deviatoric stress tensor
$\overline{I}$	Unit tensor
K_{sf}	Fluid-solid interaction coefficient ($kg \cdot m^{-3} \cdot s^{-1}$)
K_{fs}	Fluid-solid interaction coefficient ($kg \cdot m^{-3} \cdot s^{-1}$)
L_h	Horizontal length of the valve (m)
MC	Moisture content (% wet basis)
n	Unitary vector normal to the wall
p_s	Solids pressure ($N \cdot m^{-2}$)
RC	Restitution coefficient
Re_s	Reynolds solid number
SC	Specularity coefficient
t	Time (s)
$T0, T1, T2, T3, T4$	Pressure taps (Pa)
U	Aeration flowrate ($L \cdot min^{-1}$)
U_{mf}	Minimum fluidization flowrate ($L \cdot min^{-1}$)
U_{min}	Minimum aeration flowrate ($L \cdot min^{-1}$)
U_{ms}	Slug aeration flowrate ($L \cdot min^{-1}$)
V_{mf}	Minimum fluidization velocity ($m \cdot s^{-1}$)

v_{rs}	Terminal velocity ($m \cdot s^{-1}$)
$\vec{v}_f$	Fluid velocity ($m \cdot s^{-1}$)
$\vec{v}_s$	Solids velocity ($m \cdot s^{-1}$)
$v_{s,w}$	Solid velocity at the wall ($m \cdot s^{-1}$)
Ws	Solids flowrate ($g \cdot s^{-1}$)
Greek symbols	
α	Volumetric fraction
α_{slb}	Solids volume fraction at the loose bulk condition
$\alpha_{s,\,max}$	Solids packing limit
η	Parameter defined in Eq. (A32) and (A33)
$\gamma_{\theta s}$	Energy dissipation ($kg \cdot m^{-3} \cdot s^{-1}$)
ΔP_{LV}	Pressure drop in the L-valve (Pa)
ΔP_{STD}	Pressure drop in the standpipe (Pa)
$\kappa_{\theta s}$	Turbulence quantities of fluid phase ($m^2 \cdot s^{-2}$)
λ_s	Solids bulk viscosity (Pa·s)
μ_s	Solids shear viscosity (Pa·s)
$\mu_{s,col}$	Solids collisional viscosity (Pa·s)
$\mu_{s,fri}$	Solids frictional viscosity (Pa·s)
$\mu_{s,kin}$	Solids kinetic viscosity (Pa·s)
ω	Parameter defined in Eq. (A24)
p	Significance level
π	Pi number
Ψ	Mesh spacing (m)
ρ	Specific mass ($kg \cdot m^{-3}$)
ρ_{lb}	Loose bulk density ($kg \cdot m^{-3}$)
ρ_p	Particle density ($kg \cdot m^{-3}$)
ϕ	Angle of internal friction (°)
θ_s	Granular temperature ($m^2 \cdot s^{-2}$)
$\bar{\bar{\tau}}$	Stress tensor ($N \cdot m^{-2}$)
Subscripts	
f	Fluid
s	Solid

5.1.8. Appendix A. Two-fluid model equations

Tab. A1. Governing and closure equations for the simulation.

Governing equations	Eq.
Continuity equations for fluid (f) and solid (s) phase	
$\frac{\partial}{\partial t}\left(\alpha_f \rho_f\right) + \nabla \cdot \left(\alpha_f \rho_f \vec{v}_f\right) = 0$	(A1)
$\frac{\partial}{\partial t}\left(\alpha_s \rho_s\right) + \nabla \cdot \left(\alpha_s \rho_s \vec{v}_s\right) = 0$	(A2)
$\alpha_f + \alpha_s = 1$	(A3)
Momentum equations for fluid and solids phase	
$\frac{\partial}{\partial t}\left(\alpha_f \rho_f \vec{v}_f\right) + \nabla \cdot \left(\alpha_f \rho_f \vec{v}_f \vec{v}_f\right) = -\alpha_f \nabla p + \nabla . \bar{\bar{\tau}}_f + \alpha_f \rho_f \vec{g} + K_{fs}\left(\vec{v}_f - \vec{v}_s\right)$	(A4)
$\frac{\partial}{\partial t}\left(\alpha_s \rho_s \vec{v}_s\right) + \nabla \cdot \left(\alpha_s \rho_s \vec{v}_s \vec{v}_s\right) = -\alpha_s \nabla p - \nabla p_s + \nabla . \bar{\bar{\tau}}_s + \alpha_s \rho_s \vec{g} - K_{fs}\left(\vec{v}_f - \vec{v}_s\right)$	(A5)
Granular temperature equation	
$\frac{3}{2}\left[\frac{\partial}{\partial t}\left(\rho_s \alpha_s \theta_s\right) + \nabla \cdot \left(\rho_s \alpha_s \vec{v}_s \theta_s\right)\right] = \left(-p_s \bar{\bar{I}} + \bar{\bar{\tau}}_s\right) : \nabla \vec{v}_s + \nabla \cdot \left(k_{\theta_s} \nabla \theta_s\right) - \gamma_{\theta_s} - 3K_{fs}\theta_s$	(A6)
Closure equations	
Solid pressure	
$p_s = \alpha_s \rho_s \theta_s + 2\rho_s (1 + RC) {\alpha_s}^2 g_{0,ss} \theta_s$	(A7)
Solids shear viscosity	
$\mu_s = \mu_{s,col} + \mu_{s,kin} + \mu_{s,fr}$	(A8)
$\mu_{s,col} = \frac{4}{5}\alpha_s \rho_s d_s g_{0,ss}(1 + RC)\left(\frac{\theta_s}{\pi}\right)^{\frac{1}{2}}$	(A9)
$\mu_{s,kin} = \frac{10\rho_s d_s \sqrt{\theta_s \pi}}{96\alpha_s (1 + RC) g_{0,ss}}\left[1 + \frac{4}{5} g_{0,ss} \alpha_s (1 + RC)\right]^2$	(A10)
$\mu_{s,fr} = \frac{p_s \operatorname{sen} \phi}{2\sqrt{I_{2D}}}$	(A11)
Solids bulk viscosity	
$\lambda_s = \frac{4}{3}\alpha_s \rho_s d_s g_{0,ss}(1 + RC)\left(\frac{\theta_s}{\pi}\right)^{\frac{1}{2}}$	(A12)
Diffusion coefficient of granular energy	
$k_{\theta_s} = \frac{150\rho_s d_s \sqrt{(\theta \pi)}}{384(1 + RC) g_{0,ss}}\left[1 + \frac{6}{5}\alpha_s g_{0,ss}(1 + RC)\right]^2 + 2{\alpha_s}^2 \rho_s d_s (1 + RC) g_{0,ss}\sqrt{\frac{\theta_s}{\pi}}$	(A13)
Collisional energy dissipation	
$\gamma_{\theta_s} = \frac{12(1 - RC^2) g_{0,ss}}{d_s \sqrt{\pi}} \rho_s {\alpha_s}^2 {\theta_s}^{\frac{3}{2}}$	(A14)
Radial distribution function	
$g_{0,ss} = \left(1 - \frac{\alpha_s}{\alpha_{s,max}}\right)^{-2{,}5\alpha_{s,max}}$	(A15)
Solid-wall interaction	
$v_{s,w} = -\frac{6 \propto_{s,max} \mu_s}{\sqrt{3}\sqrt{\theta_s}\pi \rho_s \alpha_s g_0 SC} \frac{\partial v_{s,w}}{\partial n}$	(A16)

Tab. A2. Drag models tested in the simulations.

Gidaspow drag model	Eq.
$K_{sf} = K_{fs-Wen\&Yu} = \frac{3}{4} C_D \frac{\alpha_s \alpha_f \rho_f \left\vert \vec{v}_s - \vec{v}_f \right\vert}{d_s} {\alpha_f}^{-2,65}, \ for \ \alpha_f > 0{,}8$	(A17)
$K_{sf} = K_{fs-Ergun} = 150 \frac{\alpha_s (1-\alpha_f)\mu_f}{\alpha_f {d_s}^2} + 1{,}75 \frac{\alpha_s \rho_f \left\vert \vec{v}_s - \vec{v}_f \right\vert}{d_s}, for \ \alpha_f \leq 0{,}8$	(A18)
$C_D = \frac{24}{\alpha_f Re_s} \left[1 + 0{,}15 \left(\alpha_f Re_s \right)^{0{,}687} \right]$	(A19)
$Re_s = \frac{\rho_f d_s \left\vert \vec{v}_s - \vec{v}_f \right\vert}{\mu_f}$	(A20)
Huilin-Gidaspow drag model	
$K_{sf} = K_{fs} = \omega K_{fs-Ergun} + (1-\omega) K_{fs-Wen\&Yu}$	(A21)
$\omega = \frac{1}{2} + \frac{\arctan\left(262.5(\alpha_s - 0.2)\right)}{\pi}$	(A22)
Syamlal-O'Brien drag model	
$K_{sf} = \frac{3 \propto_s \propto_f \rho_f}{4 {v_{rs}}^2 d_s} C_D \left(\frac{Re_s}{v_{rs}} \right) \left\vert \vec{v}_s - \vec{v}_f \right\vert$	(A23)
$C_D = \left(0.63 + \frac{4.8}{\sqrt{Re_s / v_{rs}}} \right)^2$	(A24)
$v_{rs} = 0.5 \left(A - 0.06 Re_s + \sqrt{(0.06 Re_s)^2 + 0.12 Re_s (2B - A) + A^2} \right)$	(A25)
$A = \propto_f^{4.14} \ and \ B = 0.8 \propto_f^{1.28}, for \ \propto_f \leq 0.85$	(A26)
$A = \propto_f^{4.14} \ and \ B = \propto_f^{2.65}, for \ \propto_f > 0.85$	(A27)
Di Felice drag model	
$C_D = \left(0.63 + \frac{4.8}{\sqrt{Re_s}} \right)^2$	(A28)
$K_{sf} = \frac{3 C_D \left\vert \vec{v}_f - \vec{v}_s \right\vert \propto_s \rho_f}{4 d_s} \alpha_f^{2-\eta}$	(A29)
$\eta = 3.7 - 0.65 exp[-0.5(1.5 - \log(Re_s))^2]$	(A30)
Rong drag model	
$\eta = 2.65 (\propto_f + 1) - (5.3 - 3.5 \propto_f) \propto_f^2 exp[-0.5(1.5 - \log(Re_s))^2]$	(A31)

5.2 "Two-Fluid Model Simulation of Feeding Spent Coffee Ground Powders to a Riser With a Non-Mechanical L-Valve"

MASSARO SOUSA, L.; FERREIRA, M. C., HOU, Q. F., YU, A. B.

Apresentado no 9° Annual Chemical Engineering Postgraduate Association Conference, em 31 de outubro de 2019 em Melbourne, Austrália.

L-valves are non-mechanical feeders that use pneumatic actuation to control powders' flowrate to units operated under atmospheric pressure or to reactors that provide

additional resistance for solids flow (back pressure system). Experimental results have shown that these feeders might be a robust option to handle biomass residues known as Spent Coffee Grounds (SCGs), with different particle-size distributions and moisture contents. Nevertheless, design and scale-up rules for L-valves still need to be evaluated to facilitate their application on pilot and industrial levels. Two-fluid model (TFM) simulation is a cost-effective approach to meet these needs. A TFM model with the properties of the solid phase described by the Kinetic Theory of Granular Flow has already been validated for feeding SCG powders to the atmosphere with a 21 mm diameter L-valve. In this study, the model is tested for feeding of dry SCGs (the particle diameter is 400 μm) to a 2 m high riser (back-pressure system) with the L-valve air flowrate of 14 L/min and riser air flowrate of 250 (*Q1*) and 280 L/min (*Q2*), respectively. The simulations were performed using Fluent 17.1, and the predictions were compared to experimental data. The SCGs flowrate and mean void fraction in the riser were reasonably predicted with mean relative difference to the experimental data less than 25% and 1%, respectively, as shown in Fig. 5.16. The simulated solids flowrate reduced 75% in feeding the riser system than that for the atmospheric one, which agrees to the experimental measurements.

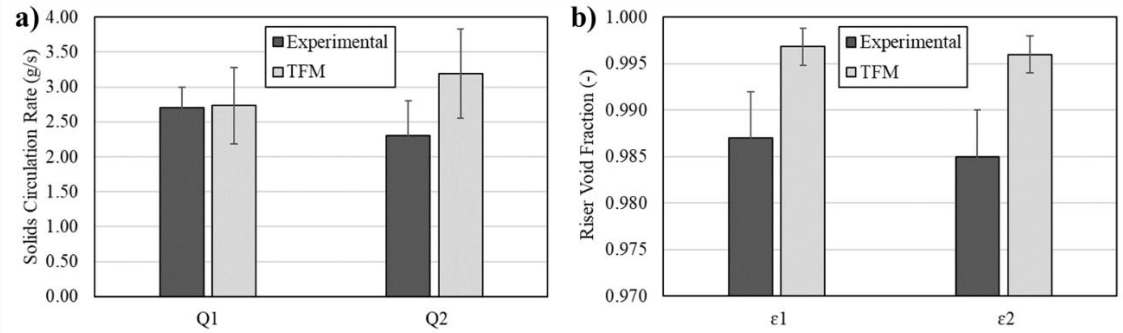

Fig. 5.16. Simulated and experimental a) solids flowrate and b) void fraction at the riser for *Q*= 250 and 280 L/min with aeration flowrate in the L-valve of 14 L/min.

Finally, the contours for air and solid velocities profiles are shown in Fig. 5.17, along with the solids fraction in the system. At the standpipe, the solids are transported

downwards in a moving bed type of flow with low solids velocity, whereas at the L-valve the flow of solids occur mainly at the top of the valve. The solids are transported upwards in the riser under a dilute regime due to the high riser gas flowrate inserted into the system, which is much greater than the aeration flowrate. At the bottom part of the riser, it is noticeable that the solids are more concentrated at the right side of the tube, whereas the typical core-annulus effect is observed at the upper parts. The validated model might be useful for future design and scale-up studies addressing L-valves operated with SCGs.

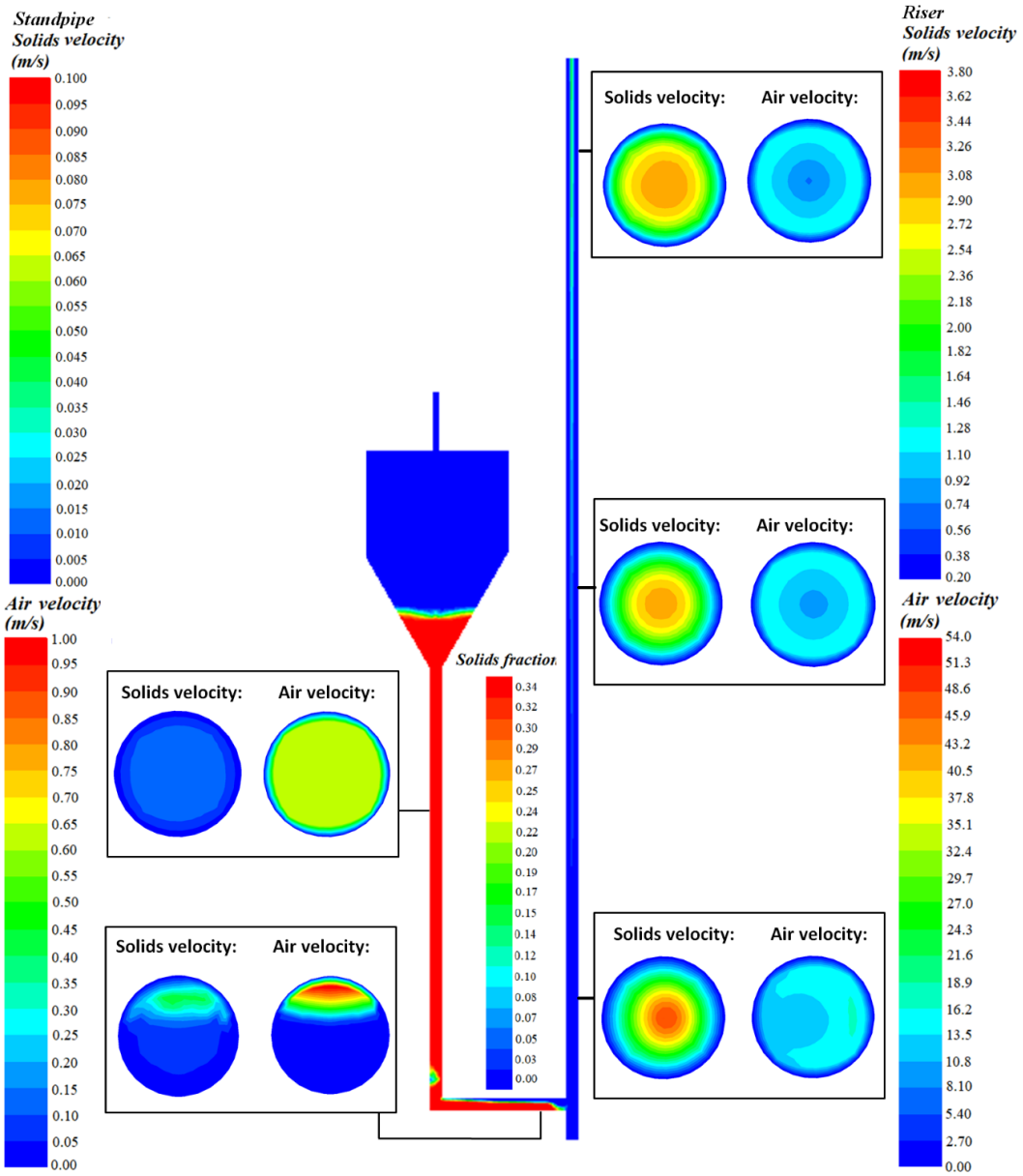

Fig. 5.17. Contours of solids fraction, solids velocity and air velocity for the L-valve feeding powder B_{100} to the riser.

CAPÍTULO 6 – ALIMENTAÇÃO DE BORRAS DE CAFÉ AO LPC COM LEITO DE JORRO: ANÁLISE EXPERIMENTAL

Neste capítulo, são apresentados os resultados experimentais da alimentação de borras de café ao LPC utilizando o alimentador tipo leito de jorro, o que está relacionado aos objetivos específicos (3) e (4) desta tese. Da mesma forma que na alimentação com a válvula-L (Capítulo 4), os ensaios apresentados neste capítulo foram realizados com as amostras de borra de café B_{100}, $B_{90}C_{10}$ e $B_{100}^{30\%}$.

Com o alimentador tipo leito de jorro, observou-se flutuação na vazão de sólidos (W_S) inferior a 20% para todas as amostras de borra de café, após o acoplamento de um bocal convergente na entrada de ar o que garantiu maior estabilidade de operação frente ao sistema sem o bocal (entrada de ar tipo orifício). A vazão de sólidos foi controlada efetivamente pela alteração da vazão de aeração (Q) e da distância entre a entrada de ar e a entrada do *riser* (z), as quais são as duas variáveis de operação para este alimentador. Os níveis das variáveis Q e z foram selecionados com base nos limites de operação estável com o alimentador na unidade experimental utilizada.

Mais especificamente, foram observadas vazões de sólidos entre 3 e 11 g/s para a amostra B_{100} e entre 1,2 e 5 g/s para a amostra $B_{90}C_{10}$, as quais são maiores que as alcançadas com a válvula-L e com menor consumo de gás para o transporte. Esses resultados evidenciam que o leito de jorro foi mais eficiente para a alimentação das borras de café secas, principalmente por existirem duas variáveis de operação neste alimentador, o que facilita o ajuste da vazão de sólidos à demanda. No caso da borra de café úmida, a qual apresenta melhor escoabilidade, ambos os alimentadores se mostraram adequados e podem ser indicados para realizar a operação.

Por fim, a vazão de sólidos foi relacionada linearmente com a pressão medida no *riser* e no bocal de entrada, indicando que W_S pode ser monitorado durante o processo

por meio de medidas simples de pressão. Para isso, correlações entre essas variáveis devem ser obtidas, englobando as particularidades de cada processo, bem como acopladas a alarmes para prevenir eventuais problemas de alimentação de sólidos.

Seguindo o padrão dos capítulos anteriores, os procedimentos experimentais e os resultados foram relatados no artigo "*On the Performance of a Spouted Bed Type Device for Feeding Spent Coffee Grounds to a Circulating Fluidized Bed Reactor*", que será apresentado a seguir.

6.1. "On the Performance of a Spouted Bed Type Device for Feeding Spent Coffee Grounds to a Circulating Fluidized Bed Reactor"

L. MASSARO SOUSA, M. C. FERREIRA

Artigo publicado na Chem. Eng. Res. and Des., volume 160, páginas 31-38, 2020.

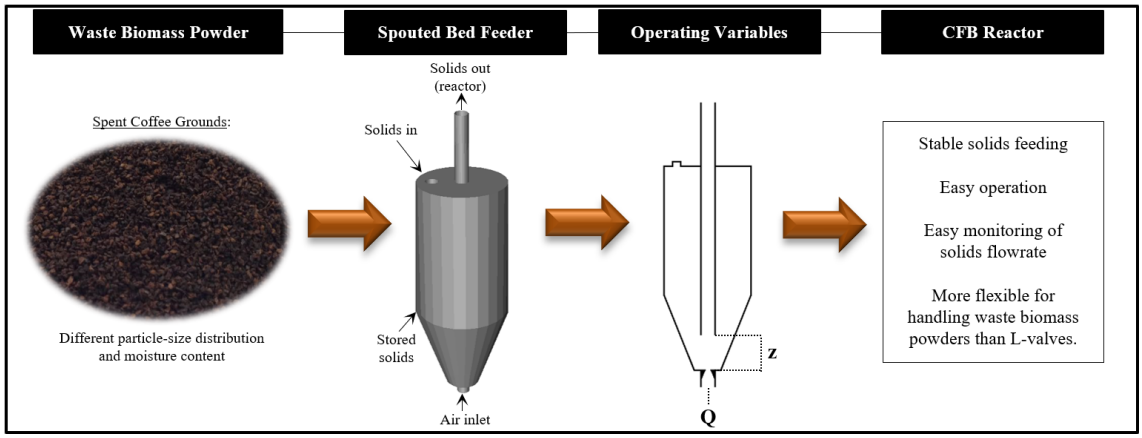

Fig. 6.1. Graphical abstract.

6.1. Abstract

Using solid biomass wastes as feedstocks for industrial generation of renewable energy is appealing to meet company's energy demands with environmental awareness; however, maintain continuous feeding of wastes to reactors remains a challenge in processing. In this study, the performance of a non-mechanical spouted bed (SB) feeder was evaluated for handling dry and moist spent coffee ground (SCG) powders to a

circulating fluidized bed reactor. A comprehensive experimental study was carried out to investigate the effects of operating variables and air inlet nozzle configuration on the solids circulation rates and pressure profiles. Using a convergent nozzle at the air inlet improved feeding stability compared to a conventional orifice air inlet. The circulation rates could be varied from $3.0<W_S<11.0$ g/s by adjusting the air flowrate and the entrainment length. Although SB performance was affected by the powder's flowability, the feeder operation was rather stable, with fluctuations less than 20% in W_S. Moreover, W_S could be accurately predicted from pressures measured at the feeder and riser. The SB showed enhanced flexibility in handling SCGs with different properties compared to a non-mechanical L-valve. It suggests that SBs might be an appealing alternative to feed waste biomass powders into reactors in a continuous mode.

6.2. Introduction

Spouted beds (SBs) provide effective contact between the fluid and solid phases within a fluidized vessel. This fluidization technique was first proposed by Mathur and Gishler (MATHUR; GISHLER, 1955) as an alternative to prevent slugging observed in fluidized beds of coarse particles. A general search in the Science Direct database shows that to date, more than 3,000 research papers have been published reporting the use of SBs in a wide variety of applications, including drying, coating, granulation and reaction operations (CUI; GRACE, 2008; JONO et al., 2000; RAHIMI-AHAR; HATAMIPOUR, 2018; SAIDI; BASIRAT TABRIZI; GRACE, 2019; SHUYAN et al., 2010). In the classical SB configuration, three characteristic regions are formed, namely the spout, annulus, and fountain zones, with a cyclic flow pattern of the solids through the different regions, which contributes to enhancing the heat and mass transfer rates. The solids circulation rates are affected by the vessel's geometry and operating conditions. The

insertion of a draft tube into a classical SB has been proposed to improve the SB performance for specific applications, as it enhances the system's stability and widens operating ranges by controlling the cross-flow of solids between the annulus and spout zones (BAO; DU; XU, 2013). Based on the principles of confinement of the solids in the annulus and pneumatic transport of the solids in the draft tube, some researchers suggested that this configuration could be used as a non-mechanical solids feeder to pneumatic conveying lines (FERREIRA; FREIRE, 1992).

The fluid dynamics behavior of SB type devices operating as solids feeders to Circulating Fluidized Beds (CFBs) has been discussed by several authors (COSTA; FERREIRA; FREIRE, 2004; FERREIRA; FREIRE, 1992; FERREIRA; SILVA; FREIRE, 1998; LITTMAN et al., 1993; LITTMAN; PACCIONE, 2015; SILVA; FERREIRA; FREIRE, 1996; SOUSA et al., 2010). In this configuration, the SB is placed underneath the riser section of the CFB, with the riser aligned with the air inlet. The solids are stored into the SB vessel and pneumatically transported to the riser by the upward airflow. The typical solids recirculation pattern in the SB occur throughout the CFB, as the riser perform like a draft tube, and the solids return from the fountain to the feeder by the return leg. The solids circulation rate in the CFB can be adjusted by varying the air flowrate (Q) and the distance between the air inlet and the lower end of the central tube (z). Although SB feeders have already proven to be effective to maintain stable feeding for glass beads (Geldart group D particles) under a wide range of conditions (COSTA; FERREIRA; FREIRE, 2004; FERREIRA; FREIRE, 1992; SOUSA et al., 2010), the feeder performance still needs to be assessed for biomass powders, whose characteristics and flow properties differ significantly from those of the glass beads.

Using waste biomass powders as feedstocks for producing renewable energy and fuels is appealing to reduce the dependence on fossil fuels, however, feeding reactors with

these materials is still a challenge in processing (DAI; CUI; GRACE, 2012; ILIC et al., 2018; RAMÍREZ-GÓMEZ, 2016). Spent Coffee Grounds (SCGs) are residues generated in huge amounts by the soluble coffee and other food industries, with recognised potential for producing thermal energy and hydrocarbon fuels (ATABANI et al., 2019; CAMPOS-VEGA et al., 2015; MCNUTT; HE, 2019; SILVA et al., 1998). Depending on the powders' particle-size distribution and moisture level, SCG's flowability can be categorized from *good* to *very poor* (MASSARO SOUSA; FERREIRA, 2019a, 2019b), hence these powders might clog mechanical feeding devices and hopper discharge orifices. Because SB feeders have a simple geometry and no moving parts, they are less expensive and suffer less wear compared to mechanical feeders. Besides, they can be used under conditions of high pressure and temperature with a reduced risk of wear and seizure. These characteristics make SB type devices a promising option for feeding waste biomass powders to reactors.

An in-depth assessment of non-mechanical feeders' performance in feeding spent coffee grounds is crucial for their successful application in CFB reactors for renewable energy generation. This paper is aimed at investigating the use of a spouted bed type device to feed SCG powders to a CFB. A comprehensive experimental study was carried out to evaluate the performance of the SB to feed dry and moist SCGs under two air flowrates (Q) and three distances between the air inlet and the bottom end of the riser (z). Two different air inlet configurations were tested, and the performance of the SB feeder was compared to results obtained using an L-valve for the same SCG powders.

6.3. Methodology

6.3.1. Materials

The physical and flow properties of the SCG samples are shown in Tab. 6.1. They consist of one moist sample (B_{100wet}), and two dry powders with different particle-size distributions. Samples B_{100wet} and B_{100} have a narrow particle-size distribution, from 300 and 500 μm. Sample $B_{90}C_{10}$ has a multimodal particle-size distribution, composed of 10% of particles with sizes from 150 to 300 μm, mixed with 90% of sample B_{100}. The methods used for samples' characterization are described in detail elsewhere (MASSARO SOUSA; FERREIRA, 2019a).

These samples were chosen to evaluate the performance of the feeding system because their sizes and moisture contents match the properties of SCG powders used in the soluble coffee industry for producing thermal energy (SILVA et al., 1998). Furthermore, these samples have quite different dynamic angles of repose (AoR^d), with flowability categorized from *very very poor* to *passable*, which might affect the feeding performance.

Tab. 6.1. Physical and flow properties of the SCG samples.

SCG sample	d_{SV} (μm)	MC (% w.b.)	U_{mf} (m/s)	ρ_p (kg/m³)	AoR^d (°)	Flowability classification
B_{100wet}	400	30.0 ± 0.3^a	0.20 ± 0.01^a	-	42 ± 2^a	Passable
B_{100}	400	2.8 ± 0.1^b	0.14 ± 0.01^b	1120 ± 20^a	62 ± 3^b	Very Poor
$B_{90}C_{10}$	370	3.2 ± 0.1^b	0.15 ± 0.01^b	1120 ± 10^a	70 ± 3^c	Very Very Poor

Values with different letters in the same column are significantly different at a 0.05 significance level.

The dynamic angles of repose (AoR^d) of the samples were measured using a rotating drum with a diameter of 10 cm and a width of 4 cm, operating under the rolling flow pattern (SANTOS; CONDOTTA; FERREIRA, 2017). The flowability classification is based on (LUMAY et al., 2012; TAN; MORTON; LARSON, 2015). The minimum fluidization velocity (U_{mf}) was determined in a fluidized bed with a diameter of 0.114 m,

a powder bed height of 9 cm, and with air injected uniformly at the bottom of the bed. All assays were performed in triplicate and the standard deviations are reported.

6.3.2. Experimental CFB unit with SB feeder

The experiments were carried out using the unit shown in Fig. 6.2a. It consists basically of a non-mechanical spouted bed feeder (1) that transports the solids stored in it to the riser (3) by adding air to the bottom inlet (2). An inclined separator (4) and a cyclone (5) collect the solids at the top of the riser and return them to the spouted bed after going through the solids' flowrate measurement system (6) and the return leg (7), thus completing the circulation loop.

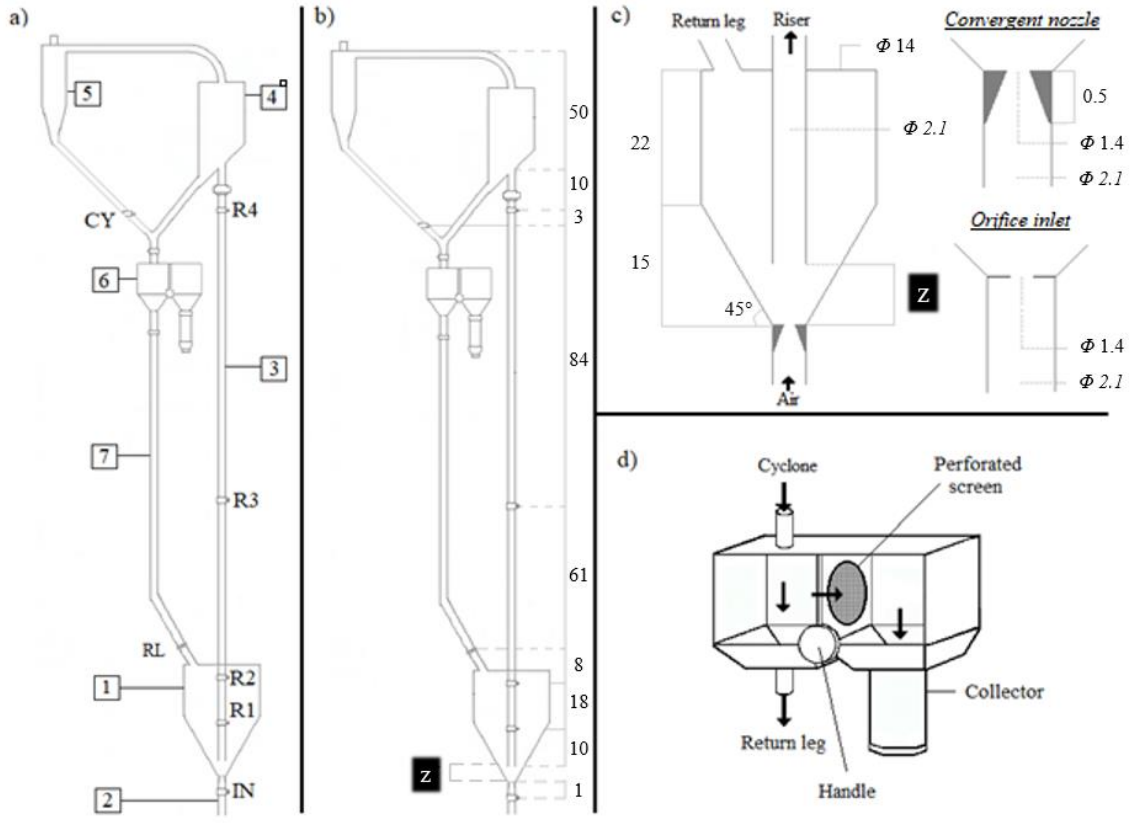

Fig. 6.2. CFB experimental setup. a) Main components and pressure tap positions: IN, R1 to R4, CY, and RL. b) Dimensions of the CFB unit. c) Components of the spouted bed feeder and details of the air inlet configurations. d) Solids' flowrate measurement system. All dimensions in cm.

The air escapes through the cyclone overflow, while the solids are kept in continuous circulation mode in the CFB by feeder's aeration. In combustion and gasification applications, SCGs react with hot gas at the riser section, and the produced gases and ashes flow out through the cyclone overflow to other process' units.

The dimensions of the cold-flow CFB are shown in Fig. 6.2b, with an overall height of 2 m and riser internal diameter of 0.021 m. The entire system is built of stainless steel, except for the spouted bed detailed in Fig. 6.2c that is made of galvanized iron with a convergent cone at the air inlet as shown in the detail. The solids circulation rate (W_S) in the CFB unit was measured using the sampler device shown in Fig. 6.2d. It consists of a reservoir divided by a perforated screen plate that can be moved to deviate the solids flow for sampling with minimum flow disturbance (COSTA; FERREIRA; FREIRE, 2004). The mass of collected powders was weighted in a digital balance model BG-4000 (Gehaka, São Paulo, Brazil) with an accuracy of 0.01 g.

The manometric pressures were measured at different taps located in the riser (R1 to R4), cyclone underflow (CY), return leg (RL), and air inlet (IN). The acquisition of pressure data was performed by a cDAQ-9172 chassis (National Instruments, Texas, USA) with the NI 9205 module (32-channel, +/−10 V, 250 kS/s, 16-bit analog input). The data was collected at a rate of 2500 samples/s and the mean values were recorded at every 4s.

6.3.3. Experimental conditions

The experiments were designed to evaluate the influence of the air flowrate (Q), the distance between the air inlet and the bottom end of the riser (z), SCG properties and air inlet configuration on the spouted bed feeder performance. The runs are summarized in Tab. 6.2 for two different values for Q and three values for z. The air inlet configuration

was modified by using a convergent nozzle at the air inlet (see the detail in Fig. 6.2c) as an alternative to the conventional air inlet through a central orifice, also shown in the detail of Fig. 6.2c.

The range of *Q* used in the assays were determined based on previous experiments with sample B_{100}. The higher limit for *Q* was set to avoid significant loss of powders at the cyclone overflow, whereas the lower limit corresponds to the minimum air flowrate that provided a stable solids flowrate in the riser. Note that pulsating unsteady transport of SCGs in this system occur at *Q*=38 L/min.

Tab. 6.2. Summary of the experimental conditions.

Runs	**SCG sample**	***z* (cm)**	***Q* (L/min)**	**Air inlet configuration (-)**
Number 1	B_{100}	3	52	Convergent Nozzle
No. 2	B_{100}	4	52	Conv. Nozzle
No. 3	B_{100}	5	52	Conv. Nozzle
No. 4	B_{100}	3	62	Conv. Nozzle
No. 5	B_{100}	4	62	Conv. Nozzle
No. 6	B_{100}	5	62	Conv. Nozzle
No. 7	B_{100wet}	3	52	Conv. Nozzle
No. 8	B_{100wet}	4	52	Conv. Nozzle
No. 9	B_{100wet}	5	52	Conv. Nozzle
No. 10	B_{100wet}	3	62	Conv. Nozzle
No. 11	B_{100wet}	4	62	Conv. Nozzle
No. 12	B_{100wet}	5	62	Conv. Nozzle
No. 13	$B_{90}C_{10}$	3	52	Conv. Nozzle
No. 14	$B_{90}C_{10}$	4	52	Conv. Nozzle
No. 15	$B_{90}C_{10}$	5	52	Conv. Nozzle
No. 16	$B_{90}C_{10}$	3	62	Conv. Nozzle
No. 17	$B_{90}C_{10}$	4	62	Conv. Nozzle
No. 18	$B_{90}C_{10}$	5	62	Conv. Nozzle
No. 19	B_{100}	4	52	Orifice
No. 20	B_{100}	5	52	Orifice
No. 21	B_{100}	4	62	Orifice
No. 22	B_{100}	5	62	Orifice

6.3.4. Experimental procedure

The experimental procedure consisted of adjusting *z* to 3, 4, or 5 cm and loading the spouted bed with 1.4 kg of SCG powder. After, the air flowrate supplied by a compressor was set to 52±2 or 62±2 L/min and inserted into the SB bottom. Every 4 s, the pressures around the CFB loop were recorded. The solids circulation rates were determined after weighing the masses collected by 10 s in the sampler. Five repetitions were carried out for each condition. The mean values for pressures and W_S under stable flow conditions are reported along with their standard deviations.

At the end of each assay, the powder that remained in the CFB unit was collected and weighted. As powder agglomeration within the system was not observed, the loss of powder in the cyclone overflow was estimated by a mass balance. The production of fine particles by attrition was determined by sifting the collected powder. The change in the powder's moisture content was also estimated by comparing the moisture content in the samples before and after the assays. It was found that the loss of powder at the cyclone overflow was less than 2% of the loaded mass. Particle-particle and particle-wall attrition were not relevant in the conditions tested, as the production of particles with sizes under 300 μm was less than 1%. The changes in the moisture content of sample B_{100wet} after the experiments were less than 4% for all conditions tested.

6.4. Results and Discussion

6.4.1. Influence of *Q* and *z* on W_S

The circulation rates for sample B_{100} under different *Q* and *z* are shown in Fig. 6.3. The flow was always stable and W_S fluctuated less than 20% during each experimental condition. Increasing *Q* and *z* increased W_S from 3.0 to 11.0 g/s, which might be attributed, respectively, to an increase in the gas phase momentum and to the wider area

available for the solids to be dragged by the airflow into the riser as the space between the riser bottom and cone wall is enlarged. Both factors contribute to enhancing the circulation rates in the CFB. The effect of *z* and *Q* on the solid flowrates qualitatively agrees with previous studies from literature (COSTA; FERREIRA; FREIRE, 2004; FERREIRA; FREIRE, 1992; SOUSA et al., 2010).

Nevertheless, the change in *Q* seems to affect *Ws* more significantly as compared to changes in *z*. By increasing *Q* by 19% (from 52 to 62 L/min), an increase of 75% on average is observed in W_S, while increasing *z* by 30% (from 3 to 4 or from 4 to 5 cm) increases W_S by only 42%. These results suggest that in processing, solids circulation rates can be easily set to the desired target by adjusting *Q* and *z*. A fine-tuning in W_S values for sample B_{100} might be done by changing *z*.

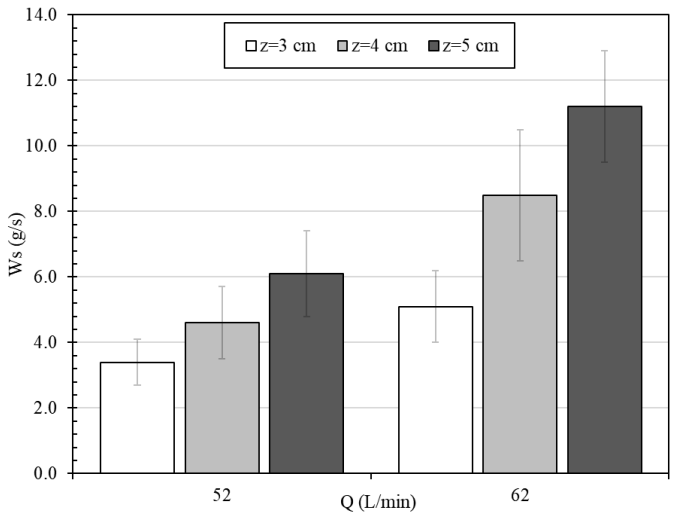

Fig. 6.3. Solids circulation rates for sample B_{100} under different *Q* and *z* and operation with the convergent nozzle at the air inlet.

6.4.2. Influence of SCG's particle-size distribution and moisture content on W_S

The circulation rates for sample B_{100wet} under different *Q* and *z* are shown in Fig. 6.4. The SB also provided stable feeding for the wet SCG sample, with fluctuations of *Ws* less than 20%. Considering the standard deviations, one can observe that the values of *Ws* for samples B_{100wet} and B_{100} (see Fig. 6.4) are similar under *Q*=52 L/min. This is because

although the minimum fluidization velocity of the wet powder is higher than that of the dry one, flowability of sample B_{100wet} is better (i.e. particle-particle interactions that restrict the flow of solids are less intense), as shown in Tab. 6.1. From a practical perspective, this means that sample B_{100} can be transported more easily in the riser at Q=52 L/min, however, the flow of solids from the annular region of the spouted bed to the riser entrance is possibly restricted by the enhanced particle-particle interactions and fluidization effects. Therefore, similar *Ws* were verified for these samples under Q=52 L/min.

Nevertheless, increasing Q from 52 to 62 L/min had a less pronounced effect on W_S for the wet sample. SCG particles have a porosity of 14% (MASSARO SOUSA; FERREIRA, 2019b) and water can penetrate into the internal voids, hence increasing the particle density and the hydrodynamic energy required to transport them as compared to the dry particles. This is corroborated by the higher values of U_{mf} of the wet sample (Tab. 6.1). Although additional energy is provided by increasing Q from 52 to 62 L/min, the increment in Q was insufficient to increase *Ws* significantly. Note that the ratio between mean gas velocity at the air inlet and minimum fluidization velocity for sample B_{100wet} ranged from 12.5 to 14.9, while it ranged from 17.9 to 21.3 for sample B_{100}. Therefore, W_S of sample B_{100wet} could be probably increased by using higher values for Q than those tested in the present study.

The effect of changing z is less pronounced for sample B_{100wet} (Fig. 6.4.) compared to B_{100} (Fig. 6.3.). As shown in Tab. 6.1, the wet sample has better flowability than the dry powder, hence the flow of particles B_{100wet} from the annular region to the riser is possibly enhanced. In turn, the effect of geometric constraints on the solids flow is weaker and for the wet sample *Ws* does not change considerably with z. Therefore, controlling W_S for wet samples with an SB feeder seems to be more effective by adjusting Q instead

of *z*. Note that the term wet, in this case, refers to a water saturation level at which the liquid bridges are not strong enough to worsen the sample's flow properties (MASSARO SOUSA; FERREIRA, 2019a).

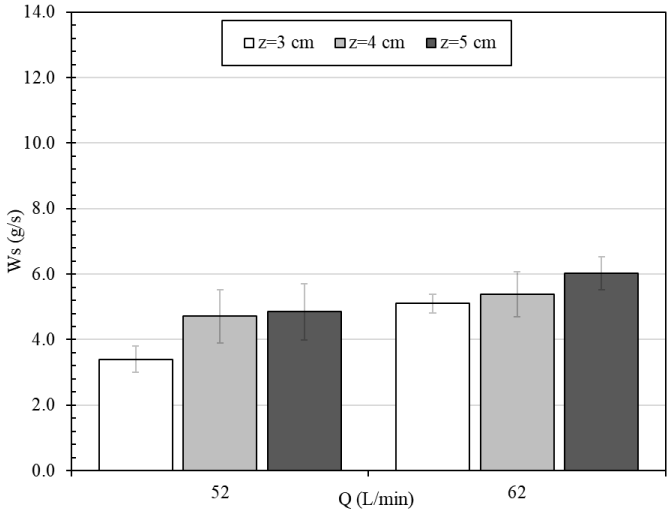

Fig. 6.4. Solids circulation rates for sample B_{100wet} under different values of *Q* and *z*.

The circulation rates of sample $B_{90}C_{10}$ under different Q and z are shown in Fig. 6.5. In this case, increasing Q increases W_S by almost four times, however, a stable operation was achieved only for a narrow range of Q and z. Besides, under the same Q and z, the circulation rates of sample $B_{90}C_{10}$ are lower than those of sample B_{100} (see Fig. 6.5.). These feeding limitations can be explained by the poorer flowability attributes of sample $B_{90}C_{10}$, as shown in Tab. 6.1.

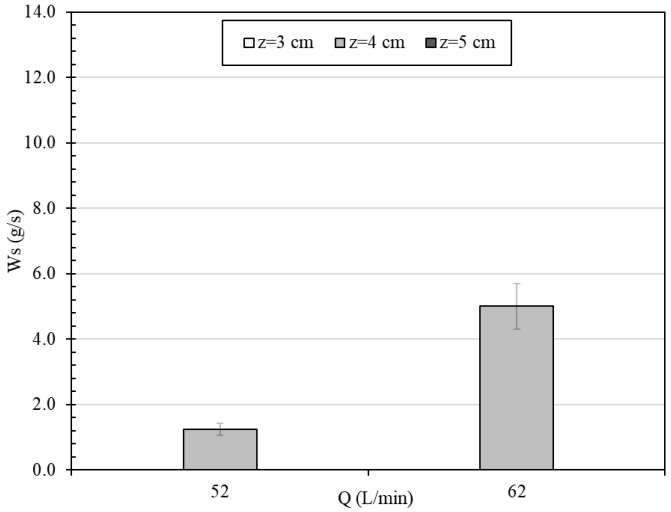

Fig. 6.5. Solids circulation rates of sample $B_{90}C_{10}$ under different values of *Q* and *z*.

Continuous and steady solids feeding is essential and critical for biomass conversion processes and the feeder is usually the most problematic component of the entire reactor system (DAI; CUI; GRACE, 2012; RAMÍREZ-GÓMEZ, 2016). From Sections 6.4.1 and 6.4.2, one can notice that the SB device provided stable solids feeding for dry and wet SCG powders under a wide range of conditions and could also operate with powders with different flowability attributes. Although feeding effectiveness might still be improved by assessing the influence of the SB design, the results shown here indicate that SBs are appealing devices to handle such biomass powders.

Furthermore, it is shown that the SB feeder performance is affected by the samples' properties and to ensure effective handling, the powder's flowability attributes and moisture content should be considered in the feeder's design. The previous knowledge of the powder's properties to be processed can be used to define adequate strategies to control W_S (i. e., based on either changing Q or z) and is useful information to avoid feeder's malfunction. Note that the poor flow properties of SCG powders are a consequence of their bio-based nature and processing, therefore, they are inherent of waste biomass powders.

6.4.3. Effect of the air inlet configuration on W_S

The circulation rates of sample B_{100} using the conventional air inlet configuration are shown in Fig. 6.6. The data present a wider dispersion compared to the operation with the convergent type nozzle under similar conditions (Fig. 6.3.). Besides, considering the standard deviations, W_S remained the same regardless of the value of Q, which is a different behavior from that observed in Fig. 6.3.

The convergent nozzle accelerates the airflow close to the riser inlet and avoids air escape to the annular region. By directing more air towards the riser, it enhances the

feeders' performance. The influence of the air inlet configuration on SB feeder stability has been investigated in previous research (SOUSA et al., 2010) and the use of a reduction nozzle at the air inlet is recommended to direct a major portion of the air jet into the riser.

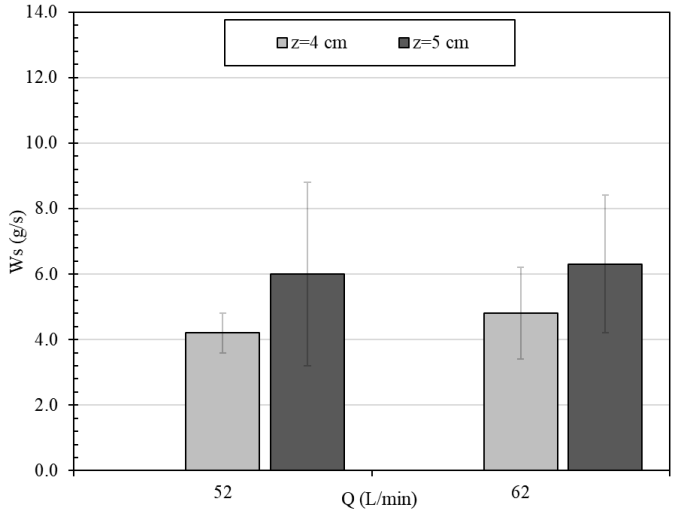

Fig. 6.6. Solids circulation rates of sample B_{100} using the conventional air inlet configuration.

6.4.4. Effect of *Q* and *z* on the pressures around the CFB loop

The pressures as a function of the height of the CFB unit are presented in Fig. 6.7. for sample B_{100} under different *Q* and *z*. Similar patterns are observed in all profiles, as follows: the highest and lowest pressure points are located respectively at the air inlet (IN) and close to the cyclone overflow (CY); a linear decrease in the pressure is observed at the riser section, from taps R2 to R4; and the pressure at the return leg is lower than in the riser, indicating that *Q* is directed mostly towards the riser.

From Fig. 6.3. and Fig. 6.7. the pressures in the feeder and riser increase as W_S rises. It means that more hydrodynamic energy is necessary to maintain the solids circulation in the CFB. The increase in the pressures is particularly evident under *Q*=52 L/min and z=3 and 5 cm, in which the profile of the latter *z* is shifted to the right in Fig. 6.7. The same behavior is observed when *Q* rises from 52 to 62 L/min with *z*=5 cm, however, in

this case, the pressure profile of the whole CFB is shifted to the right due to the presence of more air in the system.

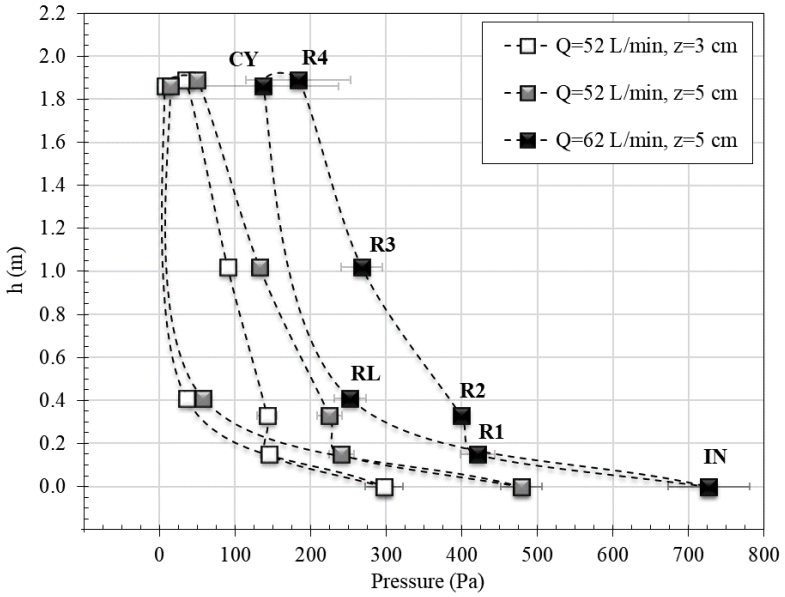

Fig. 6.7. Pressures around the CFB loop for sample B_{100} under different *Q* and *z*.

The pressure around the CFB loop for samples B_{100wet} and $B_{90}C_{10}$ under different *Q* and *z* are presented in Fig. 6.8. and Fig. 6.9., respectively.

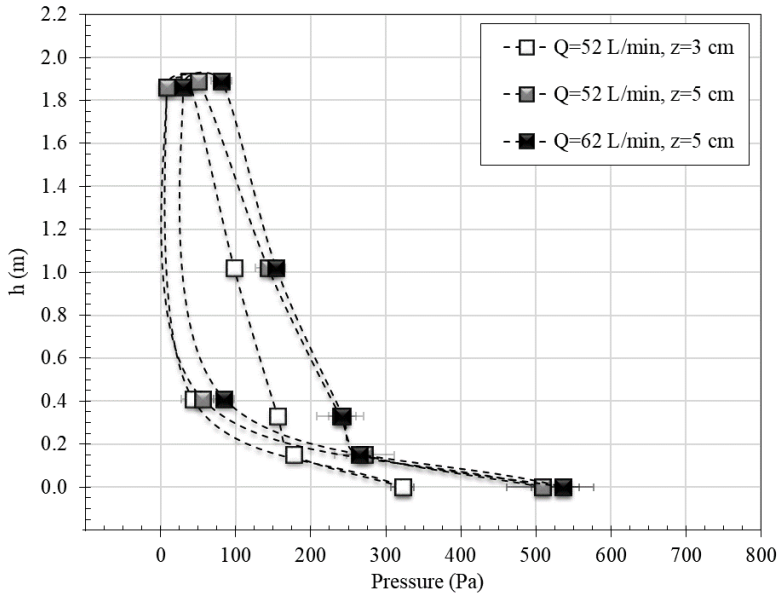

Fig. 6.8. Pressures around the CFB loop for sample B_{100wet} under different *Q* and *z*.

Similar behavior to that described for the assays with sample B_{100} can be observed here. The pressure in the feeder and in the riser are higher for the conditions of higher W_S. Therefore, in Fig. 6.8. and Fig. 6.9. the pressure profile is shifted to the right under *Q*=62

L/min in comparison to Q=52 L/min. Finally, the difference between the pressure values under different conditions in Fig. 6.8. is not as pronounced as observed in Fig. 6.7., because the effect of Q and z on W_S was less significant for the wet powder (see Fig. 6.4.).

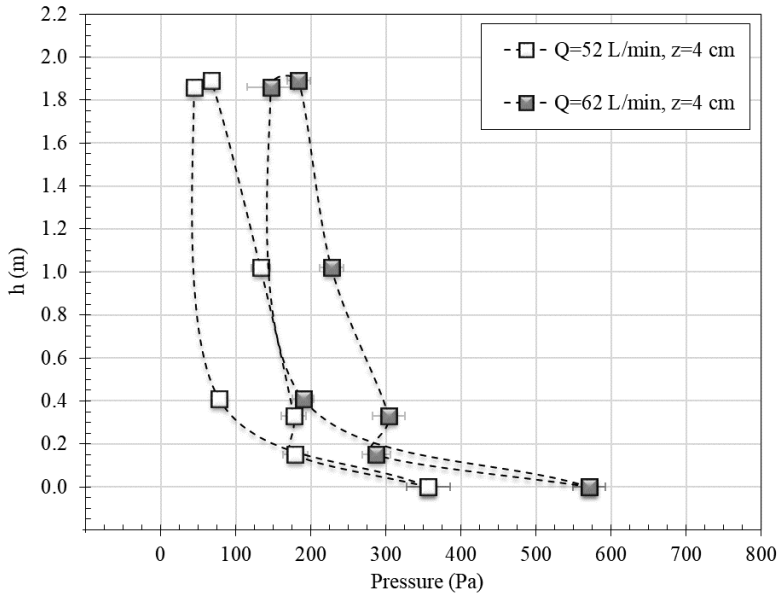

Fig. 6.9. Pressures around the CFB loop for sample $B_{90}C_{10}$ under different Q and z.

6.4.5. Correlations between SCG's circulation rate and pressure drop

As discussed in Section 6.4.4, the pressures throughout the CFB loop are linked to the solids circulation rates. It is common knowledge that in commercial units it is difficult to perform online measurements to monitor the solids flowrates. Hence, reliable correlations based on easily measurable variables might be useful and contribute to enhancing process stability, safety, automation, and performance. The manometric pressures measured at the taps IN and R1 were correlated to SCG's circulation rates, as shown in Fig. 6.10.

Linear equations were fitted from the experimental data accordingly:

$$P_{IN} = 53.60W_S + 167.2 \quad (6.1)$$

$$P_{R1} = 29.99W_S + 74.6 \quad (6.2)$$

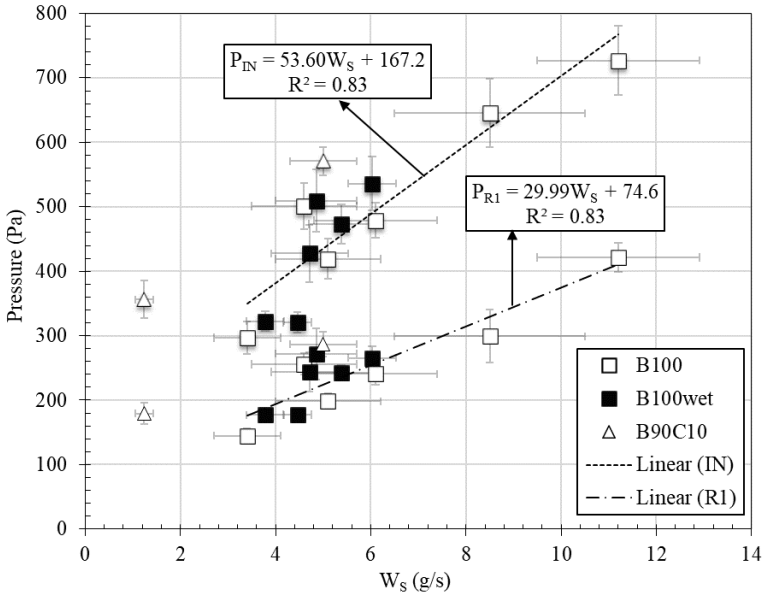

Fig. 6.10. Pressures at the air (P_{IN}) and riser inlet (P_{R1}) versus solids circulation rate.

A regression coefficient of 0.83 was obtained for Eqs. (6.1) and (6.2), and the experimental values differ from the estimated ones by 17% on average, which is within the standard deviations observed in W_S measurements. To improve the fitting, data obtained with sample $B_{90}C_{10}$ were not considered in Eqs. (6.1) and (6.2). The experimental data is randomly distributed around the lines of Eqs. (6.1) and (6.2), which is evidence of non-biased fittings. Therefore, the SCG's circulation rate can be accurately predicted based on pressure measurements carried out either in the feeder or in the riser. From the perspective of process control, this is an interesting result, as it suggests that W_S can be monitored throughout processing based on simple online pressure measurements.

Note that an accurate prediction of W_S with Eqs. (6.1) and (6.2) depends on whether operating conditions and equipment scale are like those investigated here. In our view, a more generalized correlation to be valid for different feeder scales and operating conditions could be proposed only after identifying the effects of some geometric parameters of equipment and powder properties on the feeder performance. Therefore, further research concerning the influence of the SB cone angle, riser diameter, particle-

size distribution, and moisture content on the CFB pressure distribution and W_S would be useful.

6.4.6. Mean voidage in the riser

The mean voidage in the riser section (ε_r) was estimated by:

$$\Delta P_r = \rho_p(1 - \varepsilon_r)g\Delta h_r \quad (6.3)$$

where ΔP_r is the pressure loss in the distance Δh_r measured between taps R1 and R4.

Considering all the assays, the estimated mean voidage in the riser was equal to 0.92±0.02. Based on the air properties (ρ_{air}= 1.283 kg/m^{3,} μ_{air}=0.000018 Pa.s), particle density, and on values of *Q* and *Ws*, it was verified that the CFB riser was operated always under a dilute regime, according to the diagram proposed by Bi and Grace (GRACE; AVIDAN; KNOWLTON, 1997).

6.4.7. Comparison with a non-mechanical L-valve feeding SCGs

In a previous study, a non-mechanical L-valve (LV) has been tested to feed the SCG samples shown in Tab. 6.1 to the same CFB unit of the present study (MASSARO SOUSA; FERREIRA, 2020a). Thus, the performance of both feeders can be compared in terms of solids flowrate range, feeder's pressure drops, and flexibility to handle biomass powders with different properties. The ranges of *Q*, W_S and pressure drops (ΔP) in the LV and SB feeders are shown in Tab. 6.3 for samples B_{100}, B_{100wet}, and $B_{90}C_{10}$.

Tab. 6.3. Ranges for air flowrate, solids rate, and feeders' pressure drop in handling SCGs.

Sample	***Q* (L/min)***		***W*S (g/s)**		***ΔP* (Pa)**	
	LV	SB	LV	SB	LV	SB
B_{100wet}	230 – 250	52 – 62	1.2 - 10.0	3.8 - 6.0	210 – 960	320 – 540
B_{100}	230 – 310	52 – 62	1.7 - 3.8	3.0 - 11.0	230 – 480	300 – 730
$B_{90}C_{10}$	235 – 270	52 – 62	0.6 - 0.7	1.2 - 5.0	110 – 130	360 – 570

*For the L-valve, *Q* is the sum of the aeration and riser inlet air flowrates.

Concerning the overall performance, both feeders were easy to operate and provide reliable feeding of SCG powders into the CFB, with solids flowrate fluctuations less than 20%. Besides, the solids circulation rates could be well-correlated to simple pressure drop measurements in both cases, which is interesting from the process control point of view.

In terms of pressure drop, both feeders operated under ranges of ΔP lower than 1kPa for all the samples, which suggests that they are appealing to be used in commercial applications. However, the SB feeder showed improved performance over the LV in feeding samples B_{100} and $B_{90}C_{10}$, as it provides a wider range of W_S values under lower values of Q. An important advantage of the SB feeder is that W_S can be adjusted by two operating variables (Q and z), while in the L-valve W_S is adjusted only by the air flowrate. Thus, it is easier setting W_S to the desired targets with the SB feeder, especially for the dry samples whose flowability is poorer.

In the case of the wet sample (B_{100wet}), a wider range of W_S was obtained with the L-valve, however, as mentioned in Section 6.4.2, it is possible to rise Q in the SB feeder to increase the solid circulation rates of the wet sample. Thus, both feeders can be considered adequate options for handling the wet SCG powder.

Physical and flow properties of waste biomass powders might change throughout processing. An effective feeder should provide stable solids feeding, with smooth variations in W_S even in situations in which the material's properties change. Based on our results, the SB was more flexible to handle the biomass spent coffee grounds than the L-valve. This is a relevant finding bearing in mind that L-valves have been reported to be more attractive to feed some processing powders to CFBs than other non-mechanical devices, such as the loop seal and J-valves (CHENG et al., 1998; KIM; TACHINO; TSUTSUMI, 2008).

Finally, a couple of points should be highlighted concerning the implementation of SBs in commercial applications, as summarized below.

Differently than other non-mechanical feeders, with the SB the solids are stored in the feeder itself, which may have two implications: i) the handling of solids through units before the reactor might be easier with SBs, since the use of storage silos can be reduced. Consequently, the blockage of the silo's discharge orifice, which is a common drawback when operating with biomass powders, would be avoided; ii) as part of the air flowrate is inevitably dispersed towards the annulus section, it is important to consider the possibility of combustion risks in the vessel for high-temperature processes.

Some future studies aiming at improving the SB feeder performance would be useful to address: i) the effect of some SB design parameters (such as cone angle, air inlet diameter, among others), and ii) the effect of scaling-up the feeder and riser diameters on the performance. The experimental data presented here might be valuable for validation of numerical models, which can be applied to study those geometric parameters and develop scale-up rules in a cost-effective way.

6.5. Conclusions

The non-mechanical SB is a robust feeding device to control the circulation of dry and wet SCG powders ($MC \leq 30\%$ and d_{SV} close to 400 μm) in a CFB unit. The SB can be considered a more flexible alternative for continuous handling of this biomass powder residue when compared to a traditional non-mechanical L-valve. The SCG's circulation rate in the CFB was successfully controlled with the SB, with fluctuations less than 20% in *Ws*. Besides, W_S could be easily set to desired targets by adjusting Q and z, and it can be monitored by simple pressure measurements in the feeder or in the riser as well. We verified that solids' feeding is more stable by using a convergent nozzle at the air inlet

instead of using a conventional orifice air inlet. Also, feeding performance is affected by the powder attributes, thus the samples' flowability properties and moisture level should be considered in designing spouted bed feeders. These findings might be useful to engineers and technicians interested in implementing continuous and effective feeding of SCGs to reactors for renewable energy generation and for fuel production based on biomass residues.

6.6. Acknowledgements

The authors would like to thank the São Paulo Research Foundation (2016/25946-2 and 2018/11031-8), and CAPES (Finance code 001) for financial support.

6.7. Nomenclature

AoR^d	Dynamic angle of repose (˚)
D	Riser diameter (mm)
d_{SV}	Sieve mean diameter (μm)
g	Gravitational constant ($m \cdot s^{-2}$)
H	Riser height (m)
MC	Moisture content (% wet basis)
P_{IN}	Manometric pressure measured at tap IN (Pa)
P_{R1}	Manometric pressure measured at tap R1 (Pa)
Q	Air flowrate ($L \cdot min^{-1}$)
U_{mf}	Minimum fluidization velocity ($m \cdot s^{-1}$)
Ws	Solids flowrate ($g \cdot s^{-1}$)
z	
Greek symbols	
Δh_r	Distance between taps R1 and R4 (m)
ΔP	Feeders' pressure drop (Pa)
ΔPr	Pressure drop in the riser (Pa)
ε_r	Mean voidage in the riser (-)
μ_{air}	Viscosity of the air (Pa·s)
ρ_{air}	Air density ($kg \cdot m^{-3}$)
ρ_p	Particle density ($kg \cdot m^{-3}$)

CAPÍTULO 7 – ALIMENTAÇÃO DE BORRAS DE CAFÉ AO LPC COM LEITO DE JORRO: ANÁLISE VIA CFD

Neste capítulo são apresentados os resultados e discussões referentes à simulação em CFD da alimentação de borra de café B_{100} ao LPC com o alimentador tipo jorro, o que está relacionado aos objetivos específicos (6) e (7) desta tese.

Após uma etapa de calibração dos principais parâmetros relacionados à fricção, colisão e arraste da borra B_{100}, o modelo TFM (*Two-Fluid model*) foi empregado com sucesso para a previsão da fração volumétrica e vazão de sólidos no *riser*, operando com diferentes vazões de ar (Q=52 e 62 L/min) e distância entre o bocal de entrada de ar e o *riser* (z=3, 4 e 5 cm). Os desvios entre os resultados experimentais e simulados foram de até 9%, os quais são menores que os desvios padrões das medidas (iguais a aproximadamente 20%). Após a validação das simulações, novas condições operacionais e geometrias para o sistema foram avaliadas via CFD com o intuito de melhorar a alimentação da borra de café e entender o efeito dessas variáveis sobre a fluidodinâmica do sistema, como: ângulo de cone e enchimento de sólidos no leito de jorro, bem como diâmetro do *riser*.

Em linhas gerais, os resultados mostraram que maiores vazões de sólidos no *riser* são atingidas utilizando-se de maiores vazões de gás, maiores z e maiores enchimentos no alimentador. Além disso, utilizar leitos de jorro com ângulos de cone baixos ou *riser*s com maiores diâmetros também aumenta a vazão de sólidos, o que é atraente para a operação desses alimentadores em reatores de média e grande escala. Detalhes sobre a fluidodinâmica dentro do leito de jorro e no *riser* foram obtidos via CFD, como por exemplo vetores de velocidade e contornos de fração volumétrica, os quais são dificilmente medidos experimentalmente e contribuem para o melhor entendimento da alimentação com o leito de jorro.

Por fim, destaca-se que o modelo validado neste estudo pode ser útil para a implementação de leitos de jorro em LPCs com diferentes escalas com borra de café, bem como pode ser um ponto de partida para estudar a alimentação de pós com diferentes propriedades com o leito de jorro.

Note que as propriedades da borra de café consideradas no modelo numérico foram: diâmetro médio de 400 μm, massa específica aparente de 1120 kg/m³, porosidade do leito de 0,66 e ângulo efetivo de fricção interna de 38,5°. Essas propriedades foram determinadas como mostrado no Capítulo 3.

Os procedimentos experimentais e os resultados das simulações foram apresentados no artigo "*Feeding Spent Coffee Grounds into Reactors: TFM Simulation of a Non-Mechanical Spouted Bed Type Feeder*", reproduzido na íntegra a seguir.

7.1. "Feeding Spent Coffee Grounds into Reactors: TFM Simulation of a Non-Mechanical Spouted Bed Type Feeder"

L. MASSARO SOUSA, M. C. FERREIRA, HOU, Q. F., YU, A. B.

Artigo publicado na Waste Management, volume 109, páginas 161-170, 2020.

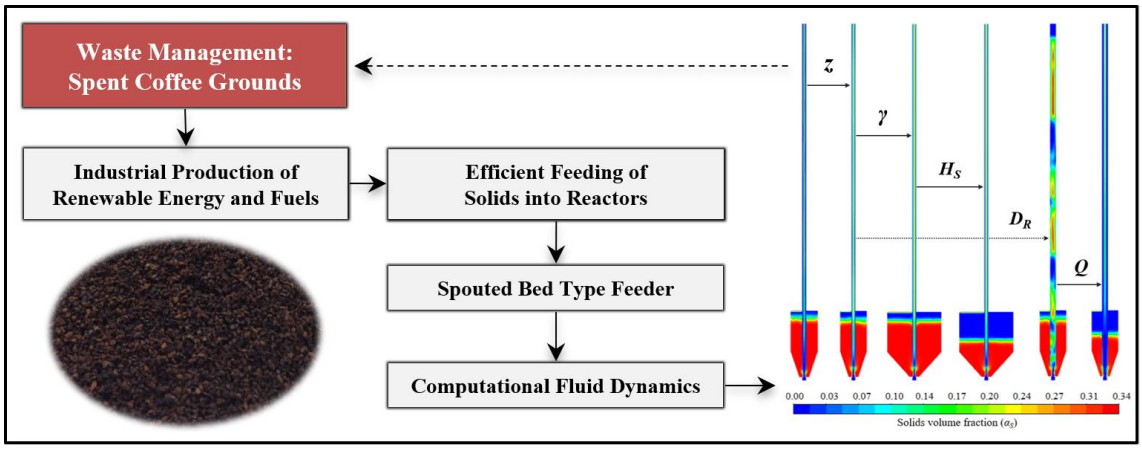

Fig. 7.1. Graphical abstract.

7.1.1. Abstract

Due to the increasing coffee production, Spent Coffee Grounds' (SCGs) generation has grown dramatically, hence appropriate management of this solid biomass waste is imperative. SCGs can be used as feedstocks for renewable energy and fuel generation provided that a stable feeding of powders to reactors is maintained. Recently, a non-mechanical spouted bed feeder proved itself an excellent alternative in feeding SCGs to a pilot-scale circulating fluidized bed reactor. Nonetheless, further studies are necessary for the feeder's implementation in commercial applications. Here the feeding of SCGs with the spouted bed feeder is addressed by using Computational Fluid Dynamics. Firstly, a Two-Fluid Model (TFM) is validated against experimental data, and then the effects of five operating and design parameters were analyzed aiming at improving the handling of SCGs. The solids flowrate (W_S) in the reactor could be stably controlled from 4 to 30 g/s depending on the settings. The feeder performance is enhanced by operating it under high gas flowrate (Q), high entrainment length (z), and high mass of solids in the feeder (H_S). Using feeders with low cone angle (γ) or reactors with large diameter (D_R) increases W_S, which is appealing for the operation of medium-to large-scale units. The proposed TFM is a cost-effective tool for implementing spouted bed feeders in commercial applications. With the feeder coupled to the process, SCGs are treated continuously in the reactor for energy generation, thus reducing the disposal problems associated with this waste and improving the management of SCGs globally.

7.1.2. Introduction

The proper management of Spent Coffee Grounds (SCGs), which is a solid biomass waste originated from brewing coffee powders, has become a challenging problem. Over the last decade, global coffee consumption has increased on average 2.1% annually,

reaching almost 10 million tonnes in 2019 (INTERNATIONAL COFFEE ORGANIZATION, 2019), consequently the generation of SCGs has grown dramatically. If disposed of in landfills without treatment, serious environmental issues may arise due to the high organic load and acidity of this waste (MUSSATTO et al., 2011). Although SCG's generation and disposal are decentralized in the case of residences and cafeterias, almost 50% of the worldwide coffee production is processed for soluble coffee making. It represents more than 2.5 million tonnes of SCGs generated annually, which are readily available for processing in the soluble coffee industry. Thus, improving the management of SCGs in the soluble coffee industry minimizes the damages associated with the improper disposal of this waste globally.

The traditional and economically appealing use for SCGs consists of generating renewable thermal energy in the industry itself. Several successful applications on adding value to SCGs are reported in the literature, as in the production of biofuels and biogas (ATABANI et al., 2019; KARMEE, 2018; KIM et al., 2017), in preparing composite films for food and flowers packaging (THIAGAMANI et al., 2017), in using this waste in composting for organic farming (SANTOS et al., 2017) and so on. These seem to be promising alternatives in managing SCGs collected from decentralized communities and small-to-medium scale food businesses. However, for large-scale processes, SCGs management should be aligned with the company's needs to improve solutions' effectiveness. Like many other large-scale processes, the production of soluble coffee is intensive in thermal energy consumption, particularly to maintain steam and hot air temperatures for the percolation and drying stages, respectively. The attractive high heating value of SCG, which is approximately 25 kJ/kg and similar to that of the coal (SILVA et al., 1998), its low ash content (MUSSATTO et al., 2011), and its availability within the industry are the main reasons to use SCGs as a renewable solid fuel. Through

the combustion of SCGs in reactors, the circular economy concept is fulfilled, and the industrial energy demands are met with environmental awareness.

Feeding waste biomass powders into reactors is commonly the most problematic operation of the entire reactor system (DAI; CUI; GRACE, 2012; RAMÍREZ-GÓMEZ, 2016). In general, waste SCGs have variable particle-size distribution and moisture content due to industrial processing, and depending on the combination of these properties their flowability may vary from *good* to *very poor* (MASSARO SOUSA; FERREIRA, 2019a). Ideal feeding devices to handle such residues should be able to provide stable solids mass flowrate regardless of the particle sizes or moisture content. However, in practice, inefficient or poorly designed feeders provide unstable or no flow of solids to the reactor, compromising the process stability, automation, safety, and performance. Minimizing feeding-related downtimes is key for improving the continuous processing of SCGs. In this way, effective handling of SCGs increases the processing capacity of this waste in existing industrial plants, thus helping to solve the SCGs management problem globally.

Recently, a non-mechanical spouted bed type feeder has proved to be a robust alternative in handling SCGs with different particle-size distributions and moisture contents (MASSARO SOUSA; FERREIRA, 2020b). Apart from that, some papers highlight the successful use of pilot-scale spouted beds to feed glass spheres into circulating fluidized beds with riser diameters of 53-147 mm and 2.8-4.0 m in height from an experimental basis (COSTA; FERREIRA; FREIRE, 2004; FERREIRA; FREIRE, 1992; SOUSA et al., 2010). Unlike mechanical feeders, such as screw and rotary valves, the solids flowrate is pneumatically controlled in the spouted bed, without the need for moving parts. Consequently, the tendency of feeders' blockage by SCGs is low and feeding-related downtimes are minimized with spouted bed feeders. Besides, they are less

expensive than mechanical feeders and might be used under conditions of high pressure and temperature with a reduced risk of wear and fracture, which are attractive characteristics for their implementation in commercial applications.

Nevertheless, design and scale-up rules for spouted bed feeders still need to be evaluated to facilitate their application on a pilot and industrial levels. Using Computational Fluid Dynamics (CFD) is a cost-effective way to meet these needs since there is no need for building various scales and designs of equipment or for gathering resources for the unit's instrumentation. Furthermore, through the simulations, some important information on feeders' operation can be estimated, which are difficult to be measured experimentally, such as solid and air distribution and velocities profiles.

Although some Two-Fluid Model (TFM) framework have been proposed for simulating gas-solid flows in spouted beds with draft tubes (DA ROSA; FREIRE, 2009; DUARTE; MURATA; BARROZO, 2008; HOSSEINI, 2016; HOSSEINI; ZIVDAR; RAHIMI, 2009; SZAFRAN; KMIEC; LUDWIG, 2005; VIEIRA NETO et al., 2008), both the apparatus and the type of powders investigated here are inherently different to those of previous studies, which results in a hydrodynamics that has not been assessed yet. Therefore, this study aims to fill some gaps in knowledge concerning the simulation of:

i) spouted beds for the feeding of solids to reactors, which results in a system with combined characteristics of spouted bed and pneumatic transport (CHENG et al., 1998; FERREIRA; FREIRE, 1992);

ii) riser-coupled solids feeder, since the hydrodynamic at the riser strongly depend on the inlet configuration (CHENG et al., 1998; KIM; TACHINO; TSUTSUMI, 2008);

iii) the feeding of waste biomass powders with TFM, whose particle and flow properties differ significantly from those of previous studies, such as glass beads, soybeans, and millets.

In this paper, first a Two-Fluid Model is proposed and validated to describe the feeding of SCGs into a pilot-scale reactor with a spouted bed type device. The model is used to study some design and operating variables for the feeder aiming at improving the handling of SCGs. The findings are of potential use to solid waste researchers and practitioners aiming at effective handling of SCGs and provide useful guidance for studying biomass materials with different materials properties. The validated model is a useful tool for further scale-up studies concerning spouted beds feeders with SCGs.

7.1.3. Methodology

7.1.3.1. Experimental settings

The feeding experiments were performed on the cold flow circulating fluidized bed (CFB) unit shown in Fig. 7.2a. The solids stored in the non-mechanical spouted bed feeder (1) are transported to the riser (3) by inserting air at the bottom inlet (2). When reaching the top of the riser, the solids are returned to the spouted bed by an inclined separator (4), a cyclone (5) and a return leg (7), thus completing the circulation loop in the system. In combustion and gasification operations, the solid fuel reacts with hot gas at the riser section, and the produced gases leave the process to other units through the cyclone overflow.

The system has an overall height of 2 m and a riser internal diameter of 0.021 m. It is entirely built of stainless steel except for the spouted bed feeder detailed in Fig. 7.2b, which is made of galvanized iron with a convergent cone nozzle at the air inlet. The air flowrate (Q) and the distance between the air inlet and the bottom end of the riser (z) are

the two operating variables used to control the solids flowrate (W_S) to the reactor with the spouted bed feeder. These variables can be easily adjusted during operation to meet the desired W_S.

In a previous experimental study, the effects of Q and z on the riser solids holdup and on W_S were analysed under two different Q equal to 52 and 62 L/min (8.67×10^{-4} and 1.03×10^{-3} m³/s) and three different z equal to 3, 4, and 5 cm (MASSARO SOUSA; FERREIRA, 2020b). These experimental data are used here to validate the proposed numerical model. The higher limit for Q was set to avoid loss of powders at the cyclone overflow, whereas the lower limit corresponds to the minimum air flowrate that provided a stable solids flowrate in the riser. Note that pulsating unsteady transport of SCGs in this system started at Q=38 L/min (6.33×10^{-4} m³/s).

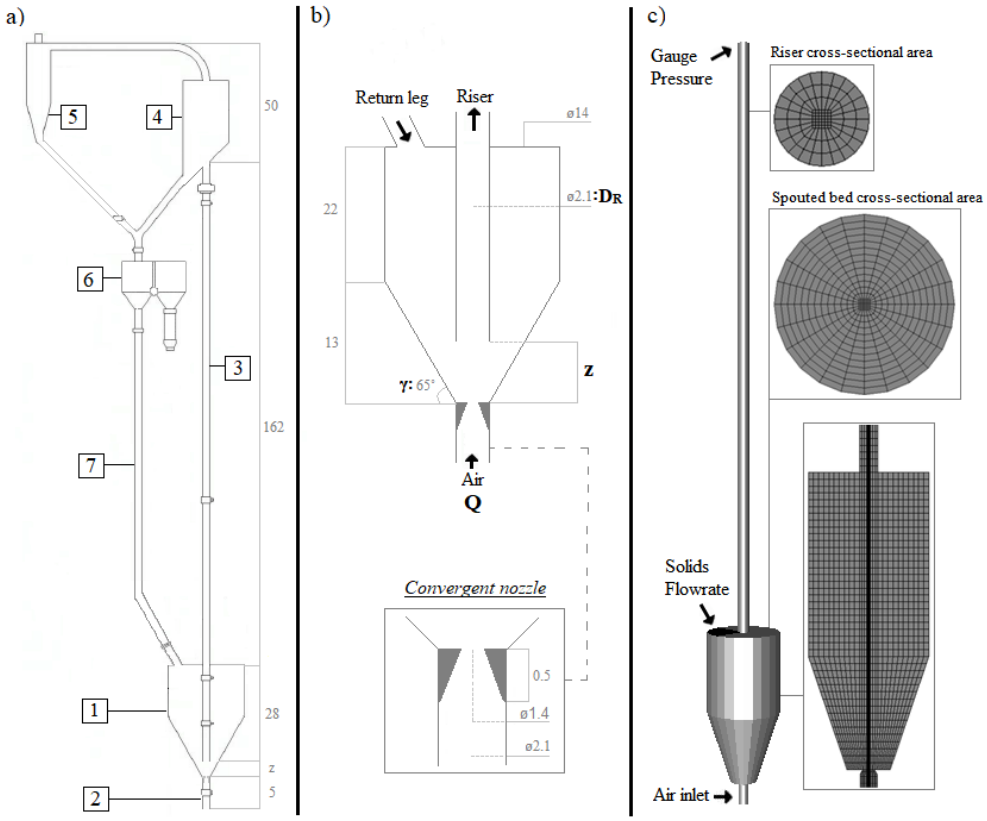

Fig. 7.2. Circulating fluidized bed unit. a) parts of the experimental unit, b) spouted bed feeder, and c) 3D mesh used in the simulations. All dimensions in cm.

7.1.3.2. Numerical model

The governing equations and the associate constitutive models are shown in Tab. 7.1. In this Euler-Euler multiphase model, the gas and solid phases are treated as interpenetrating continua with the properties of the solid described by the Kinetic Theory of Granular Flow (KTGF).

The continuity and momentum conservation equations for gas and solid phases are shown in Eqs. (7.1) to (7.5). The granular temperature for the solid phase (θ_s) is introduced by the KTGF, and it is proportional to the kinetic energy of the particles' random motion. The transport equation for θ_s is shown in Eq. (7.6), and the solid's pressure and viscosity are calculated based on the granular temperature in Eqs. (7.7) and (7.8), respectively.

The collisional, kinetic and frictional components of the solids shear viscosity are described in Eqs (7.9) to (7.11). The frictional part is added to the calculation only when the solids volume fraction exceeds the friction packing limit. The solid-wall interaction is considered by using Eq. (7.16). The turbulence model used was the standard k-ε dispersed model with a standard treatment near the wall. The same set of equations has been recently used to simulate the feeding of SCGs to the atmosphere with an L-valve type feeder (MASSARO SOUSA et al., 2020).

In terms of model inputs, the SCG properties considered are as follows: mean diameter (d_s) of 0.0004 m, particle density (ρ_s) of 1,120 kg/m^3, packing density ($\alpha_{s,max}$) of 0.34, and angle of internal friction (ϕ) of 38.5°. These values match measured SCG properties, and the characterization methods are described elsewhere (MASSARO SOUSA; FERREIRA, 2019a, 2019b).

Tab. 7.1. Numerical model.

Description	Equations	Eq.
Continuity for fluid (f) and solid (s) phase	$\frac{\partial}{\partial t}(\alpha_f \rho_f) + \nabla \cdot (\alpha_f \rho_f v_f) = 0$	(7.1)
	$\frac{\partial}{\partial t}(\alpha_s \rho_s) + \nabla \cdot (\alpha_s \rho_s v_s) = 0$	(7.2)
	$\alpha_f + \alpha_s = 1$	(7.3)
Momentum for fluid and solid phase	$\frac{\partial}{\partial t}(\alpha_f \rho_f v_f) + \nabla \cdot (\alpha_f \rho_f v_f v_f) = -\alpha_f \nabla p + \nabla . \tau_f + \alpha_f \rho_f g + K_{fs}(v_f - v_s)$	(7.4)
	$\frac{\partial}{\partial t}(\alpha_s \rho_s v_s) + \nabla \cdot (\alpha_s \rho_s v_s v_s) = -\alpha_s \nabla p - \nabla p_s + \nabla . \tau_s + \alpha_s \rho_s g - K_{fs}(v_f - v_s)$	(7.5)
Granular temperature	$\frac{3}{2}\left[\frac{\partial}{\partial t}(\rho_s \alpha_s \theta_s) + \nabla \cdot (\rho_s \alpha_s v_s \theta_s)\right] = (-p_s I + \tau_s) : \nabla v_s + \nabla \cdot (k_{\theta_s} \nabla \theta_s) - \gamma_{\theta_s} - 3K_{fs}\theta_s$	(7.6)
Solid pressure	$p_s = \alpha_s \rho_s \theta_s + 2\rho_s(1+RC)\alpha_s{}^2 g_{0,ss}\theta_s$	(7.7)
Solid shear viscosity	$\mu_s = \mu_{s,col} + \mu_{s,kin} + \mu_{s,fr}$	(7.8)
Collisional viscosity	$\mu_{s,col} = \frac{4}{5}\alpha_s \rho_s d_s g_{0,ss}(1+RC)\left(\frac{\theta_s}{\pi}\right)^{\frac{1}{2}}$	(7.9)
Kinetic viscosity	$\mu_{s,kin} = \frac{10\rho_s d_s \sqrt{\theta_s \pi}}{96\alpha_s(1+RC)g_{0,ss}}\left[1 + \frac{4}{5}g_{0,ss}\alpha_s(1+RC)\right]^2$	(7.10)
Frictional viscosity	$\mu_{s,fr} = \frac{p_s \, sen\, \phi}{2\sqrt{I_{2D}}}$	(7.11)
Solid bulk viscosity	$\lambda_s = \frac{4}{3}\alpha_s \rho_s d_s g_{0,ss}(1+RC)\left(\frac{\theta_s}{\pi}\right)^{\frac{1}{2}}$	(7.12)
Diffusion of granular energy	$k_{\theta_s} = \frac{150\rho_s d_s \sqrt{(\theta_s \pi)}}{384(1+RC)g_{0,ss}}\left[1 + \frac{6}{5}\alpha_s g_{0,ss}(1+RC)\right]^2 + 2\alpha_s{}^2 \rho_s d_s (1+RC) g_{0,ss}\sqrt{\frac{\theta_s}{\pi}}$	(7.13)
Collisional energy	$\gamma_{\theta_s} = \frac{12(1-RC^2)g_{0,ss}}{d_s\sqrt{\pi}}\rho_s \alpha_s{}^2 \theta_s{}^{\frac{3}{2}}$	(7.14)
Radial distribution	$g_{0,ss} = \left(1 - \frac{\alpha_s}{\alpha_{s,max}}\right)^{-2,5\alpha_{s,max}}$	(7.15)
Solid-wall interaction	$v_{s,w} = -\frac{6\alpha_{s,max}\mu_s}{\sqrt{3}\sqrt{\theta_s}\pi\rho_s\alpha_s g_{0,ss} SC}\frac{\partial v_{s,w}}{\partial n}$	(7.16)

In this study, the contributions of drag, friction and collision forces in the gas-solid flow are accounted for by means of the restitution coefficient (RC), specularity coefficient (SC), friction packing limit (FPL), angle of internal friction (ø), and drag models. A dedicated section for parameter analysis and selection is presented in the paper (Section 7.1.4.1.).

7.1.3.3. Simulation settings

The simulations were performed with the grid shown in Fig. 7.2c. It consists of a 3D computational mesh structured with 36,996 hexahedral elements, containing an air inlet, a spouted bed feeder, and a riser with the same dimensions of the experimental CFB unit. A mean refinement factor of 1.25 cells/cm was used for both radial and axial directions, after comparing the simulated results with finer meshes of 2.5 and 5.0 cells/cm (see Section 7.1.4.1.).

The simulation procedure consisted of setting the distance between the air inlet and the bottom end of the riser (z) to 3, 4 or 5 cm, and on packing 1.4 kg of SCGs at the spouted bed with α_s=0.34. At the bottom of the feeder, the air flowrate (Q) was set to 52 or 62 L/min. The boundary conditions at the top of riser and spouted bed (return leg) were set, respectively, as pressure outlet and solids flowrate inlet, with the experimental values as inputs (MASSARO SOUSA; FERREIRA, 2020b). From previous simulations, it was verified that the value of solids flowrate at the return leg do not affect significantly the calculated steady-state W_S in the riser. Therefore, solids flowrate was kept constant at the return leg throughout simulation for model simplicity.

The solids flowrate and solids fraction in the riser were averaged over 10 s of simulation after achieving the steady state, and the mean values are reported with the standard deviation.

After validating the numerical model against experimental data, new feeder and riser designs and operating conditions were tested aiming at improving the feeding performance of SCGs. The spouted bed cone angle (γ) was decreased from 65 to 55, 45 and 35˚, while the riser diameter (D_R) was increased from 2.1 to 2.6, 3.1 and 4.2 cm. Finally, different mass of solids was packed at the spouted bed (1.4, 2.8, 4.2, and 5.6 kg) and the effect of the initial solids inventory (H_S) on solids flowrate is investigated.

The commercial software Fluent 17.1 (Ansys Inc., Pennsylvania, USA) was used in the simulations, with the equations solved for the transient regime with integration steps of 10^{-3} s. The relaxation parameters for the momentum and volumetric fraction equations were fixed as 0.4 and 0.5, respectively, and the convergence criterion adopted for all the variables was 10^{-3}.

7.1.4. Results and Discussion

7.1.4.1. Parameter selection for SCGs

In this section, the effects of some model parameters (RC, SC, FPL, ø, and drag models) on solids flowrate are investigated. The agreement between experimental and simulated W_S for assay with Q=62 L/min and z=4 cm is used to show an appropriate combination of parameters for describing the feeding of SCGs with the spouted bed type feeder. The chosen value for each parameter is marked with a white star in Fig. 7.3.

It is worth noting that a parameter selection is necessary, in this case, to calibrate empirical constitutive equations of the numerical Two-Fluid model (see the closure equations in Tab. 7.1) with the characteristics of the biomass solid material.

The effect of the mesh refinement is shown in Fig. 7.3a. The W_S results are not statistically different among the meshes according to a two-way analysis of variance based on Tukey's test with a significance level <0.05. Thus, the mesh with 36,996 elements was selected for the simulations to achieve a compromise between accuracy and computation cost.

An overview of Fig. 7.3. shows that W_S is mainly affected by the values of RC, ø, and FPL (Fig. 7.3b-d), with values for W_S ranging from 5.0 to 15 g/s depending on the parameters values, while using either different drag models or SC at the riser section resulted in similar W_S (Fig. 7.3e-f) regardless of the parameter value or model. Therefore,

for model simplicity, the Gidaspow drag model and a medium-range specularity coefficient (SC=0.50) were selected. A detailed analysis on the selection of the values for RC, ø, and FPL is shown below.

The restitution coefficient accounts for the momentum dissipation due to particle-particle collision and is considered on the calculation of the kinetic and collisional viscosities (Eqs. 7.8 and 7.9). Since RC is difficult to be measured experimentally for residue-based powders (MASSARO SOUSA et al., 2020; MOLINER et al., 2019), a value of RC=0.9999 was used in the simulations as it gives a better match with the experimental data. From the simulations, it was verified that decreasing the restitution coefficient below 0.98 results in a dense transport of solids in the riser with solids fraction around 0.30, which is not the expected behavior from the experiments. By increasing RC over 0.99, a pneumatic conveying regime is achieved, and with RC=0.9999 *Ws* could be predicted quantitatively, as shown in Fig. 7.3b. Note that values of RC in the range of 0.90 to 0.99 have been commonly reported in the literature for describing the hydrodynamics of spouted beds operating with different materials, such as glass beads, soybean, silica sands and millets (DUARTE; MURATA; BARROZO, 2008; GUJJULA; MANGADODDY, 2015; HOOSHDARAN et al., 2017; HOSSEINI, 2016; HOSSEINI; ZIVDAR; RAHIMI, 2009; VIEIRA NETO et al., 2008).

On the other hand, ø and FPL are the parameters that calibrate the stress generation due to friction, which is considered in the simulation only in the regions that the solids volume fraction exceeds FPL. The solids flowrate is accurately predicted for FPL lower than 0.25 and a sharp increase in W_S is observed above this value (Fig. 7.3d), thus FPL=0.20 was selected. Besides, increasing ø increases the frictional contribution via Eq. 7.11 which in turn decreases W_S in Fig. 7.3c. Using the measured angle of internal friction for the SCG sample (ø=38.5°) overestimates W_S (Fig. 7.3c), which may be due to an

inaccuracy of the frictional model to predict $\mu_{s,fr}$ when extrapolated to samples with unconventional properties in terms of particle-size distribution, shape, and cohesion, as pointed out in previous studies (GHADIRIAN; ARASTOOPOUR, 2017; HOU et al., 2019; WANG et al., 2016a, 2016b). This drawback was trespassed empirically in this study by setting ø at 55°, which is the value that matches the experimental data at Q=62 L/min and z=4 cm. Under lower air flowrates the stress generated due to friction might be higher, therefore ø=80° was used in the simulations under Q=52 L/min.

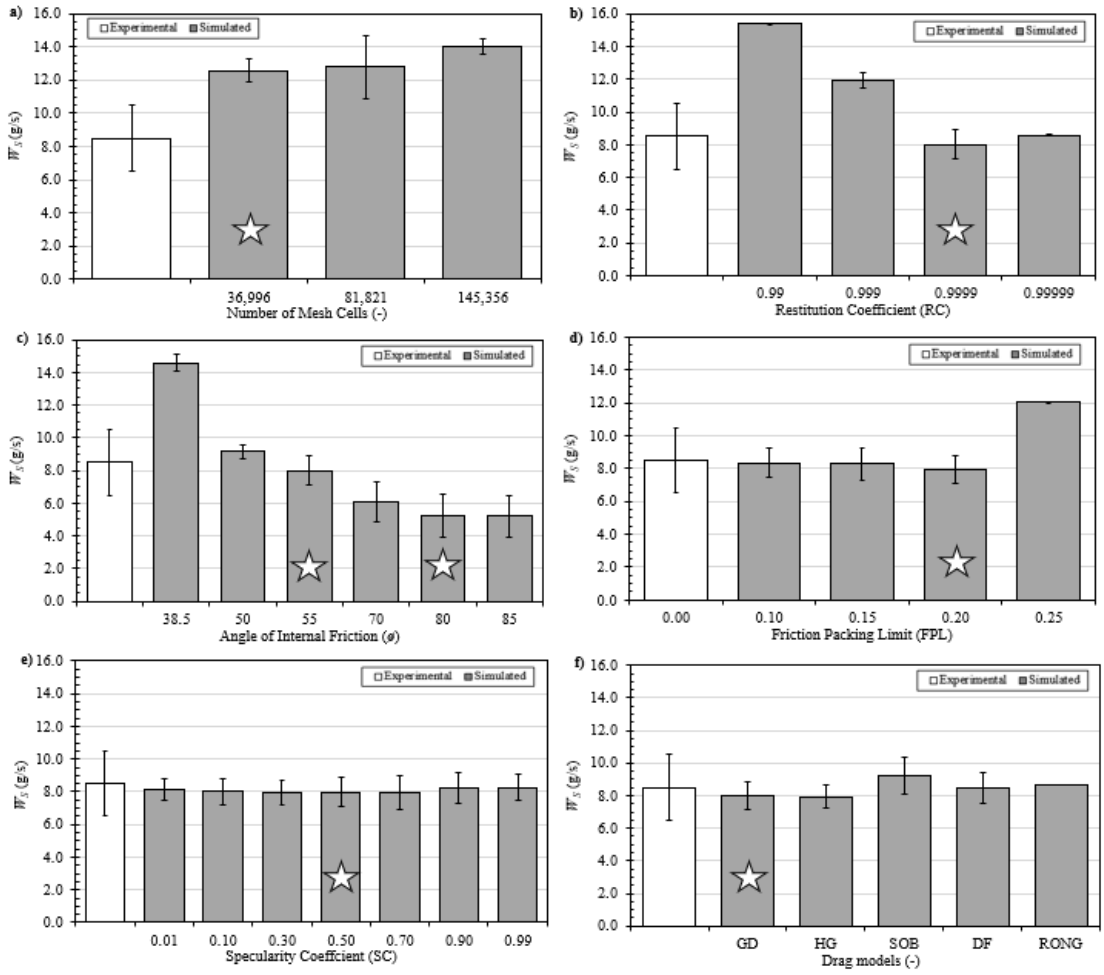

Fig. 7.3. Simulated W_S for different a) number of mesh cells, b) restitution coefficient, c) angle of internal friction, d) friction packing limit, e) specularity coefficient, and f) drag models with Q=62 L/min and z=4 cm.

In the next section, simulations under different Q and z are performed and the results are compared to experimental data aiming at validating the proposed numerical model.

7.1.4.2. Effects of the air flowrate (Q) and entrainment length (z) on W_S

The solids flowrates under different Q and z are accurately predicted by the simulations, as shown in Fig. 7.4. The mean relative difference between simulated and experimental W_S is 9%, which is lower than the experimental measurement deviation (±20%). Also, the simulated solids holdup in the riser (α_s of 0.06±0.02), calculated as the average and standard deviation among all assays, is in accordance with the experimental value of 0.08±0.02. The previous comments highlight that the proposed CFD framework is appropriate for predicting the feeding of SCGs with a spouted bed operating under different conditions. Note that the error bars shown in Fig. 7.4. represents the fluctuations of W_S when the feeder is operating under a steady-state regime. The mean value and standard deviation of W_S were calculated at the top outlet riser section during 10 s of simulation.

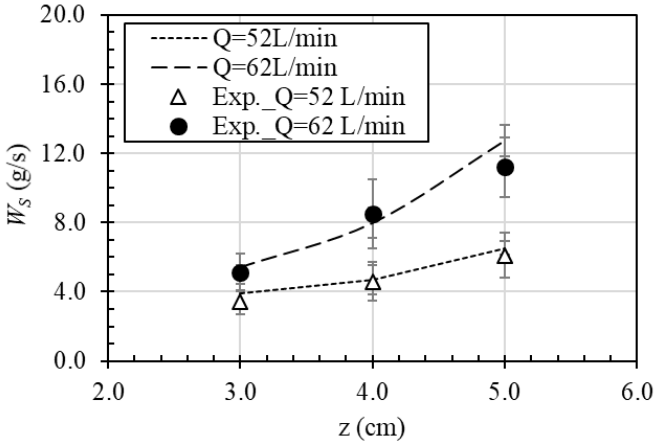

Fig. 7.4. Simulated (dashed line) and experimental (point) W_S for different Q and z.

Besides, it is shown in Fig. 7.4. that W_S rises by increasing Q and z. This is because both the gas phase momentum and the gas-solid contact area at the spouted bed bottom are enhanced under higher values of Q and z (MASSARO SOUSA; FERREIRA, 2020b). As Q and z are parameters that can be easily adjusted during processing, the solids flowrate to the reactor can be controlled and set to desired targets. In practice, it means that higher quantities of SCGs can be treated in the reactor by operating the system under

high Q and z, hence minimizing the disposal problems associated with this solid waste. In the next sections, other operating and design parameters for the system are investigated aiming at improving the feeding of SCGs into the reactor.

7.1.4.3. Effects of the cone angle (γ) and initial solids inventory (H_S) on W_S

The solids flowrate increases with decreasing cone angle (Fig. 7.5a), and with increasing solids inventory (Fig. 7.5b) because more solids are stored into the spouted bed under these conditions, hence improving feeder's sealing and performance.

For the set of simulations shown in Fig. 7.5a, H_S was packed with 84% of the total feeder volume, and the cone angle was decreased from 65 to 35° by increasing the diameter of the cylindrical part of the spouted bed with the height of the conical section fixed at 13 cm (see Fig. 7.2b). It means that feeders with lower γ are bigger and have more powders stored inside the vessel. Consequently, the packed bed resistance at the spouted bed is enhanced under lower γ and the gas-solid recirculation at the conical section is reduced. Thus, the gas and solid flows are directed mainly towards the riser, which in turn increases W_S.

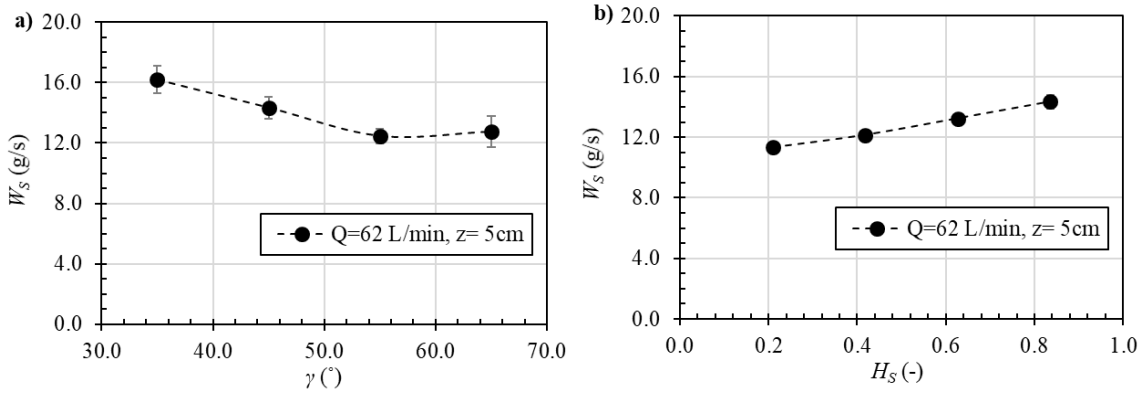

Fig. 7.5. Simulated W_S for different a) spouted bed cone angles, and b) initial solids inventory in the spouted bed, with γ=45°.

To investigate the effect of the initial height of solids on W_S, additional simulations were performed under γ=45° with different H_S, as shown in Fig. 7.5b. The solids flowrate

decreases linearly as H_S decreases, with a reduction of 21% in W_S in the interval tested. From the operation point of view, it means that, if possible, spouted bed feeders should be operated with high quantity of solids stored in the vessel so that feeder's design potential can be used. Therefore, using high H_S is recommended for improved feeder performance.

In summary, more SCGs can be treated at the reactor by using spouted bed feeders with lower cone angles and by operating them with high H_S. Also, decreasing the cone angle might be an appealing strategy to implement spouted bed feeders in larger-scale applications, as more powders can be stored into the feeder with similar W_S. It is worth noting that using spouted bed feeders can also have a positive impact on reducing the need for silos and storages in industries, as a considerable amount of solids can be stored within the feeder.

7.1.4.4. Effect of the riser diameter (D_R) on W_S

In commercial applications, the internal diameter of the reactor is usually prefixed, and the feeder is projected to meet the solids flowrate and solids holdup requirements. In this section, the spouted bed performance is assessed in feeding SCGs to risers with higher internal diameters: 2.6, 3.1, and 4.2 cm. For this analysis, the geometric and operating parameters selected were the ones that provide the highest W_S for the feeder shown in Fig. 7.2.: γ=65˚, z=5 cm, H_S=0.84 and initially Q=62 L/min. The results for the solids flowrate, solids velocity, and solids holdup at the riser are shown in Fig. 7.6.

The solids flowrate decreases as D_R increases when Q is fixed at 62 L/min (black circles, Fig. 7.6a). The larger D_R the greater the internal volume of the riser, hence more solids are initially dragged in when Q is turned on. Consequently, more hydrodynamic energy is necessary to transport the solids upwards, however as Q is fixed at 62 L/min,

the transport is slower and denser as evidenced by the increase in α_s (black circles, Fig. 7.6c) and the decrease in v_s (black circles, Fig. 7.6b). Also, it can be observed that the transport of solids is more unstable and with higher standard deviations in W_S, as shown in the results for D_R of 2.6 and 3.1 cm. At the limit, no flow of solids occurs through the riser, as in the case of D_R=4.2 cm that W_S equals to 0 g/s.

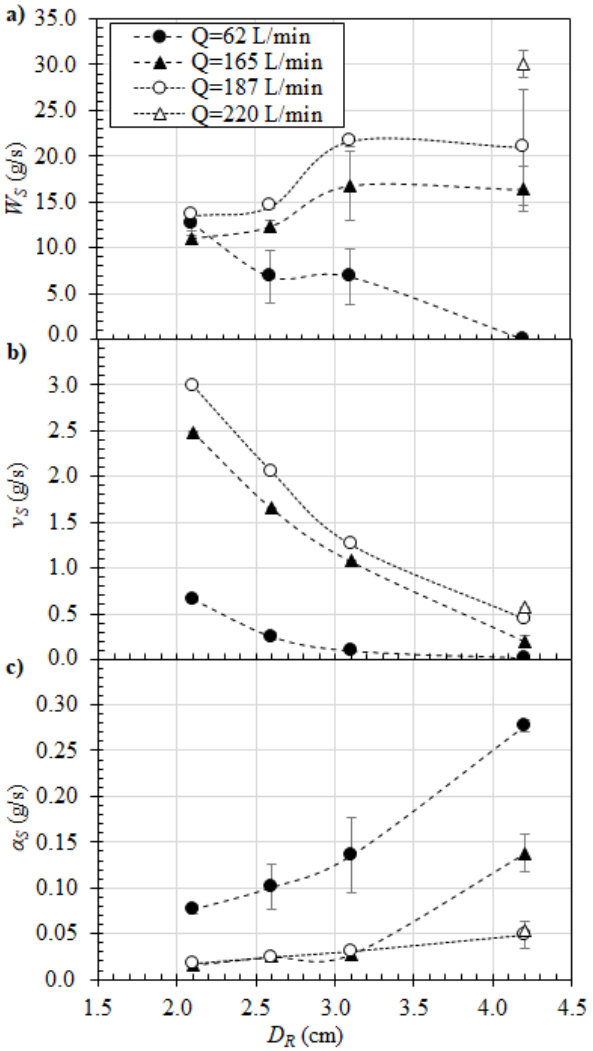

Fig. 7.6. Simulated results for different riser diameters and air flowrates: a) solids flowrate, b) solids velocity, and c) solids fraction in the riser.

Considering the above observation, additional simulations were performed using higher gas flowrates. By increasing Q from 62 to 165 L/min, v_s increases (black triangles, Fig. 7.6b) and α_s decreases (black triangles, Fig. 7.6c), because additional hydrodynamic energy is added to the system which promotes the transport of solids for all D_R tested, as

shown in Fig. 7.6a. Therefore, it means that there is a threshold air flowrate to initiate the transport of solids which is dependent on D_R. After trespassing this threshold value, further increment in Q increases W_S, until the solids flowrate stabilizes at a very dilute pneumatic conveying regime (α_s<0.05). Note that the maximum W_S for D_R=2.1, 2.6, 3.1, and 4.2 cm occurs at around Q=62, 165, 187, and 220 L/min, respectively, which is the upper limit of the feeders' operating range.

Moreover, the magnitude of W_S increases with increasing D_R because it is easier to feed solids into risers with wider opening areas. For example, for D_R=4.2 cm stable solids flowrate ranged from 15 to 30 g/s (Fig. 7.6a), while the interval for W_S with D_R=2.1 cm is within 6 and 14 g/s (Fig. 7.4. and Fig. 7.6a). These findings highlight that the spouted bed feeder performance is dependent on the reactor geometry, and that they can be successfully implemented in larger-scale processes that have different reactor diameters. In this case, adequate gas flowrate operating ranges must be used to provide stable flow of solids in the reactor.

In summary, the spouted bed feeder promoted stable feeding of SCGs into risers of different internal diameters. The larger D_R, the greater the solids flowrate in the reactor, which is appealing for improving SCGs management in larger-scale units. Also, to avoid feeders' malfunction and to save energy, the feeder should be operated with Q between the threshold value and the pneumatic conveying condition, which are the limits for the feeder's operating range. Note that these limits for Q were identified by the simulation framework proposed here.

7.1.4.5. Solids and air flow profiles for different operating and design conditions

In the previous sections, the effects of five operational and design parameters (Q, z, H_S, D_R, and γ) were analyzed aiming at the effective handling of SCGs. Here the general

flow behavior for each system is presented using the simulated profiles of SCGs volume fraction (Fig. 7.7.).

The effect of increasing *z* is shown in Fig. 7.7a to Fig. 7.7b. With *z*=5 cm, there is greater transport of solids in the riser due to 1) the longer channel formed at the spouted bed bottom that promotes improved gas-solid contact, hence dragging more solids into the riser, and 2) the displacement of the central tube edge effect farther from the air inlet, compared to the simulations with *z*=3 cm.

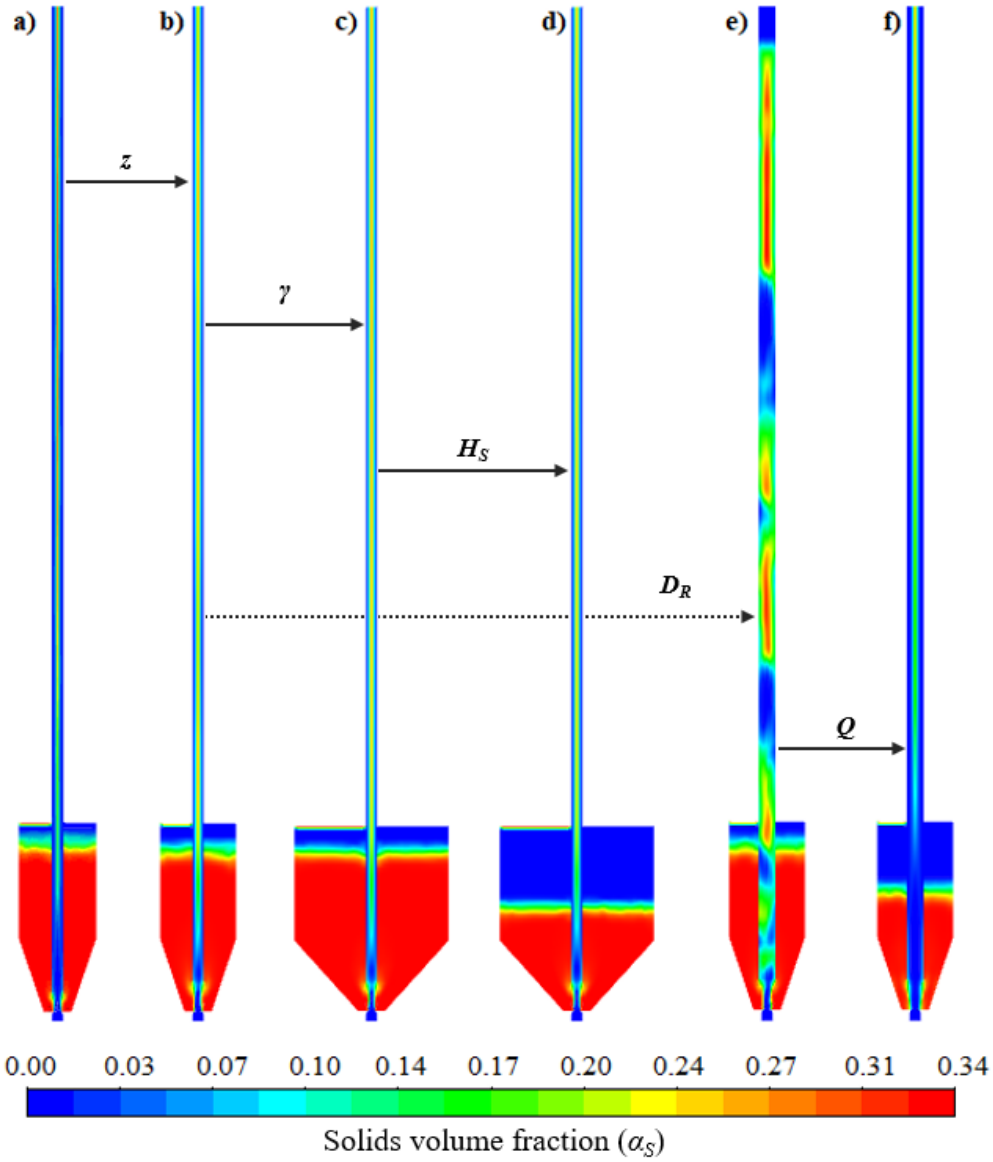

Fig. 7.7. Contours of SCGs fraction in the riser and feeder under different operating conditions and geometric factors. The conditions are fixed in all the maps as Q=62 L/min, z=5 cm, H_S=0.84, D_R=2.1 cm, and γ=65° unless otherwise stated: a) z=3 cm, b) z=5cm, c) γ=45°, d) H_S=0.42, e) D_R= 3.1 cm, and f) Q=187 L/min.

The effect of increasing γ is depicted in Fig. 7.7b and Fig. 7.7c. Both profiles are qualitatively similar with a homogeneous distribution of solids at the axial and radial directions, however using lower γ allows allocating more solids into the feeder, which might be interesting for larger-scale applications, as previously mentioned in Section 7.1.4.3. Nonetheless, decreasing H_S worsens feeder performance as evidenced by the more dilute transport of solids at the riser in Fig. 7.7d compared to Fig. 7.7c.

The effect of increasing D_R alone can be observed by comparing Fig. 7.7b with Fig. 7.7e. Although the qualitative behavior inside the feeder is similar to different D_R, the transport of solids at the riser is more unstable and in the form of denser plugs with D_R=3.1 cm and Q=62 L/min. On average, this causes lower values for W_S with higher fluctuations compared to D_R=2.1 cm, as commented in Section 7.1.4.4. By increasing Q (Fig. 7.7f), not only the transport of solids in the riser becomes diluted and stabilized again, but also W_S increases until the upper operating limit of the feeder is reached.

The general behavior for air and solids velocities under stable, steady-state operation are presented in Fig. 7.8. The vectors in Fig. 7.8a indicate that the flow of solids is mainly directed downwards by gravity, and that there is no formation of dead zones in the feeder. From the contours, the solids enter the riser predominantly at the upper parts of the cone (in this case, close to z=5 cm), whereas less amount of SCGs start the upward transport from the spouted bed bottom. At the riser, the core-annulus effect is observed with higher solid velocities at the center of the tube.

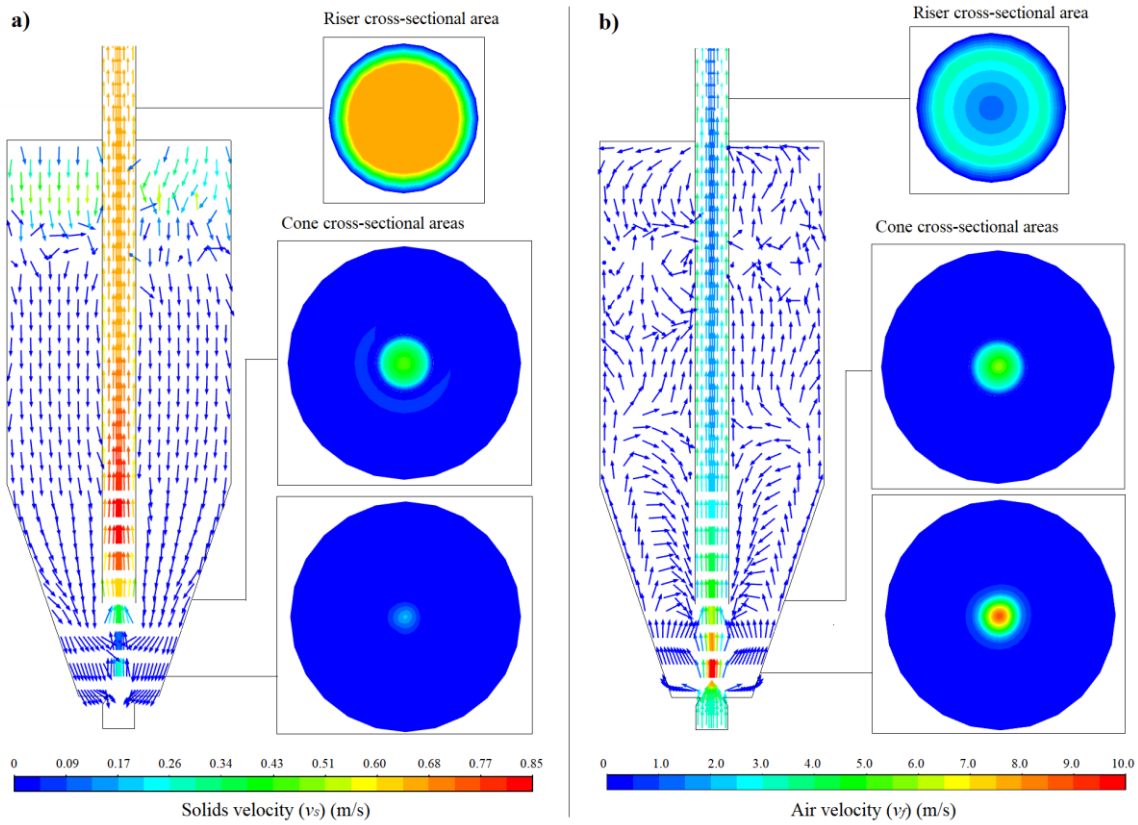

Fig. 7.8. Vectors and radial contours of SCGs and air velocities at the feeder and riser. Extracted from simulation under Q=62 L/min, z=5 cm, D_R= 2.1 cm, γ=65°, and H_S=0.84.

From the vectors in Fig. 7.8b, the gas flowrate is mainly directed to the riser section, which is a consequence of using a convergent nozzle at the air inlet (MASSARO SOUSA; FERREIRA, 2020b). Also, there is an air recirculation zone at the conical section that contributes to direct the solids to the riser. Finally, as the gas momentum is transferred for solids transport, the air velocities decrease from the riser bottom to its upper parts, as shown in the contours of Fig. 7.8b.

7.1.4.6. General equations for the feeding of SCG with spouted beds

In this section, the average effect of the five investigated parameters on W_S is presented in a quantitative way through equations derived from the simulated data shown in Fig. 7.4 to Fig. 7.6. The aim is to provide a quick estimative of W_S in case of variations in z, D_R, Q, H_S and γ:

$$\Delta W_S/\Delta z = 3.40 \quad (7.17)$$

$$\Delta W_S/\Delta D_R = 6.90 \quad (7.18)$$

$$\Delta W_S/\Delta Q = 0.25 \quad (7.19)$$

$$\Delta W_S/\Delta H_S = 4.80 \quad (7.20)$$

$$\Delta W_S/\Delta \gamma = -0.12 \quad (7.21)$$

Linear equations fitted the experimental data accordingly with R^2 higher than 0.90, and indicating no fitting bias, as data is randomly distributed throughout the fittings.

As shown in Eqs. (7.17) to (7.21), higher W_S are obtained by increasing z, D_R, Q and H_S, as well as by decreasing γ. For example, increasing z in 1 cm or Q in 10 L/min, increases SCGs flowrate generally by 3.4 and 2.5 g/s, respectively, whereas decreasing γ in 10° rises W_S by around 1.2 g/s. Besides, while a decrease in H_S by 0.21 decreases W_S by 1.0 g/s, feeding SCGs to 2 cm wider diameter risers increases W_S by 13.8 g/s, provided that an appropriate gas flowrate for stable, steady solids transport in the riser is used (Section 7.1.4.4.). Although Eqs. (7.17) to (7.21) are inherently valid for the system presented here, and in the range of parameter values studied, they might also be useful for comparative purposes of further scale-up and optimization studies concerning the feeding of powders with spouted bed feeders.

7.1.5. Conclusions

The validated numerical model is a reliable and cost-effective tool to address the feeding of SCGs to CFB risers with a spouted bed type feeder. It is useful to promote effective handling of SCGs into reactors, hence improving industrial and global management of this solid waste.

It is demonstrated numerically that higher solids flowrates to the reactor could be achieved by using higher gas flowrate (Q), higher distance between the air and riser inlets

(z), as well as by maintaining high solids inventories within the feeder vessel. Besides, in terms of the system design, a lower spouted bed cone angle (γ) increases both the solids flowrate and the solids storage capacity, which is appealing for feeder's implementation in larger-scale processes. The spouted bed is also reliable to feed SCGs into risers of different internal diameters (D_R), which is appealing for their implementation in existing units. The larger D_R, the greater the solids flowrate achieved in the reactor, however with increasing demand for Q to reach pneumatic transport.

The CFD framework can be further used to meet specific requirements of industrial processes with SCGs and may be extended for the feeding of SCGs with different size and moisture content. Finally, it can be also used to study the feeding of other biomass residues after validation against experimental data.

7.1.6. Acknowledgements

The authors would like to thank the São Paulo Research Foundation (2016/25946-2 and 2018/11031-8), the Australian Research Council (IH140100035, DE180100266) and CAPES (Finance code 001) for financial support.

7.1.7. Nomenclature

D_R	Riser diameter (cm)
d_s	Solid phase diameter (m)
FPL	Friction packing limit
g	Gravitational constant ($m \cdot s^{-2}$)
$g_{0,ss}$	Radial distribution function
H_S	Solids inventory in the spouted bed
I_{2D}	Second invariant of deviatoric stress tensor
I	Unit tensor
K_{fs}	Fluid-solid interaction coefficient ($kg \cdot m^{-3} \cdot s^{-1}$)
n	Unitary vector normal to the wall
p	Static pressure ($kg \cdot m^{-1} \cdot s^{-2}$)
p_s	Solids pressure ($kg \cdot m^{-1} \cdot s^{-2}$)
Q	Gas flowrate ($L \cdot min^{-1}$)
RC	Restitution coefficient

SC	Specularity coefficient
v_f	Fluid velocity ($m \cdot s^{-1}$)
v_s	Solids velocity ($m \cdot s^{-1}$)
$v_{s,w}$	Solid velocity at the wall ($m \cdot s^{-1}$)
W_S	Solids flowrate ($g \cdot s^{-1}$)
z	Distance of gas inlet and rise bottom riser end (cm)
Greek symbols	
α_f	Gas volume fraction
α_s	Solids volume fraction
$\alpha_{s,max}$	Solids packing limit
Δ	Parameter variation (-)
$\gamma_{\theta s}$	Energy dissipation ($kg \cdot m^{-3} \cdot s^{-1}$)
γ	Spouted bed cone angle (°)
$\kappa_{\theta s}$	Turbulence quantities of fluid phase ($m^2 \cdot s^{-2}$)
λ_s	Solids bulk viscosity ($kg \cdot m^{-1} \cdot s^{-1}$)
μ_s	Solids shear viscosity ($kg \cdot m^{-1} \cdot s^{-1}$)
$\mu_{s,col}$	Solids collisional viscosity ($kg \cdot m^{-1} \cdot s^{-1}$)
$\mu_{s,fri}$	Solids frictional viscosity ($kg \cdot m^{-1} \cdot s^{-1}$)
$\mu_{s,kin}$	Solids kinetic viscosity ($kg \cdot m^{-1} \cdot s^{-1}$)
π	Pi number
ρ_f	Air density ($kg \cdot m^{-3}$)
ρ_s	Particle density ($kg \cdot m^{-3}$)
ϕ	Angle of internal friction (°)
θ_s	Granular temperature ($m^2 \cdot s^{-2}$)
τ_f	Air stress tensor ($kg \cdot m^{-1} \cdot s^{-2}$)
τ_s	Particle stress tensor ($kg \cdot m^{-1} \cdot s^{-2}$)

CAPÍTULO 8 – CONSIDERAÇÕES FINAIS

Nesta tese foi mostrada a viabilidade da utilização de válvulas não-mecânicas tipo L e tipo leito de jorro para promover a alimentação contínua de pós de resíduos de biomassa a reatores tipo LPC. Abaixo são elencadas as principais conclusões da tese, cumprindo os objetivos específicos propostos na Seção 1.1:

- Realizou-se a caracterização física de borras de café com tamanhos médios entre 225 e 550 μm e com umidade até aproximadamente 60%. As amostras foram classificadas como *Geldart A* e *Geldart B* e com densidade *bulk* entre 262 e 471 kg/m³ dependendo do estado de compactação e da porcentagem de partículas finas na amostra. A massa específica real e aparente das amostras secas foram de 1315 e 1120 kg/m³, respectivamente, e as micrografias eletrônicas mostraram partículas irregulares e com rugosidades superficiais para este resíduo de biomassa;
- A escoabilidade das amostras de borra de café foi avaliada por meio de diferentes técnicas, observando-se *IH* entre 1,17 e 1,62 (classificação de *boa* a *péssima*), AoR^e entre 42,0 e 54,9° (classificação de *razoável* a *ruim*) e AoR^d entre 42 e 70º (classificação de *boa* a *muito ruim*). Em geral, observou-se piora da escoabilidade com a presença de maior quantidade de partículas finas na amostra e de umidade acima de 50%, devido à intensificação de forças do tipo van der Waals e tipo pontes líquidas, respectivamente. Verificou-se, ainda, melhora na escoabilidade para amostras com 30% de umidade, indicando que houve ação lubrificante da água nesta condição de saturação. Por fim, foram propostos uma correlação entre o índice de Hausner e o ângulo de repouso estático e um diagrama ternário de

composições granulométricas visando facilitar o monitoramento e controle da escoabilidade de borras de café durante o processamento.

- Avaliou-se, experimentalmente, a alimentação de borras de café secas com tamanho médio de 400 μm e com 10% de finos de 225 μm, bem como com 30% de umidade e 400 μm para um *riser* de 21 mm de diâmetro, utilizando a válvula-L e o leito de jorro. Em geral, os dispositivos se mostraram promissores para manter a estabilidade da vazão de borras de café ao reator pneumático, com flutuação da vazão de sólidos inferior a 20% em condições de operação estável dos alimentadores. Destaca-se, ainda, a fácil operação dos dispositivos e a boa correlação entre a vazão de sólidos e a pressão medida, o que permite o monitoramento e controle da alimentação de sólidos ao reator durante o processamento. O ângulo de repouso dinâmico foi relacionado qualitativamente com o escoamento das amostras de borra de café nos alimentadores, verificando-se menor e maior vazão de sólidos para as amostras de pior e melhor escoabilidades, respectivamente.
- Mais especificamente, verificou-se que a alimentação de borras de café com umidade de 30% e tamanho médio de 400 μm foi adequadamente controlada com ambos os alimentadores, com faixa de vazão de sólidos entre 1,2 e 10 g/s para a válvula-L e entre 3,8 e 6,0 g/s para o leito de jorro. No entanto, o leito de jorro apresentou menos instabilidades de operação e melhores resultados na dosagem das amostras secas, com faixa de vazão de sólidos entre 1,2 e 11 g/s, portanto sendo considerado um alimentador mais versátil que a válvula-L na escala experimental analisada. Ambos os alimentadores apresentaram perda de carga inferior a 1 kPa o que é atrativo para sua implementação em processos de maior escala.

- A alimentação de borra de café com a válvula-L e com o leito de jorro foram quantitativamente descritas via simulações em *CFD* utilizando o modelo duplo-fluido (*Two-Fluid Model*, TFM). A diferença entre a vazão de sólidos experimental e a predita pelas simulações, para diversas condições de operação, foi, em geral, inferior a 20% para a válvula-L e inferior a 10% para o leito de jorro, o que está compreendido nas flutuações de vazão de sólidos em regime de operação estável. Com as simulações *TFM* validadas, verificou-se detalhes sobre a dinâmica de escoamento gás-sólido nas diversas regiões dos alimentadores e do *riser*, em termos de contornos de fração volumétrica e vetores de velocidade de ar e sólido, o que são informações de difícil obtenção experimentalmente. Ademais, destacou-se a importância em se realizar uma calibração prévia dos parâmetros do modelo relativos ao araste gás-sólido, bem como à interação sólido-sólido e sólido-equipamento para a obtenção de resultados confiáveis em termos quantitativos e qualitativos.
- Por fim, analisou-se, via *CFD*, novas condições de operação e diferentes geometrias de alimentador e *riser* para a alimentação de borra de café com o leito de jorro. Em resumo, a vazão de sólidos máxima pôde ser aumentada de 11 g/s para 30 g/s por meio da utilização de maiores vazões de ar no leito de jorro; com o aumento da distância entre as entradas de ar e do *riser*; por meio da operação do leito de jorro preenchido com sólidos; com a utilização de leitos de jorro com cones mais inclinados; e por meio da alimentação de reatores com maiores diâmetros internos.

- As simulações se mostraram ferramentas eficazes e com vantajoso custo-benefício para otimizar a alimentação de borras de café ou implementar os alimentadores em aplicações comerciais de maior escala.

Em virtude dos resultados mostrados nesta tese e ciente que ainda há muitas investigações para serem efetuadas, deixo algumas sugestões para trabalhos futuros:

- Otimizar a alimentação de borras de café com os alimentadores tipo leito de jorro e válvula-L, por exemplo, por meio da utilização de simulações TFM, objetivando: avaliar novas condições de operação e geometrias para os alimentadores; representar a alimentação de borras de café com diferentes propriedades (umidade e distribuição granulométrica); auxiliar na construção de alimentadores para experimentos com objetivos específicos.
- Comparar os resultados da alimentação de borras de café via simulações TFM com simulações utilizando a abordagem CFD-DEM.
- Avaliar experimentalmente a alimentação de borras de café com os alimentadores tipo leito de jorro e válvula-L para leitos pneumáticos circulantes de maior escala.
- Avaliar o desempenho de alimentadores mecânicos para a alimentação de borras de café com diferentes propriedades;
- Analisar a alimentação de outros resíduos de biomassas de interesse industrial e com escoabilidade dificultada utilizando os alimentadores não-mecânicos.
- Propor equações com parâmetros adimensionais para o projeto e operação de alimentadores tipo válvula-L e leito de jorro.

LISTA DE PUBLICAÇÕES E CONGRESSOS

Os resultados desta tese foram divulgados em congressos nacionais e internacionais, bem como via publicações em periódicos, conforme listado abaixo.

Artigos publicados em periódicos

R6. **MASSARO SOUSA, L.**; FERREIRA, M. C.; HOU, Q. F.; YU, A. B. (2020) "Feeding of Spent Coffee Grounds to Reactors: TFM Modelling of a Non-mechanical Spouted Bed Type Feeder". Waste Management, v. 109, pp. 161-170.

R5. **MASSARO SOUSA, L.**; FERREIRA, M. C. (2020) "On the Performance of a Spouted Bed Device for Feeding Spent Coffee Grounds to a Circulating Fluidized Bed Reactor". Chemical Engineering Research and Design, v. 160, pp. 31-38.

R4. **MASSARO SOUSA, L.**; FERREIRA, M. C. (2020) "Analysis of the Performance of an L-Valve Feeding Spent Coffee Ground Powders into a Circulating Fluidized Bed". Powder Technology, v. 362, pp. 759-769.

R3. **MASSARO SOUSA, L.**; FERREIRA, M. C.; HOU, Q. F.; YU, A. B. (2020) "Feeding Spent Coffee Ground Powders with a Non-Mechanical L-valve: Experimental Analysis and TFM Simulation". Powder Technology, v. 360, pp. 1055-1066.

R2. **MASSARO SOUSA, L.**; FERREIRA, M. C. (2019) "Densification Behavior of Dry Spent Coffee Ground Powders: Experimental Analysis and Predictive Methods. Powder Technology, v. 357, pp. 149-157.

R1. **MASSARO SOUSA, L.**; FERREIRA, M. C. (2019) "Spent Coffee Grounds as a Renewable Source of Energy: Analysis of Bulk Powder Flowability". Particuology, v. 43, pp. 92-100.

Trabalhos publicados em anais de congressos

C9. **MASSARO SOUSA, L.**; FERREIRA, M. C.; HOU, Q. F.; YU, A. B. (2019) "Two-Fluid Model Simulation of Feeding Spent Coffee Ground Powders to a Riser with a Non-Mechanical L-valve". In: 9th Annual Chemical Engineering Postgraduate Association (CEPA) Conference, Clayton, Australia.

C8. **MASSARO SOUSA, L.**; FERREIRA, M. C. (2019) "Analysis of L-Valve Performance Feeding Spent Coffee Ground Powders into a Circulating Fluidized Bed". In: XVI Fluidization, Guilin, China.

C5. SOUSA, M. M.; **MASSARO SOUSA, L.**; FREIRE, J. T. (2019) "Avaliação do Desempenho de uma Célula de Dawes Utilizando Açúcar VHP". In: XIII Congresso Brasileiro de Engenharia Química em Iniciação Científica (COBEQ-IC), Belo Horizonte, Brasil.

C4. **MASSARO SOUSA, L.**; GENEROSO, B.; ZUTIN, G. M.; ITO, K. K. M.; MELO, M. B.; FERREIRA, M. C.; FREIRE, F. B. (2019) "Influência da Umidade nos Ângulos de Repouso Estático e Dinâmico de Diferentes Tipos de Açúcares". In: Simpósio Comemorativo dos 40 Anos da Área de Sistemas Particulados do DEQ/UFSCar, São Carlos, Brasil.

C3. **MASSARO SOUSA, L.**; FERREIRA, M. C. (2019) "Dispositivos Alimentadores de Sistemas Particulados e sua Operação com Pós de Escoabilidade Difícil". In: Simpósio Comemorativo dos 40 Anos da Área de Sistemas Particulados DEQ/UFSCar, São Carlos, Brasil.

C4. **SOUSA, L. M**.; FERREIRA, M. C. (2018) "Analysis of the Operation of an L-valve Feeding Dry Spent Coffee Ground". In: XXII Congresso Brasileiro de Engenharia Química (COBEQ), São Paulo, Brasil.

C3. **SOUSA, L. M.**; FERREIRA, M. C. (2018) "Flowability of Dry Spent Coffee Ground (SCG) Powders". In: 8º World Congress on Particle Technology, Orlando, USA.

C2. **SOUSA, L. M.**; FERREIRA, M. C. (2017) "Estudo sobre o Escoamento Aerado de Pós de Serragem de Pinheiro (*Pinus elliottii*) na Descarga de Reservatórios". In: XXXVIII Congresso Brasileiro de Sistemas Particulados (ENEMP), Maringá, Brasil.

C1. **SOUSA, L. M.**; FERREIRA, M. C. (2017) "Análise sobre a Compactação Gravitacional de Pós de Serragem de Pinheiro (*Pinus elliottii*)". In: 69ª Reunião Anual da SBPC, Belo Horizonte, Brasil.

Capítulos de livros

L1. **MASSARO SOUSA, L.**; FERREIRA, M. C. (2019) "Dispositivos Alimentadores de Materiais Particulados e sua Operação com Pós de Escoabilidade Difícil". In: Freire, J. T.; Albini, G. (org.) Tópicos Especiais em Sistemas Particulados, Edição Comemorativa dos 40 Anos da Área de Sistemas Particulados do DEQ/UFSCar, ISBN: 978-859-131-163-1, v. 5, pp. 117-143, São Carlos, Brasil.

REFERÊNCIAS BIBLIOGRÁFICAS

ABDULLAH, E.; GELDART, D. The use of bulk density measurements as a flowability indicator. **Powder Technology**, v. 102, p. 151–165, 1999.

AL-HAMAMRE, Z. et al. Oil extracted from spent coffee grounds as a renewable source for fatty acid methyl ester manufacturing. **Fuel**, v. 96, p. 70–76, 2012.

ALTHAUS, T. O.; WINDHAB, E. J. Characterization of wet powder flowability by shear cell measurements and compaction curves. **Powder Technology**, v. 215–216, p. 59–65, 2012.

ARASTOOPOUR, H. Computational Fluid Dynamics (CFD) Application in Fluid/Particle Flow Systems. **Journal of Powder Metallurgy & Mining**, v. 02, n. 1, p. 1–2, 2013.

ARASTOOPOUR, H.; GIDASPOW, D.; ABBASI, E. **Computational Transport Phenomena of Fluid-Particle Systems**. 1. ed. [s.l.] Springer International Publishing, 2017.

ARENA, U.; LANGELI, C. B.; CAMMAROTA, A. L-valve behaviour with solids of different size and density. **Powder Technol**, v. 98, p. 231–240, 1998.

ASTM INTERNATIONAL. Standard test method for measuring the angle of repose of free-flowing mold powders. **ASTM C1444-00**, n. 1, p. 15–16, 2000.

ASTM INTERNATIONAL. Standard test method for sieve analysis of fine and coarse aggregates. **ASTM C136-01**, p. 1–5, 2010.

ATABANI, A. E. et al. Valorization of spent coffee grounds into biofuels and value-added products: Pathway towards integrated bio-refinery. **Fuel**, v. 254, n. 115640, p. 1–20, 2019.

BALLESTEROS, L. F.; TEIXEIRA, J. A.; MUSSATTO, S. I. Chemical, functional, and structural properties of spent coffee grounds and coffee silverskin. **Food and**

Bioprocess Technology, v. 7, n. 12, p. 3493–3503, 2014.

BAO, X.; DU, W.; XU, J. An overview on the recent advances in computational fluid dynamics simulation of spouted beds. **The Canadian Journal of Chemical Engineering**, v. 91, n. 11, p. 1822–1836, 2013.

BENEDITO, W. M. et al. An investigation of CFD simulations capability in treating non-spherical particle dynamics in a rotary drum. **Powder Technology**, v. 332, p. 171–177, 2018.

BODHMAGE, A. **Correlation between physical properties and flowability indicators for fine powders**. [s.l.] University of Saskatchewan, 2006.

BRAZILIAN COFFEE EXPORTERS COUNCIL. **Monthly coffee report**. Disponível em: <http://www.cecafe.com.br/en/publications/monthly-exports-report/>. Acesso em: 2 mar. 2018.

BRIDGWATER, A. V. Renewable fuels and chemicals by thermal processing of biomass. **Chemical Engineering Journal**, v. 91, p. 87–102, 2003.

CAMPOS-VEGA, R. et al. Spent coffee grounds: a review on current research and future prospects. **Trends in Food Science & Technology**, v. 45, p. 24–36, 2015.

CAMPOS, M. M.; FERREIRA, M. C. A comparative analysis of the flow properties between two alumina-based dry powders. **Advances in Materials Science and Engineering**, v. 2013, n. 519846, p. 1–7, 2013.

CASTELLANOS, A. The relationship between attractive interparticle forces and bulk behaviour in dry and uncharged fine powders. **Advances in Physics**, v. 54, n. 4, p. 263–376, 2005.

CHAN, C. W. et al. Particle motion in L-valve as observed by positron emission particle tracking. **Powder Technology**, v. 193, p. 137–149, 2009.

CHENG, Y. et al. Inlet and outlet effects on flow patterns in gas-solid risers. **Powder**

Technology, v. 98, n. 2, p. 151–156, 1998.

CHOVICHIEN, N.; PIPATMANOMAI, S.; CHUNGPAIBULPATANA, S. Comprehensive study of pressure-drop balance and performance of an l-valve in a circulating fluidized bed. **Chemical Engineering Communications**, v. 200, p. 1483–1502, 2013.

CHU, K. W. et al. Model A vs. Model B in the modelling of particle-fluid flow. **Powder Technology**, v. 329, p. 47–54, 2018.

COSTA, I. A.; FERREIRA, M. C.; FREIRE, J. T. Analysis of regime transitions and flow instabilities in vertical conveying of coarse particles using different solids feeding systems. **The Canadian Journal of Chemical Engineering**, v. 82, n. 1, p. 48–59, 2004.

CUI, H.; GRACE, J. R. Spouting of biomass particles: A review. **Bioresource Technology**, v. 99, n. 10, p. 4008–4020, 2008.

DA ROSA, C. A.; FREIRE, J. T. Fluid dynamics analysis of a draft-tube continuous spouted bed with particles bottom feed using CFD. **Ind. Eng. Chem. Res.**, v. 48, p. 7813–7820, 2009.

DAI, J.; CUI, H.; GRACE, J. R. Biomass feeding for thermochemical reactors. **Progress in Energy and Combustion Science**, v. 38, p. 716–736, 2012.

DAOUS, M. A.; AL-ZAHRANI, A. A. Modeling solids and gas flow through an L-valve. **Powder Technology**, v. 99, p. 86–89, 1998.

DHIMAN, J. et al. Physical, ignition, and volatilization properties of biomass feedstocks dusts. **Transactions of the ASABE**, v. 58, n. 6, p. 1425–1437, 2016.

DI FELICE, R. The voidage function for fluid-particle interaction systems. **International Journal of Multiphase Flow**, v. 20, n. 1, p. 153–159, 1994.

DUARTE, C. R.; MURATA, V. V.; BARROZO, M. A. S. Experimental and numerical

study of spouted bed fluid dynamics. **Brazilian Journal of Chemical Engineering**, v. 25, n. 1, p. 95–107, 2008.

ELSAYED, K.; LACOR, C. Numerical modeling of the flow field and performance in cyclones of different cone-tip diameters. **Computers and Fluids**, v. 51, n. 1, p. 48–59, 2011.

FERREIRA, M. C.; FREIRE, J. T. Fluid Dynamics Characterization of a Pneumatic Bed Using a Spouted Bed Type Solid Feeding System. **The Canadian Journal of Chemical Engineering**, v. 70, p. 905–909, 1992.

FERREIRA, M. C.; SILVA, E. M. V.; FREIRE, J. T. Analysis of a one-dimensional fluid dynamic model for dilute gas-solid flow in a pneumatic dryer with a spouted bed type solid feeding system. **Drying Technology**, v. 16, n. 9–10, p. 1971–1985, 1998.

GELDART, D. Types of gass fluidization. **Powder Technology**, v. 7, n. 5, p. 285–292, 1973.

GELDART, D. et al. Characterization of powder flowability using measurement of angle of repose. **China Particuology**, v. 4, n. 3–4, p. 104–107, 2006.

GELDART, D.; JONES, P. The behaviour of L-valves with granular powders. **Powder Technol**, v. 67, p. 163–174, 1991.

GHADIRIAN, E.; ABBASIAN, J.; ARASTOOPOUR, H. CFD simulation of gas and particle flow and a carbon capture process using a circulating fluidized bed (CFB) reacting loop. **Powder Technology**, v. 344, p. 27–35, 2019.

GHADIRIAN, E.; ARASTOOPOUR, H. Numerical analysis of frictional behavior of dense gas–solid systems. **Particuology**, v. 32, p. 178–190, 2017.

GIDASPOW, D. **Multiphase flow and fluidization**. [s.l.] Academic Press, 1994.

GIDASPOW, D.; BEZBURUAH, R.; DING, J. Hydrodynamics of circulating fluidized beds: kinetic theory approach. **7th Fluidization Conference**, p. 1–5, 1992.

GIDASPOW, D.; JIRADILOK, V. **Computational techniques: The multiphase CFD approach to fluidization and green energy technologies**. [s.l.] Nova Science Publishers, 2009.

GRACE, J. R.; AVIDAN, A. A.; KNOWLTON, T. M. **Circulating Fluidized Beds**. 1. ed. [s.l.] Chapman & Hall, 1997.

GUJJULA, R.; MANGADODDY, N. Prediction of Solid Recirculation Rate and Solid Volume Fraction in an Internally Circulating Fluidized Bed. **International Journal of Computational Methods**, v. 12, n. 4, p. 1540005-1–24, 2015.

GUO, Z. et al. Study of flow characteristics of biomass and biomass-coal blends. **Fuel**, v. 141, p. 207–213, 2015.

HOOSHDARAN, B. et al. CFD modeling of heat transfer and hydrodynamics in a draft tube conical spouted bed reactor under pyrolysis conditions: Impact of wall boundary condition. **Appied Thermal Engineering**, v. 127, p. 224–232, 2017.

HOSSEINI, S. H. Influences of geometric factors on CFD results of a draft tube cylindrical spouted bed. **Progress in Computational Fluid Dynamics**, v. 16, n. 2, p. 78–87, 2016.

HOSSEINI, S. H.; ZIVDAR, M.; RAHIMI, R. CFD simulation of gas–solid flow in a spouted bed with a non-porous draft tube. **Chemical Engineering and Processing**, v. 48, p. 1539–1548, 2009.

HOU, Q. et al. How to generate valid local quantities of particle–fluid flows for establishing constitutive relations. **AIChE Journal**, v. 65, n. e16690, p. 13, 2019.

HUILIN, L.; GIDASPOW, D. Hydrodynamics of binary fluidization in a riser: CFD simulation using two granular temperatures. **Chemical Engineering Science**, v. 58, p. 3777–3792, 2003.

ILIC, D. et al. On the challenges facing the handling of solid biomass feedstocks.

Biofuels, Bioproducts and Biorefining, v. 12, n. 2, p. 187–202, 2018.

INSTANT COFFEE MARKET. **Instant coffee market: global industry trends, share, size, growth, opportunity and forecast 2018-2023**. Disponível em: <http://www.imarcgroup.com/instant-coffee-processing-plant>. Acesso em: 15 jul. 2019.

INTERNATIONAL COFFEE ORGANIZATION. **Total coffee production by all exporting countries**. Disponível em: <http://www.ico.org/prices/po-production.pdf>. Acesso em: 2 mar. 2018.

INTERNATIONAL COFFEE ORGANIZATION. **World Coffee Consumption**. Disponível em: <http://www.ico.org/>. Acesso em: 15 nov. 2019.

JONO, K. et al. A review of particulate design for pharmaceutical powders and their production by spouted bed coating. **Powder Technology**, v. 113, n. 3, p. 269–277, 2000.

KARMAKAR, M. K.; DATTA, A. B. Hydrodynamics of a dual fluidized bed gasifier. **Advanced Powder Technology**, v. 21, p. 521–528, 2010.

KARMEE, S. K. A spent coffee grounds based biorefinery for the production of biofuels, biopolymers, antioxidants and biocomposites. **Waste Management**, v. 72, p. 240–254, 2018.

KELKAR, S. et al. Pyrolysis of spent coffee grounds using a screw-conveyor reactor. **Fuel Processing Technology**, v. 137, p. 170–178, 2015.

KIM, J. et al. Anaerobic co-digestion of spent coffee grounds with different waste feedstocks for biogas production. **Waste Management**, v. 60, p. 322–328, 2017.

KIM, J.; TACHINO, R.; TSUTSUMI, A. Effects of solids feeder and riser exit configuration on establishing high density circulating fluidized beds. **Powder Technol**, v. 187, p. 37–45, 2008.

KNOWLTON, T. M.; HIRSAN, I. L-valves characterized for solids flow. **Hydrocarbon Processing**, v. 57, n. 3, p. 149–156, 1978.

KONDAMUDI, N.; MOHAPATRA, S. K.; MISRA, M. Spent coffee grounds as a versatile source of green energy. **Journal of Agricultural and Food Chemistry**, v. 56, p. 11757–11760, 2008.

KYZAS, G. Z.; LAZARIDIS, N. K.; MITROPOULOS, A. C. Removal of dyes from aqueous solutions with untreated coffee residues as potential low-cost adsorbents: Equilibrium, reuse and thermodynamic approach. **Chemical Engineering Journal**, v. 189–190, p. 148–159, 2012.

LAM, P. S.; SOKHANSANJ, S. Engineering properties of biomass. In: SHASTRI, Y. et al. (Eds.). . **Engineering and Science of Biomass Feedstock Production and Provision**. 1. ed. New York: Springer New York, 2014. v. 1p. 17–35.

LI, P.; KANDA, H.; MAKINO, H. Simultaneous production of bio-solid fuel and bio-crude from vegetal biomass using liquefied dimethyl ether. **Fuel**, v. 116, p. 370–376, 2014.

LI, Q. et al. Interparticle van der Waals force in powder flowability and compactibility. **International Journal of Pharmaceutics**, v. 280, p. 77–93, 2004.

LIM, J. H. et al. Pressure change and control of the solid circulation rate of Geldart A particles in a small diameter L-valve. **Powder Technology**, v. 243, p. 139–148, 2013.

LITTMAN, H. et al. Modeling and measurement of the effective drag coefficient in decelerating and non-accelerating turbulent gas—solids dilute phase flow of large particles in a vertical transport pipe. **Powder technology**, v. 77, p. 267–283, 1993.

LITTMAN, H.; PACCIONE, J. D. New Type of Draft Tube Spout-Fluid Bed. Part 2: Modeling and Design of the Acceleration Section of the Riser for the Pneumatic Transport of 1 mm Glass Spheres. **Industrial and Engineering Chemistry Research**,

v. 54, n. 23, p. 6187–6198, 2015.

LIU, Y. et al. Direct transesterification of spent coffee grounds for biodiesel production. **Fuel**, v. 199, p. 157–161, 2017.

LOPES, C. S. et al. Influence of the entrance configuration on the performance of a Non-Mechanical Solid Feeding Device for a pneumatic dryer. **Drying Technology**, v. 29, n. 10, p. 1186–1194, 2011a.

LOPES, C. S. Estudo da alimentação de sólidos em sistemas de transporte pneumático. **Tese de doutorado em Engenharia Química, Universidade Federal de São Carlos**, p. 147, 2011.

LOPES, C. S. et al. Influence of the entrance configuration on the performance of a non-mechanical solid feeding device for a pneumatic dryer. **Drying Technology**, v. 29, p. 1186–1194, 2011b.

LUMAY, G. et al. Measuring the flowing properties of powders and grains. **Powder Technology**, v. 224, p. 19–27, 2012.

LUN, C. K. K. et al. Kinetic theories for granular flow: Inelastic particles in Couette flow and slightly inelastic particles in a general flowfield. **Journal of Fluid Mechanics**, v. 140, n. June, p. 223–256, 1984.

MARCHELLI, F. et al. Comparison of different drag models in CFD-DEM simulations of spouted beds. **Powder Technol**, p. Accepted, 2019.

MARINELLI, J.; CARSON, J. W. Solve solids flow problems in bins, hoppers, and feeders. **Chemical Engineering Progress**, v. 88, n. 5, p. 22–28, 1992.

MASSARO SOUSA, L. et al. Feeding Spent Coffee Ground Powders with a Non-Mechanical L-valve: Experimental Analysis and TFM Simulation. **Powder Technology**, v. 360, p. 1055–1066, 2020.

MASSARO SOUSA, L.; FERREIRA, M. C. Spent coffee grounds as a renewable

source of energy: An analysis of bulk powder flowability. **Particuology**, v. 43, p. 92–100, 2019a.

MASSARO SOUSA, L.; FERREIRA, M. C. Densification behavior of dry spent coffee ground powders: Experimental analysis and predictive methods. **Powder Technology**, v. 357, p. 149–157, 2019b.

MASSARO SOUSA, L.; FERREIRA, M. C. Analysis of the Performance of an L-Valve Feeding Spent Coffee Ground Powders into a Circulating Fluidized Bed. **Powder Technology**, v. 362, p. 759–769, 2020a.

MASSARO SOUSA, L.; FERREIRA, M. C. On the Performance of a Spouted Bed type Device for Feeding Spent Coffee Grounds to a Circulating Fluidized Bed Reactor. **Chemical Engineering Research and Design**, v. 160, p. 31–38, 2020b.

MATHUR, K. B.; GISHLER, P. E. A technique for contacting gases with coarse solid particles. **AIChE Journal**, v. 1, n. 2, p. 157–164, 1955.

MCKENDRY, P. Energy production from biomass (part 1): overview of biomass. **Bioresouce Technology**, v. 83, p. 37–46, 2002.

MCNUTT, J.; HE, Q. Spent coffee grounds: A review on current utilization. **Journal of Industrial and Engineering Chemistry**, v. 71, p. 78–88, 2019.

MOLINER, C. et al. Sensitivity analysis and validation of a Two Fluid Method (TFM) model for a spouted bed. **Chemical Engineering Science**, v. 207, p. 39–53, 2019.

MONAZAM, E. R. et al. Analysis of solids flow rate through nonmechanical L-valve in an industrial-scale circulating fluidized bed using group B particles. **Industrial and Engineering Chemistry Research**, v. 57, p. 11439–11451, 2018.

MURTHY, P. S.; NAIDU, M. M. Production and application of xylanase from Penicillium sp. utilizing coffee by-Products. **Food Bioprocess Technol.**, v. 5, p. 657–664, 2012.

MUSSATTO, S. I. et al. Production, composition, and application of coffee and its industrial residues. **Food and Bioprocess Technology**, v. 4, p. 661–672, 2011.

NELSON, R. D. **Why study particle science?**

NIKOLOPOULOS, A. et al. Investigation of proper modeling of very dense granular flows in the recirculation system of CFBs. **Particuology**, v. 10, n. 6, p. 699–709, 2012.

OSMAN, A. I. et al. Reusing, recycling and up-cycling of biomass: A review of practical and kinetic modelling approaches. **Fuel Processing Technology**, v. 192, p. 179–202, 2019.

PÁDUA, T. F.; BÉTTEGA, R.; FREIRE, J. T. Gas-solid flow behavior in a pneumatic conveying system for drying applications: coarse particles feeding with a venturi device. **Advances in Chemical Engineering and Science**, v. 05, p. 225–238, 2015.

RAHIMI-AHAR, Z.; HATAMIPOUR, M. S. Hydrodynamics, numerical study and application of spouted bed. **Reviews in Chemical Engineering**, v. 34, n. 6, p. 743–766, 2018.

RAMAGE, J.; SCURLOCK, J. Biomass. In: BOYLE, G. (Ed.). . **Renewable energy: power for a sustainable future**. [s.l.] Oxford University Press, 1996. v. 1p. 137–182.

RAMÍREZ-GÓMEZ, A. Research needs on biomass characterization to prevent handling problems and hazards in industry. **Particulate Science and Technology**, v. 34, n. 4, p. 432–441, 2016.

ROACHE, P. J. Perspective: A method for uniform reporting of grid refinement studies. **Journal of Fluids Engineering**, v. 116, n. 1994, p. 405–413, 1994.

RONG, L. W.; DONG, K. J.; YU, A. B. Lattice-Boltzmann simulation of fluid flow through packed beds of uniform spheres: Effect of porosity. **Chemical Engineering Science**, v. 99, p. 44–58, 2013.

SAIDI, M.; BASIRAT TABRIZI, H.; GRACE, J. R. A review on pulsed flow in gas-

solid fluidized beds and spouted beds: Recent work and future outlook. **Advanced Powder Technology**, v. 30, n. 6, p. 1121–1130, 2019.

SANTOS, C. et al. Effect of different rates of spent coffee grounds (SCG) on composting process, gaseous emissions and quality of end-product. **Waste Management**, v. 59, p. 37–47, 2017.

SANTOS, D. A. et al. Experimental and CFD study of the hydrodynamic behavior in a rotating drum. **Powder Technology**, v. 250, p. 52–62, 2013.

SANTOS, L. C.; CONDOTTA, R.; FERREIRA, M. C. Flow properties of coarse and fine sugar powders. **Journal of Food Process Engineering**, v. 41, n. 2, p. 1–10, 2017.

SHUYAN, W. et al. Hydrodynamic simulations of gas-solid spouted bed with a draft tube. **Chemical Engineering Science**, v. 65, n. 4, p. 1322–1333, 2010.

SILVA, E. M. V.; FERREIRA, M. C.; FREIRE, J. T. Mean voidage measurements and fluid dynamic analysis in a circulating fluidized bed with a spouted bed type solid feeding system. **2nd European Thermal-Sciences conference**, p. 1–8, 1996.

SILVA, M. A. et al. The use of biomass residues in the Brazilian soluble coffee industry. **Biomass and Bioenergy**, v. 14, n. 5–6, p. 457–467, 1998.

SINGH, P. C. et al. Thermophysical properties of fresh and roasted coffee powders. **Journal of Food Process Engineering**, v. 20, n. 1, p. 31–50, 1997.

SMOLDERS, K.; BAEYENS, J. The operation of L-valves to control standpipe flow. **Advanced Powder Technology**, v. 6, n. 3, p. 163–176, 1995.

SOUSA, R. C. et al. Analysis of fluid dynamics and thermal behavior using a vertical conveyor with a spouted bed feeder. **Drying Technology**, v. 28, n. 11, p. 1277–1287, 2010.

SWART, S. D.; BOATENG, A. A. Dual fluidised bed design for the fast pyrolysis of biomass. **Tappsa Journal**, v. 2, p. 231–243, 2012.

SYAMLAL, M.; O´BRIEN, T. J. Computer Simulation of Bubbles in a Fluidized Bed. **AICHE Symp.**, n. 85, p. 22–31, 1989.

SZAFRAN, R. G.; KMIEC, A.; LUDWIG, W. CFD modeling of a spouted-bed dryer hydrodynamics. **Drying Technology**, v. 23, n. 8, p. 1723–1736, 2005.

TAN, G.; MORTON, D. A. V.; LARSON, I. On the methods to measure powder flow. **Current Pharmaceutical Design**, v. 21, n. 40, p. 5751–5765, 2015.

THIAGAMANI, S. M. K. et al. Utilization of chemically treated municipal solid waste (spent coffee bean powder) as reinforcement in cellulose matrix for packaging applications. **Waste Management**, v. 69, p. 445–454, 2017.

TONG, H. et al. Hydrodynamic modeling of the L-valve. **Powder Technology**, v. 129, n. 1–3, p. 8–14, 2003.

VIEIRA NETO, J. L. et al. Effect of a draft tube on the fluid dynamics of a spouted bed: Experimental and CFD studies. **Drying Technology**, v. 26, n. 3, p. 299–307, 2008.

WAHYUDI, H.; CHU, K.; YU, A. 3D particle-scale modeling of gas-solids flow and heat transfer in fluidized beds with an immersed tube. **International Journal of Heat and Mass Transfer**, v. 97, p. 521–537, 2016.

WANG, D.; FAN, L. L-valve behavior in circulating fluidized beds at high temperatures for group D particles. **Industrial and Engineering Chemistry Research**, v. 54, p. 4468–4473, 2015.

WANG, M. et al. Full-loop simulation of gas-solids flow in a pilot-scale circulating fluidized bed. **Chemical Engineering and Technology**, v. 42, n. 4, p. 932–939, 2019.

WANG, Y. et al. Pressure drop prediction with a modified frictional-kinetic model for alumina in bypass pneumatic conveying system. **International Journal of Multiphase Flow**, v. 79, p. 159–171, 2016a.

WANG, Y. et al. Gas–solid flow behaviour prediction for sand in bypass pneumatic

conveying with conventional frictional-kinetic model. **Applied Mathematical Modelling**, v. 40, n. 23–24, p. 9947–9965, 2016b.

WORLD HEALTH ORGANIZATION. **Bulk density and tapped density of powders**. Disponível em: <https://particle.dk/methods-analytical-laboratory/bulk-and-tapped-density/>. Acesso em: 2 mar. 2018.

WOUTERS, I. M. F.; GELDART, D. Characterising semi-cohesive powders using angle of repose. **Particle & Particle Systems Characterization**, v. 13, p. 254–259, 1996.

XIONG, X. et al. Value-added chemicals from food supply chain wastes: State-of-the-art review and future prospects. **Chemical Engineering Journal**, v. 375, n. 121983, p. 1–24, 2019.

XU, Y. et al. Numerical simulation and experimental study of the gas-solid flow behavior inside a full-loop circulating fluidized bed: evaluation of different drag models. **Industrial and Engineering Chemistry Research**, v. 57, n. 2, p. 740–750, 2018.

XUEYAO, W. et al. Numerical simulation for the loop seal in the circulating fluidized bed and experimental validation. **Applied Thermal Engineering**, v. 52, p. 141–149, 2013.

YANG, J. et al. The impact of downstream processing methods on the yield and physiochemical properties of hydrothermal liquefaction bio-oil. **Fuel Processing Technology**, v. 178, p. 353–361, 2018.

YANG, T. Y.; LEU, L. P. Multi-resolution analysis of wavelet transform on pressure fluctuations in an L-valve. **International Journal of Multiphase Flow**, v. 34, p. 567–579, 2008.

YANG, W. C.; KNOWLTON, T. M. L-valve equations. **Powder Technol**, v. 77, p. 49–

54, 1993.

YU, A. B.; BRIDGWATER, J.; BURBIDGE, A. On the modelling of the packing of fine particles. **Powder Technology**, v. 92, n. 3, p. 185–194, 1997.

YU, A. B.; STANDISH, N. Estimation of the porosity of particle mixtures by a linear-mixture packing model. **Industrial and Engineering Chemistry Research**, v. 30, n. 6, p. 1372–1385, 1991.

YU, A. B.; ZOU, R. P.; STANDISH, N. Modifying of the linear packing model for predicting the porosity of nonspherical particle mixtures. **Industrial and Engineering Chemistry Research**, v. 35, n. 10, p. 3730–3741, 1996.

ZARRINBAKHSH, N. et al. Characterization of wastes and coproducts from the coffee industry for composite material production. **BioResources**, v. 11, n. 3, p. 7637–7653, 2016.

ZHAO, W. Computation as a powerful tool for understanding particle systems: an interview with Aibing Yu. **National Science Review**, v. 5, n. 3, p. 342–345, 2018.

ZHONG, W. et al. DEM/CFD-DEM Modelling of Non-spherical Particulate Systems: Theoretical Developments and Applications. **Powder Technology**, v. 302, p. 108–152, 2016a.

ZHONG, W. et al. CFD simulation of dense particulate reaction system: Approaches, recent advances and applications. **Chemical Engineering Science**, v. 140, p. 16–43, 2016b.

ZHU, H. P. et al. Linking discrete particle simulation to continuum process modelling for granular matter: Theory and application. **Particuology**, v. 9, n. 4, p. 342–357, 2011.